

WELDING OF DISSIMILAR A5754-A5083 AND A6061- A6082 ALUMINIUM ALLOYS FOR AUTOMOTIVE APPLICATIONS

Thesis

submitted in partial fulfilment of the requirements for the degree of

DOCTOR OF PHILOSOPHY

by

R. RAJESHKUMAR
(158032MT15F09)



DEPARTMENT OF METALLURGICAL AND MATERIALS ENGINEERING
NATIONAL INSTITUTE OF TECHNOLOGY KARNATAKA
SURATHKAL, MANGALORE – 575025
OCTOBER, 2021

DECLARATION

I hereby declare that the Ph.D. Thesis entitled “**Welding of dissimilar A5754-A5083 and A6061- A6082 aluminium alloys for automotive applications**” which is being submitted to **National Institute of Technology Karnataka, Surathkal**, for the partial fulfillment of the requirement for the award of degree of **Doctor of Philosophy** in the **Department of Metallurgical and Materials Engineering** is a bonafide report of the work carried out by me. The material contained in this Ph. D. Thesis has not been submitted to any university or Institution for the award of any degree.



R. RAJESHKUMAR (158032MT15F09)

Department of Metallurgical and Materials Engineering,
National Institute of Technology Karnataka,
Surathkal, Mangalore, Karnataka, India

Place: NITK, SURATHKAL

Date: 11 OCTOBER 2021

CERTIFICATE

This is to certify that the Ph.D. Thesis entitled “**Welding of dissimilar A5754-A5083 and A6061- A6082 aluminium alloys for automotive applications**” submitted by **R. Rajeshkumar (158032MT15F09)**, as the record of the work carried out by him, is accepted as the Ph.D. Thesis submission in partial fulfillment of the requirements for the award of the degree of Doctor of Philosophy.



Dr. Kumkum Banerjee

Research Guide and Associate Professor,
Department of Metallurgical and
Materials Engineering,
National Institute of Technology Karnataka,
Surathkal, Mangalore, Karnataka, India



Dr. K. Devakumaran

Research Co-Guide and Manager,
Advanced Technology Products (ATP),
Bharat Heavy Electricals Limited (BHEL),
Trichy, Tamilnadu, India



Prof. K. N. Prabhu

Chairman – DRPC & Professor (HAG) and Head,
Department of Metallurgical and Materials Engineering,
National Institute of Technology Karnataka,
Surathkal, Mangalore, Karnataka, India

Chairman - DRPC

Dept. of Metallurgical and Materials Engineering
National Institute of Technology Karnataka, Surathkal,
Post Srividyannagar, Mangaluru - 575 025
Karnataka, India

Abstract

In the present study, dissimilar aluminium alloy combinations A6061 T6-A6082 T6 and A5754 H111-A5083 H111 were welded using the cold metal transfer (CMT), tungsten inert gas (TIG) welding and friction stir welding (FSW) processes. Each dissimilar combination was welded by two different fillers, such as ER4043 and ER5356, in CMT and TIG. Since FSW is a solid-state welding process, no filler materials were used. The miniature tensile samples were extracted from the interface regions of the TIG and CMT welded joints and the stir zone (SZ) of the FSWed joint. The TIG and CMT welded alloys' individual interface microstructure has been correlated with mechanical properties. The SZ of FSWed parts is of prime importance because this zone primarily decides the resulting property of the welded joint. Therefore, the microstructural features and mechanical properties of the SZ in the FSWed joints have been investigated in detail. The tensile properties of the overall weld region samples have been determined using macro-tensile testing samples. The dissimilar A6061-T6 and A6082-T6 joints welded by CMT and TIG welding processes using two different fillers (ER5356 and ER4043) exhibited higher strength in the A6082 interface in comparison to the A6061 interface. When the dissimilar A5754 and A5083 alloys were welded by CMT and TIG welding processes using two different fillers (ER5356 and ER4043) fillers, the interface region of the A5083 side exhibited higher strength than the interface region of the A5754. In the FSWed joints, the refined grain structure in SZ increased the hardness and strength. The overall joint tensile properties of the dissimilar joints are essential for identifying a suitable welding process to join A6061-A6082 and A5754-A5083 dissimilar alloys. Among the A6061-A6082 dissimilar joints, the CMT joint produced by ER5356 filler and the FSW joint exhibited higher tensile properties than the other joints. The tensile properties of the A6061-A6082 dissimilar CMT joint produced by ER5356 filler and the FSW joint are nearly the same. However,

the FSW process does not use any shielding gas, filler materials, and the surface preparation is also not critical for the process. These factors can play a vital role to reduce the cost of welding effectively. Also, the FSW process is environment friendly, due to the absence of fumes and shielding gases. In the case of A5754-A5083 dissimilar joints, the FSW joint shows higher tensile properties than the other joints. Therefore, the FSW process can be recommended as the preferable joining method among all the investigated processes.

Keywords: Welding, Dissimilar aluminium alloys, Microstructure, Mechanical properties

TABLE OF CONTENTS

LIST OF FIGURES	i
LIST OF TABLES	xxvii
NOMENCLATURE	xxxiii
CHAPTER 1	
INTRODUCTION	1
CHAPTER 2	
LITERATURE SURVEY	5
2.1 Joining	5
2.2 Classification of fusion welding process	6
2.3 Electric arc welding	
2.4 Common problems associated with fusion welding of aluminium alloys	8
2.5 Cold metal transfer welding process (CMT) of aluminium alloys	9
2.6 Gas tungsten arc welding process (GTAW) of aluminium alloys	13
2.7 Solid state welding	18
2.8 Friction stir welding (FSW) of aluminium alloys	19
2.8.1 Tool design for FSW	23
2.8.2 FSW parameters	26
2.9 Scientific motivation and critical comparison of the TIG, CMT and FSW techniques	27
2.10 Objectives	31
CHAPTER 3	
MATERIALS AND METHODS	33
3.1 Material	33
3.2 Edge preparation	34
3.3 Cleaning of materials	35
3.4 Backing plate	35
3.5 Clamping setup for materials	36

3.6	Shielding gases	37
3.7	Electrode used for TIG welding	37
3.8	Tool used for FSW	38
3.9	Welding equipment	39
3.9.1	TIG welding equipment	39
3.9.2	CMT welding equipment	40
3.9.3	FSW equipment	42
3.10	Metallography	43
3.11	Electron Back Scattered Diffractometry	45
3.12	Hardness and Tensile Testing	46
CHAPTER 4		
RESULTS AND DISCUSSION		51
4.1	Cold metal transfer (CMT) welding of dissimilar A6061-T6 and A6082-T6 using ER4043 filler wire	51
4.1.1	Surface appearance of the CMT welded A6061-T6 and A6082-T6 joint using ER4043 filler wire	51
4.1.2	Macrostructure of the CMT welded A6061-T6 and A6082-T6 joint using ER4043 filler wire	52
4.1.3	Microstructures of the interfaces and WMZ in CMT welded A6061-T6 and A6082-T6 joint using ER4043 filler wire	52
4.1.4	SEM-EDS of the CMT welded A6061-T6 and A6082-T6 joint interfaces using ER4043 filler wire	58
4.1.5	SEM-EDS of the precipitates at the HAZs in CMT welded A6061-T6 and A6082-T6 joint using ER4043 filler wire	61
4.1.6	Microhardness of the CMT welded A6061-T6 and A6082-T6 joint using ER4043 filler wire	65
4.1.7	Tensile properties of the CMT welded A6061-T6 and A6082-T6 joint using ER4043 filler wire	67

	SEM fractographs of the CMT welded A6061-T6 and A6082-T6 joint using ER4043 filler wire	70
4.1.8		
4.2	Cold metal transfer (CMT) welding of dissimilar A6061-T6 and A6082-T6 using ER5356 filler material	74
4.2.1	Surface appearance of the CMT welded A6061-T6 and A6082-T6 joint using ER5356 filler material	74
4.2.2	Macrostructure of the CMT welded A6061-T6 and A6082-T6 joint using ER5356 filler material	75
4.2.3	Optical microstructure of the CMT welded A6061-T6 and A6082-T6 joint using ER5356 filler material	75
4.2.4	SEM microstructure of the interfaces in CMT welded A6061-T6 and A6082-T6 joint using ER5356 filler material	78
4.2.5	SEM-EDS of the interfaces in CMT welded A6061-T6 and A6082-T6 joint interfaces using ER5356 filler material	81
4.2.6	SEM-EDS of precipitates at HAZs of the CMT welded A6061-T6 and A6082-T6 joint using ER5356 filler material	84
4.2.7	Al-Mg binary phase diagram	85
4.2.8	Micro hardness of the CMT welded A6061-T6 and A6082-T6 joint using ER5356 filler material	87
4.2.9	Tensile properties of the CMT welded A6061-T6 and A6082-T6 joint using ER5356 filler material	88
4.2.10	SEM fractography of the CMT welded A6061-T6 and A6082-T6 joint using ER5356 filler material	91
4.3	Cold metal transfer (CMT) welding of dissimilar A5754-H111 and A5083-H111 using ER4043 filler wire	94
4.3.1	Surface appearance and macrostructure of the CMT welded A5754-H111 and A5083-H111 joint using ER4043 filler wire	94

4.3.2	Optical microstructures of interfaces and WMZ center in CMT welded A5754-H111 and A5083-H111 joint using ER4043 filler wire	95
4.3.3	Schematic diagram of zone evolution	97
4.3.4	SEM-EDS of WMZ center in CMT welded A5754-H111 and A5083-H111 joint using ER4043 filler wire	100
4.3.5	SEM of HAZ in CMT welded A5754-H111 and A5083-H111 joint using ER4043 filler wire	103
4.3.6	SEM-EDS of interface regions and WMZ center in CMT welded A5754-H111 and A5083-H111 joint using ER4043 filler wire	104
4.3.7	Microhardness of the CMT welded A5754-H111 and A5083-H111 joint using ER4043 filler wire	109
4.3.8	Tensile results of the CMT welded A5754-H111 and A5083-H111 joint using ER4043 filler wire	111
4.3.9	SEM images of fracture surface in CMT welded A5754-H111 and A5083-H111 joint using ER4043 filler wire	113
4.4	Cold metal transfer (CMT) welding of dissimilar A5754-H111 and A5083-H111 using ER5356 filler wire	115
4.4.1	Surface appearance and macrostructure of the CMT welded A5754-H111 and A5083-H111 joint using ER5356 filler wire	115
4.4.2	SEM of interface regions of the CMT welded A5754-H111 and A5083-H111 joint using ER5356 filler wire	116
4.4.3	SEM-EDS of the interface regions of CMT welded A5754-H111 and A5083-H111 joint using ER5356 filler wire	120
4.4.4	SEM-EDS of WMZ center in CMT welded A5754-H111 and A5083-H111 joint using ER5356 filler wire	123

4.4.5	SEM-EDS of WMZ center in CMT welded A5754-H111 and A5083-H111 joint using ER5356 filler wire	125
4.4.6	Microhardness of the CMT welded A5754-H111 and A5083-H111 joint using ER5356 filler wire	132
4.4.7	Tensile properties of the CMT welded A5754-H111 and A5083-H111 joint using ER5356 filler wire	134
4.4.8	SEM of fracture surface in CMT welded A5754-H111 and A5083-H111 joint using ER5356 filler wire	138
4.5	Gas tungsten arc welding (GTAW) of dissimilar A6061-T6 and A6082-T6 using ER4043 filler wire	139
4.5.1	Surface appearance and macrostructure of the TIG welded A6061-T6 and A6082-T6 joint using ER4043 filler wire	139
4.5.2	SEM microstructure and EDS of WMZ center in TIG welded A6061-T6 and A6082-T6 joint using ER4043 filler wire	140
4.5.3	SEM microstructure of interface regions of the TIG welded A6061-T6 and A6082-T6 joint using ER4043 filler wire	143
4.5.4	SEM-EDS of weld interface in TIG welded A6061-T6 and A6082-T6 joint using ER4043 filler wire	147
4.5.5	SEM-EDS analysis of PMZ and HAZ precipitates in TIG welded A6061-T6 and A6082-T6 joint using ER4043 filler wire	150
4.5.6	Microhardness of the TIG welded A6061-T6 and A6082-T6 joint using ER4043 filler wire	156
4.5.7	Tensile properties of the TIG welded A6061-T6 and A6082-T6 joint using ER4043 filler wire	157

4.5.8	Fractography analysis of TIG welded A6061-T6 and A6082-T6 joint using ER4043 filler wire	160
4.6	Gas tungsten arc welding (GTAW) of dissimilar A6061-T6 and A6082-T6 using ER5356 filler wire	162
4.6.1	Surface appearance of TIG welded A6061-T6 and A6082-T6 joint using ER5356 filler wire	162
4.6.2	Macrostructure of transverse section of the TIG welded A6061-T6 and A6082-T6 joint using ER5356 filler wire	163
4.6.3	Optical microstructure of WMZ center in TIG welded A6061-T6 and A6082-T6 joint using ER5356 filler wire	164
4.6.4	Optical microstructure of weld interface regions of the TIG welded A6061-T6 and A6082-T6 joint using ER5356 filler wire	165
4.6.5	SEM microstructure of PMZs in TIG welded A6061-T6 and A6082-T6 joint using ER5356 filler wire	168
4.6.6	SEM-EDS analysis of WMZ center in TIG welded A6061-T6 and A6082-T6 joint using ER5356 filler wire	168
4.6.7	SEM microstructure and SEM-EDS analysis of HAZ precipitates in TIG welded A6061-T6 and A6082-T6 joint using ER5356 filler wire	172
4.6.8	Microhardness of the TIG welded A6061-T6 and A6082-T6 joint using ER5356 filler wire	175
4.6.9	Tensile properties of the TIG welded A6061-T6 and A6082-T6 joint using ER5356 filler wire	177
4.6.10	Fractography of the TIG welded A6061-T6 and A6082-T6 joint using ER5356 filler wire	180

4.7	Gas tungsten arc welding (GTAW) of dissimilar A5754-H111 and A5083-H111 using ER4043 filler wire	182
4.7.1	Surface appearance of the TIG welded A5754-H111 and A5083-H111 joint using ER4043 filler wire	182
4.7.2	Macrostructure of transverse section of the TIG welded A5754-H111 and A5083-H111 joint using ER4043 filler wire	183
4.7.3	SEM of interface regions of the TIG welded A5754-H111 and A5083-H111 joint using ER4043 filler wire	184
4.7.4	SEM of WMZ and HAZs of the TIG welded A5754-H111 and A5083-H111 joint using ER4043 filler wire	185
4.7.5	SEM-EDS of WMZ in TIG welded A5754-H111 and A5083-H111 joint using ER4043 filler wire	186
4.7.6	SEM-EDS of weld interface regions in TIG welded A5754-H111 and A5083-H111 joint using ER4043 filler wire	190
4.7.7	SEM-EDS analysis of HAZ precipitates in TIG welded A5754-H111 and A5083-H111 joint using ER4043 filler wire	193
4.7.8	Microhardness of the TIG welded A5754-H111 and A5083-H111 joint using ER4043 filler wire	196
4.7.9	Tensile properties of the TIG welded A5754-H111 and A5083-H111 joint using ER4043 filler wire	197
4.7.10	Fractography of the TIG welded A5754-H111 and A5083-H111 joint using ER4043 filler wire	199
4.8	Gas tungsten arc welding (GTAW) of dissimilar A6061-T6 and A6082-T6 using ER5356 filler wire	201
4.8.1	Surface appearance of the TIG welded A5754-H111 and A5083-H111 joint using ER5356 filler wire	201

4.8.2	Macrostructure of transverse section of the TIG welded A5754-H111 and A5083-H111 joint using ER5356 filler wire	202
4.8.3	SEM microstructures of interface regions in TIG welded A5754-H111 and A5083-H111 joint using ER5356 filler wire	202
4.8.4	SEM microstructure of WMZ center in TIG welded A5754-H111 and A5083-H111 joint using ER5356 filler wire	205
4.8.5	SEM-EDS of WMZ center in TIG welded A5754-H111 and A5083-H111 joint using ER5356 filler wire	206
4.8.6	SEM-EDS of WMZ center and interface regions of the TIG welded A5754-H111 and A5083-H111 joint using ER5356 filler wire	210
4.8.7	SEM-EDS of HAZs in TIG welded A5754-H111 and A5083-H111 joint using ER5356 filler wire	214
4.8.8	Vickers microhardness of the TIG welded A5754-H111 and A5083-H111 joint using ER5356 filler wire	219
4.8.9	Tensile properties of the TIG welded A5754-H111 and A5083-H111 joint using ER5356 filler wire	220
4.8.10	Fractography of the TIG welded A5754-H111 and A5083-H111 joint using ER5356 filler wire	222
4.9	Friction stir welding (FSW) of dissimilar A6061-T6 and A6082-T6	224
4.9.1	Surface appearance of the FSWed A6061-T6 and A6082-T6	224
4.9.2	Macrostructure of transverse section of FSWed A6061-T6 and A6082-T6	224

4.9.3	EBSD maps of BMs and different zones of the FSWed A6061-T6 and A6082-T6	225
4.9.4	Grain boundary character maps of BMs and FSWed A6061-T6 and A6082-T6	227
4.9.5	KAM maps of BMs and FSWed A6061-T6 and A6082-T6 joint	229
4.9.6	GOS maps of BMs and FSWed A6061-T6 and A6082-T6 joint	232
4.9.7	Microhardness analysis of the FSWed A6061-T6 and A6082-T6	235
4.9.8	Tensile properties of FSWed A6061-T6 and A6082-T6	237
4.9.10	Fractography of the FSWed A6061-T6 and A6082-T6	239
4.10	Friction stir welding (FSW) of dissimilar A5754-H111 and A5083-H111	240
4.10.1	Surface appearance of the FSWed A5754-H111 and A5083-H111	240
4.10.2	Macrostructure of transverse section of the FSWed A5754-H111 and A5083-H111	240
4.10.3	EBSD maps of BMs and FSWed A5754-H111 and A5083-H111	242
4.10.4	Grain boundary character maps of BMs and FSWed A5754-H111 and A5083-H111	245
4.10.5	KAM maps of BMs and FSWed A5754-H111 and A5083-H111	248
4.10.6	GOS maps of BMs and FSWed A5754-H111 and A5083-H111	250

4.10.7	Microhardness of the FSWed A5754-H111 and A5083-H111	254
4.10.8	Tensile properties of the FSWed A5754-H111 and A5083-H111	256
4.10.9	Fractography of the FSWed A5754-H111 and A5083-H111	258

CHAPTER 5

COMPARATIVE STUDY OF DISSIMILAR JOINTS **259**

5.1	Comparative study of interface tensile properties of dissimilar A6061-T6 and A6082-T6 joint	259
5.1.1	Analysis of tensile properties of A6061-T6 interface using ER4043 filler	259
5.1.2	Analysis of tensile properties of A6061-T6 interface using ER5356 filler	260
5.1.3	Analysis of tensile properties of A6082-T6 interface using ER4043 filler	262
5.1.4	Analysis of tensile properties of A6082-T6 interface using ER5356 filler	263
5.2	Comparative study on interface tensile properties of dissimilar A5754-H111 and A5083-H111 joint	265
5.2.1	Analysis of tensile properties of A5754 interface using ER4043 filler	265
5.2.2	Analysis of tensile properties of A5754 interface using ER5356 filler	266
5.2.3	Analysis of tensile properties of A5083 interface using ER4043 filler	268
5.2.4	Analysis of tensile properties of A5083 interface using ER5356	269

5.3	Comparative study of overall joint tensile properties of dissimilar joints	271
5.4	Summary of joint strength results	275
CHAPTER 6		
	SUMMARY AND CONCLUSIONS	279
	REFERENCES	282
	LIST OF PUBLICATIONS	301
	CURRICULUM VITAE	305

LIST OF FIGURES

Figure	Caption	Page.No.
Figure 1.1	Classification of aluminium alloys	2
Figure 1.2	Some typical automotive aluminum alloy applications	3
Figure 2.1	Classification of joining technologies based on the nature of the bond attained	6
Figure 2.2	Classification of fusion welding processes based on energy source. Classification of fusion welding processes based on energy source	7
Figure 2.3	Stages of cold metal transfer (CMT) welding process	9
Figure 2.4	Cross section macrostructures of CMT joint shows (a) porosities; Surface appearance of weld (b) Top view and (c) Bottom view	11
Figure 2.5	Optical microstructures of CMT joint shows A6061 weld metal interface welded by (a) Low heat input; (b) High heat input; A5754 weld metal interface welded by (c) Low heat input; (d) High heat input	13
Figure 2.6	Schematic illustration of gas tungsten arc welding (GTAW) process	14
Figure 2.7	Macrostructure of (a) GMAWed A5083 weldments show	18

numerous porosities and (b) GTAWed A5083 weldments show no porosities

Figure 2.8	Classification of solid-state welding process	19
Figure 2.9	(a) Schematic illustration of friction stir welding (FSW) process and (b) Friction stir welded surface	20
Figure 2.10	Different welded zones of friction stir weldments	22
Figure 2.11	Different tool shoulder geometries	25
Figure 2.12	Different tool pin profiles of friction stir welding tool	26
Figure 3.1	V groove butt joint design for TIG and CMT welding	35
Figure 3.2	Clamping set up to hold the specimens in a TIG and CMT (a) Side view (b) Top view	37
Figure 3.3	FSW tool (a) Front view (b) Top view	38
Figure 3.4	(a) Gas Tungsten Arc Welding (GTAW) equipment and (b) Welding torch	40
Figure 3.5	(a) Cold metal transfer (CMT) welding machine and (b) Welding torch	41
Figure 3.6	(a) FSW equipment and (b) FSW equipment shows tool	42
Figure 3.7	(a) Hot mounting machine and (b) Disc polishing machine	44
Figure 3.8	(a) Optical microscope and (b) Optical microscope	45

Figure 3.9	Tensile testing machine	47
Figure 3.10	Geometry and dimensions of tensile specimens (a) Macro specimen and (b) Miniature specimen for interface regions	47
Figure 3.11	A schematic diagram shows tensile sample preparation from the TIG and CMT welds (a) Miniature sample from interface regions; (b) Miniature sample from WMZ center and (c) Macro tensile sample from over all region	49
Figure 3.12	A schematic diagram shows tensile sample preparation from the FSW joint (a) Miniature sample from stir zone (SZ) and (b) Macro tensile sample from over all region	50
Figure 4.1	Surface appearance of the CMT welded A6061-T6 and A6082-T6 joint using ER4043 filler wire: (a) Top view and (b) Bottom view	51
Figure 4.2	Macrostructure of transverse section of the CMT welded A6061-T6 and A6082-T6 joint using ER4043 filler wire	52
Figure 4.3	SEM microstructure of the CMT welded A6061-T6 and A6082-T6 joint using ER4043 filler wire: (a) Interface region of 6061- T6 (b) HAZ of 6061- T6 (c) PMZ and CCZ at the interface region of 6061- T6	54
Figure 4.4	SEM microstructure of the CMT welded A6061-T6 and A6082-T6 joint using ER4043 filler wire: (a) Interface	55

	region of 6082- T6 (b) HAZ of 6082- T6 (c) PMZ and CCZ at the interface region of 6082- T6	
Figure 4.5	Al-Si binary phase diagram	56
Figure 4.6	SEM microstructure of the WMZ center in CMT welded A6061-T6 and A6082-T6 joint using ER4043 filler wire at (a) Low magnification and (b) High magnification	57
Figure 4.7	SEM microstructures of the PMZ in CMT welded A6061- T6 and A6082-T6 joint using ER4043 filler wire (a) A6061- T6 interface and (b) A6082- T6 interface	58
Figure 4.8	SEM-EDS analysis of the A6061-T6 weld interface in CMT welded A6061-T6 and A6082-T6 joint using ER4043 filler wire: (a) mapping images and (b) EDS spectra	59
Figure 4.9	SEM-EDS analysis of the 6082-T6 weld interface in CMT welded A6061-T6 and A6082-T6 joint using ER4043 filler wire (a) mapping images and (b) EDS spectra	60
Figure 4.10	SEM-EDS analysis of precipitates present at weld HAZ in CMT welded A6061-T6 and A6082-T6 joint using ER4043 filler wire (a) A6061-T6 and (b) A6082-T6 (c-d) EDS spectra of precipitates present at HAZ of A6061- T6 (e-f) EDS spectra for precipitates present at HAZ of A6082- T6	64
Figure 4.11	Vickers micro hardness profile of the CMT welded A6061-	66

T6 and A6082-T6 joint using ER4043 filler wire

- Figure 4.12 Tensile properties of the BMs and CMT welded A6061-T6 and A6082-T6 joint using ER4043 filler wire weld joint (OR-over all weld region, Int-Interface and WMZ- weld metal zone) 69
- Figure 4.13 SEM images of fracture surfaces of the over-all weld region in CMT welded A6061-T6 and A6082-T6 joint using ER4043 filler wire (a) low magnification image and (b) high magnification image 71
- Figure 4.14 SEM images of fracture surfaces of the A6061- T6 weld interface in CMT welded A6061-T6 and A6082-T6 joint using ER4043 filler wire (a) porosities and (b) higher magnification images shows micro-cracks along interdendritic regions 72
- Figure 4.15 SEM images of fracture surfaces of the A6082- T6 weld interface in CMT welded A6061-T6 and A6082-T6 joint using ER4043 filler wire: (a) low magnification image shows tiny dimples; and (b) serpentine sliding and blade type edges and (c) microcracks at higher magnification 73
- Figure 4.16 Surface appearance of the CMT welded A6061-T6 and A6082-T6 joint using ER5356 filler wire (a) Top view and (b) Bottom view 74

Figure 4.17	Macrostructure of transverse section of the CMT welded A6061-T6 and A6082-T6 joint using ER5356 filler wire	75
Figure 4.18	Optical microstructure of the interface in CMT welded A6061-T6 and A6082-T6 joint using ER5356 filler wire (a) A6061 side and (b) A6082 side	77
Figure 4.19	Schematic diagram representing different zones of both sides of the CMT welded A6061-T6 and A6082-T6 joint using ER5356 filler wire	77
Figure 4.20	Optical microstructure of the interface showing liquation in CMT welded A6061-T6 and A6082-T6 joint using ER5356 filler wire (a) EQZ on A6061 side and (b) PMZ on A6082 side	78
Figure 4.21	SEM images of interface showing liquation cracks in CMT welded A6061-T6 and A6082-T6 joint using ER5356 filler wire (a) EQZ on A6061 side and (b) PMZ on A6082 side	80
Figure 4.22	SEM images of interface in CMT welded A6061-T6 and A6082-T6 joint using ER5356 filler wire (a) HAZ of A6061 side and (b) HAZ of A6082 side	81
Figure 4.23	SEM-EDS mapping images of A6061-T6 interface in CMT welded A6061-T6 and A6082-T6 joint using ER5356 filler wire	82

Figure 4.24	SEM-EDS mapping images of 6082-T6 interface in CMT welded A6061-T6 and A6082-T6 joint using ER5356 filler wire	83
Figure 4.25	SEM-EDS spot analysis of precipitates in CMT welded A6061-T6 and A6082-T6 joint using ER5356 filler wire (a- b) HAZ of A6061 side and (c) HAZ of A6082 side	84
Figure 4.26	Al-Mg binary phase diagram	86
Figure 4.27	Vickers micro hardness profiles of the CMT welded A6061-T6 and A6082-T6 joint using ER5356 filler wire	88
Figure 4.28	Tensile properties of BMs and CMT welded A6061-T6 and A6082-T6 joint using ER5356 filler wire (OR-over all weld region, Int-Interface and WMZ- weld metal zone)	90
Figure 4.29	Fractography images of CMT welded A6061-T6 and A6082-T6 joint using ER5356 filler wire: (a) low magnification and (b) high magnification	92
Figure 4.30	Fractography images of CMT welded A6061-T6 and A6082-T6 joint using ER5356 filler wire: (a) A6061 and (b) A6082	93
Figure 4.31	Surface appearance of the CMT welded A5754-H111 and A5083-H111 joint using ER4043 filler wire	94

Figure 4.32	Macrostructure of transverse section of the CMT welded A5754-H111 and A5083-H111 joint using ER4043 filler wire	95
Figure 4.33	Optical images of CMT welded A5754-H111 and A5083-H111 joint using ER4043 filler wire (a) A5754 interface and (b) A5083 interface	96
Figure 4.34	Optical images of WMZ center in CMT welded A5754-H111 and A5083-H111 joint using ER4043 filler wire: (a) Low magnification and (b) High magnification	97
Figure 4.35	Typical zones in fusion welds: (a) conventional Al alloys (b) present study (CMT welded A5754-H111 and A5083-H111 joint using ER4043 filler wire) showing unique EQZ at both interfaces	98
Figure 4.36	(a) EDS spot analysis of WMZ center in CMT welded A5754-H111 and A5083-H111 joint using ER4043 filler wire and (b-d) EDS spectra for corresponding spots	102
Figure 4.37	SEM images of HAZ in CMT welded A5754-H111 and A5083-H111 joint using ER4043 filler wire: (a) A5754 interface and (b) A5083 interface	104

Figure 4.38	Elemental maps showing distribution of elements at the 5754 interface in CMT welded A5754-H111 and A5083-H111 joint using ER4043 filler wire	105
Figure 4.39	Elemental maps showing distribution of elements at the A5083 interface in CMT welded A5754-H111 and A5083-H111 joint using ER4043 filler wire	106
Figure 4.40	Elemental maps showing distribution of elements at the center of WMZ in CMT welded A5754-H111 and A5083-H111 joint using ER4043 filler wire	107
Figure 4.41	EDS spectra mapping images of the CMT welded A5754-H111 and A5083-H111 joint using ER4043 filler wire: (a) A5754 interface; (b) A5083 interface and (c) WMZ center	108
Figure 4.42	Vickers micro hardness profiles of the CMT welded A5754-H111 and A5083-H111 joint using ER4043 filler wire	110
Figure 4.43	Tensile properties of BMs and welded regions of the CMT welded A5754-H111 and A5083-H111 joint using ER4043 filler wire (OR-over all weld region, Int-Interface and WMZ-weld metal zone)	112

Figure 4.44	SEM images of fractured surfaces of the CMT welded A5754-H111 and A5083-H111 joint using ER4043 filler wire: (a-b) A6061 interface; (c-d) A6082 interface and (e-f) Over all weld region	114
Figure 4.45	Top and bottom views of the CMT welded A5754-H111 and A5083-H111 joint using ER5356 filler wire	115
Figure 4.46	Macroscopic cross-sectional view of the CMT welded A5754-H111 and A5083-H111 joint using ER5356 filler wire	116
Figure 4.47	(a-c) SEM images of A5754 interface regions in CMT welded A5754-H111 and A5083-H111 joint using ER5356 filler wire	118
Figure 4.48	(a-c) SEM images of A5083 interface region in CMT welded A5754-H111 and A5083-H111 joint using ER5356 filler wire	119
Figure 4.49	Elemental maps and its EDS spectra at 5754 interface in CMT welded A5754-H111 and A5083-H111 joint using ER5356 filler wire	121
Figure 4.50	Elemental maps and its EDS spectra of A5083 interface in CMT welded A5754-H111 and A5083-H111 joint using ER5356 filler wire	122

Figure 4.51	Elemental maps and its EDS spectra of the WMZ center in CMT welded A5754-H111 and A5083-H111 joint using ER5356 filler wire	125
Figure 4.52	SEM-EDS spot analysis and its EDS spectra at the center of WMZ in CMT welded A5754-H111 and A5083-H111 joint using ER5356 filler wire	128
Figure 4.53	Elemental maps and its EDS spectra at PMZ of 5754 interface in CMT welded A5754-H111 and A5083-H111 joint using ER5356 filler wire	130
Figure 4.54	Elemental maps and its EDS spectra at PMZ of 5083 interface in CMT welded A5754-H111 and A5083-H111 joint using ER5356 filler wire	131
Figure 4.55	Microhardness profile of the CMT welded A5754-H111 and A5083-H111 joint using ER5356 filler wire	133
Figure 4.56	Tensile properties of BMs and weld regions of the CMT welded A5754-H111 and A5083-H111 joint using ER5356 filler wire (OR-over all weld region, Int-Interface, WMZ-weld metal zone)	136
Figure 4.57	Fracture surface of the interface regions of CMT welded A5754-H111 and A5083-H111 joint using ER5356 filler	138

	wire: (a) A5754 side and (b) A5083 side and (c) over-all weld joint	
Figure 4.58	Surface appearance of the TIG welded A6061-T6 and A6082-T6 joint using ER4043: (a) Top view and (b) Bottom view	139
Figure 4.59	Macrostructure of transverse section of the TIG welded A6061-T6 and A6082-T6 joint using ER4043	140
Figure 4.60	SEM microstructure of WMZ center in TIG welded A6061-T6 and A6082-T6 joint using ER4043: (a) low magnification image and (b) high magnification image	141
Figure 4.61	(a) SEM-EDS spot analysis of WMZ center in TIG welded A6061-T6 and A6082-T6 joint using ER4043 (b) EDS spectra of spot 1 and (c) EDS spectra of spot 2	143
Figure 4.62	SEM microstructure of TIG welded A6061-T6 and A6082-T6 joint using ER4043: (a) low magnification image of interface region of A6061-T6 (c) high magnification image of interface region of A6061-T6 (d) PMZ of A6061-T6	145
Figure 4.63	SEM microstructure of TIG welded A6061-T6 and A6082-T6 joint using ER4043: (a) low magnification image of interface region of A6082-T6 (c) high magnification image of interface region of A6082-T6 (d) PMZ of A6082-T6	146

Figure 4.64	(a-b) SEM-EDS mapping images and its EDS spectra of A6061-T6 interface in TIG welded A6061-T6 and A6082-T6 joint using ER4043	148
Figure 4.65	(a-b) SEM-EDS mapping images and its EDS spectra of A6082-T6 interface in TIG welded A6061-T6 and A6082-T6 joint using ER4043	149
Figure 4.66	SEM-EDS analysis of precipitates present at PMZ of interface in TIG welded A6061-T6 and A6082-T6 joint using ER4043 (a) A6061-T6 and (b) A6082-T6 (c-d) EDS spectra for precipitates present at PMZ of A6061-T6 (e-f) EDS spectra for precipitates present at PMZ of A6082-T6	152
Figure 4.67	SEM-EDS analysis of precipitates present at HAZ of interfaces in TIG welded A6061-T6 and A6082-T6 joint using ER4043 (a) HAZ of A6061-T6 and (b) HAZ of A6082-T6; (c-e) EDS spectra for precipitates present at HAZ of A6061-T6; (f-g) EDS spectra for precipitates present at HAZ of A6082-T6	155
Figure 4.68	Vickers microhardness profile of the TIG welded A6061-T6 and A6082-T6 joint using ER4043	157
Figure 4.69	Tensile properties of the BMs and different regions of TIG welded A6061-T6 and A6082-T6 joint using ER4043 (OR-	159

over all weld region, Int-Interface and WMZ- weld metal zone)

Figure 4.70	SEM images of fracture surface of the different regions of TIG welded A6061-T6 and A6082-T6 joint using ER4043: (a-b) A6061 interface region; (c-d) A6082 interface region and (e-f) over-all weld joint	161
Figure 4.71	Surface appearance of the TIG welded A6061 and A6082 joint using ER5356 (a) Top view and (b) Bottom view	162
Figure 4.72	Macrostructure of transverse section of the TIG welded A6061 and A6082 joint using ER5356	163
Figure 4.73	Optical microstructure of WMZ center in TIG welded A6061 and A6082 joint using ER5356: (a) low magnification and (b) high magnification	165
Figure 4.74	Optical microstructure of interface regions of the TIG welded A6061 and A6082 joint using ER5356 (a) A6061-T6 and (b) A6082-T6	166
Figure 4.75	Optical microstructure of interface regions of the TIG welded A6061 and A6082 joint using ER5356 (a&c) A6061-T6 and (b&d) A6082-T6	167

Figure 4.76	SEM microstructure of PMZ (black arrow indicates GB liquation) in TIG welded A6061 and A6082 joint using ER5356 (a) A6061-T6 and (b) A6082-T6	168
Figure 4.77	(a-e) EDS spot analysis and its EDS spectra at WMZ center of the TIG welded A6061 and A6082 joint using ER5356	171
Figure 4.78	SEM microstructure of HAZ of the TIG welded A6061 and A6082 joint using ER5356: (a) A6061-T6; (b) A6082-T6	173
Figure 4.79	SEM-EDS spot analysis of HAZs and its EDS spectra in TIG welded A6061 and A6082 joint using ER5356: (a) A6061-T6; (b) A6082-T6; (c) EDS spectra of spots in A6061-T6 and (d-e) EDS spectra of spots in A6082-T6	174
Figure 4.80	Vickers microhardness profile of the TIG welded A6061 and A6082 joint using ER5356	177
Figure 4.81	Tensile properties of the BMs and different regions of TIG welded A6061 and A6082 joint using ER5356 (OR-over all weld region, Int-Interface and WMZ-weld metal zone)	178
Figure 4.82	Fracture surface of the TIG welded A6061 and A6082 joint using ER5356 (a) A6061 interface region; (b) A6082 interface region and (c) over-all weld joint	181

Figure 4.83	Surface appearance of the TIG welded A5754-H111 and A5083-H111 joint using ER4043: (a) Top view and (b) Bottom view	182
Figure 4.84	Macrostructure of transverse section of the TIG welded A5754-H111 and A5083-H111 joint using ER4043	183
Figure 4.85	SEM microstructure of the TIG welded A5754-H111 and A5083-H111 joint using ER4043 (a) low magnification image of interface region of A5754 (b) high magnification image of interface region of A5754	184
Figure 4.86	SEM microstructure of the TIG welded A5754-H111 and A5083-H111 joint using ER4043: (a) low magnification image of Interface region of A5083 (b) high magnification image of interface region of A5083	185
Figure 4.87	SEM microstructure of the TIG welded A5754-H111 and A5083-H111 joint using ER4043: (a) WMZ center (b) HAZ of A5754 and (b) HAZ of A5083	186
Figure 4.88	SEM EDS spot analysis of the WMZ center and its EDS spectra in TIG welded A5754-H111 and A5083-H111 joint using ER4043	189

Figure 4.89	(a-b) SEM-EDS mapping images of A5754 interface and its EDS spectra in TIG welded A5754-H111 and A5083-H111 joint using ER4043	191
Figure 4.90	(a-b) SEM-EDS mapping images of A5083 interface and its EDS spectra in TIG welded A5754-H111 and A5083-H111 joint using ER4043	192
Figure 4.91	SEM-EDS analysis of precipitates present at HAZ of the TIG welded A5754-H111 and A5083-H111 joint using ER4043 (a) HAZ of A5754 and (b) HAZ of A5083(c) EDS spectra for precipitates present at HAZ of A5754 (d-e) EDS spectra for precipitates present at HAZ of A5083	195
Figure 4.92	Vickers microhardness distribution of the TIG welded A5754-H111 and A5083-H111 joint using ER4043	197
Figure 4.93	Tensile properties of the BMs and different regions of TIG welded A5754-H111 and A5083-H111 joint using ER4043 (OR--over all weld region, Int—Interface and WMZ-weld metal zone)	198
Figure 4.94	SEM image of fracture surface of the TIG welded A5754-H111 and A5083-H111 joint using ER4043: (a-b) A5754 interface at low and high magnification; (c-d) A5083 interface at low and high magnification and (e-f) Over- all weld joint at low and high magnification	200

Figure 4.95	Surface appearance of the TIG welded A5754 and A5083 joint using ER5356: (a) Top view and (b) Bottom view	201
Figure 4.96	Macrostructure of transverse section of the TIG welded A5754-H111 and A5083-H111 joint using ER5356	202
Figure 4.97	Fig. 4.97 SEM microstructure of the TIG welded A5754-H111 and A5083-H111 joint using ER5356: (a) low magnification image of Interface region of A5754; high magnification image of (b) PMZ of A5754 and (c) HAZ of A5754	203
Figure 4.98	SEM microstructure of the TIG welded A5754-H111 and A5083-H111 joint using ER5356: (a) low magnification image of interface region of A5083; high magnification image of interface region of A5083 (b) PMZ of A5083 and (c) HAZ of A5083	204
Figure 4.99	SEM microstructure of WMZ center in TIG welded A5754-H111 and A5083-H111 joint using ER5356	206
Figure 4.100	SEM-EDS spot analysis of the TIG welded A5754-H111 and A5083-H111 joint using ER5356: (a) WMZ center; (b-e) EDS spectra of spot analysis	209
Figure 4.101	SEM-EDS mapping images and its EDS spectra of WMZ center in TIG welded A5754-H111 and A5083-H111 joint	211

	using ER5356	
Figure 4.102	SEM-EDS mapping images and its EDS spectra of A5754 interface in TIG welded A5754-H111 and A5083-H111 joint using ER5356	212
Figure 4.103	SEM-EDS mapping images and its EDS spectra of A5083 interface in TIG welded A5754-H111 and A5083-H111 joint using ER5356	213
Figure 4.104	SEM EDS spot analysis of HAZ of the TIG welded A5754-H111 and A5083-H111 joint using ER5356 (a) A5754; (b) A5083; (c-e) EDS spectra for spots on A5754 and (f-i) EDS spectra for spots on A5083	217
Figure 4.105	Vickers microhardness distribution of the TIG welded A5754-H111 and A5083-H111 joint using ER5356	220
Figure 4.106	Tensile properties of the BMs and different regions of TIG welded A5754-H111 and A5083-H111 joint using ER5356 (OR--over all weld region, Int--Interface, WMZ-weld metal zone)	221
Figure 4.107	SEM images of fracture surface of the TIG welded A5754-H111 and A5083-H111 joint using ER5356: (a-b) A5754 interface at low and high magnification; (c-d) A5083	223

	interface at low and high magnification and (e-f) Over- all weld joint at low and high magnification	
Figure 4.108	Surface appearances of the FSWed A6061-T6 and A6082-T6 joint	224
Figure 4.109	Macrostructure of transverse section of FSWed A6061-T6 and A6082-T6 joint (AS denotes advancing side and RS denotes retreating side of the weldment)	225
Figure 4.110	OIM images of retreating side (RS) for A6061-T6 alloy in FSWed A6061-T6 and A6082-T6 joint: (a) BM; (b) HAZ;(c) TMAZ ;(d) SZ and (e) Orientation triangle that shows the correspondence between colors and crystallographic orientations	226
Figure 4.111	OIM images of advancing side (AS) for A6082-T6 alloy in FSWed A6061-T6 and A6082-T6 joint: (a) BM; (b) HAZ; (c) TMAZ ;(d) SZ and (e) Orientation triangle that shows the correspondence between colors and crystallographic orientations	227
Figure 4.112	Grain boundary character maps of retreating side (RS) of A6061-T6 alloy in FSWed A6061-T6 and A6082-T6 joint (a) BM; (b) HAZ; (c) TMAZ and (d) SZ	228

Figure 4.113	Grain boundary character maps of advancing side (AS) of A6082-T6 alloy in FSWed A6061-T6 and A6082-T6 joint (a) BM; (b) HAZ; (c) TMAZ and (d) SZ	229
Figure 4.114	KAM maps of retreating side (RS) of A6061-T6 alloy in FSWed A6061-T6 and A6082-T6 joint (a) BM; (b) HAZ; (c) TMAZ and (d) SZ	231
Figure 4.115	KAM maps of advancing side (AS) of A6082-T6 alloy in FSWed A6061-T6 and A6082-T6 joint (a) BM; (b) HAZ; (c) TMAZ and (d) SZ	232
Figure 4.116	GOS maps of retreating side (RS) of A6061-T6 alloy in FSWed A6061-T6 and A6082-T6 joint (a) BM; (b) HAZ; (c) TMAZ and (d) SZ	233
Figure 4.117	GOS maps of advancing side (AS) of A6082-T6 alloy in FSWed A6061-T6 and A6082-T6 joint (a) BM; (b) HAZ; (c) TMAZ and (d) SZ	234
Figure 4.118	Microhardness profile of the FSWed A6061-T6 and A6082-T6 joint	235
Figure 4.119	Tensile properties of BMs and FSWed A6061-T6 and A6082-T6 joint (SR-stir region and OR-over-all region)	238

Figure 4.120	Fractography of fractured specimen in FSWed A6061-T6 and A6082-T6 joint (a) FSW (SZ) and (b) FSW (over-all region)	239
Figure 4.121	The surface appearance of the FSWed A5754-H111 and A5083-H111 joint	240
Figure 4.122	Macrostructures of transverse section of FSWed A5754-H111 and A5083-H111 joint (AS denotes advancing side and RS denotes retreating side of the weldment)	242
Figure 4.123	OIM images of advancing side (AS) for A5754-H111 alloy in FSWed A5754-H111 and A5083-H111 joint: (a) BM; (b) HAZ; (c) TMAZ and (d) SZ (Orientation triangle that shows the correspondence between colors and crystallographic orientations)	243
Figure 4.124	OIM images of retreating side (RS) for A5083-H111 alloy in FSWed A5754-H111 and A5083-H111 joint: (a) BM; (b) HAZ; (c) TMAZ and (d) SZ (Orientation triangle that shows the correspondence between colors and crystallographic orientations)	244
Figure 4.125	Grain shape aspect ratio of different zones of BMs and weld regions in FSWed A5754-H111 and A5083-H111 joint (a) advancing side (AS) and (b) retreating side (RS)	245

Figure 4.126	Grain boundary character maps of advancing side (AS) of A5754-H111 alloy in FSWed A5754-H111 and A5083-H111 joint: (a) BM; (b) HAZ; (c) TMAZ and (d) SZ	246
Figure 4.127	Grain boundary character maps of retreating side (RS) of A5083-H111 alloy in FSWed A5754-H111 and A5083-H111 joint (a) BM; (b) HAZ; (c) TMAZ and (d) SZ	247
Figure 4.128	Fraction of LAGBs and HAGBs at different zones in advancing side (AS) and retreating side (RS) of the FSWed A5754-H111 and A5083-H111 joint	248
Figure 4.129	KAM maps of advancing side (AS) of A5754-H111 alloy in FSWed A5754-H111 and A5083-H111 joint (a) BM; (b) HAZ; (c) TMAZ and (d) SZ	249
Figure 4.130	KAM maps of retreating side (RS) of A5083-H111 alloy in FSWed A5754-H111 and A5083-H111 joint (a) BM; (b) HAZ; (c) TMAZ and (d) SZ	250
Figure 4.131	GOS maps of advancing side (AS) of A5754-H111 alloy in FSWed A5754-H111 and A5083-H111 joint (a) BM; (b) HAZ; (c) TMAZ; (d) SZ; (e) Color code map for GOS map of BM and (f) Color code map for GOS maps of HAZ, TMAZ and SZ	253
Figure 4.132	GOS maps of retreating side (RS) of A5083-H111 alloy in FSWed A5754-H111 and A5083-H111 joint (a) BM; (b)	254

HAZ; (c) TMAZ; (d) SZ; (e) Color code map for GOS map of BM and (f) Color code map for GOS maps of HAZ, TMAZ and SZ

Figure 4.133	Vickers microhardness of the FSWed A5754-H111 and A5083-H111 joint	255
Figure 4.134	Tensile properties of BMs and FSWed A5754-H111 and A5083-H111 joint (over-all region (OR) and stir zone (SZ))	257
Figure 4.135	Fractography of fractured specimen in FSWed A5754-H111 and A5083-H111 joint (a) FSW (SZ) and (b) FSW (over-all region)	258
Figure 5.1	Comparison of tensile properties of A6061 interface in dissimilar A6061-T6 and A6082-T6 joint produced using TIG and CMT welding processes (using ER4043 and ER5356 filler wires)	261
Figure 5.2	Comparison of tensile properties of A6082 interface in dissimilar A6061-T6 and A6082-T6 weld joint produced using TIG and CMT welding processes (using ER4043 and ER5356 filler wires)	264
Figure 5.3	Comparison of tensile properties of A5754 interface in dissimilar A5754 and A5083 weld produced using TIG and	267

CMT welding processes (using ER4043 and ER5356 filler wires)

Figure 5.4 Comparison of tensile properties of A5083 interface in 270
dissimilar A5754 and A5083 weld produced using TIG and
CMT welding processes (using ER4043 and ER5356 filler
wires)

Figure 5.5 Comparison of tensile properties of over-all region in 272
A6061-A6082 dissimilar joint with respect to welding
process

Figure 5.6 Comparison of tensile properties of over-all region in 274
A5754-A5083 dissimilar joint with respect to welding
process

LIST OF TABLES

Table	Caption	Page.No
Table 1.1	Advantages of AA6xxx and AA5xxx alloys and the main criteria for alloy selection	4
Table 2.1	Effects of polarity in GTAW process	16
Table 3.1	Chemical composition of base aluminium alloys and filler materials	33
Table 4.1	EDS mapping compositional details for the interface regions in CMT welded A6061-T6 and A6082-T6 joint using ER4043 filler wire	61
Table 4.2	EDS analysis of precipitates present at HAZ in CMT welded A6061-T6 and A6082-T6 joint using ER4043 filler wire	64
Table 4.3	Tensile properties of the CMT welded A6061-T6 and A6082-T6 joint using ER4043 filler wire	70
Table 4.4	EDS analysis on precipitates present at weld HAZ of interface in CMT welded A6061-T6 and A6082-T6 joint using ER5356 filler wire	85
Table 4.5	Tensile properties of the BMs and different regions of the CMT welded A6061-T6 and A6082-T6 joint using ER5356 filler wire	91

Table 4.6	SEM-EDS spot analysis of different phases in WMZ center of CMT welded A5754-H111 and A5083-H111 joint using ER4043 filler wire	103
Table 4.7	EDS mapping results of the CMT welded A5754-H111 and A5083-H111 joint using ER4043 filler wire	109
Table 4.8	Tensile properties of the base alloys and different regions of CMT welded A5754-H111 and A5083-H111 joint using ER4043 filler wire	113
Table 4.9	EDS mapping results of the interface regions in CMT welded A5754-H111 and A5083-H111 joint using ER5356 filler wire	123
Table 4.10	SEM-EDS spot analysis of different phases in WMZ of the CMT welded A5754-H111 and A5083-H111 joint using ER5356 filler wire	128
Table 4.11	EDS mapping results of the PMZ of interface regions and WMZ in CMT welded A5754-H111 and A5083-H111 joint using ER5356 filler wire	132
Table 4.12	Tensile properties of the CMT welded A5754-H111 and A5083-H111 joint using ER5356 filler wire	137

Table 4.13	EDS analysis on precipitates present at WMZ center in TIG welded A6061-T6 and A6082-T6 joint using ER4043	143
Table 4.14	EDS mapping results of interface regions in TIG welded A6061-T6 and A6082-T6 joint using ER4043	150
Table 4.15	EDS analysis of precipitates present at PMZ of interfaces in TIG welded A6061-T6 and A6082-T6 joint using ER4043	153
Table 4.16	EDS analysis of precipitates present at HAZ of interfaces in TIG welded A6061-T6 and A6082-T6 joint using ER4043	155
Table 4.17	Tensile properties of the BMs and different regions of TIG welded A6061-T6 and A6082-T6 joint using ER4043	160
Table 4.18	EDS analysis of precipitates present at WMZ center of the TIG welded A6061 and A6082 joint using ER5356	172
Table 4.19	EDS analysis of precipitates present at HAZ of the TIG welded A6061 and A6082 joint using ER5356	175
Table 4.20	Tensile properties of the BMs and different regions of TIG welded A6061 and A6082 joint using ER5356	179
Table 4.21	EDS analysis on precipitates present at WMZ center in TIG welded A5754-H111 and A5083-H111 joint using ER4043	190
Table 4.22	EDS mapping results of interface regions of the TIG welded A5754-H111 and A5083-H111 joint using ER4043	193

Table 4.23	EDS analysis on precipitates present at HAZ of the TIG welded A5754-H111 and A5083-H111 joint using ER4043	195
Table 4.24	Tensile properties of the BMs and different regions of TIG welded A5754-H111 and A5083-H111 joint using ER4043	199
Table 4.25	EDS analysis on precipitates present at WMZ center in TIG welded A5754-H111 and A5083-H111 joint using ER5356	209
Table 4.26	EDS mapping results of the interface regions and WMZ center in TIG welded A5754-H111 and A5083-H111 joint using ER5356	214
Table 4.27	EDS analysis of precipitates present at HAZ of A5754 in TIG welded A5754-H111 and A5083-H111 joint using ER5356	218
Table 4.28	EDS analysis of precipitates present at HAZ of A5083 in TIG welded A5754-H111 and A5083-H111 joint using ER5356	218
Table 4.29	Tensile properties of the BMs and different regions of TIG welded A5754-H111 and A5083-H111 joint using ER5356	222
Table 4.30	Tensile properties of the BMs and FSWed A6061-T6 and A6082-T6 joint	238
Table 4.31	Tensile properties of the FSWed A5754-H111 and A5083-H111 joint	257

Table 5.1	Tensile properties of A6061-T6 interface in dissimilar A6061-T6 and A6082-T6 joint produced using TIG and CMT welding processes (using ER4043 and ER5356 filler wires)	262
Table 5.2	Tensile properties of A6082-T6 interface in dissimilar A6061-T6 and A6082-T6 joint produced using TIG and CMT welding processes (using ER4043 and ER5356 filler wires)	265
Table 5.3	Tensile properties of A5754 interface in dissimilar A5754 and A5083 weld produced using TIG and CMT welding processes (using ER4043 and ER5356 filler wires)	267
Table 5.4	Tensile properties of A5083 interface in dissimilar A5754 and A5083 weld produced using TIG and CMT welding processes (using ER4043 and ER5356 filler wires)	270
Table 5.5	Tensile properties of over-all region in A6061-A6082 dissimilar joint with respect to welding process	273
Table 5.6	Tensile properties of over-all region in A5754-A5083 dissimilar joint with respect to welding process	275

NOMENCLATURE

CMT	Cold metal transfer
TIG	Tungsten inert gas
GTAW	Gas tungsten arc welding
GMAW	Gas metal arc welding
FSW	Friction stir welding
BM	Base metal
HAZ	Heat affected zone
PMZ	Partially melted zone
CCZ	Columnar crystal zone
EQZ	Non-dendritic equiaxed zone
WMZ	Weld metal zone
SZ	Stir zone
TMAZ	Thermo mechanically affected zone
AS	Advancing side
RS	Retreating side
LAGB	Low angle grain boundary
HAGB	High angle grain boundary
KAM	Kernel average misorientation
GOS	Grain orientation spread
MZ	Mushy zone
CTE	Coefficient of thermal expansion

AC	Alternating current
DC	Direct current
DCEP	Direct current electrode positive
DCEN	Direct current electrode negative
T6	Solution heat treated and artificially aged
H111	Work hardening imparted by shaping process but less than required for H11
GP	Guiner-Preston zone
SEM	Scanning Electron Microscope
EDS	Energy dispersive X-ray spectroscopy
FESEM	Field Emission Scanning Electron Microscope
EBSA	Electron back scattered diffractometry
EDM	Electric discharge machining
GB	Grain boundary
GI	Grain interior
DB	Dendrite boundary
YS	Yield strength
UTS	Ultimate tensile strength
T_{\max}	Peak temperature
T_m	Melting point
v	Tool transverse speed
ω	Rotational speed

Chapter 1

INTRODUCTION

The number of automobiles increasing day by day has led to increased fuel consumption and greenhouse gas emissions. Due to this, the automotive industry aims to increase fuel efficiency and control emission of CO₂ gas (Dehghani et al. 2013). The steel density range is between 7.75 g/cm³ and 8.05 g/cm³ and the Al density range is between 2.64 g/cm³ and 2.81 g/cm³. It is reported that a weight reduction of the vehicle by 57 kg increases fuel economy of 0.09–0.21 km per litre (Han and Clark 1995). Aluminium alloys are the primary choice for automotive manufacturers because of their light weight, good corrosion resistance, excellent formability and good recycling capability (Yang et al. 2013). The use of aluminium alloys in auto body structures in place of steel can decrease the overall weight of the vehicle. Aluminium alloy sheets of various grades are used in inner, outer and structural applications. The benefits such as greater weight saving, high recyclability and good crash energy absorption like steel with just over half the weight makes aluminium alloy sheets desirable candidates for automotive applications. In the present scenario, the automotive industries are mainly focusing their effort to produce light weight vehicles by replacing the automotive body material from the frequently used low carbon steels to multi materials such as low carbon steels, high strength steels, advanced high strength steels, aluminium alloys, magnesium alloys and fibre reinforced polymers. The acceptance of these materials will depend not only on their structural performance and manufacturability, but also on the joining methods that can be used to assemble them in a rapid, robust and

reliable manner. Among the mix of materials used in automotive applications, aluminium alloys are emerging as the principal material option for auto body construction and their usage is increasing day by day. Aluminum alloys are classified into two categories; namely, cast and wrought aluminum alloys (as shown in Fig.1.1). Wrought aluminium alloys can be used to manufacture several body panels, including interior and external parts of the vehicles (Ramasamy and Albright 2001). Aluminum alloys such as 1xxx, 3xxx, 4xxx, and 5xxx series are non-heat treatable wrought alloys. Aluminum alloys such as 2xxx, 6xxx, and 7xxx series aluminum alloys are classified as heat treatable wrought alloys. Fig. 1.2 shows some typical automotive applications of aluminium.

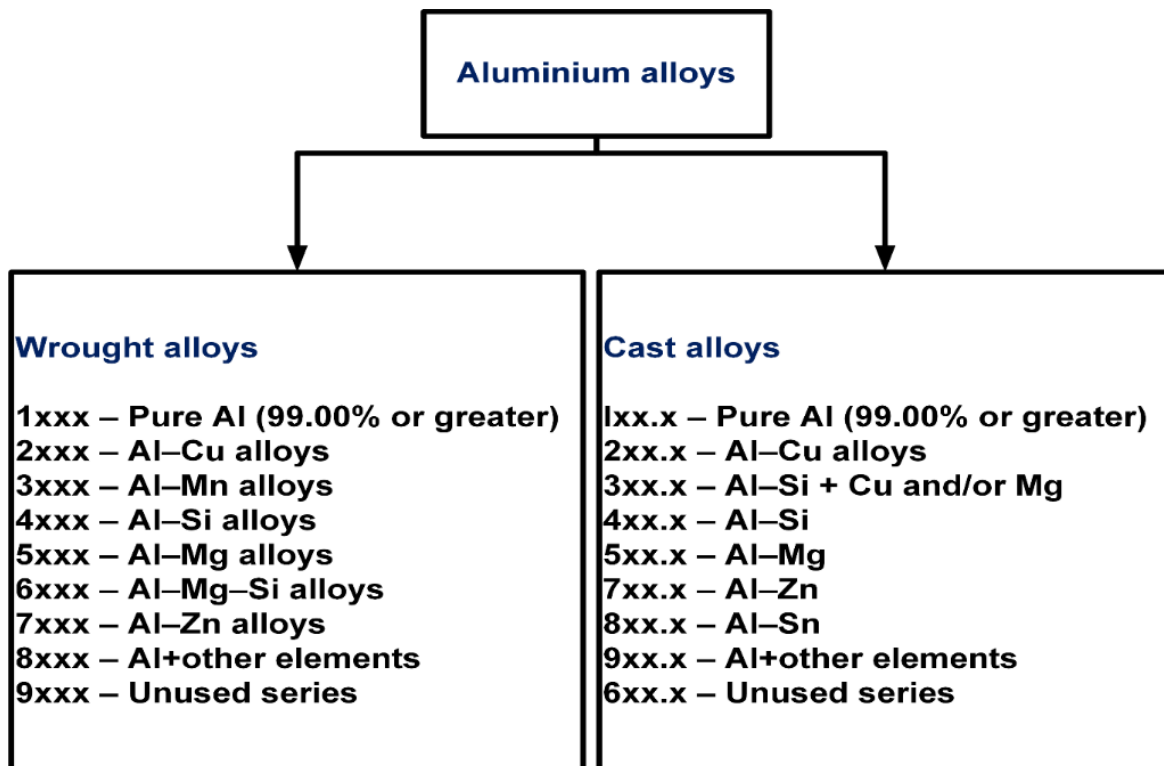


Fig. 1.1 Classification of aluminium alloys

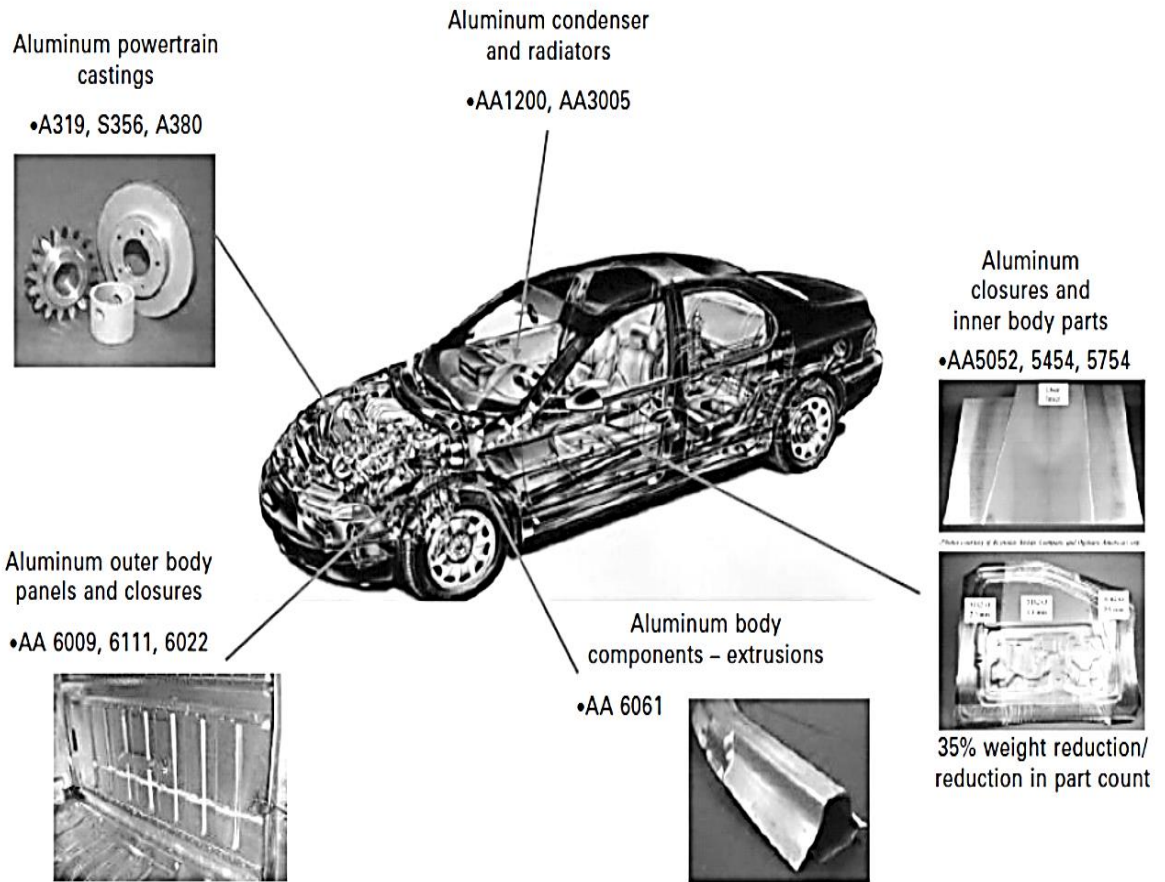


Fig. 1.2 Some typical automotive aluminum alloy applications (Benedyk 2010)

Table 1.1 lists the advantages of AA6xxx and AA5xxx alloys and the main criteria for alloy selection. Among the aluminium alloys, 6xxx series alloys (Al-Mg-Si) are exclusively used for visible inner closure panels and outer body applications due to their very good surface quality (Hirsch 2011). Wrought 5xxx series alloys are used in most of the invisible interior parts due to their poor surface appearance (Hirsch 2011).

Table 1.1 Advantages of A6xxx and A5xxx alloys and the main criteria for alloy selection (Bloeck 2012)

Criteria for alloy selection	A5xxx	A6xxx
Formability	Excellent	Good
Crash performance	Excellent	Excellent
Corrosion resistance	Excellent	Good
Visual surface appearance	Poor	Excellent
Strength	Moderate	Excellent

Since it is difficult or unfeasible to replace each and every part of a vehicle with similar type Al alloy counterparts, hence the structures made by dissimilar Al alloys joints, now become inevitable. Joining of these dissimilar joints by using different welding process will extend its application in automotive sectors. A huge research gap is identified in welding of A5754-A5083 and A6061-A6082 dissimilar aluminium alloys combinations. Hence, the present work is aimed to weld dissimilar combinations of A5754-A5083,

A6061- A 6082 by tungsten inert gas (TIG) welding, cold metal transfer welding (CMT) and friction stir welding (FSW) techniques and to study their structure property correlation.

Chapter 2

LITERATURE SURVEY

2.1 Joining

In general, two types of approaches are used for joining. The first joining approach is mechanical joining in which the parts are held to each other by mechanical means (Messler 2004); In the case of second approach, the bonding between similar or dissimilar materials occurs at the atomic/molecular level. Fusion welding, solid state welding, brazing and soldering, and adhesive bonding come under the second approach. During welding the joint is formed by a metallurgical bond under the action of heat, pressure or both (Messler Jr 1999). In fusion welding processes, the joint is formed in the liquid state, while in solid state welding processes, joining is accomplished without the melting of the workpieces (Messler Jr 1999). In brazing, the workpieces do not get melted ; a molten filler, which melts above $\sim 450^{\circ}\text{C}$, is forced into a close-fitting joint by capillary action. The adhesives undergo physical or chemical reaction that results in a weaker chemical bond (such as Van der Waals) in the joining for adhesive bonding (Adderley 1988). Fig. 2.1 shows the classification of joining technologies based on the nature of the bond attained.

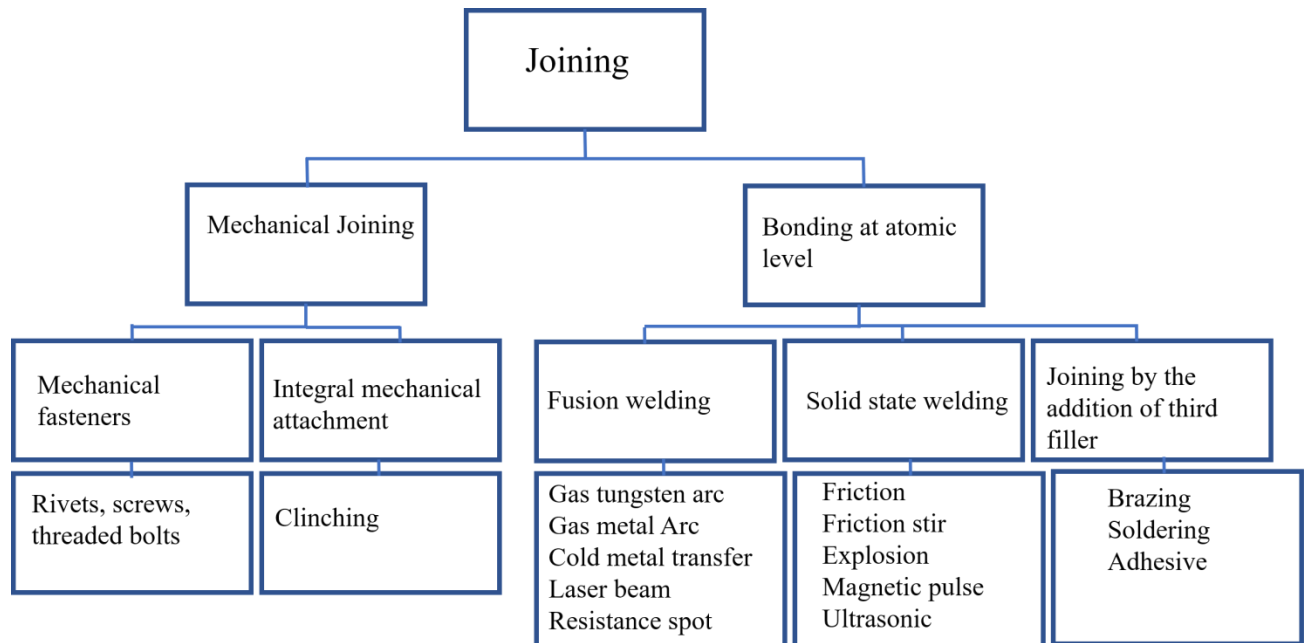


Fig. 2.1 Classification of joining technologies based on the nature of the bond attained.

2.2 Classification of fusion welding process

The fusion welding is classified according to its energy sources (Fig.2.2). In general, chemical, electrical or a high-energy beam can be used as a heat source for fusion welding process (Messler Jr 1999). Chemical sources of heat include exothermic combustion of a fuel gas by air or oxygen. The heat from an electrical arc or resistance heating are examples where electrical energy is the source while high-energy beams provide heat by the conversion of the kinetic energy of the particles in the beam upon collision with the work (Messler Jr 1999).

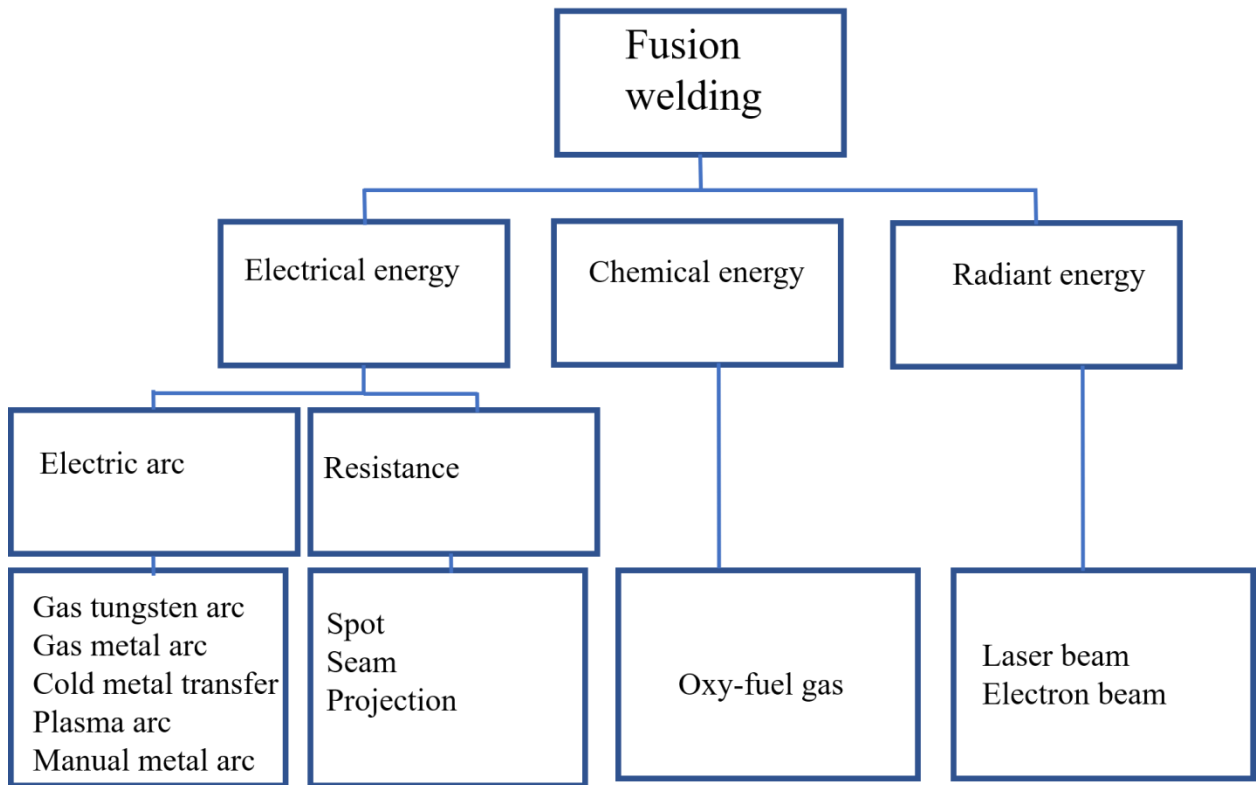


Fig. 2.2 Classification of fusion welding processes based on energy source

2.3 Electric arc welding

The electric arc produced between an electrode and workpiece can be used to produce the joint (Connor and O'Brien 1991). Two types of electrodes are used for welding namely consumable and non-consumable electrode. The consumable electrode can act as both electrode and filler material whereas the non-consumable electrode acts only as an electrode. In order to avoid chemical reaction between molten pool and the surrounding atmosphere, inert gas or slag can be used for shielding (Mathers 2002).

2.4 Common problems associated with fusion welding of aluminium alloys

The main problem in Al alloy is the aluminium oxide layer on the surface. Compared with Al alloys, the melting temperature of Al_2O_3 layer is three times higher which is around 2035 °C (Mathers 2002). Moreover, this Al_2O_3 layer can absorb moisture (source of H_2) from air resulting porosities in Al fusion welds. The other hydrogen sources are oil, lubricants, paint and various surface contaminants. The solubility of H_2 in molten Al weld pool is significantly higher, whereas during solidification the temperature decreases that reduces the solubility of H_2 in Al (Mathers 2002). Due to this, during solidification the dissolved hydrogen is rejected that gives rise to porosities in the weld. Most aluminum alloys welded by arc welding are weaker than the base Al alloys. Among the aluminum alloys used for automotive body applications, the 5000-series alloys have higher weldability than the 6000-series alloys (Mathers 2002). The 5000-series alloys can be welded with or without any filler material, while the 6000-series alloys need a filler material to prevent shrinkage cracking, generated during the solidification of the liquid weld pool. The filler material commonly used with aluminum alloys is a high Mg content aluminum alloy, such as the 5356 alloy (Al-5% Mg). A second filler material used with the 6000-series alloys is a high Si-content aluminum alloy, such as the 4043 alloy (Al-5% Si). The distortion associated with the heat is another problem in weld Al alloys.

2.5 Cold metal transfer welding (CMT) of aluminium alloys

Cold metal transfer (CMT) technology is a modified gas metal arc welding process (GMAW). Initially the filler metal is moved towards the weld pool (Fig. 2.3 (a)). Once the filler metal touches the weld pool the arc is extinguished, and the welding current is lowered (Fig. 2.3 (b)). When the wire moves back, the droplet is detached and the short circuit current becomes small (Fig.2.3 (c)). The filler wire is finally reversed back and again the process is continued (Fig.2.3 (d)).

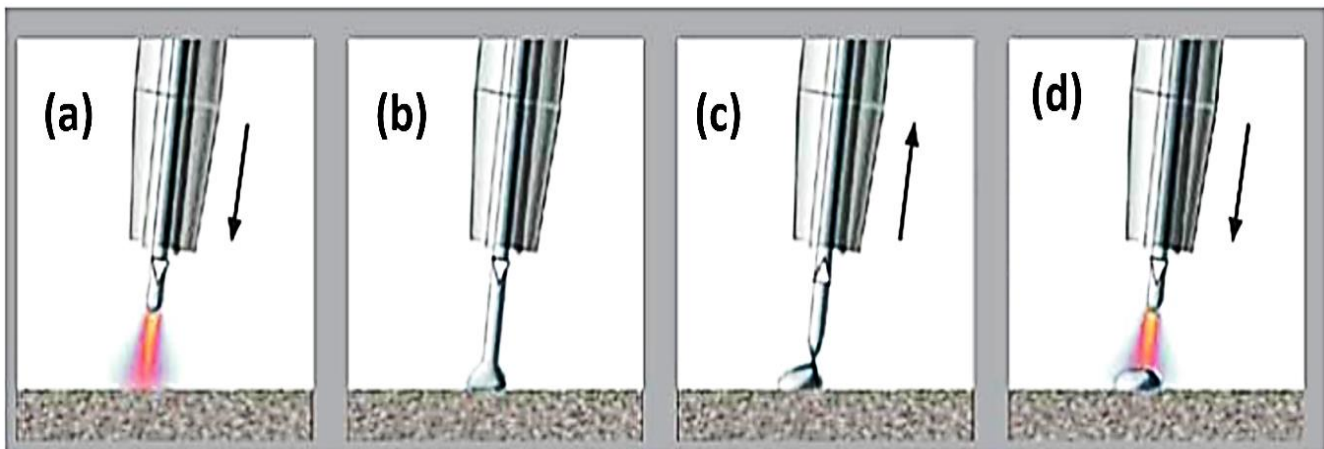


Fig. 2.3 (a-d) demonstrates stages of cold metal transfer (CMT) welding process (Gungor et al. 2014b)

The reciprocating movement of filler wire causes the fall of metal droplets without any large splashes. This process has advantages such as low heat input, low dilution rate, low residual stress and no spatter (Cao et al. 2013b, 2014; Lin et al. 2013; Wang et al. 2008). Due to low thermal input, the heat related issues in the weldment are reduced significantly.

Because of the above-mentioned advantages this process is preferred for welding of thin aluminium alloy sheets in the automobile bodies (Pickin et al. 2011).

It is reported that welding of A5083-H111 and A6082-T65 by CMT welding resulted in yield strengths higher than those obtained by other processes (Gungor et al. 2014b). CMT welding of A6061-T6 alloys produces a spatter free and solidification crack free weld (Pavan et al. 2016). A comparative study of CMT with MIG reports that with reduced heat input, the CMT process exhibited good depth of penetration and good deposition (Pickin and Young 2006). It is reported that 7075-T6 alloy welded through CMT produced a weld bead with no cracks and spatter (Fig.2.4 (b-c)), however a few porosities (Fig.2.4 (a)) were noticed in the weld macrostructure (Elrefaey 2015). These pores are less than 1.1% of weld metal zone (WMZ), and do not influence the tensile strength. Because of the above-mentioned reasons, the joint exhibits better strength and elongation as compared to MIG welding of the same alloy (Elrefaey 2015). Moreover, CMT has been reported to be a well suited process to weld dissimilar materials such as aluminium with zinc coated steel and magnesium with aluminium (Shang et al. 2012; Zhang et al. 2009). The dissimilar welding of aluminium with magnesium and aluminium with nickel using CMT process significantly decreases the volume fraction the intermetallic compounds, thus improving mechanical properties (Cao et al. 2013a; Liu et al. 2015).

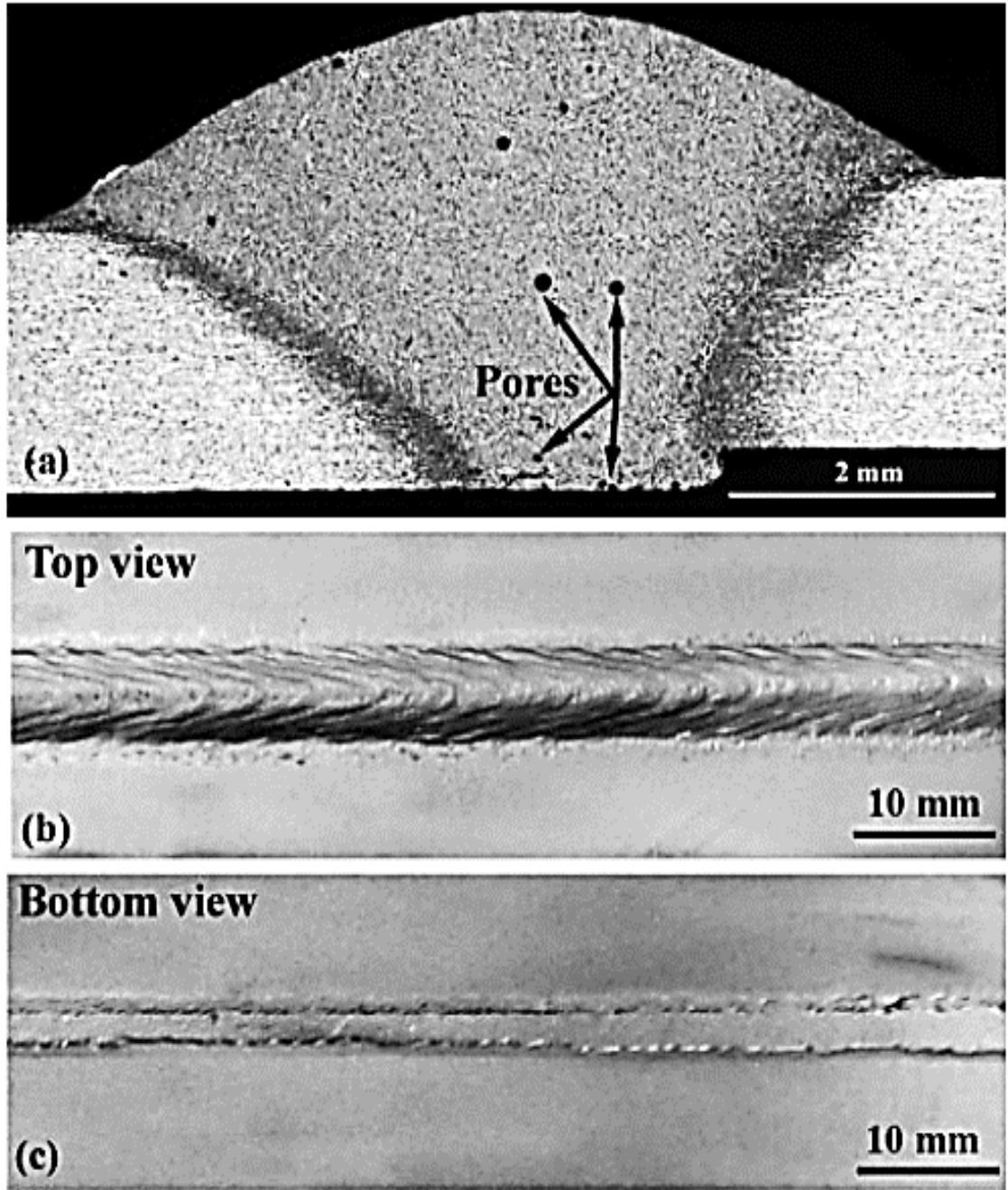


Fig. 2.4 Cross section macrostructures of CMT joint shows (a) porosities, and surface appearance of weld (b) top view and (c) bottom view (Elrefaey 2015)

Comez et al (Çömez and Durmuş 2019) have studied the effect of heat input on microstructure, mechanical and corrosion behavior in CMT welded A5754-A6061 dissimilar aluminium alloys. The microstructure of both the interfaces shows that columnar grains have grown epitaxially from the partially melted zone (PMZ) and the width of the PMZ of both the interfaces is increased as the heat input increases (Fig.2.5 (a-d)). The authors have further reported that higher amount of heat input causes grain coarsening in HAZ of A5754 and overageing in HAZ of 6061 leading to a reduction in tensile strength.

Gungor et al (Gungor et al. 2014b) have studied the microstructure and mechanical properties of CMT welded dissimilar A5083-H111 and A6082-T651 aluminium alloys and have reported that the CMT weld joint provides good joint efficiency and better tensile and fatigue performance. A study on the role of pulse correction in CMT welding of dissimilar A5754 and galvanized steel reports that the thickness of the intermetallic layer varies with variation in pulse correction (Milani and Paidar 2016). Process parameters optimization in CMT welding of dissimilar A5754-H111 and galvanized steel is reported (Ünel and Taban 2017) and the study has revealed that intermetallic phase Fe_2Al_5 is formed at the galvanized steel side and $FeAl_3$ is formed on the Al alloy side. Dutra et al (Dutra et al. 2015) have studied the effect of filler materials in CMT welded A5083 alloy and have reported that better mechanical properties are achieved with ER5087 electrode as compared to ER5183.

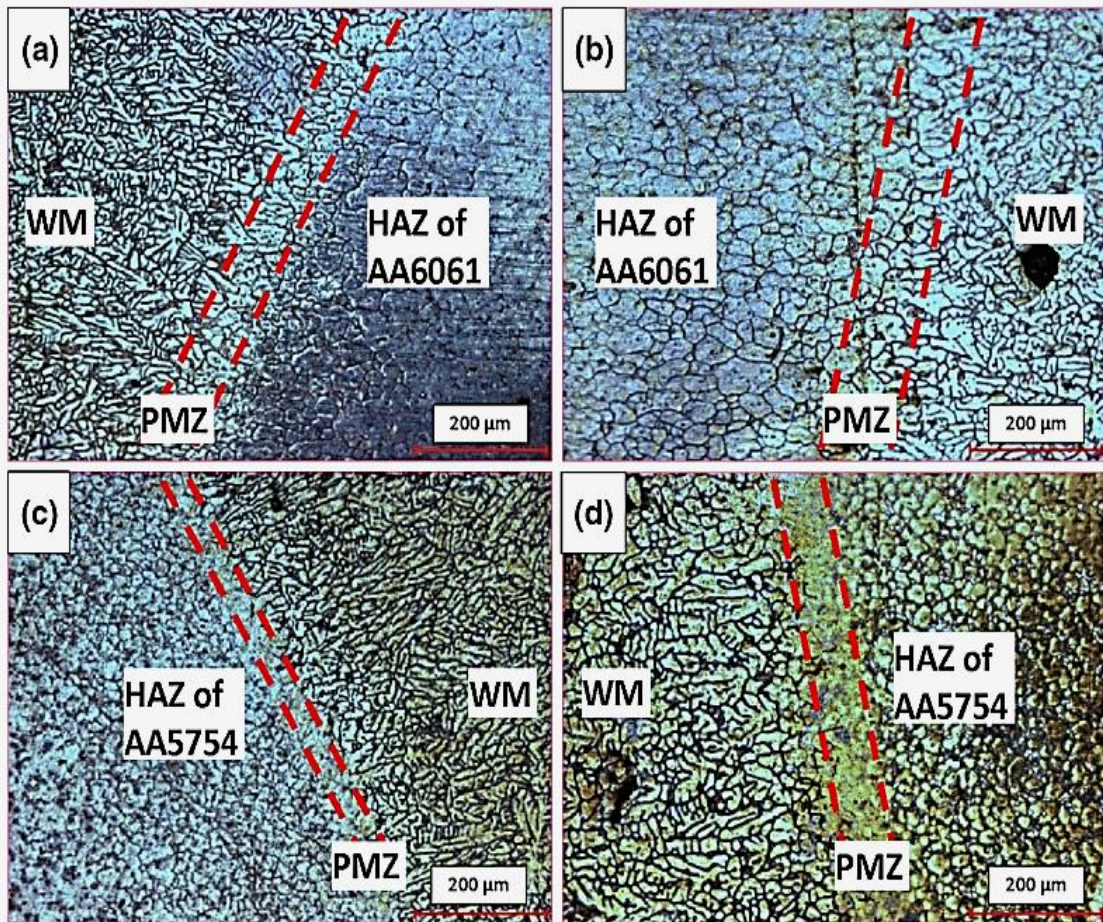


Fig. 2.5 Optical microstructures of CMT joint shows A6061 weld metal interface welded by (a) Low heat input; (b) High heat input and A5754 weld metal interface welded by (c) Low heat input; (d) High heat input

2.6 Tungsten inert gas (TIG) welding of aluminium alloys

Fig. 2.6 demonstrates schematic illustration of tungsten inert gas (TIG) welding process. In tungsten inert gas (TIG) welding, the electric arc is created between a non-consumable tungsten electrode and the parts to be joined (Connor and O'Brien 1991).

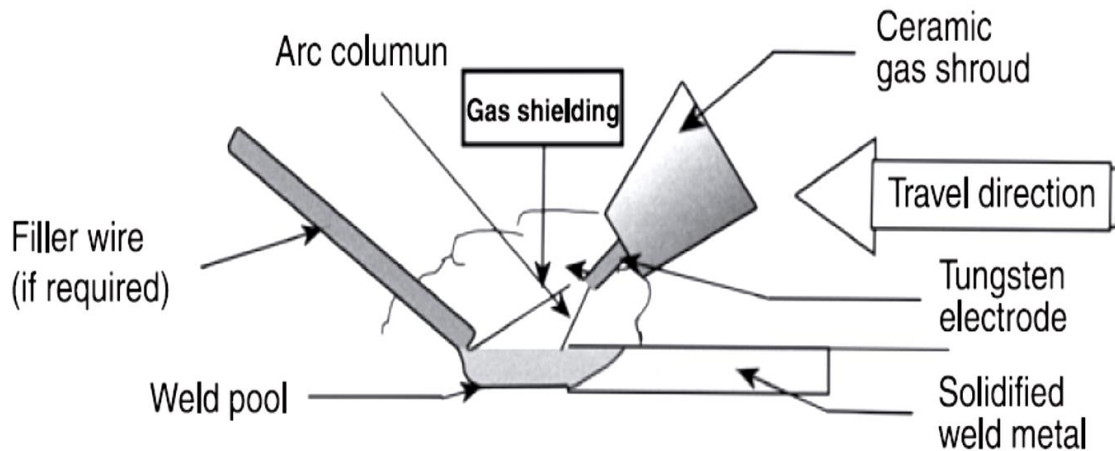
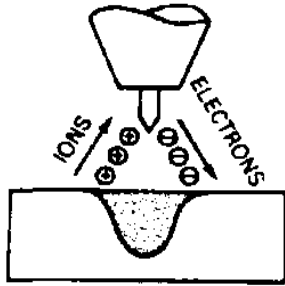
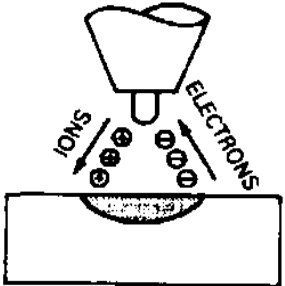
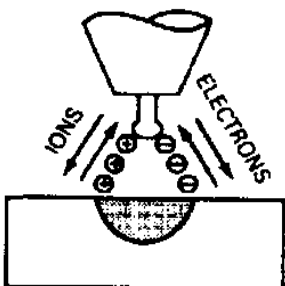


Fig. 2.6 Schematic illustration of tungsten inert gas (TIG) welding process (Mathers 2002)

In the case of aluminum, the electrode itself is used to break up the oxide layer on the aluminum sheet surface (Mathers 2002). When a filler material is used, it is fed into the weld site from a separate rod or wire instead of feeding it through the electrode. The filler material is melted by the arc and is added to the weld pool. This welding process is well suited for welding aluminum. The slower welding process being most suited for all position welding. Aluminum welding is mostly associated with the tungsten inert gas (TIG) welding process. This is more in case of metals of a lower thickness. Many other processes, of course, can join aluminum, but for the lighter gauges of material, TIG is the most suitable process. The popularity of aluminum in automotive applications has brought TIG welding to more prominence. Mechanically strong and visually appealing, TIG welding is the number one process chosen by professional welders for professional racing teams and avid auto enthusiasts and hobbyist.

TIG welding may be conducted using either direct current (DC) or alternating current (AC). In the former case, the tungsten electrode may be connected either to the positive or the negative terminal of the power supply resulting in direct current electrode positive (DCEP) and direct current electrode negative (DCEN) modes. With DCEN, 70% of the heat is generated at the anode (workpiece) and 30% at the cathode (electrode); the reverse occurs with DCEP. The higher heat input to the workpiece with DCEN mode results in deeper weld penetration than in the DCEP mode. Conversely, in DCEP mode, the higher heat generation at the tungsten electrode means that water cooling of the electrode holder is required. DCEP mode also results in a cathodic cleaning action on the workpiece as a result of the large positive ions that strike the surface, removing the oxide layer present there. This mode is thus important in the joining of aluminium with its ubiquitous oxide layer but the beneficial cleaning action is countermanded by the limited current-carrying ability of the tungsten electrode without overheating it (Oates and Saitta 1998). When TIG is conducted with AC, periodic reversal of the electrode polarity occurs. Thus, AC can combine the cathodic cleaning action of electrode positive with the deep penetration characteristic of electrode negative. Table 2.1 shows effects of polarity in TIG welding process.

Table 2.1 Effects of polarity in TIG process(Mathers 2002)

CURRENT TYPE	DCEN	DCEP	AC (BALANCED)
ELECTRODE POLARITY	NEGATIVE	POSITIVE	
ELECTRON AND ION FLOW			
PENETRATION CHARACTERISTICS			
OXIDE CLEANING ACTION	NO	YES	YES-ONCE EVERY HALF CYCLE
HEAT BALANCE IN THE ARC (APPROX.)	70% AT WORK END 30% AT ELECTRODE END	30% AT WORK END 70% AT ELECTRODE END	50% AT WORK END 50% AT ELECTRODE END
PENETRATION	DEEP; NARROW	SHALLOW; WIDE	MEDIUM
ELECTRODE CAPACITY	EXCELLENT e.g., 1/8 in. (3.2 mm) 400 A	POOR e.g., 1/4 in. (6.4 mm) 120 A	GOOD e.g., 1/8 in. (3.2 mm) 225 A

The mechanical properties and microstructural features of aluminum 5083 (Al5083) weldments processed by tungsten inert gas (TIG) welding and gas metal arc welding (GMAW) were investigated (Liu et al. 2012). The authors observed microstructural difference in TIG and GMAW weldments. TIG weldment showed a homogeneous non-directional equiaxed grain structure in the middle, whereas GMAW weldment showed a typical directional solidified microstructure in the middle of the weldment. The solidified grain structures varying from columnar to equiaxed could have resulted from the difference in solidification velocity. In general, TIG has slower melt convection than GMAW. Therefore, solidification interfaces in TIG welds develop slowly and result in steadily

growing coarse crystals. On the contrary, GMAW welds solidify faster to form growing dendritic crystals and finer crystals. The same authors reported that Al5083 weldments processed by TIG are more reliable than those by GMAW. The former bears higher strength, more ductility, and no apparent microstructural defects. Perceivable porosities in weldments by GMAW (Liu et al. 2012) were found (as shown in Fig.2.7 (a)), which could account for the distinct difference in mechanical properties between weldments processed by TIG and GMAW. Wrought aluminum sheets were square butt-welded by friction stir welding (FSW) and tungsten inert gas (TIG) welding methods (Fahimpour et al. 2012). Friction stir welding formed various regions such as stir region (SZ), thermomechanical affected zone (TMAZ) and heat affected zone (HAZ), while in the TIG weld, due to the melting of the alloy, dendritic-like structure with many equiaxed grains was observed. The influence of shielding gas parameter on mechanical properties and microstructures of heat-affected zone and fusion zone of tungsten inert gas (TIG) welding in aluminium alloy AA 5083 is reported (Peasura and Watanapa 2012). Experimental results have shown that the argon condition produced smaller grain size, resulting in higher hardness both in weld metal and HAZ.

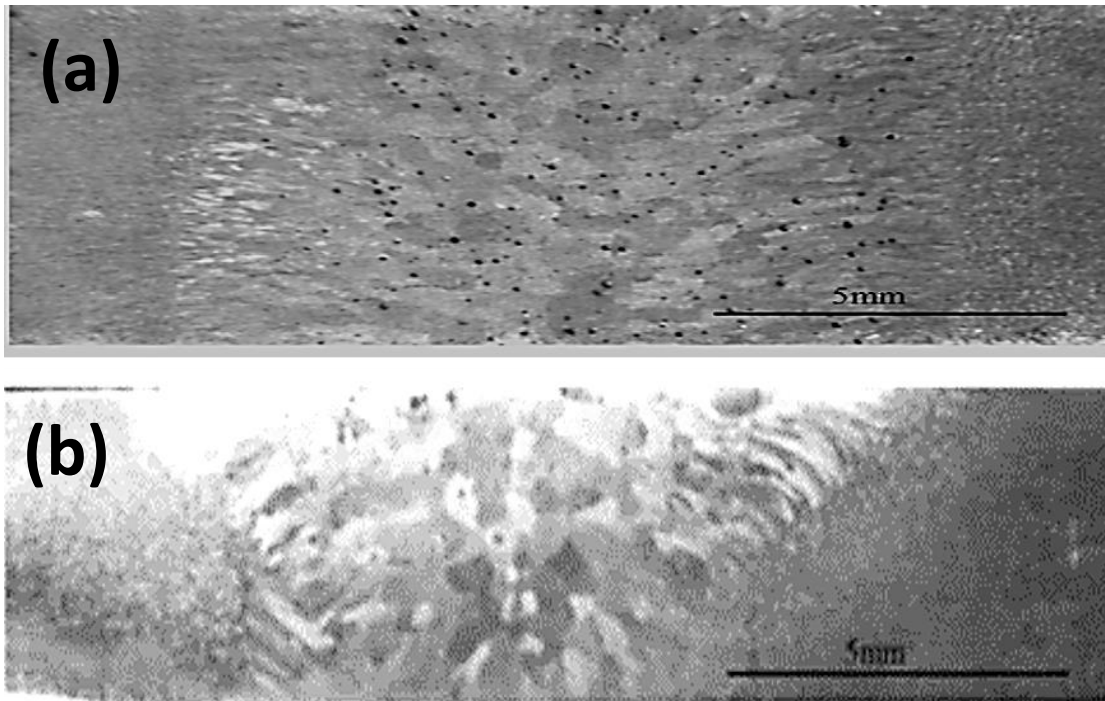


Fig. 2.7 Macrostructure of (a) GMAW welded A5083 weldments showing numerous porosities and (b) TIG welded A5083 weldments showing no porosities (Liu et al. 2012)

2.7 Solid state welding

Solid state welding processes are a group of processes that accomplish joining at the faying surfaces of parts, principally but not exclusively, through plastic deformation of the parent material(s) due to the application of pressure, at temperatures below their melting point, without the addition of a filler material (Messler Jr 1999). Solid-state diffusion occurs during welding that leads to form a metallurgical bond. Heat sources for solid state welding process are generally mechanical in nature, either directly applied pressure or derived from frictional forces. Heat and pressure, either individually or in combination, together with

time, bring about coalescence at the faying surfaces of the part being joined. Solid state welding processes offer several advantages over fusion processes (Messler Jr 1999). As no melting occurs generally and the heat input is lower than in fusion processes, there is less disruption of the microstructures of the materials being joined and hence less effect on their properties. The problems of hot cracking and porosity, as well as a cast solidification microstructure at the weld, are avoided. In the absence of fusion, intermixing of the materials involved tends to be minimal on a macroscopic scale in most of these processes, and so materials of dissimilar compositions can often be joined. The classification of solid-state welding processes is shown in the Fig. 2.8

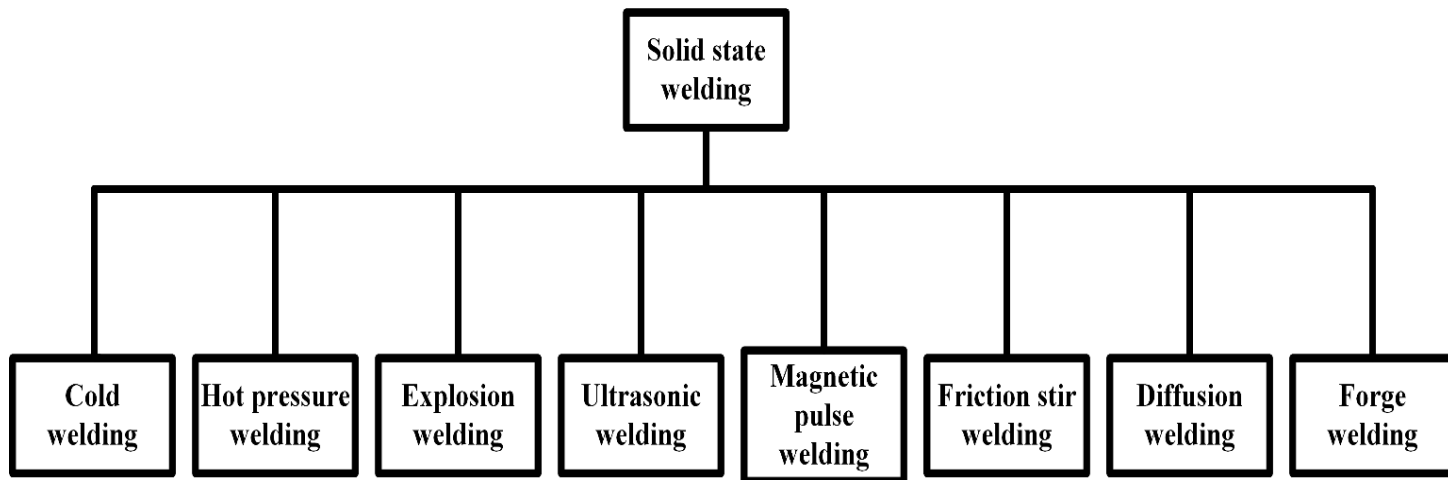


Fig .2.8 Classification of solid-state welding process

2.8 Friction stir welding (FSW) of aluminium alloys

Friction Stir Welding (FSW) is a solid state hot shearing joining method (Dawes and Thomas 1996), whereby a rotating tool pin with a shoulder plunges and moves along the butting surface of two plates as shown in Fig. 2.9 (a).

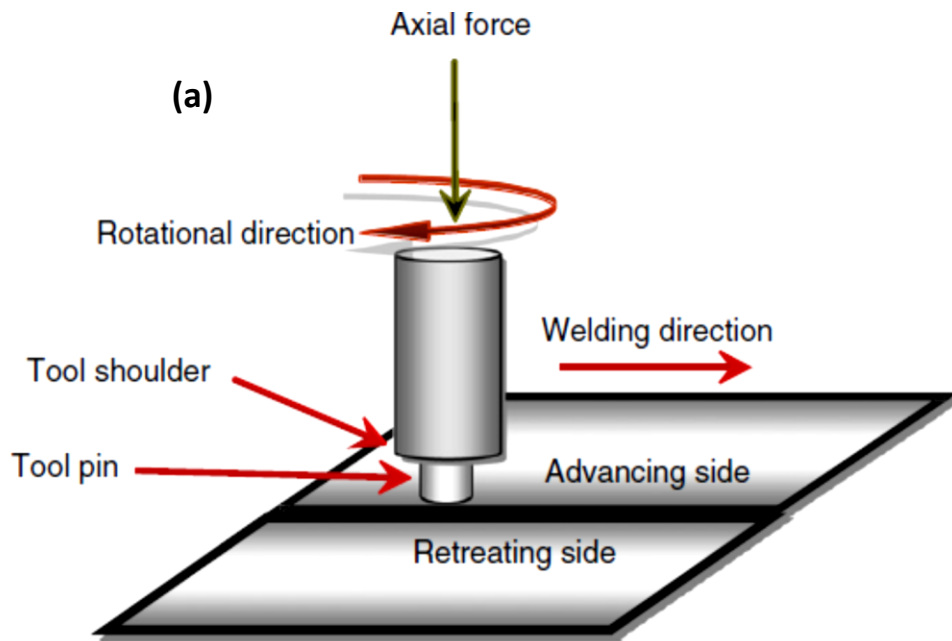


Fig. 2.9 (a) Schematic illustration of friction stir welding (FSW) process and (b) Friction stir welded surface (Dawood et al. 2015a)

The friction generated between the workpiece and tool as well as severe plastic deformation of the work piece material during welding produces heat. The rotating tool pin plunges gradually into the work piece till the shoulder of the tool touches the upper surface (Singh et al. 2014). When the rotating tool translates along the welding direction, the material gets softened, and this softened material transported from the front to back of the pin where

it is forged into a joint. Normally, a friction stir welded (FSWed) material exhibits two sides, namely, advancing side (AS) and retreating side (RS). The side at which the tool rotation and the welding direction are the same, is known to be advancing side (AS) and the other side as retreating side (RS). Because of this, the material flow and temperature (Commin et al. 2009) are not symmetrical on both sides. Due to this the properties of AS and RS in FSWed joint vary significantly. Rao et al (Rao et al. 2013) showed that the FSWed butt joint of A-5083 had asymmetry in microstructure, hardness and tensile strength at both the sides of the weld. It is generally recognized that FSW of the workpiece could produce three different zones, such as nugget zone (NZ), thermo-mechanically affected zone (TMAZ) and heat affected zone (HAZ) (as shown in Fig.2.10). Among the three zones, nugget zone could be significantly affected by severe heat and plastic deformation. Normally this nugget zone contains equiaxed fine grains formed due to the occurrence of dynamic recovery recrystallization phenomenon (Simoncini and Forcellese 2012). Next to nugget zone, TMAZ was generated on both advancing and retreating sides. This zone was affected by both heat as well as plastic deformation. Surrounding TMAZ zone, on both the sides HAZ was produced during welding. In this zone the material was only affected by heat and not by plastic deformation.

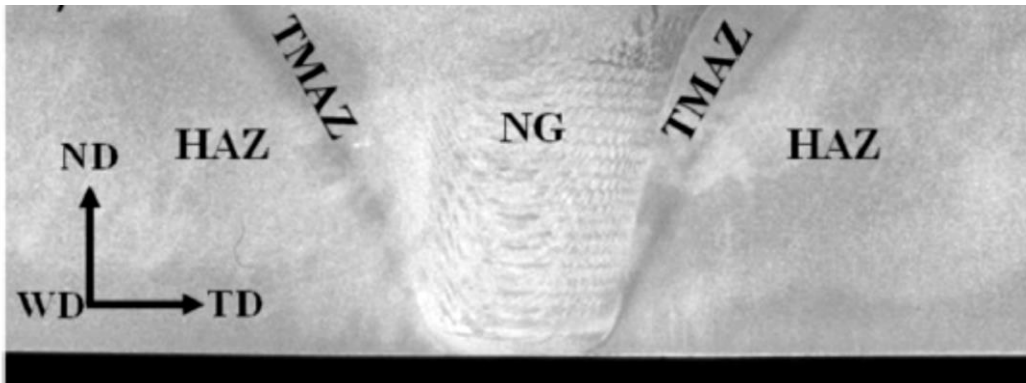


Fig.2.10 Different welded zones of friction stir weldments (Hamada et al. 2015)

It is reported that relative positioning of dissimilar Al-Mg-Zn and Al-Mg-Si alloys has a strong effect on material stirring and mixing (Yan et al. 2016). When Al-Mg-Zn alloy is kept on the advancing side (AS) and Al-Mg-Si alloy on the retreating side (RS), Al-Mg-Si alloy moves from RS to AS in small amounts, whereas if the positions are reversed, Al-Mg-Zn alloy does not move from the RS to AS. According to Kim et al (Kim et al. 2009), when the high strength Al alloy is placed on AS, the material flow is limited and consequently more defects are induced in a FSWed sample. These regions are microstructurally different because of the difference in temperature, strain and strain rate (Patel et al. 2019). As compared to other zones, the SZ of the FSWed sample is of prime importance because the resulting property is mainly decided by this zone (Patel et al. 2019). This apart, surface roughness was found to have reduced the weld heat affected zone width of a 6061 aluminium alloy weldment (Dawood et al. 2015a). Zhuanning Sun et al. [67] investigated the local microstructure, strength and toughness of different zones in AA6061-T6 stationary shoulder friction stir welds. They have found that, the most significant weakening for both strength and toughness is in HAZ close to SZ. The microstructure of SZ includes recrystallized fine grains with high density of dislocations,

homogeneous constituent particles distribution and re-precipitated of G.P. zones resulting in the recovery of local strength and the improvement for both plasticity and toughness. In HAZ, the grain structure and constituent particle distribution inherit the characteristics of base metal, but β'' precipitates are dissolved and the reprecipitated β' particles are coarsened. This results in the decrease of yield strength, tensile strength, crack initial energy and propagation energy of HAZ, especially near SZ.

2.8.1 Tool design for FSW

In FSW tool design is an important factor which influences material flow, generation of heat, welding quality, microstructure and mechanical properties of the welded joint. Considering tool material selection, the following factors such as (1) tool wear (2) hardness (3) ductility (4) reactivity of tool with work piece material (5) cost of the tool (6) load bearing capability plays a significant role. In general, lightweight materials like aluminium alloys and aluminium matrix composites can be welded by using tool steels (Nami et al. 2011; Singh et al. 2011). During FSW process majority of the heat is generated by the shoulder portion of the tool material. Moreover, the shoulder arrests the plasticized material from running away from the work piece. Therefore, it is clearly understood that the shoulder diameter and surface geometries are the significant decisive factors in the case of FSW. Regarding the shoulder diameter, designing a shoulder with larger diameter extends the area of contact. Due to this, the TMAZ (Thermo mechanical affected zone) and HAZ (Heat affected zone) also became wider, hence mechanical properties of the joints are lowered significantly. On the other hand, designing a shoulder with smaller diameter leads to produce inadequate heat because of lesser contact area. From this, it is clear that

designing a tool with optimum diameter is very important to achieve good quality as well as mechanical properties. Process parameters and tool design play a significant role in controlling the microstructure in FSWed joints (Dawood et al. 2015b). In another work, the effect of tool pin geometry and welding speed were studied in AA5754-H22 thin sheets and it was reported that there were no significant changes in the strength of the weldment by changing the tool geometry (Costa et al. 2015). However, a significant difference in weldment strength was noticed when the welding speed was varied (Costa et al. 2015), and an excessive tool rotational speed in FSWed A-5083 alloy produced an imperfect joint with many defects (Han et al. 2009). Arora et al (Arora et al. 2011) have investigated the optimum tool shoulder diameter through heat transfer and material flow modeled FSW process. They have chosen shoulder diameters of 15 mm, 16 mm and 18 mm with three different rotational speeds such as 900, 1200 and 1500 rpm. The results showed that, a shoulder diameter of 18mm [Pin dia 6mm so $D/d=3$] with 1200 rpm exhibited greater mechanical properties. Recently, Costa et al (Costa et al. 2015) have studied cylindrical, conical pin shape with different pin diameters. They have reported that a conical pin geometry with low shoulder to pin diameter (D/d) ratio produces a good quality weld. The effect of shoulder geometries on defects and tensile properties of the FSWed joint is discussed in a recent research work (Trueba Jr et al. 2015). The authors used six different shoulder designs (as shown in Fig.2.11) and found that a shoulder with a raised spiral (tool C) geometrical feature displayed good weld quality as well as higher mechanical properties. The role of tool rotational speed and pin profile on tensile properties of dissimilar AA5083-H111 and AA6351-T6 alloys was examined (Palanivel et al. 2012).

They studied five different pin geometries such as straight square (SS), straight octagon (SO), straight hexagon, tapered square (TS), tapered octagon (TO) (as shown in Fig.2.12) with three rotational speed of 600 rpm, 950 rpm and 1300 rpm. After subsequent microstructural and mechanical characterization, they have concluded that the straight square (SS) at a rotational speed of 950 rpm resulted in higher tensile strength. Another research work used two different pin profiles such as triflute and taper screw thread pin with various traverse speed for welding AA6082-O alloy (Suresha et al. 2011). The experimental study of friction stir welding of A6061 alloy with five various pin profiles namely straight cylindrical, threaded cylindrical, triangular and square has revealed that square shape pin produces a good quality weld (Elangovan et al. 2008).

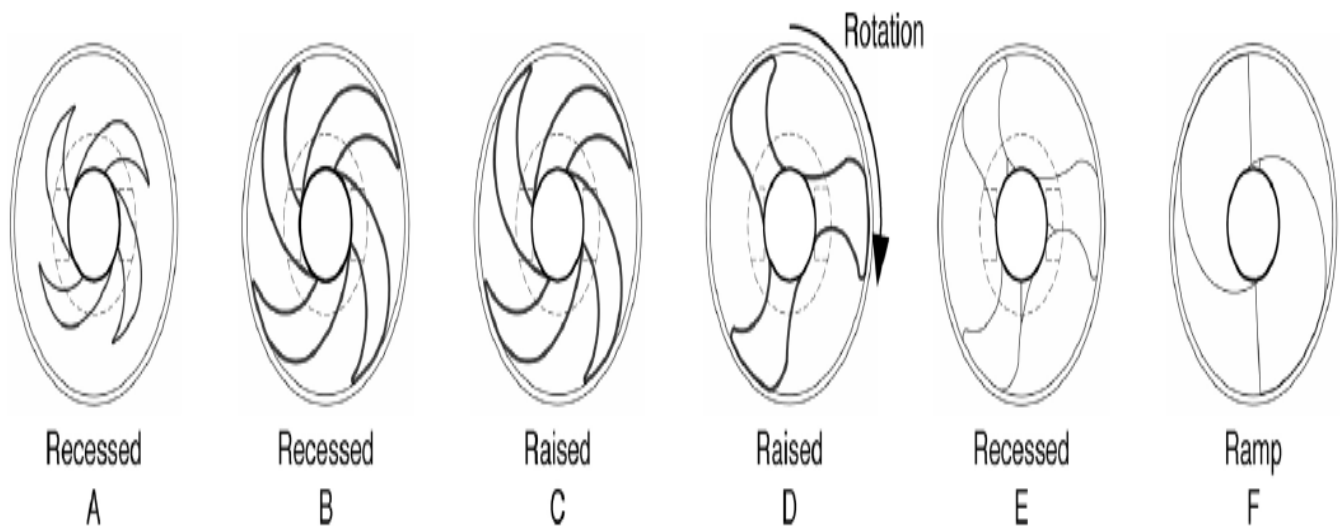


Fig. 2.11 Different tool shoulder geometries (Trueba Jr et al. 2015).



Fig.2.12 Different tool pin profiles of friction stir welding tool (Palanivel et al. 2012).

2.8.2 FSW parameters

Tool rotational speed, tool transverse speed and tool tilt angle are the important welding parameters of FSW. It is well known that the properties of the material depend on its microstructure. The aforementioned parameters play a significant role in controlling the microstructure of the welded joint. Thus, a proper understanding about these parameters and its effect in AA5xxx and AA6xxx series welded joints is considered to be an important factor for industrial purpose. Among the welding parameters, tool rotational speed is more important, because of its major contribution in heat generation. It is reported that, lower tool rotational speed generates lesser heat input (Balasubramanian 2008). This leads to affect the flow of the material to insufficient and plasticization effect in stir zone also became lesser. This phenomenon causes deterioration in mechanical properties of the welded joints. On the other hand, higher tool rotational speed induces more heat generation during FSW. As a consequence, the material flows in a turbulent manner and coarsening

of grains in weld zone occurs. This phenomenon can also lower the mechanical properties of the welded joint. Based on the above discussion, it is clear that heat input during FSW process should neither to be lower nor to be higher, because both of these lead to reduce the tensile properties significantly. Hence, in order to achieve a welded joint with higher mechanical properties the heat input needs to be optimum. By controlling the tool rotational speed, it is possible to control the heat input in optimum level thereby improving mechanical properties. A study on effect of tool rotational speeds on microstructure and mechanical properties of the FSWed A6061-T6 has found that, higher hardness and tensile strength is achieved with a higher tool rotational speed at 800 rpm (Wang et al. 2016b).

2.9 Scientific motivation and critical comparison of the TIG, CMT and FSW techniques

Now-a-days the use of lightweight materials in automotive parts is an effective strategy to reduce fuel consumption and greenhouse emissions. Automotive industries are mainly focusing their effort to produce lightweight vehicles by replacing automotive body material from the frequently used low carbon steels to multi-materials such as interstitial-free low carbon steels, high strength steels, advanced high strength steels, aluminium alloys, magnesium alloys and fibre reinforced polymers. Among the mix of materials used in automotive applications, aluminium alloys are emerging as the principal material option for auto body construction and their usage is increasing day by day. The critical property of aluminum that makes it so attractive is its low density (2.69 g/cm^3), which is 1/3 that of steel (Bloeck 2012). Moreover, aluminum alloys offer a greater strength to weight ratio than steel. Lightweight aluminium sheet is being used for automotive applications due to a

number of benefits (Bloeck 2012): (1). Aluminium offers high potential for weight saving, improving vehicle fuel efficiency and handling characteristics, while reducing at the same time the total greenhouse gas emissions throughout the life of the vehicle;(2). The metal is easily and widely recycled, saving energy and raw materials; (3). Aluminium will absorb the same amount of crash energy as steel, at just over half the weight. Because of the present-day multi-material design approach, the joining of dissimilar materials, most importantly dissimilar aluminium alloys, is getting a momentum. A comparative investigation on microstructural and mechanical characteristics of TIG and FSW weldments of dissimilar A6061 and A356 aluminum alloy plates (Tehyo et al. 2018) has shown that the ultimate tensile strength of dissimilar FSWed joints was superior to those of the TIG (with filler) and TIG (without filler) weldments. Kotari et al. have compared the microstructure and mechanical characteristics of AA6061 and AA7075 dissimilar joints produced by FSW and TIG welding (Kotari et al. 2020). The presence of finer grains and the higher amount of Mg_2Si precipitates in FSWed joint increased its strength by 19% than that of the TIG joint (Kotari et al. 2020). The mechanical properties and microstructural features of dissimilar aluminum 6061 T6 and 5083 O weldments processed by TIG, GMAW and FSW were investigated (Jannet et al. 2014). The width of the heat affected zone of the FSWed joint was narrower than the fusion welded joints. Moreover, the tensile strength obtained with FSW was higher as compared to the conventional fusion welding process. The dissimilar aluminum alloys of 5083-H12 and 6061-T6 were welded by FSW and TIG welding techniques (Ghaffarpour et al. 2017). The results have shown that the welds produced by FSW indicated a considerably higher

quality and also improved mechanical properties than those of the TIG welding. A previous research work on CMT welded dissimilar A5083-H111 and A6082-T651 aluminium alloys has reported that good joint efficiency was achieved with high welding speed (Gungor et al. 2014a). The effect of weld heat input on mechanical properties of CMT welded A5754-A6061 dissimilar aluminium alloys was investigated (Çömez and Durmuş 2019). Higher heat input caused grain coarsening in the HAZ of AA5754 and overaging in AA6061 base metal that led to reduced tensile strength of the joints. Palanivel et al have studied the effect of tool rotational speed and pin profile on the microstructure and tensile strength of the dissimilar AA5083-H111 and AA6351-T6 alloys joints (Palanivel et al. 2012). They have found that the straight square (SS) pin profile at a rotational speed of 950 rpm exhibited higher tensile strength. Zhongjie Yan et al have studied the influences of sheet configuration on microstructure and mechanical properties of the FSWed dissimilar Al–Mg–Si/Al–Zn–Mg aluminum alloys joints. They have observed that when the Al–Zn–Mg alloy was located at the advancing side (AS), the joints displayed better fatigue properties. The high strength steels such as dual phase steels (DP steel), transformation induced plasticity steels (TRIP steel), twinning induced plasticity steels (TWIP steel) (Tisza and Czinege 2018) used in inner body panels, splash guards, heat shields, air cleaner trays, covers, structural parts and load floors can be replaced by the aluminium alloys such as A5754 and A5083 (Benedyk 2010). Moreover, the high strength steels such as dual phase steels (DP steel), transformation induced plasticity steels (TRIP steel), twinning induced plasticity steels (TWIP steel) (Tisza and Czinege 2018) used in outer body panels, hood, front fenders, doors, trunk lids can be

replaced by the aluminium alloys such as A6061 and A6082 (Benedyk 2010). Based on the mentioned literature and to the author's best knowledge, the joining of dissimilar combinations of A5754-A5083, A6061- A6082 aluminium alloys through by conventional tungsten inert gas welding (TIG), cold metal transfer welding (CMT) and friction stir welding (FSW) techniques have not been reported till date. Therefore, joining dissimilar A5754-A5083, A6061- A6082 aluminium alloys through TIG, CMT and FSW that are much in demand as multimaterial assemble in automotive is quite promising for their higher strength to weight ratio, lower greenhouse gas emissivity and lower fuel consumption than steel, the conventional automotive material, having a higher density (7.8 g/cm^3) than the aluminium alloys (2.7 g/cm^3). Also, in the reported investigations on CMT and TIG welding of dissimilar materials, tensile tests were performed only on macro-specimens consisting of the weld metal, base metals and HAZs of both the materials (Babu et al. 2019; Chuaiphan and Srijaroenpramong 2020; Gungor et al. 2014b; Kavitha et al. 2021); tensile properties of the individual interfacial regions of CMT and TIG weldments were not examined. The correlation of individual interfacial microstructure with mechanical properties is essential to understand the complete behavior of the dissimilar alloy weldments. Likewise, several researchers have conducted macro tensile studies on friction stir weldments of dissimilar alloys constituting base metals, heat affected zones (HAZs), thermo-mechanically affected zones (TMAZs) and stir zones (SZs) of both the metals (Fu et al. 2015; Jamshidi Aval 2015; Rodriguez et al. 2015). However, macro tensile testing is inadequate to determine the mechanical properties of individual zones, particularly the SZ. The SZ of FSWed parts is of prime importance because the

resulting property of the welded joint is mainly decided by this zone. To correlate the microstructure and mechanical properties of individual interface regions in the dissimilar weld of CMT and TIG welds and SZ of FSWed sample it is necessary to prepare miniature tensile sample. Hence, the present work is aimed to weld dissimilar combinations of A5754-A5083, A6061- A 6082 by tungsten inert gas (TIG) welding, cold metal transfer welding (CMT) and friction stir welding (FSW) techniques and to study their structure property correlation. The study further correlates the microstructure and mechanical properties of the interface regions CMT and TIG welds and SZ of FSWed sample.

2.10 Objectives

- To weld sheets of dissimilar A5754-A5083, A6061-A6082 combinations by using tungsten inert gas (TIG) welding, cold metal transfer welding (CMT), and friction stir welding (FSW) techniques.
- To carry out microstructure and mechanical characterization of welded alloy.
- To analyze the structure property correlation of the joined alloys.

Chapter 3

MATERIALS AND METHODS

3.1 Material

A6061-T6, A6082-T6, A5754-H111 and A5083-H111 aluminium alloy sheets of 3-mm thickness were used as base materials. Nominal compositions of the alloys are presented in Table 3.1.

Table 3.1 Chemical composition of base aluminium alloys and filler materials (wt.%)

Alloys	Al	Mg	Mn	Si	Fe	Cr	Cu	Ti	Zn
A6061	Bal.	1.1	0.1	0.7	0.28	0.19	0.2	0.15	0.2
A6082	Bal.	0.8	0.9	1.1	0.3	0.25	0.1	0.1	0.2
A5754	Bal.	2.6	0.5	0.4	0.4	0.3	0.1	0.15	0.2
A5083	Bal.	4.5	1.0	0.4	0.4	0.2	0.1	0.15	0.25
ER-4043	Bal.	0.05	0.05	5	0.7	-	0.3	0.02	0.1
ER5356	Bal.	5	0.15	0.2	0.2	0.1	0.05	0.1	0.1

The aluminium alloys were procured from PMC Corporation, Bangalore, India. The procured alloys are non-heat treatable wrought aluminum alloys such as A5754- H111,

A5083-H111 and heat treatable wrought aluminum alloys such as A6061-T6, A6082-T6. The T6 condition represents solution heat-treatment followed by artificial ageing. No filler materials were used for FSW. The ER5356 and ER4043 wires of 2.4 mm diameter were selected as filler materials for TIG and CMT welding. The aluminium alloys weld through fusion welding need filler material to prevent shrinkage cracking generated during the solidification of the liquid weld pool. The filler material commonly used for aluminum alloys is a high Mg content aluminum alloy, such as the ER5356 alloy and a high Si-content aluminum alloy, such as the ER4043 alloy. In the present study, ER4043 and ER5356 filler materials were used for welding.

3.2. Edge preparation

Samples of dimension, 50x220x3 mm³ [for TIG and CMT welding] and 90x220x3 mm³ [for FSW] were cut perpendicular to the rolling direction using a semi-automatic shear cutting machine. In the case of TIG and CMT welding, samples with single V groove butt joint design were prepared for welding [as shown in Fig 3.1]. The joint configuration has a single V groove with 60° included angle and root height of 1mm. At the same time, no V groove design was prepared for FSW. The edges of the cut sheets used for FSW were subsequently skin milled, so that the edges maintained zero-gap during welding. The square butt joint design was used in the present experiments.

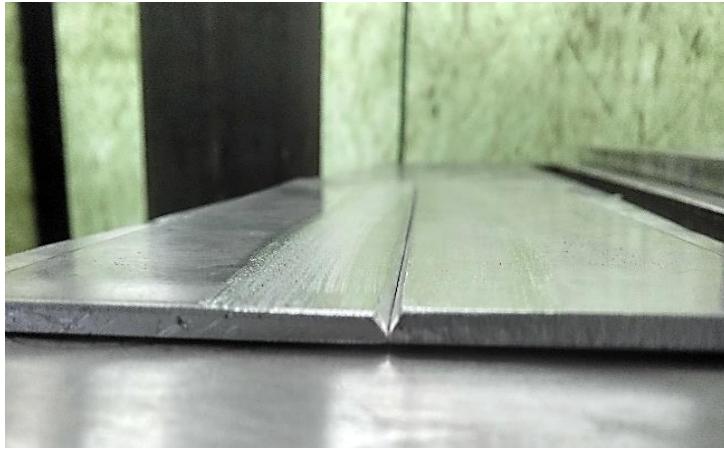


Fig. 3.1 V groove butt joint design for TIG and CMT welding

3.3 Cleaning of materials

After cutting and grooving typically impurities such as oil, grease and dust were present in the material. Prior to welding the edges and surface of the prepared samples were initially cleaned using buffing machine to remove the oxide layer. Finally, acetone was applied at the surfaces and edges of the sheets to remove oil, dust, grease and other contaminants.

3.4 Backing plate

In the case of TIG and CMT welding, austenitic stainless-steel plate was used as a backing plate in this experiment. The use of austenitic stainless steel avoids arc blow due to its non-magnetic property that reduces the possibility of iron pickup and offers longer life time against arc damage. Since FSW is a solid-state process, mild steel plate was used as a backing plate.

3.5 Clamping set up for materials

In the case of TIG and CMT welding, to avoid movement of the sheets from their initial position, both the end portion sides were tack welded at a few mm (around 5 mm) distance prior to the welding. The sheets were clamped properly by using suitable clamps to avoid distortion. Subsequently, the cleaned samples were kept on backing plate in flat (1G) position and clamping was done using G clamps to maintain the alignment and gap [as shown in Fig 3.2. (a-b)]. In the case of FSW, the cleaned samples were kept on a backing plate in flat (1G) position and clamping was done using the clamp setup attached in the FSW machine.





Fig. 3.2 Clamping set up to hold the specimens in a TIG and CMT (a) Side view (b) Top view.

3.6 Shielding gases

Argon gas (purity of 99.95%) was used as shielding gas which could protect the arc, molten pool and tungsten electrode from the surrounding atmosphere. Moreover, during the welding it provides conduction path between the workpiece and the electrodes. Argon offers better arc stability and cleaning action of the weld pool. Hence in the present experiment argon is chosen as the shielding gas.

3.7 Electrode used for TIG and CMT welding

In the case of TIG, EWZr-1 electrode with a diameter of $\text{Ø}2.4\text{mm}$ was used to weld the dissimilar joints and the filler materials (diameter $\text{Ø}1.6\text{ mm}$) were added separately. The ball shaped electrode tip was used for TIG welding. The zirconated tungsten electrodes are less likely to contaminate aluminium, hence these electrodes were selected for TIG

welding. While, in the case of CMT welding, the ER4043 and ER5356 filler materials act as both filler materials and electrodes. The diameter of these fillers was $\text{Ø}1.6$ mm.

3.8 Tool used for FSW

A high-carbon high-chromium tool (HCHCR D3) was used for welding of the dissimilar aluminium alloy sheets. Fig.3.3 shows front view and top view of the FSW tool. After clamping the sheets, the tool was positioned 0.5 mm offset from the center line towards A5083 in 5xxx series dissimilar joint and towards A6061 in 6xxx series dissimilar joint. The butt friction stir welding was carried out perpendicular to the rolling direction of the sheets.

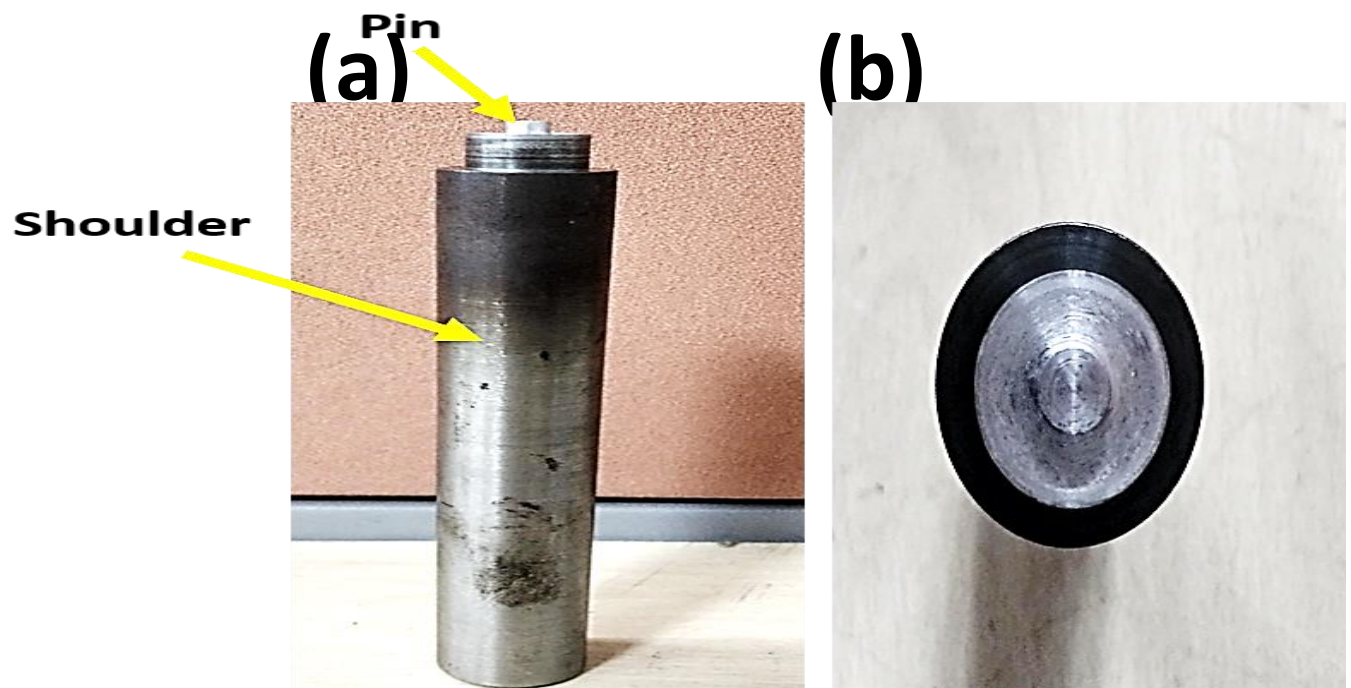


Fig. 3.3 FSW tool (a) Front view (b) Top view

3.9 Welding equipment

3.9.1 TIG welding equipment

A Lincoln electric (square wave tig-355) equipment with constant current power source was used for welding the prepared samples [Fig.3.4 (a)]. The balanced square wave AC was used as a polarity during welding. The experiments were conducted through manual TIG welding process by using vertically positioned water cooled TIG welding torch [Fig. 3.4 (b)] in a single pass. Fig. 3.4 (a) shows FSW equipment.





Fig. 3.4 (a) Tungsten inert gas (TIG) welding equipment and (b) Welding torch

3.9.2 CMT welding equipment

The welding system comprised a Fronius Transpuls synergic 5000 welding power source with a full digital microprocessor controller and a Fronius (model: A4600 Wels) cooling equipment. The wire feeding system was composed of a VR 7000 CMT wire feeder with a welding torch. The wire feeder was used to feed the filler wire of $\text{Ø } 1.2 \text{ mm}$ diameter accurately. A constant voltage power source with a DCEP mode was used for welding. Fig.3.5 (a) and (b) shows cold metal transfer (CMT) welding machine and welding torch, respectively.



Fig. 3.5 (a) Cold metal transfer (CMT) welding machine and (b) Welding torch

3.9.3 FSW equipment

Fig. 3.6 shows the Grease FSW equipment that was used for welding. Fig. 3.6 (a) shows the clamping set up in FSW machine. A high-carbon high-chromium tool (HCHCR D3) was fitted in a tool holder, as shown in Fig. 3.6(b).

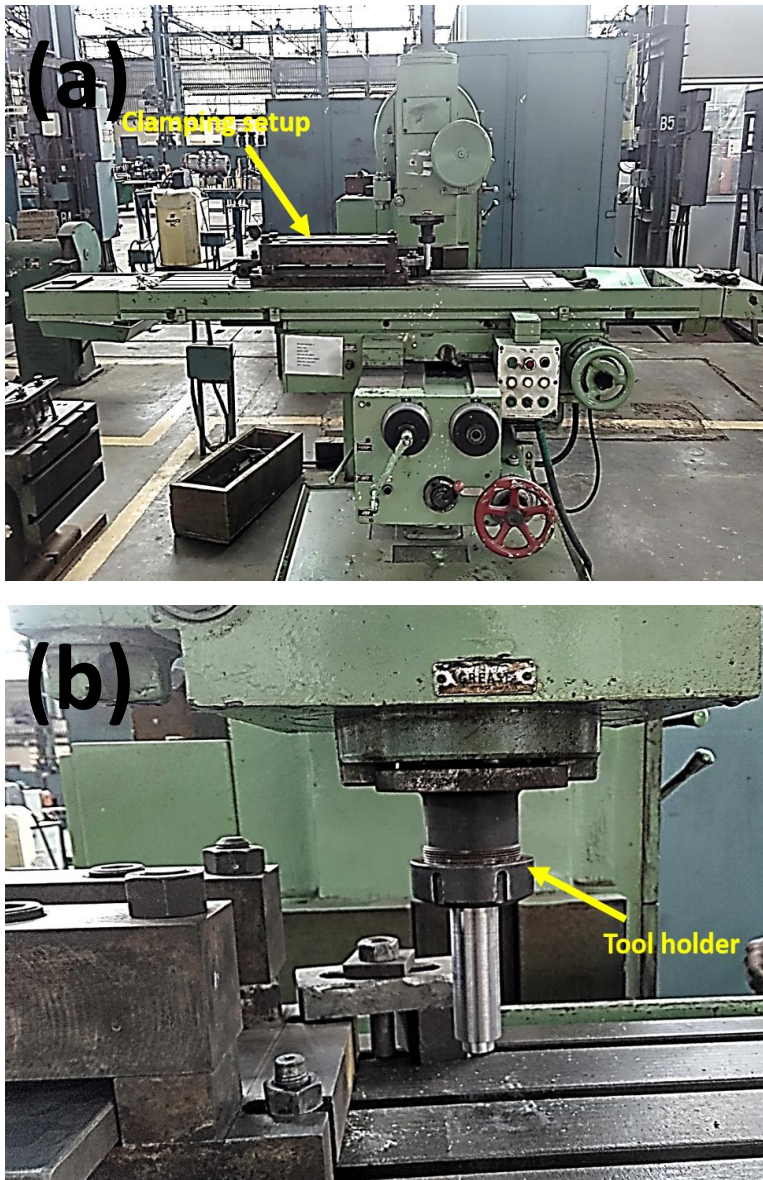


Fig. 3.6 (a) FSW equipment and (b) Tool holder

3.10 Metallography

The photograph of the surface appearance of weldments was taken using a Xiomi Redmi 2 camera (8 Mega pixel). Macrostructural images of the welded specimens were taken using a Leica light microscope. For microstructural examination, metallographic specimens of dimension $15 \times 30 \text{ mm}^2$ were machined from the welded joints and were prepared following the standard metallographic procedure. Prior to polishing, the samples were mounted using hot mounting process [Fig. 3.7 (a)]. During the hot mounting process the temperature and pressure were maintained as 170°C and 180 bar, respectively. The process conditions such as heating time, cooling time and the overall cycle time were 8 min, 12 min and 25 min, respectively. Initial grinding and final polishing of the samples were performed using SiC emery papers and a disc polisher [Fig.3.7 (b)] sprinkled with Al_2O_3 particles. For etching, Poulton's reagent (12 ml HCl, 30 ml HNO_3 , 1 ml HF, 40 ml H_2O and 4g chromic acid) was used. Microstructural characterization of the welded samples was carried out using an Olympus BX51M optical microscope and a scanning electron microscope (6380LA, JEOL operating at 20kV), equipped with an energy dispersive spectroscope. The views of the Leica light microscope and the Olympus BX51M optical microscope are shown in Fig 3.8.



Fig. 3.7 (a) Hot mounting machine and (b) Disc polishing machine



Fig. 3.8 (a) Optical microscope and (b) Optical microscope

3.11 Electron Back Scattered Diffractometry

Electron back scattered diffractometry (EBSD) studies were conducted using a FEI Quanta Field Emission Gun–Scanning Electron Microscope (FEG-SEM) operating at 30 kV with a scan step size of 0.2 μm . Two types of clean-up methods were used for EBSD data. In

the first place, the data were cleaned up by grain C.I. (confidence index) standardization with a grain tolerance angle of 5° and a minimum grain size of 2 μm. Secondly, the data are cleaned up with neighbor orientation correlation with a minimum confidence index of 0.1. To analyze misorientation of the grains, the minimum and maximum angles used were 2° and 65°, respectively. Samples for EBSD studies were electropolished using a solution of 80% methanol and 20% perchloric acid kept at -12°C for 20s.

3.12 Hardness and Tensile Testing

Microhardness test was carried out using a Vickers microhardness tester (Omni tech testing machine) with a load and indentation time of 0.2 kg and 10s, respectively. Macro tensile test experiments were conducted at a strain rate of 1mm/min, using a Zwick Roell tensile testing machine [Fig.3.9]. The specimens were prepared perpendicular to the welding direction using milling machine. For each weldment, three tensile specimens were machined out. Tensile samples for macro tensile test were prepared as per ASTM -E8 standard with a gauge length of 25mm. Miniature tensile test was conducted using a mini tensile testing machine (BISS) at a strain rate of 0.001mm/min. Geometry and dimension of the macro and miniature tensile specimens are shown in Fig. 3.10 (a & b).

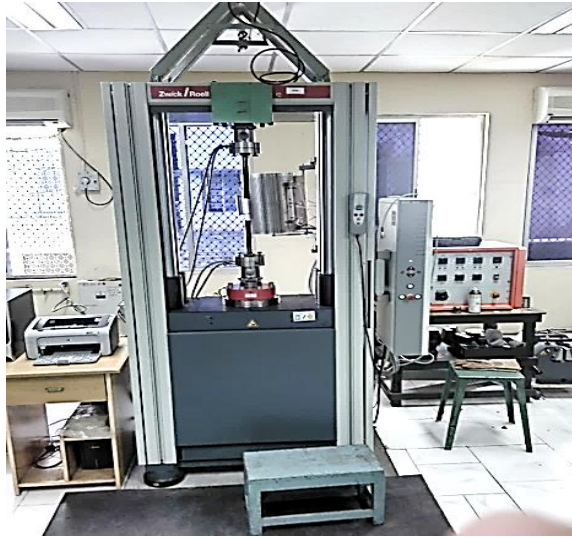


Fig. 3.9 Tensile testing machine

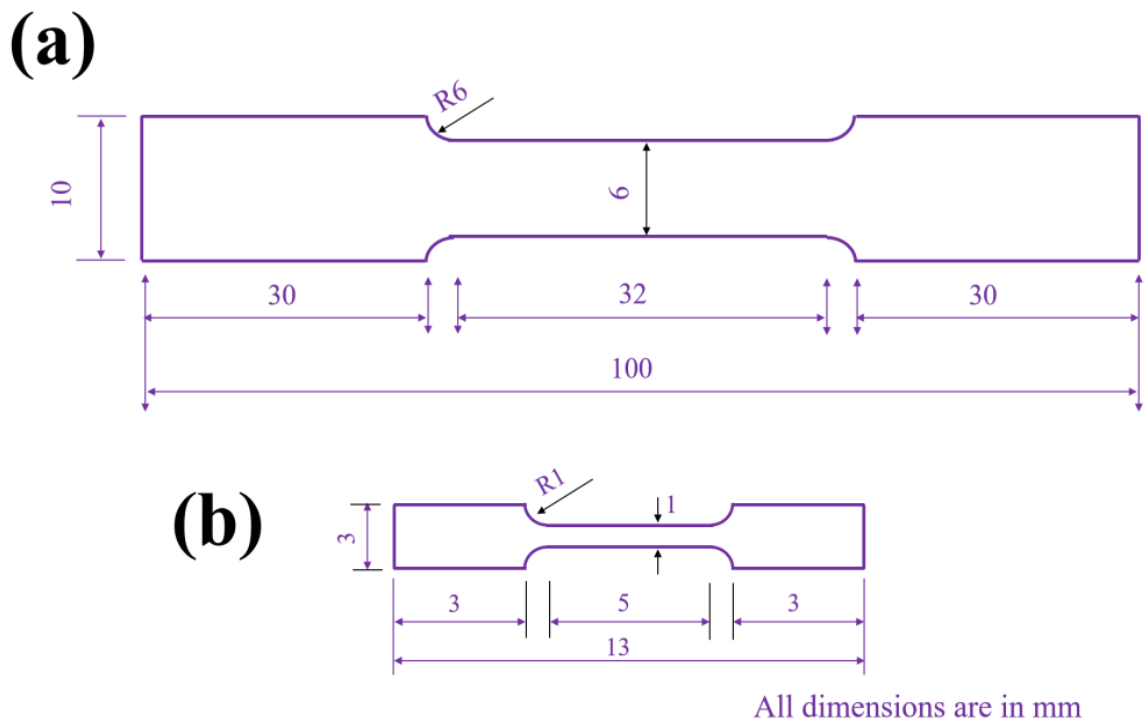


Fig 3.10 Geometry and dimensions of tensile specimens (a) Macro specimen and (b) Miniature specimen from interface regions

Miniature tensile specimens were prepared from the individual interface regions of the welded joint and WMZ center in fusion welds (TIG and CMT). For FSW joints, miniature tensile specimens were salvaged from SZs (stir zones). The machining was done using a wire electric discharge machine (DK7740, Concord wire EDM, 0.18 mm diameter molybdenum wire). Schematic diagrams [Fig. 3.11(a-b)] show the preparation of miniature tensile test samples from various regions in the fusion welds (TIG and CMT). The macro tensile samples were prepared from over all region in fusion welds (TIG and CMT) as shown in Fig. 3.11 (c). Miniature tensile test samples were prepared from SZ and macro tensile samples were prepared from over all region in FSW joint as shown in Fig. 3.12 (a) and Fig. 3.12 (b) respectively.

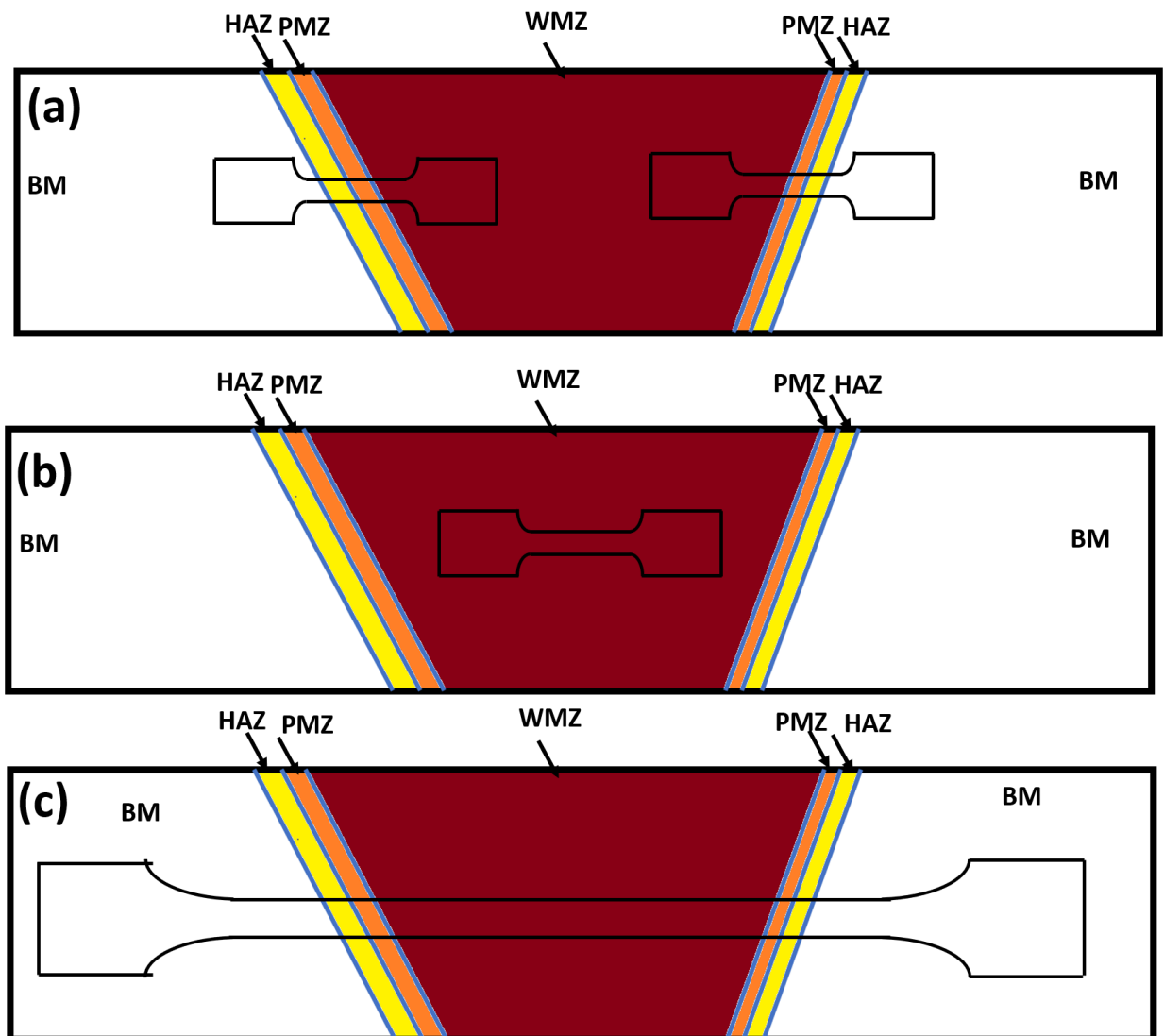


Fig 3.11 Schematic diagrams showing tensile sample preparation from the TIG and CMT welds (a) Miniature sample from interface regions, (b) Miniature sample from WMZ center and (c) Macro tensile sample from over all region

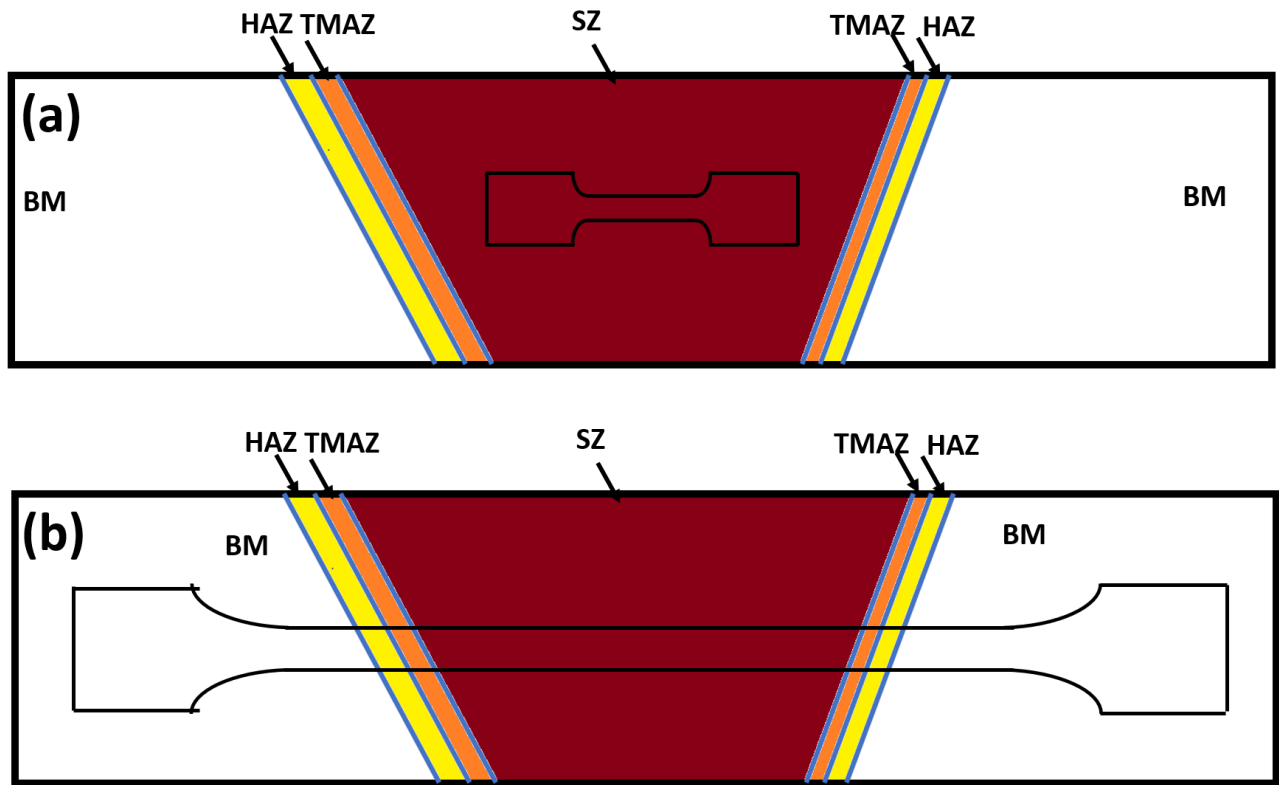


Fig 3.12 Schematic diagrams showing tensile sample preparation from the FSW joint (a) Miniature sample from stir zone (SZ) and (b) Macro tensile sample from over all region

Chapter 4

RESULTS AND DISCUSSION

4.1. Cold metal transfer (CMT) welding of dissimilar A6061-T6 and A6082-T6 using ER4043 filler wire

4.1.1 Surface appearance of the CMT welded A6061-T6 and A6082-T6 joint using ER4043 filler wire

Fig. 4.1 (a-b) shows the surface appearance of CMT welded A6061-T6 and A6082-T6 dissimilar joints produced by using ER4043 filler wire. Visual examination confirms that there are no defects on the surface. The dissimilar joint has wavy edges in the weld. The joint does not exhibit cracks and spatter in the weldment. The back side of the dissimilar joint does not show any lack of fusion, and full penetration is achieved with the used parameters.

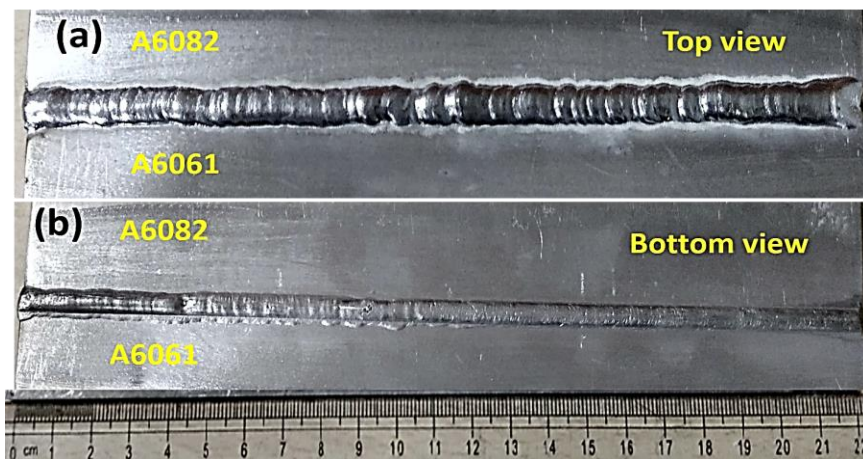


Fig. 4.1 Surface appearance of the CMT welded A6061-T6 and A6082-T6 joint using ER4043 filler wire: (a) Top view and (b) Bottom view

4.1.2 Macrostructure of the CMT welded A6061-T6 and A6082-T6 joint using ER4043 filler wire

Fig. 4.2 shows the macrostructure of transverse section of the CMT welded A6061-T6 and A6082-T6 dissimilar joint. The joint exhibits a weld without any defect. Complete depth of penetration is achieved in the joint. The shape of the weld metal is found to be almost symmetrical with respect to the center line of the weld.

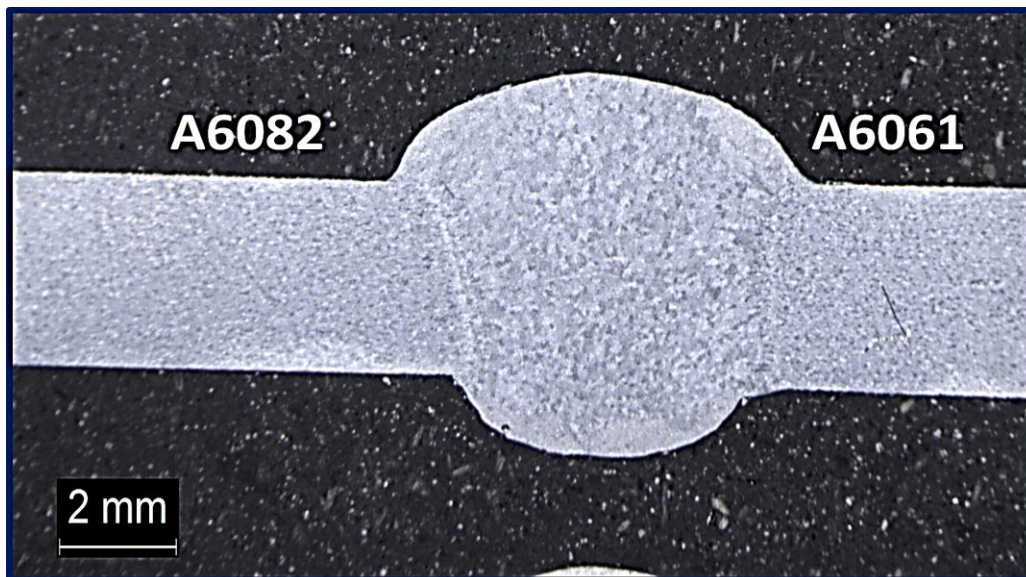


Fig. 4.2 Macrostructure of transverse section of the CMT welded A6061-T6 and A6082-T6 joint using ER4043 filler wire

4.1.3 Microstructures of the interfaces and WMZ in CMT welded A6061-T6 and A6082-T6 joint using ER4043 filler wire

Figs. 4.3 and 4.4 show SEM microstructures of the weld interface regions of 6061-T6 and 6082-T6, respectively. Three zones, viz. heat affected zone (HAZ), partially melted zone

(PMZ) and columnar crystal zone (CCZ) are clearly observed at the interfaces. At the PMZs, the respective Al base metals (6061-T6 at interface of 6061-T6 and 6082-T6 at interface region of 6082-T6) are partially melted and mixed with the Al filler material. During solidification, when the liquid metal temperature drops sufficiently below its freezing point, stable nuclei form at various locations in the liquid. The nuclei, act as centers for further solidification. As temperature continues to drop during cooling, more atoms attach themselves to the existing nuclei, in the certain preferred directions, usually along the crystal axes, or form new nuclei in the liquid. Each nucleus grows in three dimensions in this fashion into the crystal lattice. This results in a 'tree-like' structure that is termed as, dendrite. The columnar dendrites near the fusion line have formed due to a large temperature gradient during solidification of the WM. It can be seen that the growth of CCZ has taken place from PMZ toward the center of weld (Fig. 4.3 (c) & Fig. 4.4 (c)). Next to the fusion line, PMZ is visible at both the interfaces of the joint. The temperature at PMZ was very high that led to the dissolution of precipitates. The reprecipitation phenomenon did not occur in PMZ due to insufficient time during cooling. However, no precipitation was observed in the cooled samples, taking into consideration the limitations of the SEM facility. The presence of gas pores and shrinkage pores are clearly visible at the 6061-T6 interface, as shown in Fig. 4.3 (a). The dendrites at the center of the WM are smaller in size as compared to the dendrites near the fusion lines (6061-T6 and 6082-T6 sides). This can mainly be attributed to the increase in cooling rate from the edge to the center of the molten pool. This implies that the cooling rate near the fusion lines on both

the interfaces is lower compared to the center of the WM. Due to this, the center of the WM exhibits finer dendrites and the interfaces exhibit coarser dendrites.

A difference in dendrite size has been observed in CCZ of 6061-T6 and 6082-T6 interfaces (Fig. 4.3(c) and 4.4(c)). This is mainly because of the difference in thermal conductivity of the individual alloys. The thermal conductivity of A6082-T6 alloy (170 W/m. K) is higher than that of A6061-T6 alloy (167 W/m. K) (Hamilton et al. 2008). Because of the higher thermal conductivity of A6082-T6, the cooling rate during solidification is larger at the 6082-T6 interface than that at the 6061-T6 interface. Therefore, the dendrite size in CCZ of 6082-T6 interface is finer than the dendrite size in CCZ of 6061-T6 interface.

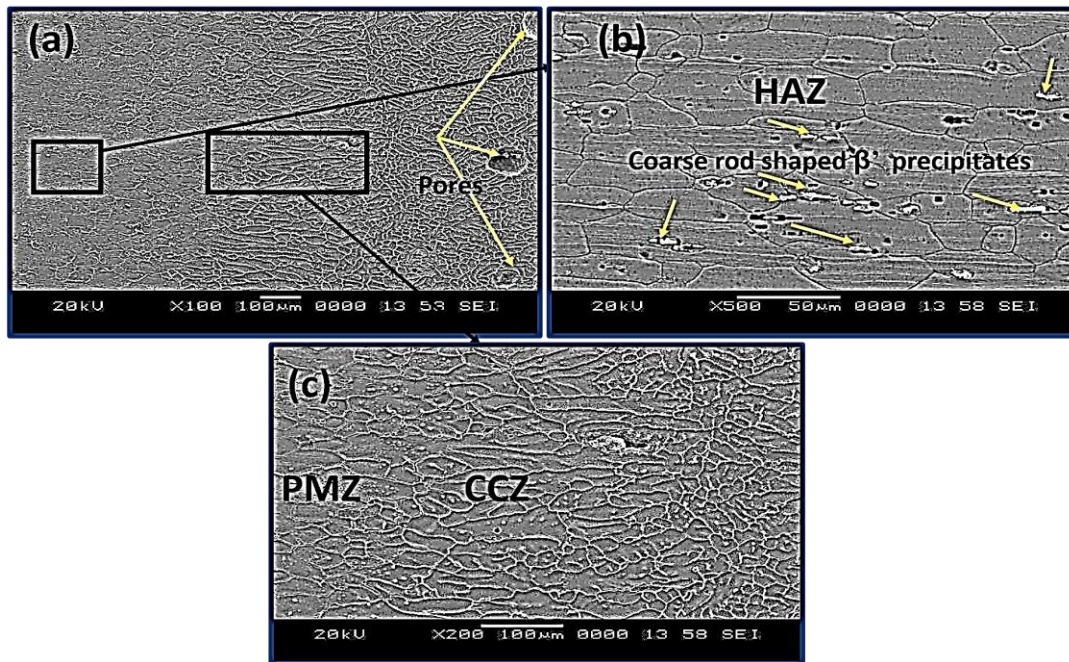


Fig. 4.3. SEM microstructure of the CMT welded A6061-T6 and A6082-T6 joint using ER4043 filler wire: (a) Interface region of 6061- T6 (b) HAZ of 6061- T6 (c) PMZ and CCZ at the interface region of 6061- T6

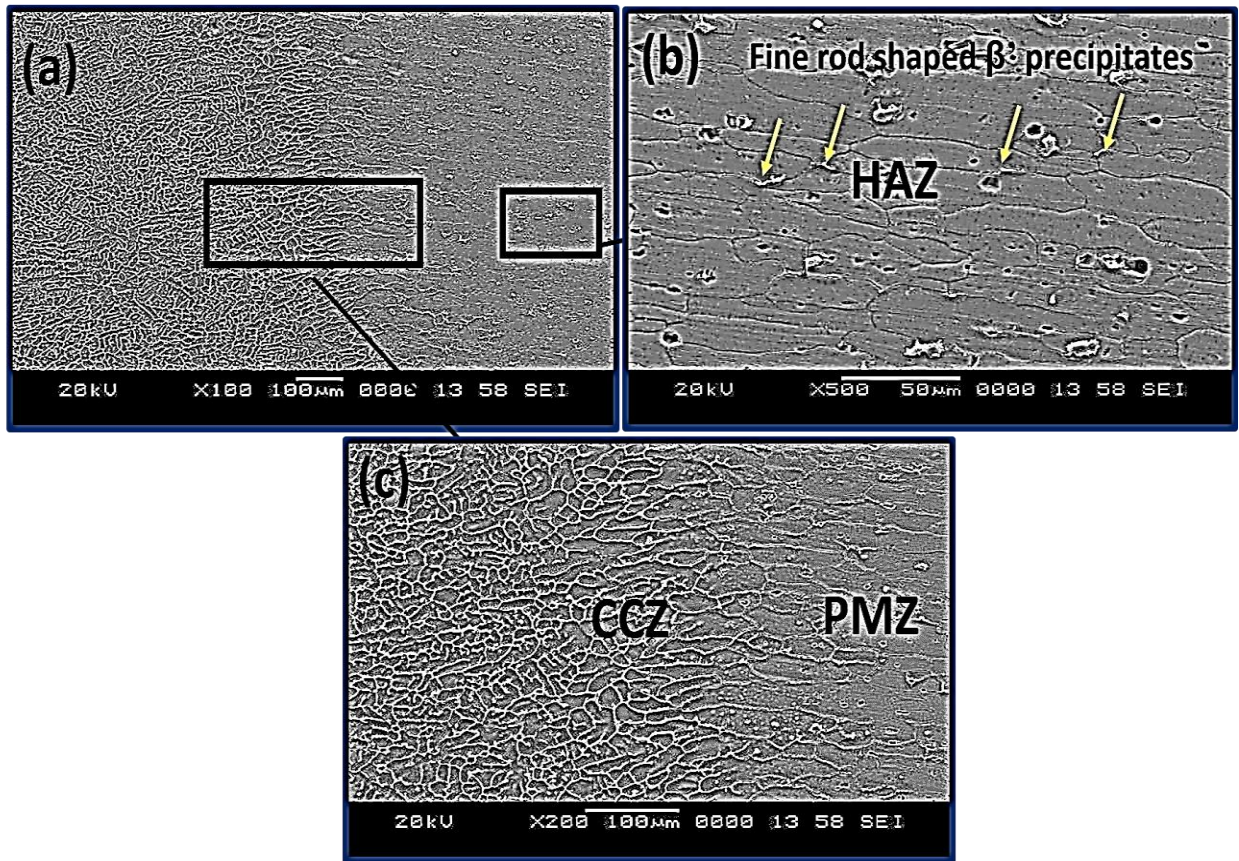


Fig. 4.4. SEM microstructure of the CMT welded A6061-T6 and A6082-T6 joint using ER4043 filler wire: (a) Interface region of 6082- T6 (b) HAZ of 6082- T6 (c) PMZ and CCZ at the interface region of 6082- T6

Fig. 4.5 shows Al-Si binary phase diagram (Massalski et al. 1990). As can be seen, the melting temperature of pure Al and eutectic (Al-12.6Si) is 660°C and 577°C, respectively. For Al rich alloys, the maximum solubility of Si at the eutectic temperature (577⁰ C) is 1.6 wt.%. The solubility decreases as the temperature decreases and it is almost negligible at the room temperature. In the present study ER4043 filler having a composition of Al-5 wt.% Si is used, which at room temperature has led to the formation of solid solution of Al

(α -Al) and eutectic phases. The center of the WMZ consists of equiaxed dendrites as shown in Fig. 4.6(a-b). Equiaxed dendrites are the dendrites which have approximately the same size in every direction. In general, the center of weld metal zone exhibits this structure because of the higher under cooling. The microstructure of the WMZ center shows a dendritic structure consisting of solid solution of aluminium (α -Al) and Al-Si eutectic along the GBs. The silicon which is precipitated in the eutectic in aluminum-silicon alloys is known as eutectic Si. The Si needle is observed in the eutectic. The Al-Si phases are low melting eutectic phases distributed almost uniformly. However, at a few places these Al-Si phases are agglomerated in the WM.

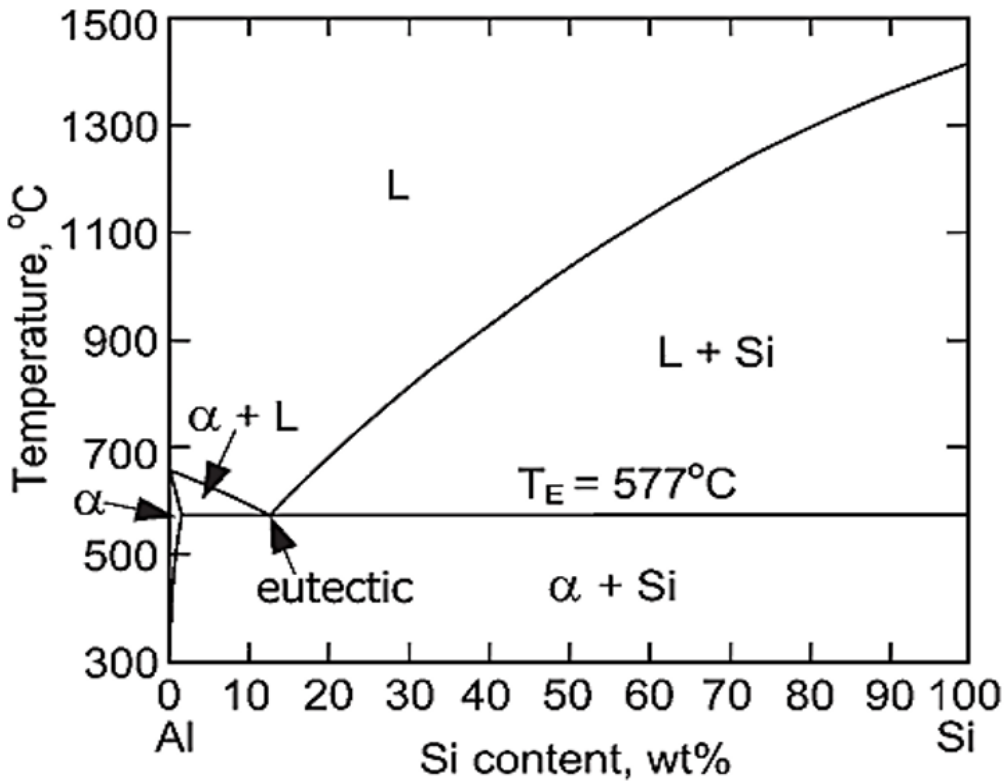


Fig. 4.5. Al-Si binary phase diagram (Massalski et al. 1990)

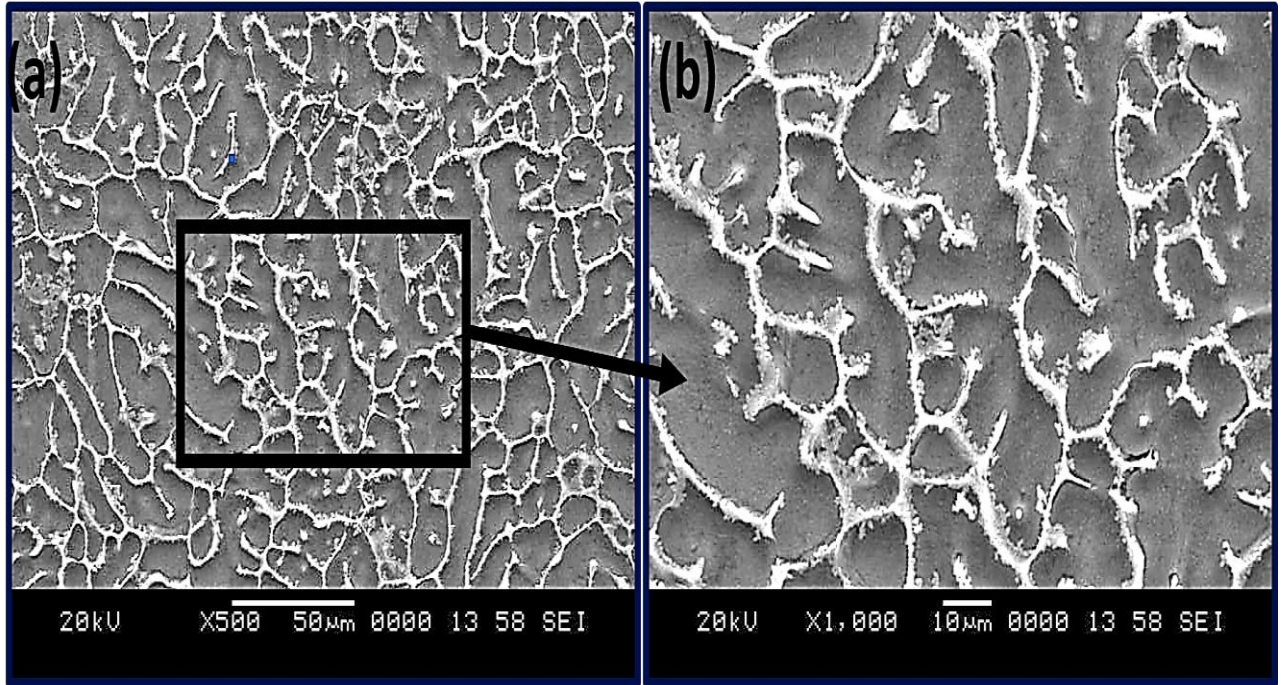


Fig. 4.6. SEM microstructure of the WMZ center in CMT welded A6061-T6 and A6082-T6 joint using ER4043 filler wire at (a) Low magnification and (b) High magnification

Fig. 4.7(a-b) displays microstructure of PMZ of the weld interface regions of 6061-T6 and 6082-T6. Liquation phenomenon at GBs and within the grains have occurred at PMZ of 6061-T6 interface as shown in Fig. 4.7(a). However, in the case of PMZ of 6082-T6 interface as seen from Fig. 4.7(b), the liquation phenomenon at GBs and grain interiors is completely absent.

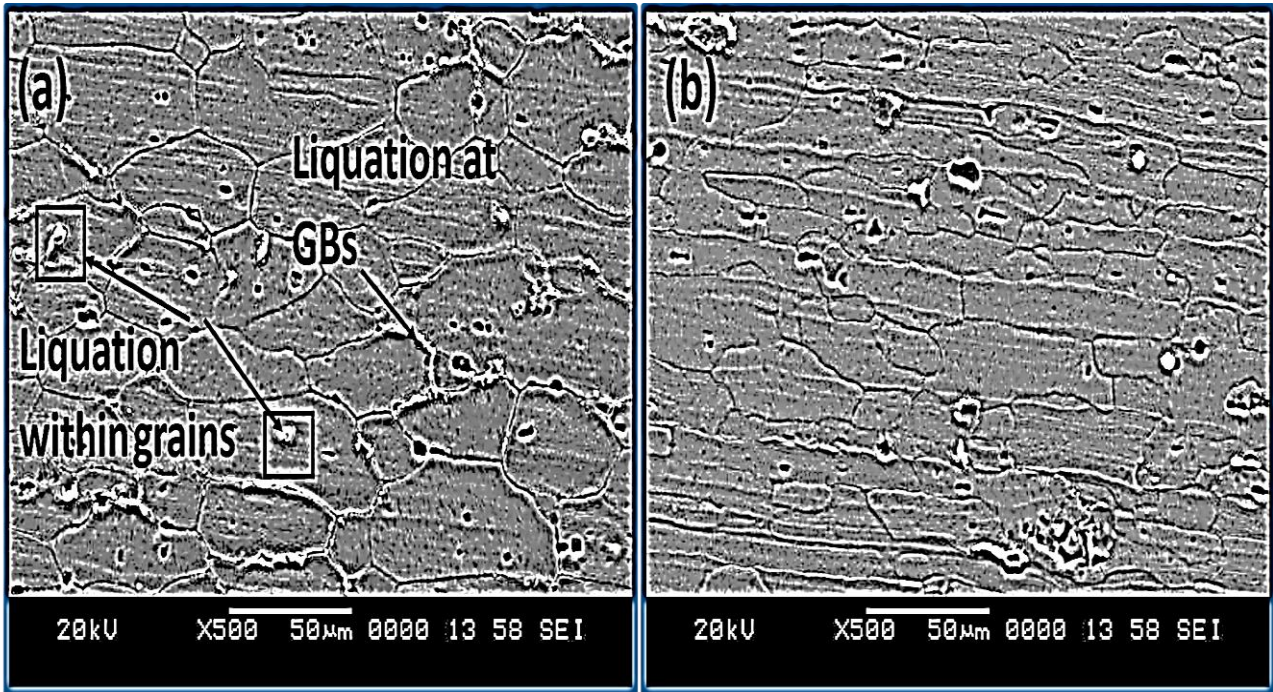


Fig. 4.7 SEM microstructures of the PMZ in CMT welded A6061-T6 and A6082-T6 joint using ER4043 filler wire (a) A6061- T6 interface and (b) A6082- T6 interface

4.1.4 SEM-EDS of the CMT welded A6061-T6 and A6082-T6 joint interfaces using ER4043 filler wire

Fig. 4.8 and Fig. 4.9 show the SEM-EDS mapping images of 6061-T6 and 6082-T6 interfaces, respectively. As seen from the figures, the amount of Si has gradually decreased from WM to HAZ at both the interfaces. However, the quantity of Mg has only slightly increased. The figure clearly shows the segregation of Si at dendritic boundaries. Table 4.1 shows percentage (at. % and wt.%) of the elements present in the A6061- T6 and A6082- T6 interface regions.

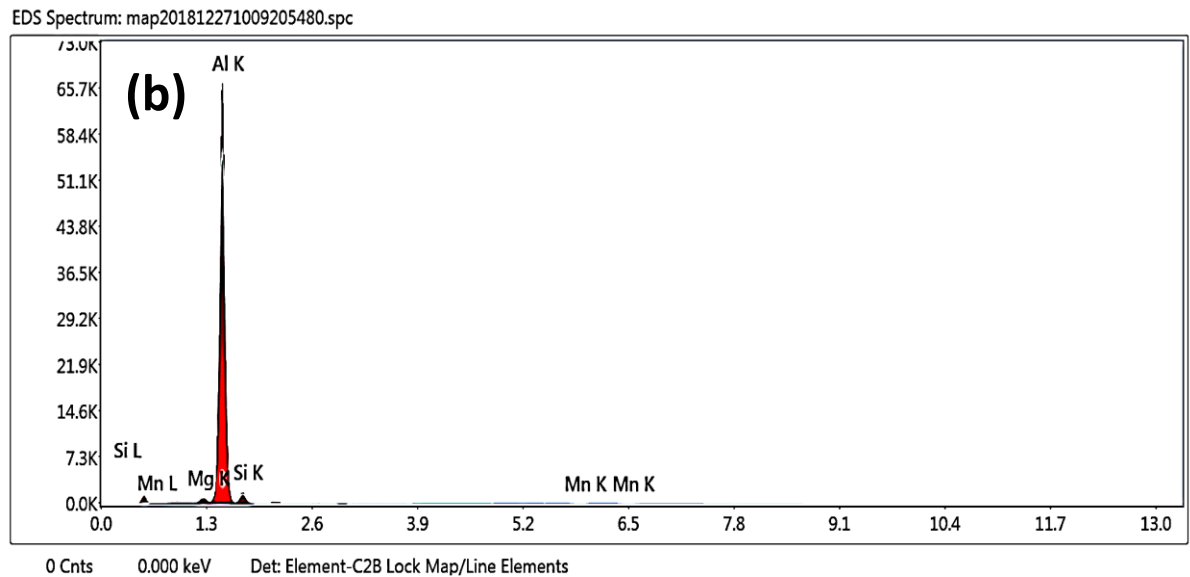
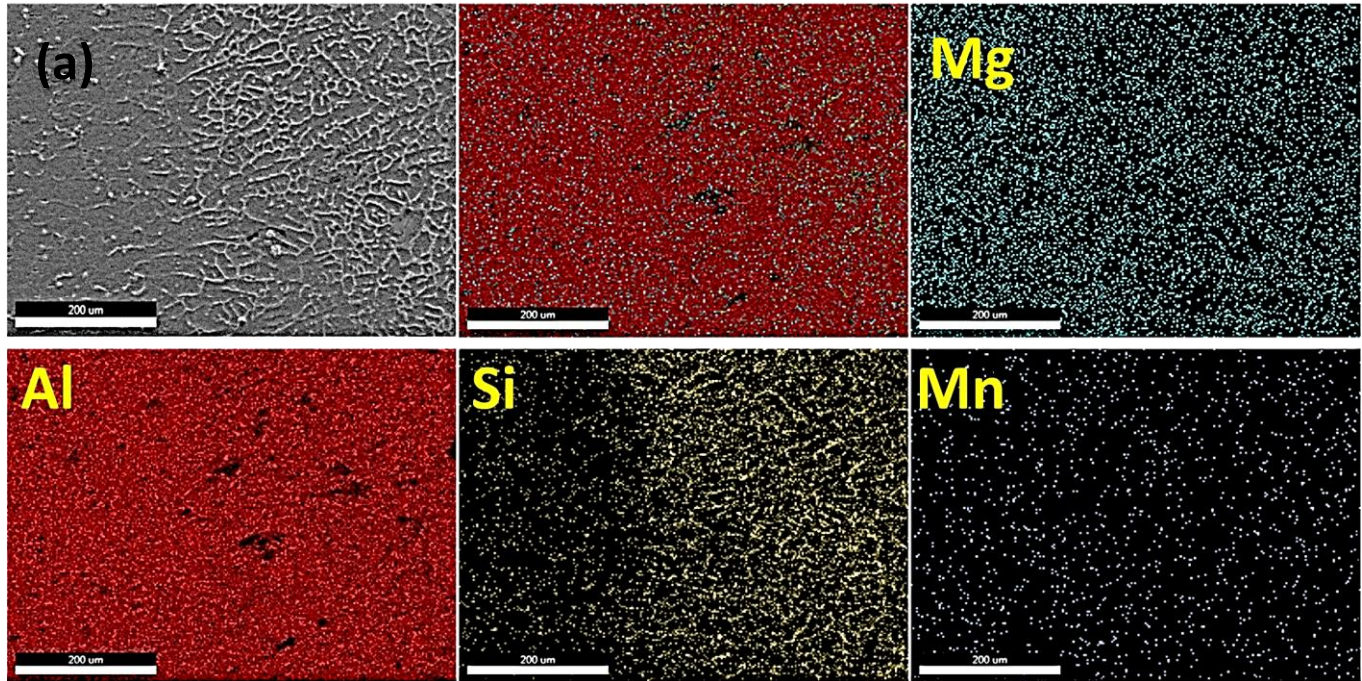
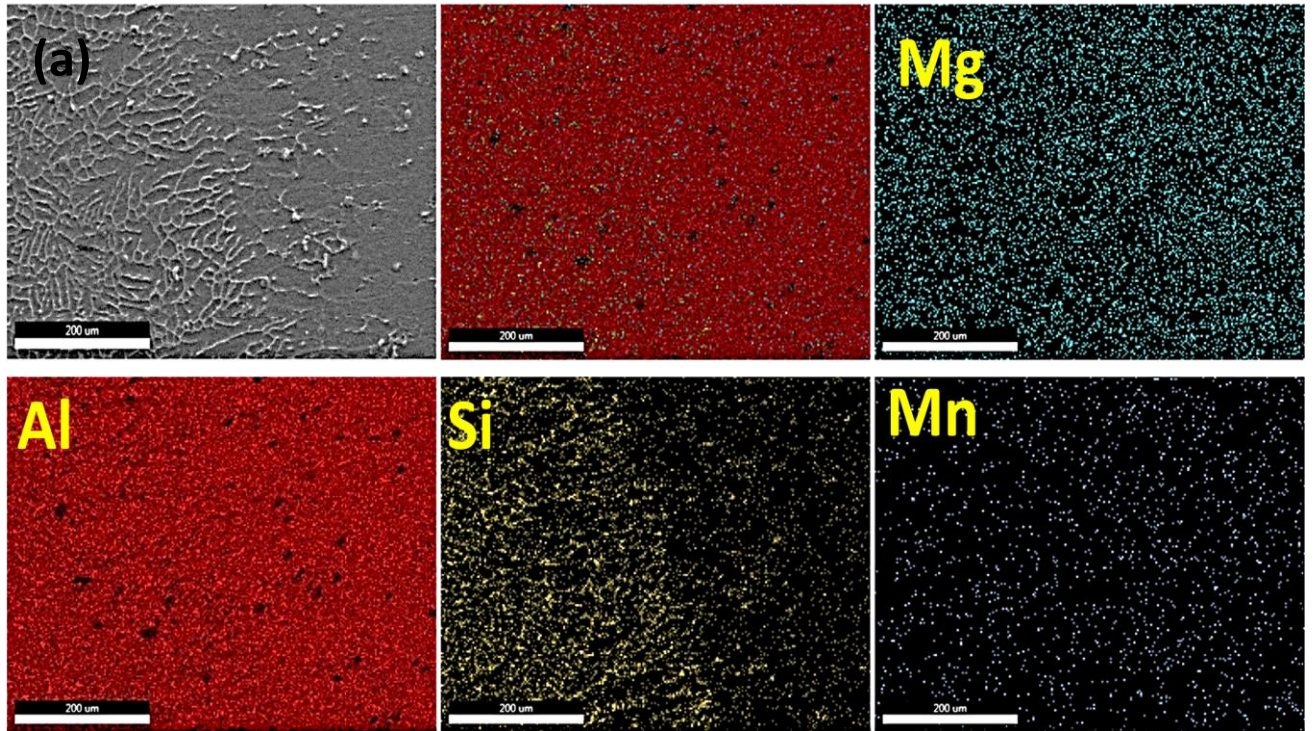


Fig. 4.8 SEM-EDS analysis of the A6061-T6 weld interface in CMT welded A6061-T6 and A6082-T6 joint using ER4043 filler wire: (a) mapping images and (b) EDS spectra



EDS Spectrum: map201812271021097730.spc

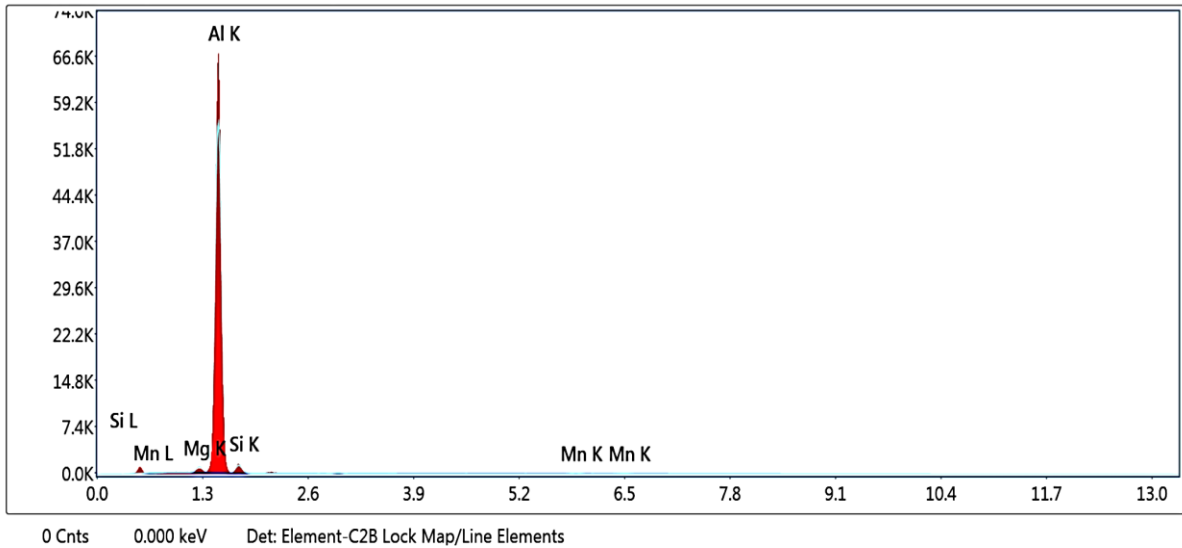


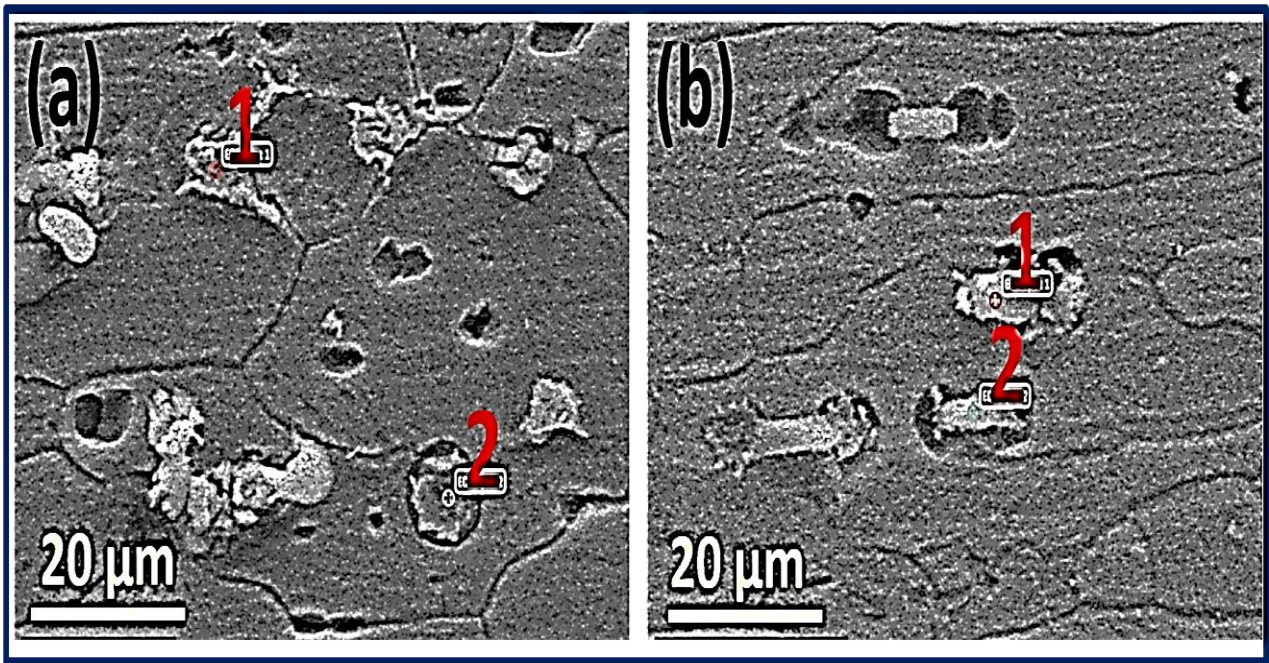
Fig. 4.9 SEM-EDS analysis of the 6082-T6 weld interface in CMT welded A6061-T6 and A6082-T6 joint using ER4043 filler wire (a) mapping images and (b) EDS spectra

Table 4.1 EDS mapping compositional details for the interface regions in CMT welded A6061-T6 and A6082-T6 joint using ER4043 filler wire

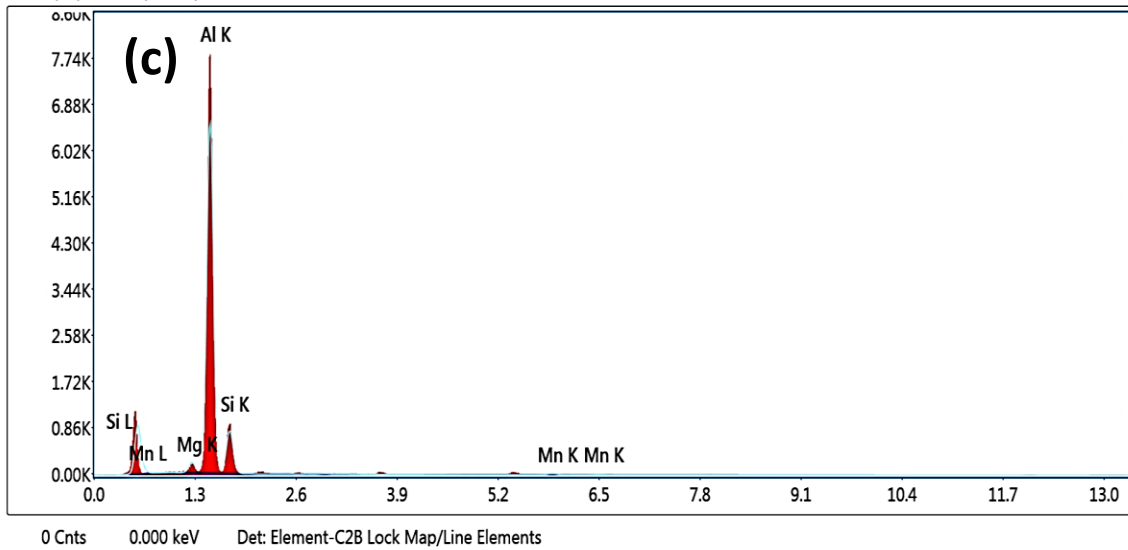
Interface	Al	Mg	Si	Mn	Al	Mg	Si	Mn
	(wt. %)				(at. %)			
A6061	Bal.	1.9	6.31	0.47	Bal.	1.66	6.08	0.23
A6082	Bal.	1.48	5.53	0.71	Bal.	1.65	5.33	0.35

4.1.5 SEM-EDS of the precipitates at the HAZs in CMT welded A6061-T6 and A6082-T6 joint using ER4043 filler wire

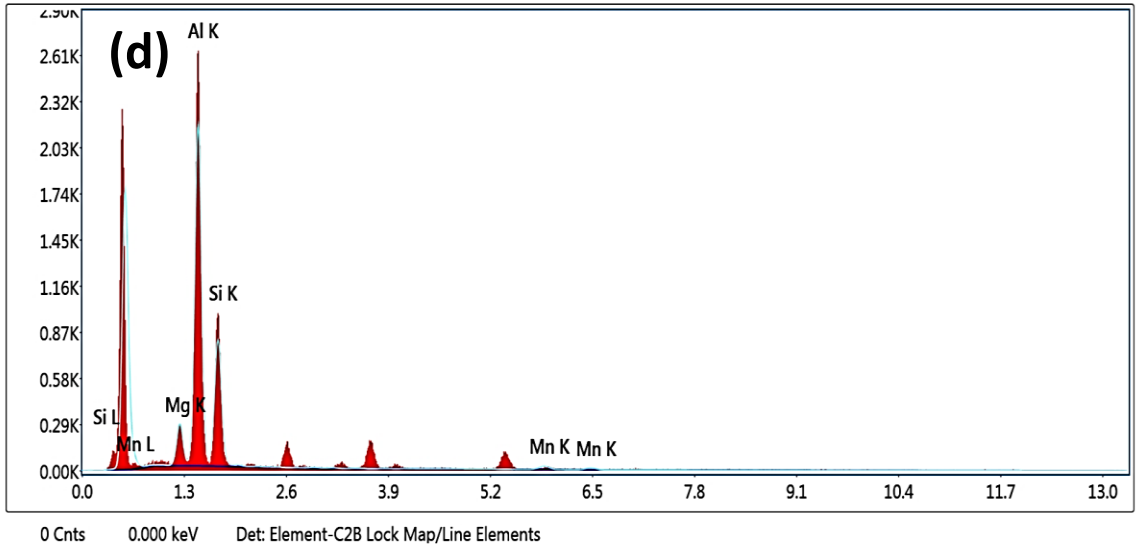
Fig. 4.10 shows micrographs of the EDS results of the precipitates at HAZs of the interfaces. The precipitates at HAZ of 6061-T6 alloy consist of higher amount of Al (76.8 at. % for point 1 and 56.6 at. % for point 2), as shown in Table 4.2. The precipitates at HAZ of 6082-T6 alloys contain larger amounts of Si (70.3 at. % and 61.1 at. % for point 1 and point 2, respectively).



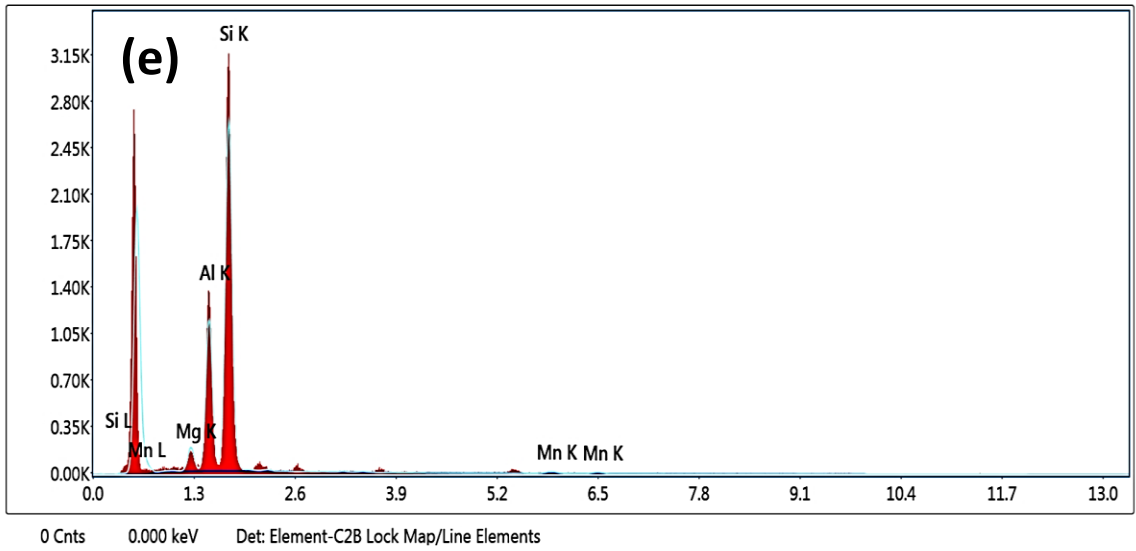
27-12 | 5 | Area 11 | EDS Spot 1



27-12 | 5 | Area 11 | EDS Spot 2



27-12 | 5 | Area 14 | EDS Spot 1



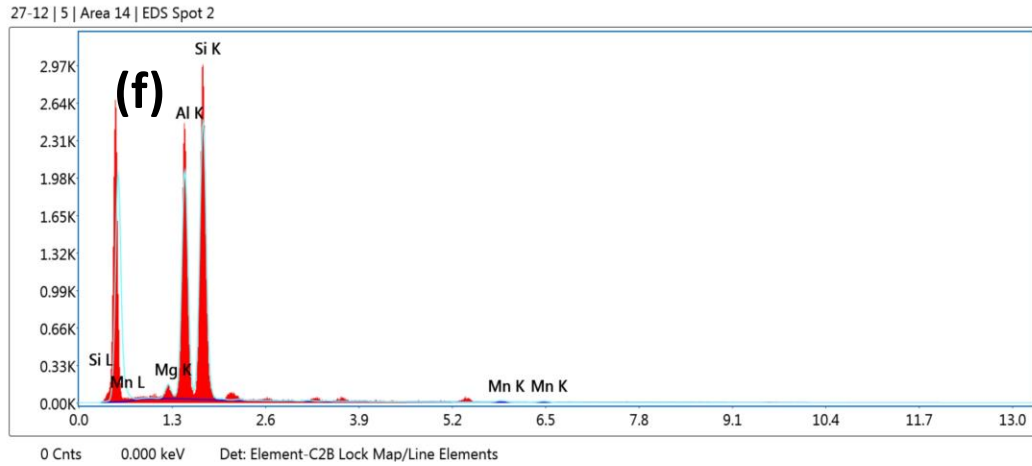


Fig. 4.10 SEM-EDS analysis of precipitates present at weld HAZ in CMT welded A6061-T6 and A6082-T6 joint using ER4043 filler wire (a) A6061-T6 and (b) A6082-T6 (c-d) EDS spectra of precipitates present at HAZ of A6061-T6 (e-f) EDS spectra for precipitates present at HAZ of A6082-T6

Table 4.2 EDS analysis of precipitates present at HAZ in CMT welded A6061-T6 and A6082-T6 joint using ER4043 filler wire

	Al	Mg	Si	Mn	Al	Mg	Si	Mn
	(wt. %)				(at. %)			
Point 1 (A6061- T6)	Bal.	2.17	20.76	1.25	Bal.	2.44	20.19	0.62
Point 2 (A6061- T6)	Bal.	6.14	35.95	2.49	Bal.	6.96	35.2	1.2
Point 1 (A6082- T6)	Bal.	3.60	70.89	1.46	Bal.	4.12	70.31	0.74
Point 2 (A6082- T6)	Bal.	2.15	61.84	1.22	Bal.	2.45	61.13	0.62

4.1.6 Microhardness of the CMT welded A6061-T6 and A6082-T6 joint using ER4043 filler wire

Fig. 4.11 shows Vickers microhardness values across the cross section of dissimilar A6061-T6 and A6082-T6 joint. The readings are taken from the middle portion of the cross section. It can be seen that microhardness value of the WMZ is lower as compared to the other zones. The average hardness values of 6082-T6 and 6061-T6 base metals are 81 HV and 78 HV, respectively. However, the WMZ hardness is found to be 65 HV. The hardness of WMZ exhibits ~80 % of BM 6082-T6 alloy and ~83 % of BM 6061-T6 alloy. The amount of Mg migrated from the BMs to the center of the WMZ, due to dilution effect, cannot be significant. Due to this, the formation of Mg_2Si precipitates can be considerably low that decreases the hardness of WMZ. This is in good agreement with the research work, which reported that the decreased amount of Mg_2Si precipitates in WMZ in welding of A6061-T6 alloy with ER4043 filler material decreased the hardness of WMZ (Lakshminarayanan et al. 2009).

The Al-Mg-Si series alloys are precipitation hardening alloys and the precipitates are obtained through ageing treatment. In general, the precipitation sequence in Al-Mg-Si alloys is reported as follows; α -SSS \rightarrow G.P zone $\rightarrow \beta''$ precipitates (needle shaped metastable precipitates) $\rightarrow \beta'$ precipitates (rod shaped metastable precipitates) $\rightarrow \beta$ precipitates (stable precipitates) (Tsao et al. 2006). In the case of artificially aged Al-Mg-Si alloys, fine needle shaped β'' precipitates are the main strengthening phases (Myhr et al. 2001). These β'' precipitates provide barriers for the dislocation movement that increases the hardness significantly (Fang et al. 2010). During welding, as the temperature rises above 250⁰ C in

HAZ, the finer β'' precipitates dissolve into α -Al matrix and the larger β'' precipitates grow further and become coarser (Myhr et al. 2004). When the temperature in HAZs lies between 250⁰ C-480⁰ C, there is a possibility of formation of rod shaped β' precipitates (Myhr et al. 2004). The rod shaped precipitates are present in the HAZ of both the interfaces in the present work (Fig. 4.3 (b) and Fig. 4.4 (b)) that has affected the hardness in HAZ. Since 6xxx series alloys are precipitation hardening alloys, PMZ and HAZ became partially solution treated zone because of the welding heat and some of the precipitates got dissolved (Gungor et al. 2014b). Due to the above-mentioned reasons, PMZ (Fig. 4.3 (c) & Fig. 4.4 (c)) and HAZ (Fig. 4.3 (b) & Fig. 4.4 (b)) at respective interfaces show lower hardness than the BMs.

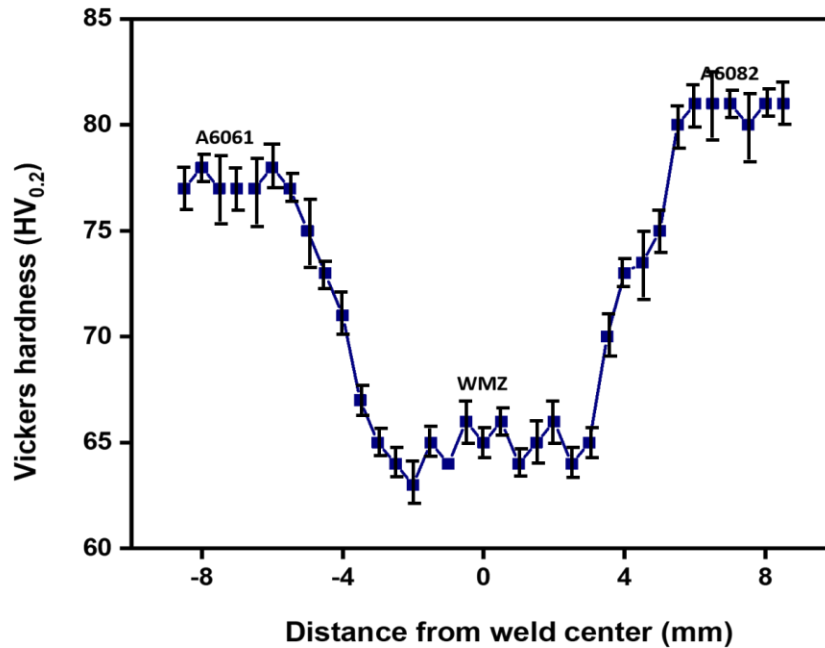


Fig. 4.11 Vickers micro hardness profile of the CMT welded A6061-T6 and A6082-T6 joint using ER4043 filler wire

4.1.7 Tensile properties of the CMT welded A6061-T6 and A6082-T6 joint using ER4043 filler wire

Table 4.3 shows tensile properties of BMs, overall region of the CMT weld joint, 6061-T6 interface region of the CMT weld joint and 6082-T6 interface region of the CMT weld joint. The fusion boundary on both the interfaces was taken as the center of the gage portion of the miniature tensile samples and the miniature samples were prepared from the interfaces. The gage area of miniature samples prepared from 6061-T6 side consists of base metal of 6061-T6, HAZ of 6061-T6, PMZ of 6061-T6, and WMZ, adjacent to the 6061-T6 fusion boundary. In a similar way, the gage area of miniature samples of 6082-T6 side comprised base 6082-T6, HAZ of 6082-T6, PMZ of 6082-T6 and WMZ, adjacent to 6082-T6 fusion boundary. The gage length of the overall weld region consisted of BMs, HAZs, PMZs of both 6061-T6 as well as 6082-T6 alloys and the combined WM region.

Fig. 4.12 shows tensile properties of the BMs, weld regions, interfacial regions and the overall weld region. The results show that among the interface regions, 6082-T6 region exhibits higher tensile properties than the 6061-T6 interface region. The presence of fine dendrites in CCZ at 6082-T6 interface (Fig. 4.4 (c)) is one of the possible reasons for the improvement in tensile properties. The fine dendrites in CCZ makes the material more tough, hence during the solidification of the WM, the shrinkage strain can be accommodated by the material. Thus, the weld tensile residual stresses can get reduced significantly in 6082-T6 interface than the 6061-T6 interface. PMZ cracking susceptibility mainly depends on GB liquation and weld tensile residual stress (Ghaini et al. 2009). GB liquation phenomenon is completely absent in the PMZ of 6082-T6 interface, whereas, it

is severe in the PMZ of 6061-T6 interface. Thus, it is evident that the possibility of PMZ cracking susceptibility is more at the 6061-T6 interface than that at the 6082-T6 interface. The presence of finer dendrites and the absence of GB liquation, made the 6082-T6 interface stronger and tougher than the 6061-T6 interface.

A number of porosities were viewed at the 6061-T6 interface (Fig. 4.3 (a)) whereas any such porosities were absent at the 6082-T6 interface (Fig. 4.4 (a)). During welding, the solubility of H₂ in molten metal is greatly influenced by the amount of Mg (Haboudou et al. 2003). The presence of Mg tends to increase solubility of H₂ in the molten pool leading to supersaturation of H₂ at the solid-liquid interface (Kutsuna and Yan 1999). Between the 6061-T6 and 6082-T6 alloys, Mg content is slightly higher in the case of 6061-T6 alloy. Thus, the formation of porosities in 6061-T6 may be attributed to the presence of larger amount of Mg. Due to the existence of porosities in the weld joints, there was a decrease in load bearing area and, as a result, tensile properties of the joints were reduced significantly.

During welding of Al-Mg-Si alloys, β'' precipitates transform to rod shaped β' precipitates at HAZ (Myhr et al. 2004). These β' precipitates were coarser in HAZ of 6061-T6 interface (Fig. 4.3 (b)) than in the 6082-T6 interface (Fig. 4.4 (b)). This also caused reduction in the strength of the 6061-T6 interface as compared to 6082-T6 interface as seen in Fig. 4.12. Other than the β' precipitates, a considerable amount of Si rich precipitates was also found in the HAZs of both the interfaces. The Si enriched precipitates appeared to be coarser in size at 6061-T6 interface than at the 6082-T6 interface. The coarser Si rich precipitates are

ineffective to restrict the motion of dislocations, resulting in the reduction in tensile strength. This may as well be another possible reason for the reduction in tensile strength at the 6061-T6 interface. The gauge length of the tensile samples prepared from interface regions was 5 mm. The % elongation in welds at A6082-T6 interface is significantly higher than the % elongation in welds at A6061-T6 interface (Fig. 4.12 and Table 4.3).

According to a previous research work, both strength and ductility of the weld joint have decreased with the presence of porosities (He et al. 2018). Therefore, the lower % elongation in welds at A6061-T6 interface is possibly due to the presence of porosities.

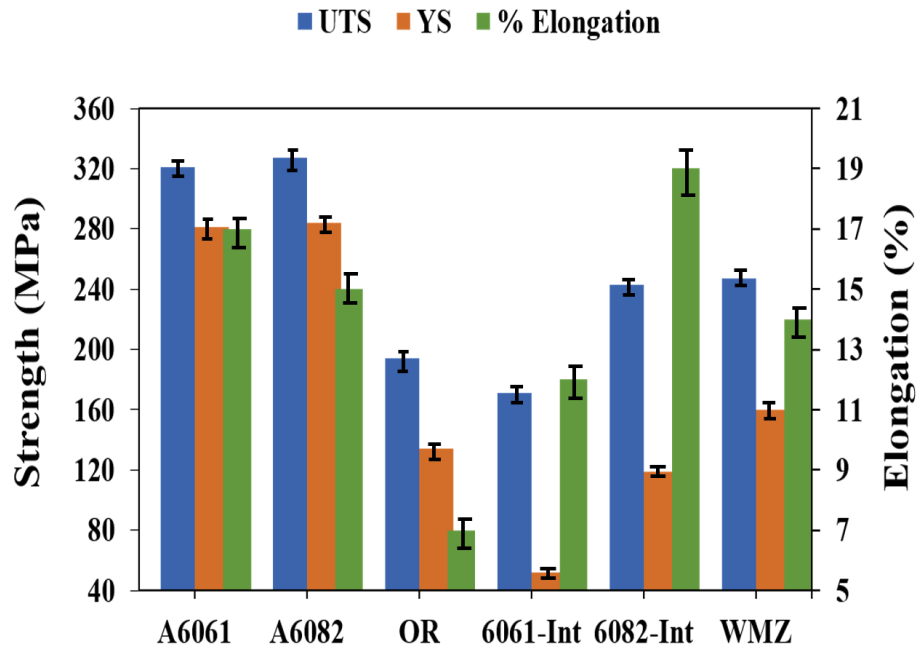


Fig. 4.12 Tensile properties of the BMs and CMT welded A6061-T6 and A6082-T6 joint using ER4043 filler wire weld joint (OR-over all weld region, Int-Interface and WMZ-weld metal zone; Gauge length of BMs & OR is 25 mm and gauge length of interfaces and WMZ is 5 mm)

Table 4.3 Tensile properties of the CMT welded A6061-T6 and A6082-T6 joint using ER4043 filler wire

Sample	UTS (MPa)	YS (MPa)	Elongation (%)
A6061	321	281	17
A6082	327	284	15
CMT weld joint (over-all region)	194	134	7
CMT weld joint (6061-T6 interface)	171	52	12
CMT weld joint (6082-T6 interface)	243	119	19
CMT weld joint (WMZ)	247	160	14

4.1.8 SEM fractographs of the CMT welded A6061-T6 and A6082-T6 joint using ER4043 filler wire

Fig. 4.13, Fig. 4.14 and Fig. 4.15 represent SEM images of fracture surfaces of over-all weld joint, A6061-T6 interface and A6082-T6 interface, respectively, using ER4043 filler wire. The fracture surface of over-all weld joint is composed of porosities and cracks. The fracture surface of A6061-T6 interface also contains a large number of porosities. The pre-existing porosities, generated during welding, appeared to have got enlarged under the tensile force during tensile test. Microcracks along the interdendritic regions, are also noticeable on fracture surface of both the interfaces. The strength and toughness of the

material can be correlated with the size of dimples. The dimples present in the A6082-T6 interface are very small, which implies good toughness and strength in the material. As seen from Table 4.3, YS (119),UTS (243) and % elongation (19) of the A6082-T6 interface are higher than the YS (52),UTS (171) and % elongation(12) of the A6061-T6 interface. The walls of dimples in A6082-T6 interface display blade type edges and also serpentine sliding that are indicative of high plastic deformation capacity of the material (Zhou et al. 2014).

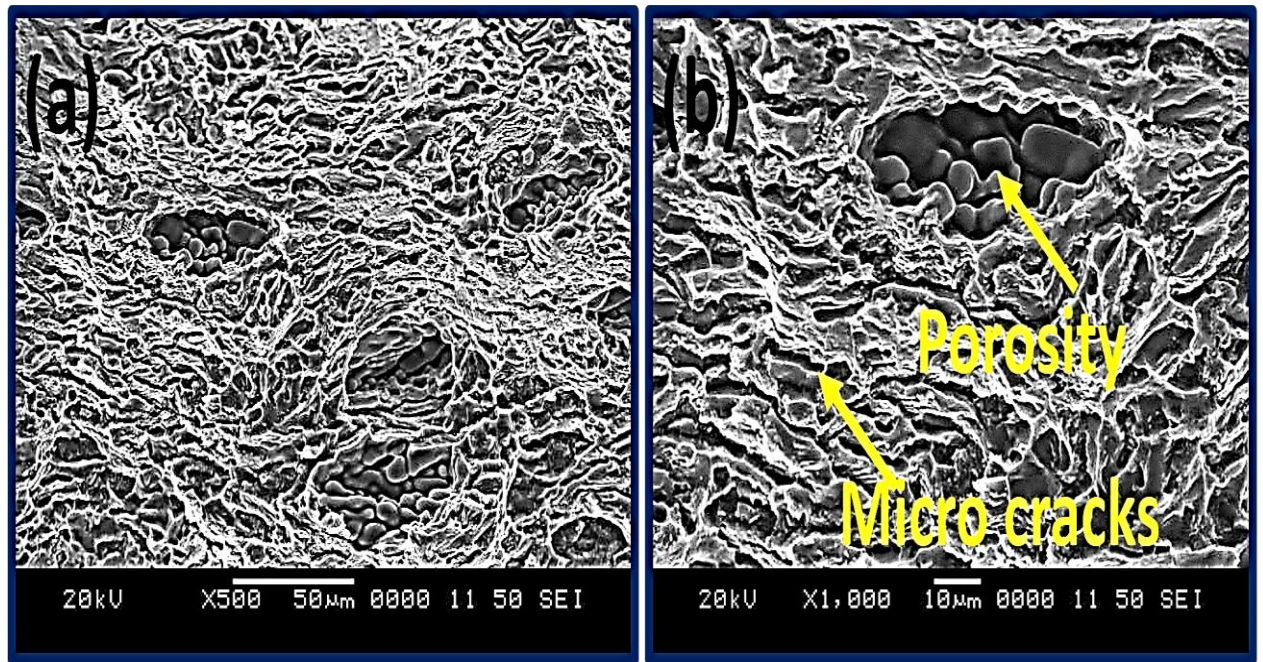


Fig. 4.13 SEM images of fracture surfaces of the over-all weld region in CMT welded A6061-T6 and A6082-T6 joint using ER4043 filler wire (a) low magnification image and (b) high magnification image

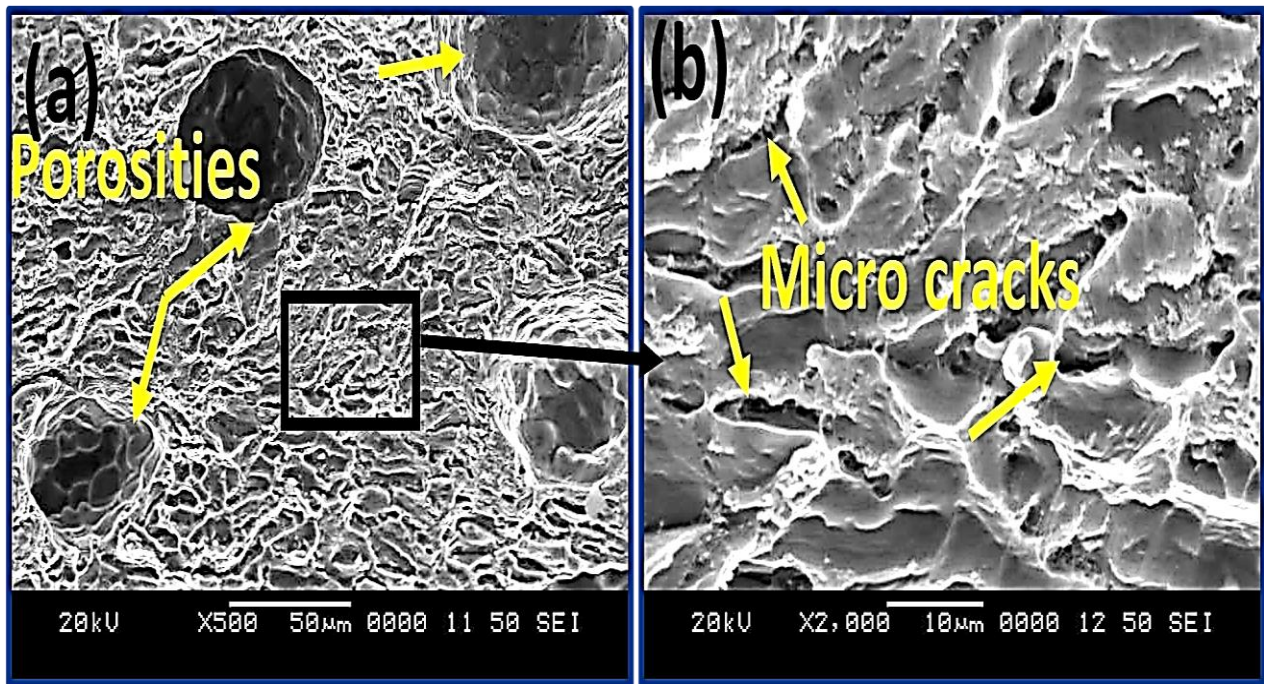


Fig. 4.14 SEM images of fracture surfaces of the A6061- T6 weld interface in CMT welded A6061-T6 and A6082-T6 joint using ER4043 filler wire (a) porosities and (b) higher magnification images shows micro-cracks along interdendritic regions

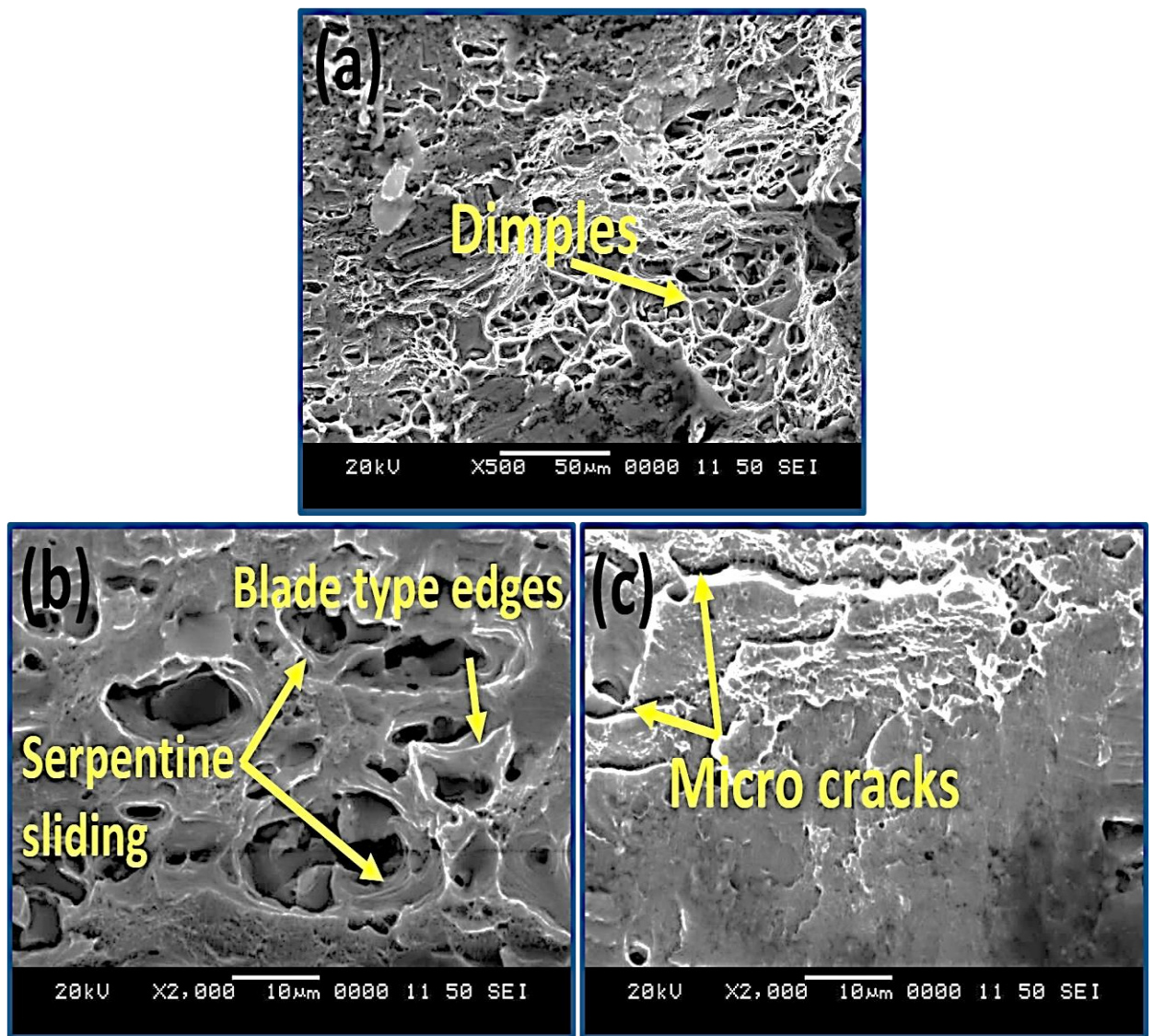


Fig. 4.15 SEM images of fracture surfaces of the A6082- T6 weld interface in CMT welded A6061-T6 and A6082-T6 joint using ER4043 filler wire: (a) low magnification image shows tiny dimples; and (b) serpentine sliding and blade type edges and (c) microcracks at higher magnification

4.2 Cold metal transfer (CMT) welding of dissimilar A6061-T6 and A6082-T6 using ER5356 filler material

4.2.1 Surface appearance of the CMT welded A6061-T6 and A6082-T6 joint using ER5356 filler material

Fig. 4.16 shows the over-all surface appearance of CMT welded A6061-T6 and A6082-T6 dissimilar joint produced using ER5356 filler wire. No defect is present on the surface. There are no cracks and spatter in the weldment. As can be seen from back side of the joint, full penetration is achieved.

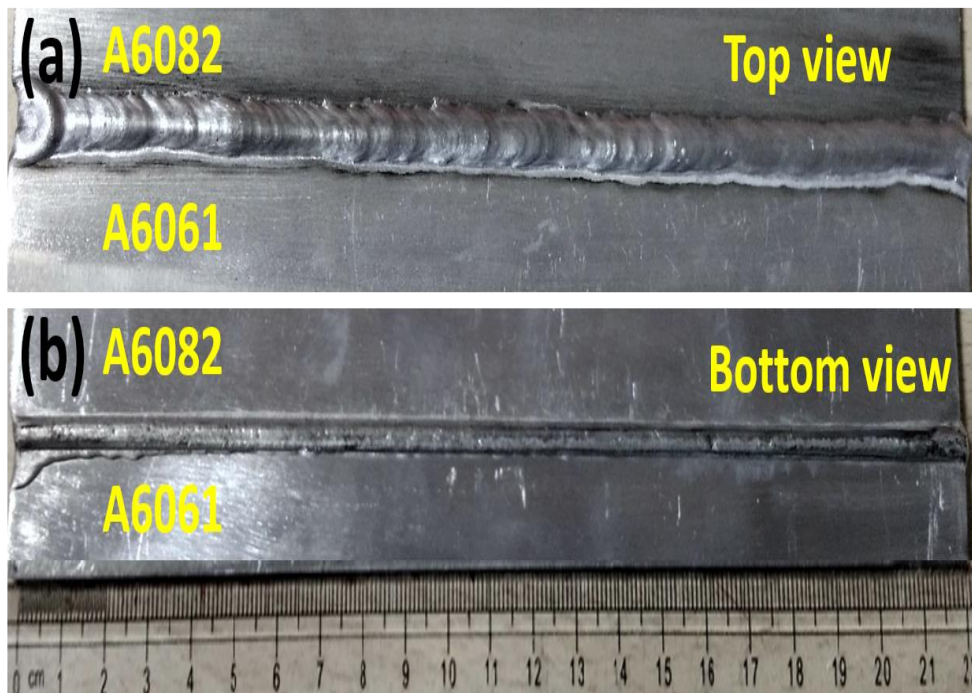


Fig. 4.16 Surface appearance of the CMT welded A6061-T6 and A6082-T6 joint using ER5356 filler wire (a) Top view and (b) Bottom view

4.2.2 Macrostructure of the CMT welded A6061-T6 and A6082-T6 joint using ER5356 filler material

Fig. 4.17 shows the macrostructure of transverse section of the joint. This confirms that no defects are present in the joint and complete depth of penetration is achieved in the joint.

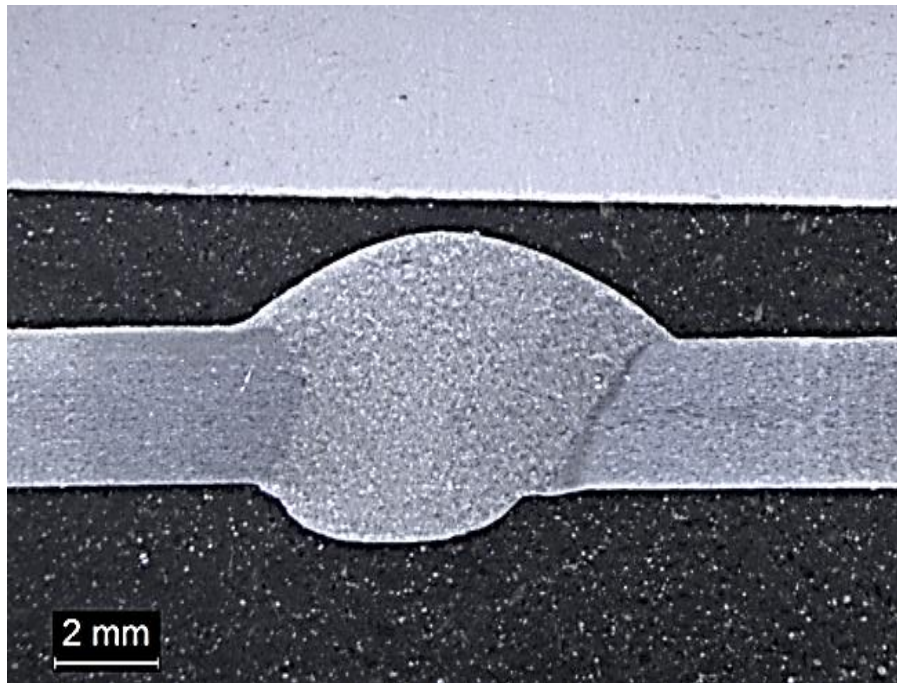


Fig. 4.17 Macrostructure of transverse section of the CMT welded A6061-T6 and A6082-T6 joint using ER5356 filler wire

4.2.3 Optical microstructure of the CMT welded A6061-T6 and A6082-T6 joint using ER5356 filler material

Fig. 4.18 (a-b) shows the interfaces of A6061 and A6082 in the dissimilar weld joint. It is worth noting that non-dendritic equiaxed zone (EQZ) is formed between CCZ and PMZ at the A6061 interface, but not at the A6082 interface. The BMs composition play a crucial

role in the formation EQZ (Kostrivas and Lippold 2006). The chemical composition of the alloying elements are varied between BMs. Particularly, Si and Mn is significantly higher in A6082-T6 than the A6061-T6 [Table 3.1]. Therefore, it is believed that due to this chemical composition variation, EQZ is not formed on the A6082-T6 side in the joint. Columnar grains have grown along EQZ in A6061 interface and along PMZ in A6082. The EQZ is an fine equiaxed non-dendritic grains surrounded by grain boundary eutectic products formed near fusion line of the joint (Reddy et al. 1998). EQZ is completely different from the typical micro structures evolution in fusion welded structures such as planar, cellular, dendritic which is explained by constitutional undercooling theory (A. Kostrivas 2006). The presence of eutectic constituents at GBs of EQZ diminishes mechanical and corrosion properties (Dev et al. 2008). Since EQZ is located next to CCZ at A6061 interface, GB liquation has occurred in EQZ. However, due to the absence of EQZ at A6082 interface, GB liquation has occurred in PMZ. Fig. 4.19 shows schematic diagram representing different zones evolution at both the interfaces. Fig. 4.20 (a) shows liquation at GBs and grain interiors (GIs) in EQZ of the A6061 side. Since non-dendritic equiaxed fine zone (EQZ) is present next to CCZ, liquation is significant in this zone, but not so in PMZ as it is distant from CCZ [Fig. 4.20(a)]. Due to the absence of EQZ, liquation is significant in PMZ of the A6082 side [Fig. 4.20(b)]. GB liquation normally leads to produce liquation cracking, but as per Yan et al (Yan et al. 2017) not all the grains which have liquation in their boundaries tend to form cracks.

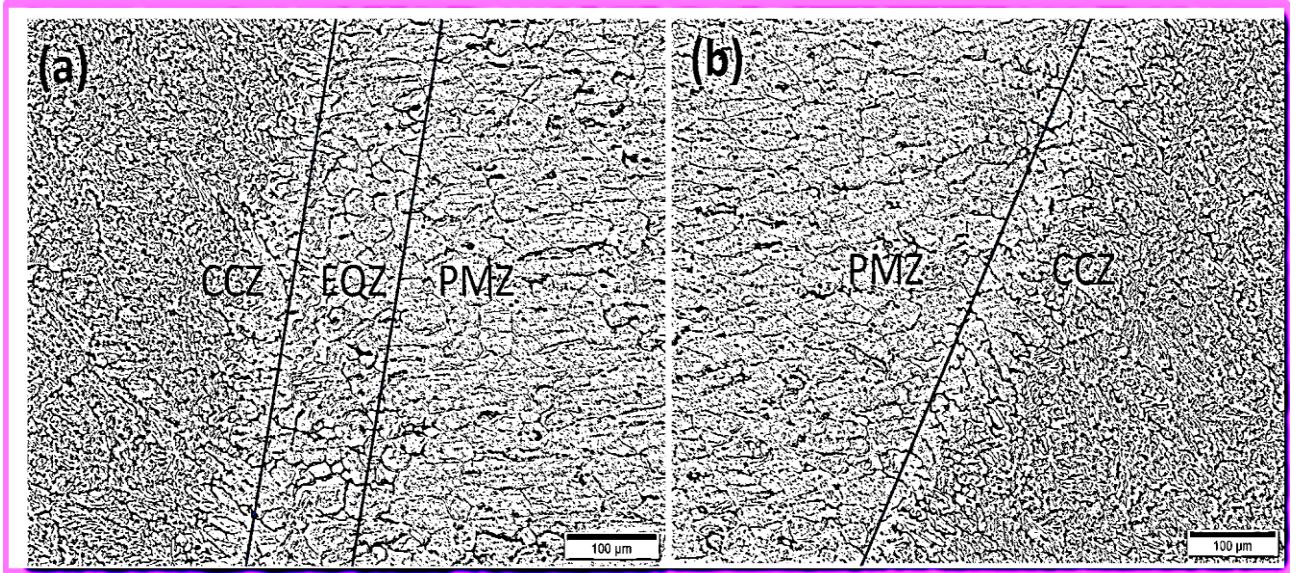


Fig. 4.18 Optical microstructure of the interface in CMT welded A6061-T6 and A6082-T6 joint using ER5356 filler wire (a) A6061 side and (b) A6082 side

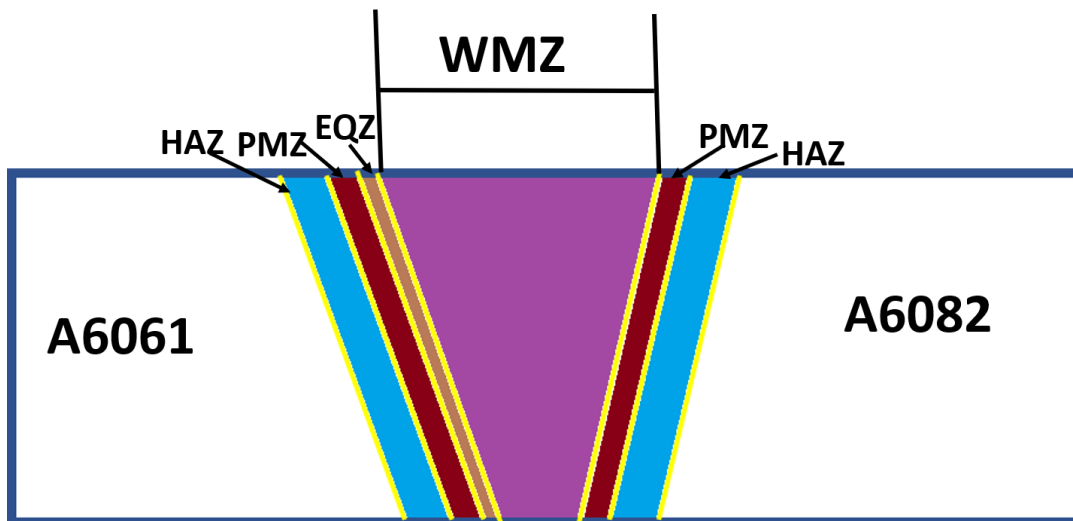


Fig. 4.19 Schematic diagram representing different zones of both sides of the CMT welded A6061-T6 and A6082-T6 joint using ER5356 filler wire

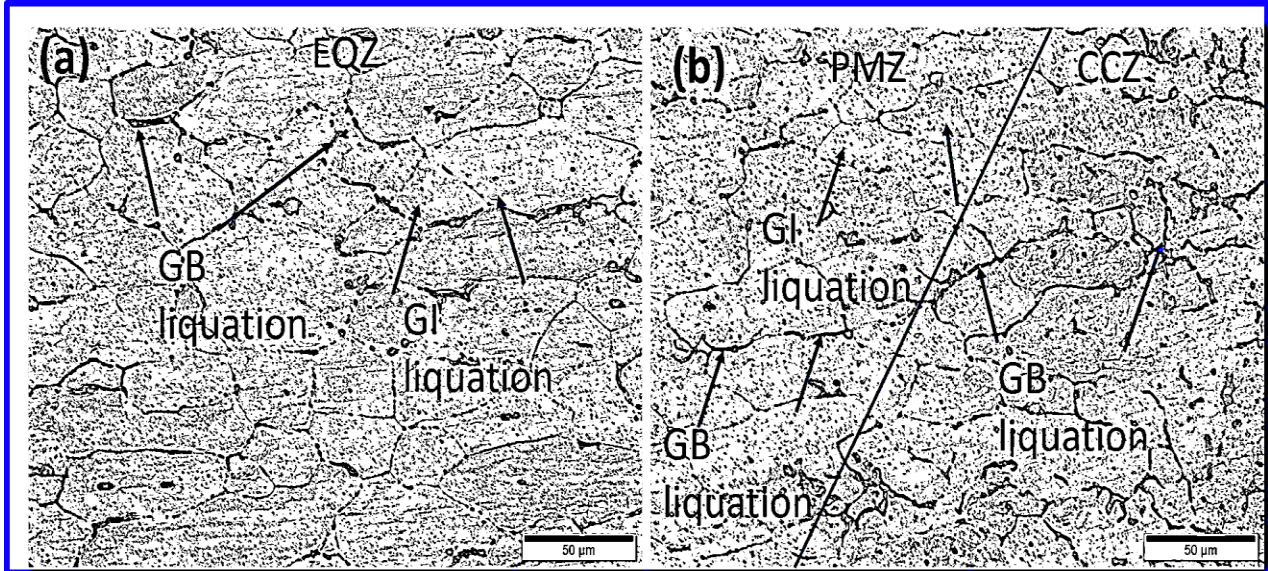


Fig. 4.20 Optical microstructure of the interface showing liquation in CMT welded A6061-T6 and A6082-T6 joint using ER5356 filler wire (a) EQZ on A6061 side and (b) PMZ on A6082 side

4.2.4 SEM microstructure of the interfaces in CMT welded A6061-T6 and A6082-T6 joint using ER5356 filler material

Figs. 4.21 (a) and (b) show liquation cracks at EQZ on the A6061 side and PMZ on the A6082 side, respectively. The exhibited liquation cracks are more at EQZ on the A6061 side than the PMZ on the A6082 side. GB liquation is exhibited in PMZ of A6082 since EQZ is absent, but this GB liquation is insufficient to produce cracks at most of the GBs. Thus, only very few liquation cracks are noticed in PMZ of A6082 [Fig. 4.21(b)]. At the

same time, due to the presence of significant liquation at GBs of EQZ, a greater number of liquation cracks are exhibited [Fig. 4.21(a)]

The evolution of liquation cracks mainly depends on shrinkage stresses and the severity of GB eutectic films. The degree of restraint can be lowered by reducing heat input, thereby reducing the tendency for formation of liquation cracks. The magnitude of heat input is mainly influenced by the welding process and process parameters. In general, the conventional fusion welding processes such as gas metal arc welding (GMAW) or tungsten inert gas welding (TIG) employ heat input in a range of 1-4 KJ mm⁻¹ (Sivashanmugam et al. 2010, 2014). CMT is a low heat input welding process, and in the present study a heat input of 0.2 KJ mm⁻¹ was used, which is significantly lower than the conventional welding process. With this lower level of heat input, the severity of liquation cracks is reduced, though the presence of cracks is unavoidable.

The mathematical equation, $\sigma=2\gamma L/h$, correlates the minimum stress (σ) required for initiating liquation cracks, surface tension of the grain boundary liquid film (γL) and the thickness of the eutectic liquid film (h) (Guo and Li 2011). From this it is understandable that as the thickness of liquid film increases, correspondingly there is a decrease in the stress required for crack initiation and vice-versa. When more amounts of eutectic GB liquids are present, the binding force between the adjacent grains is less and the prevailing stress is enough to produce liquation cracks. The liquation in EQZ of the A6061 interface is higher than in PMZ of both the interfaces. Hence, the magnitude of the binding force between adjacent grains becomes lower than the magnitude of shrinkage stress produced during solidification that induces liquation cracks in this zone.

Fig. 4.22 shows SEM images of HAZ of both the interfaces. The precipitate shape and size are different in the respective HAZs. The precipitates at HAZ of A6061 are rod and spherical shaped. In the HAZ of A6082, coarse spherical particles are present along with the smaller spherical particles. The outer edge of the coarse spherical precipitates displays white color and inner region grey color.

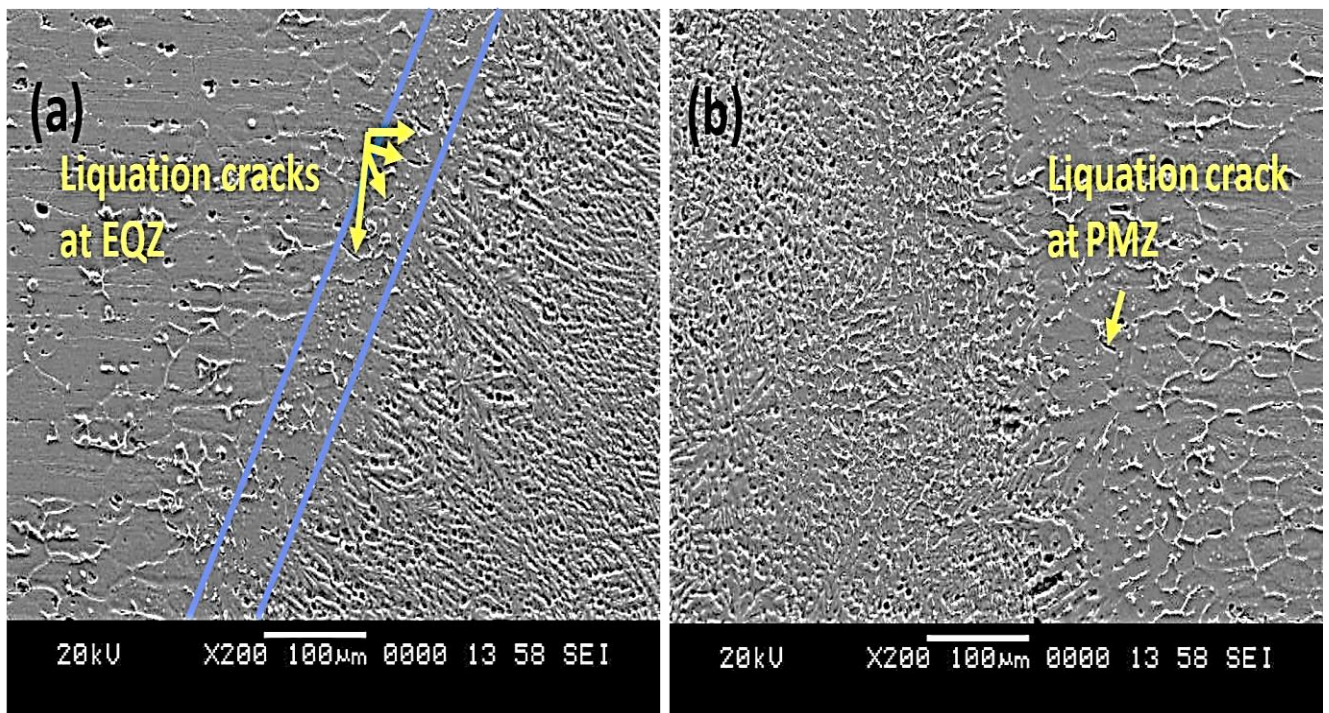


Fig. 4.21 SEM images of interface showing liquation cracks in CMT welded A6061-T6 and A6082-T6 joint using ER5356 filler wire (a) EQZ on A6061 side and (b) PMZ on A6082 side

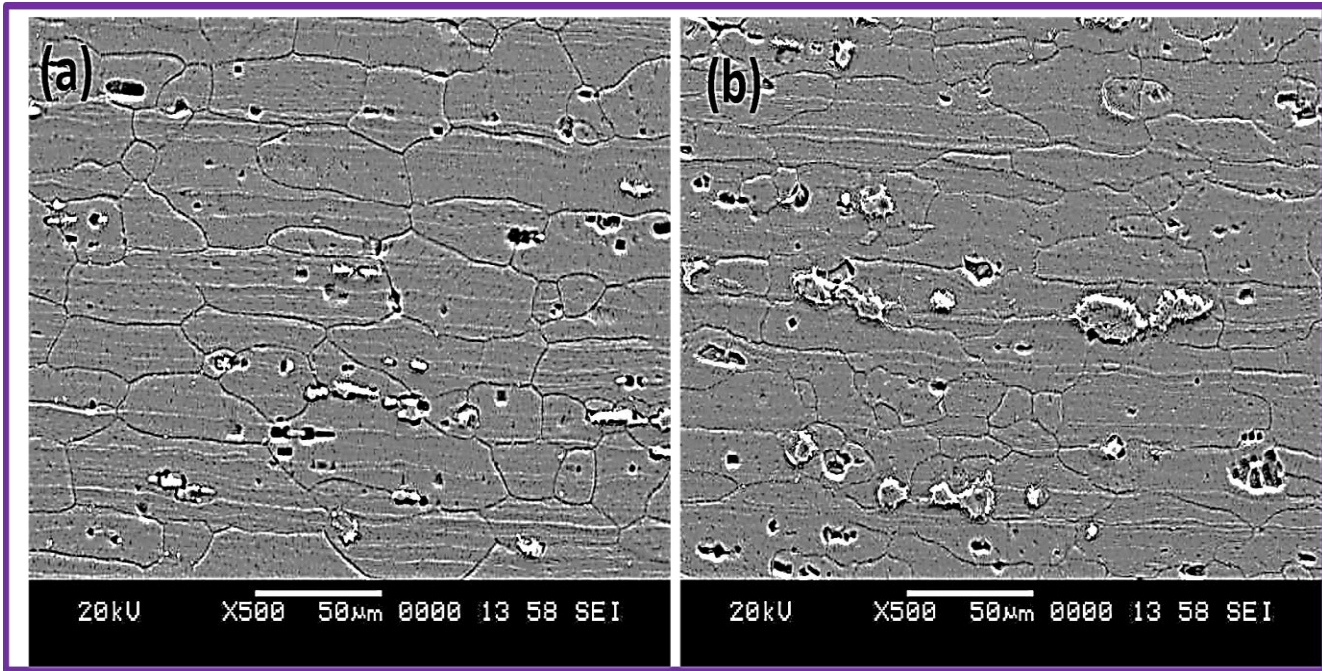


Fig. 4.22 SEM images of interface in CMT welded A6061-T6 and A6082-T6 joint using ER5356 filler wire (a) HAZ of A6061 side and (b) HAZ of A6082 side

4.2.5 SEM-EDS of the interfaces in CMT welded A6061-T6 and A6082-T6 joint interfaces using ER5356 filler material

Fig. 4.23 and 4.24 show SEM-EDS mapping images of A6061 and A6082 interface, respectively, of the dissimilar weld joint. Since the used filler material is Al-5Mg alloy, Mg element in the fusion zone appears brighter, but upon crossing CCZ towards BM it becomes dull in color. It is worth noting that Si element is segregated in EQZ of the A6061 side [Fig. 4.25]. Liquation cracks in EQZ of A6061 side can mainly be attributed to the segregation of Si element at GBs.

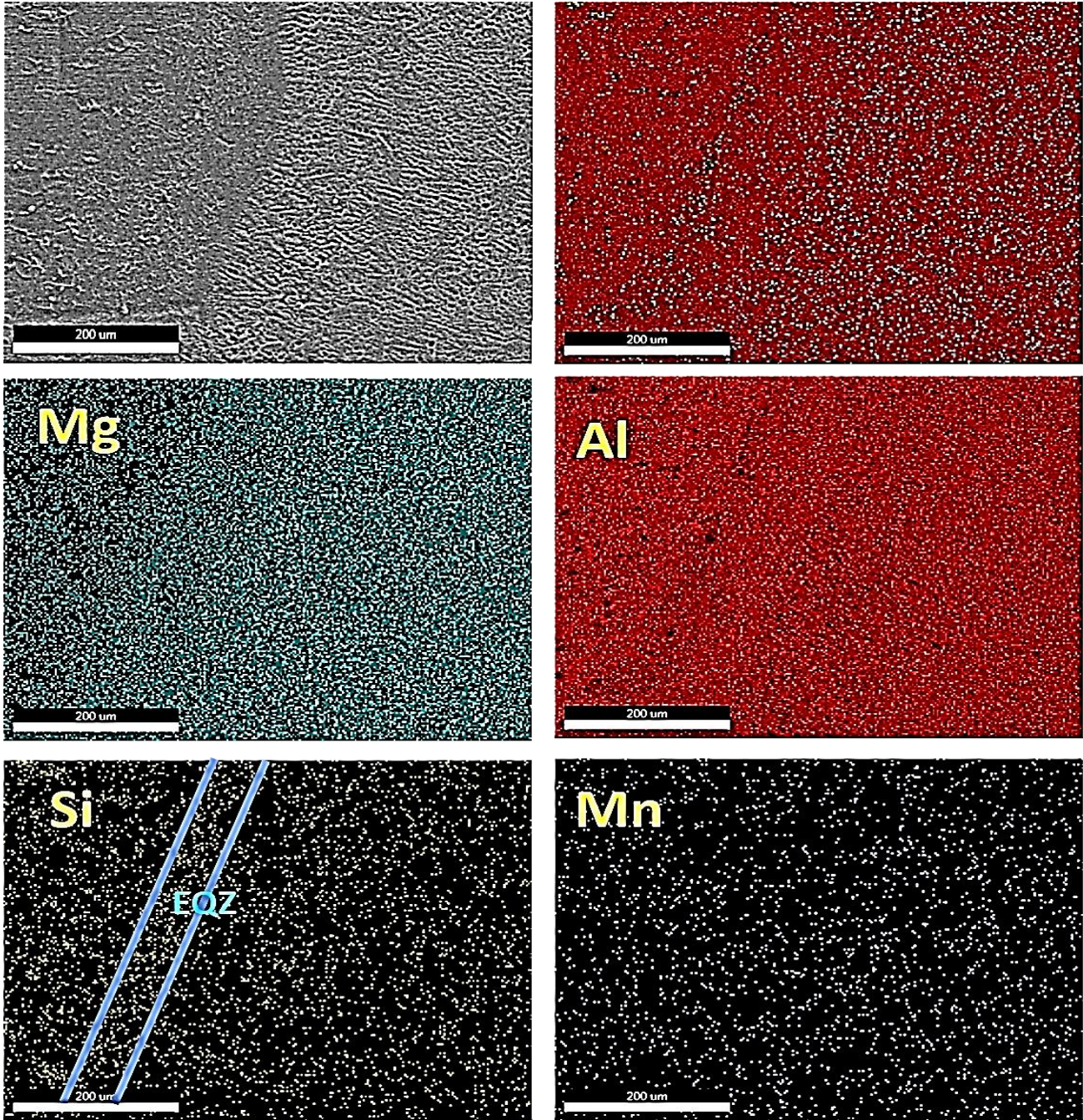


Fig. 4.23 SEM-EDS mapping images of A6061-T6 interface in CMT welded A6061-T6 and A6082-T6 joint using ER5356 filler wire

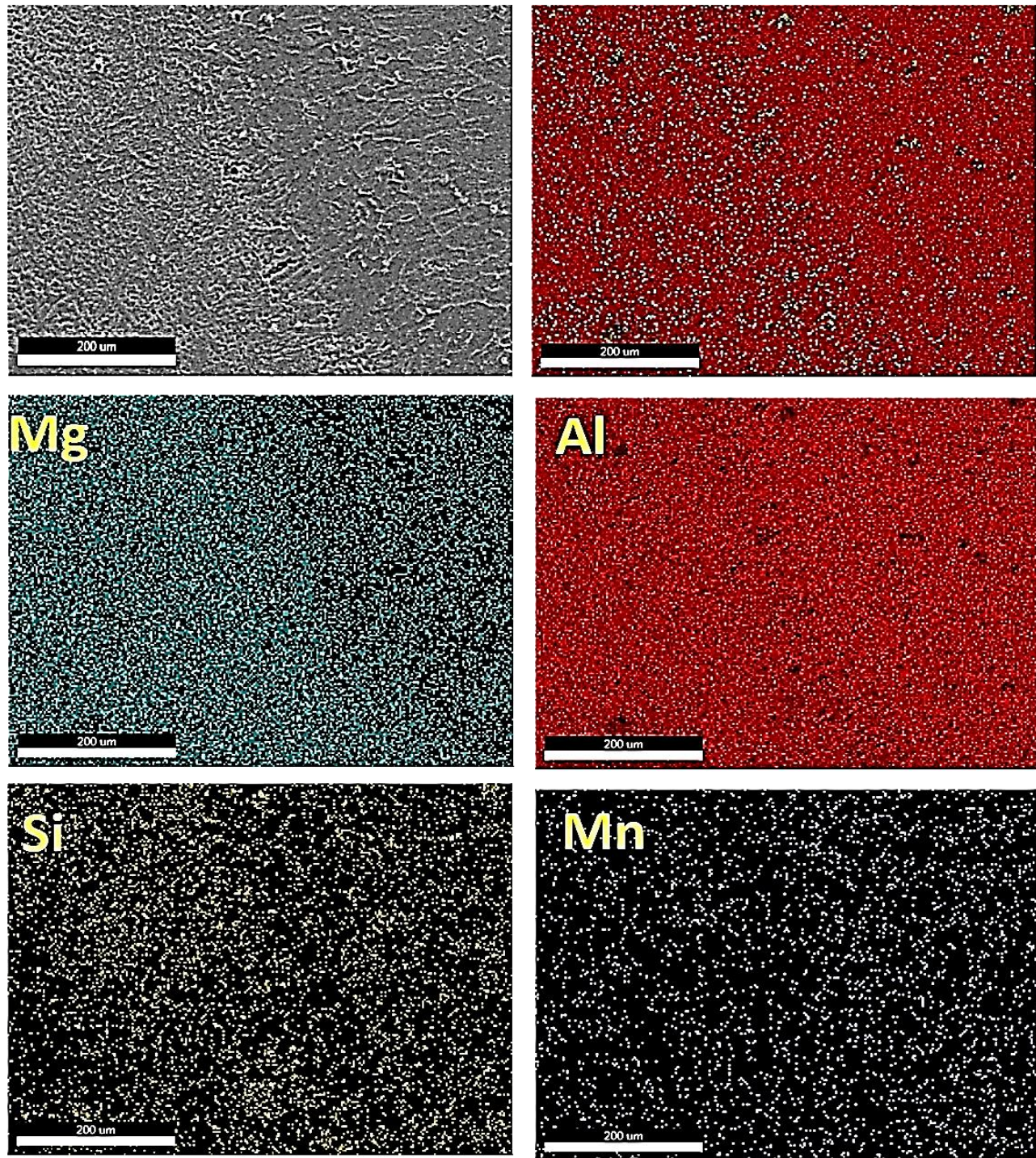


Fig. 4.24 SEM-EDS mapping images of 6082-T6 interface in CMT welded A6061-T6 and A6082-T6 joint using ER5356 filler wire

4.2.6 SEM-EDS of precipitates at HAZs of the CMT welded A6061-T6 and A6082-T6 joint using ER5356 filler material

The EDS analysis of precipitates at the interfaces is shown in Fig. 4.25. As can be seen from table 4.4, all the precipitates contain high amount of Si. Silicon content in the rod-shaped precipitates is about two times the silicon content in other precipitates.

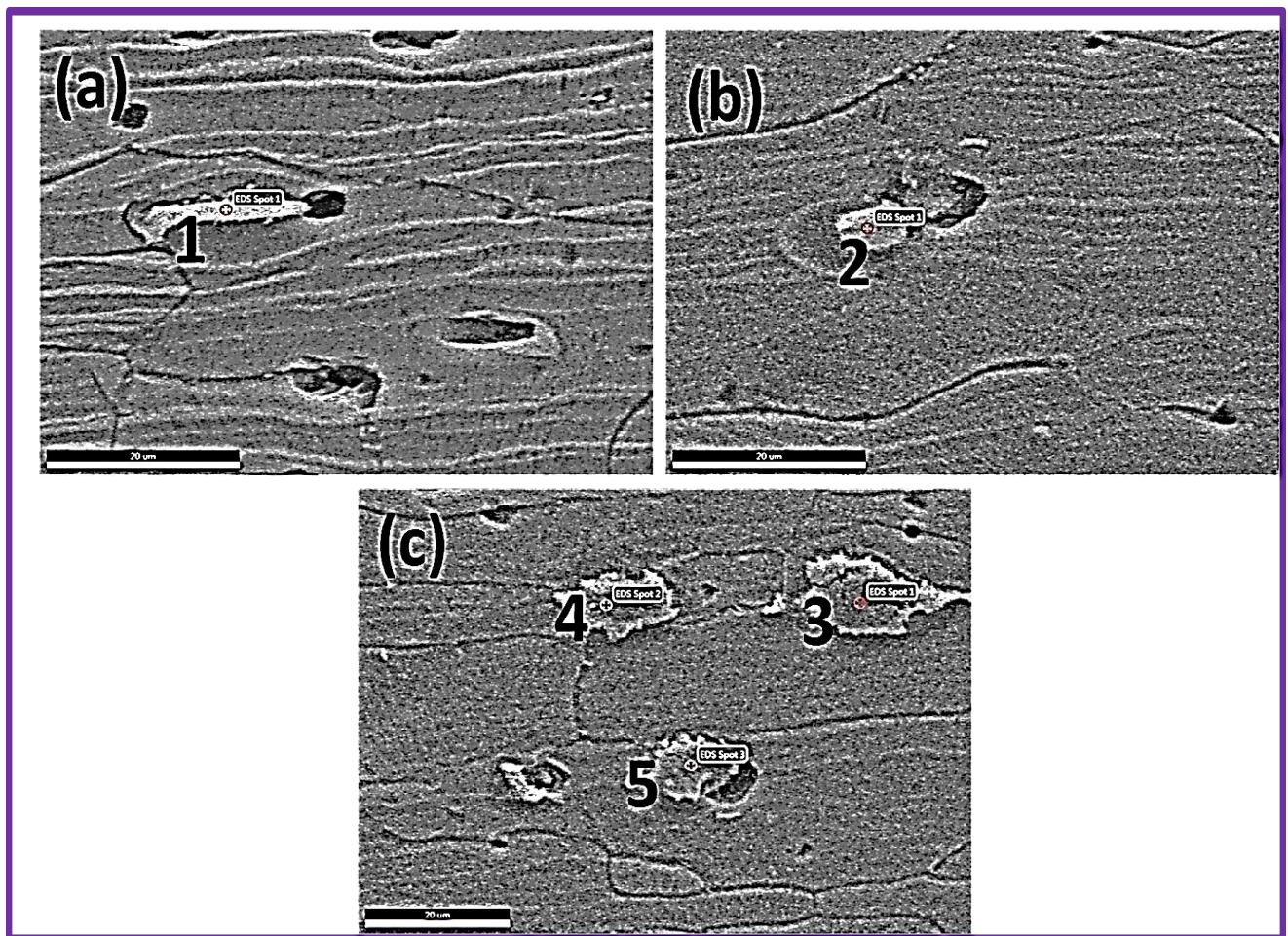


Fig. 4.25 SEM-EDS spot analysis of precipitates in CMT welded A6061-T6 and A6082-T6 joint using ER5356 filler wire (a-b) HAZ of A6061 side and (c) HAZ of A6082 side

Table 4.4 EDS analysis on precipitates present at weld HAZ of interface in CMT welded A6061-T6 and A6082-T6 joint using ER5356 filler wire

	Al	Mg	Si	Mn	Al	Mg	Si	Mn
	(wt. %)				(at. %)			
Point 1	Bal.	2.09	60.16	0.89	Bal.	2.38	59.33	0.45
Point 2	Bal.	2.05	39.35	1.00	Bal.	2.31	35.24	1.25
Point 3	Bal.	5.27	29.70	1.39	Bal.	5.93	28.90	0.69
Point 4	Bal.	4.10	38.83	0.94	Bal.	4.62	37.89	0.47
Point 5	Bal.	3.13	34.84	1.07	Bal.	3.53	34.00	0.53

4.2.7 Al-Mg binary phase diagram

Fig. 4.26 shows the Al-Mg binary phase diagram. It can be seen that for Al rich alloys, when the Mg solute amount exceeds its solubility in aluminium, Al_3Mg_2 phase can be precipitated and for Mg rich alloys when the Al solute amount exceeds its solubility in magnesium, $Mg_{17}Al_{12}$ phase can be precipitated. Based on the composition of filler used in the present study (Al-5wt.%Si), it is understandable that it is an Al rich alloy. For Al rich alloys, the maximum solubility of Mg at the eutectic temperature (450^0 C) is 17.1 wt.%, and the solubility decreases to 1.7 wt.% at the room temperature. Since the wt.% of Mg in

filler material is higher than 1.7 wt.% (maximum solubility of Mg in Al at room temperature), along with the solid solution of Al (α -Al), Al_3Mg_2 phases can also be formed.

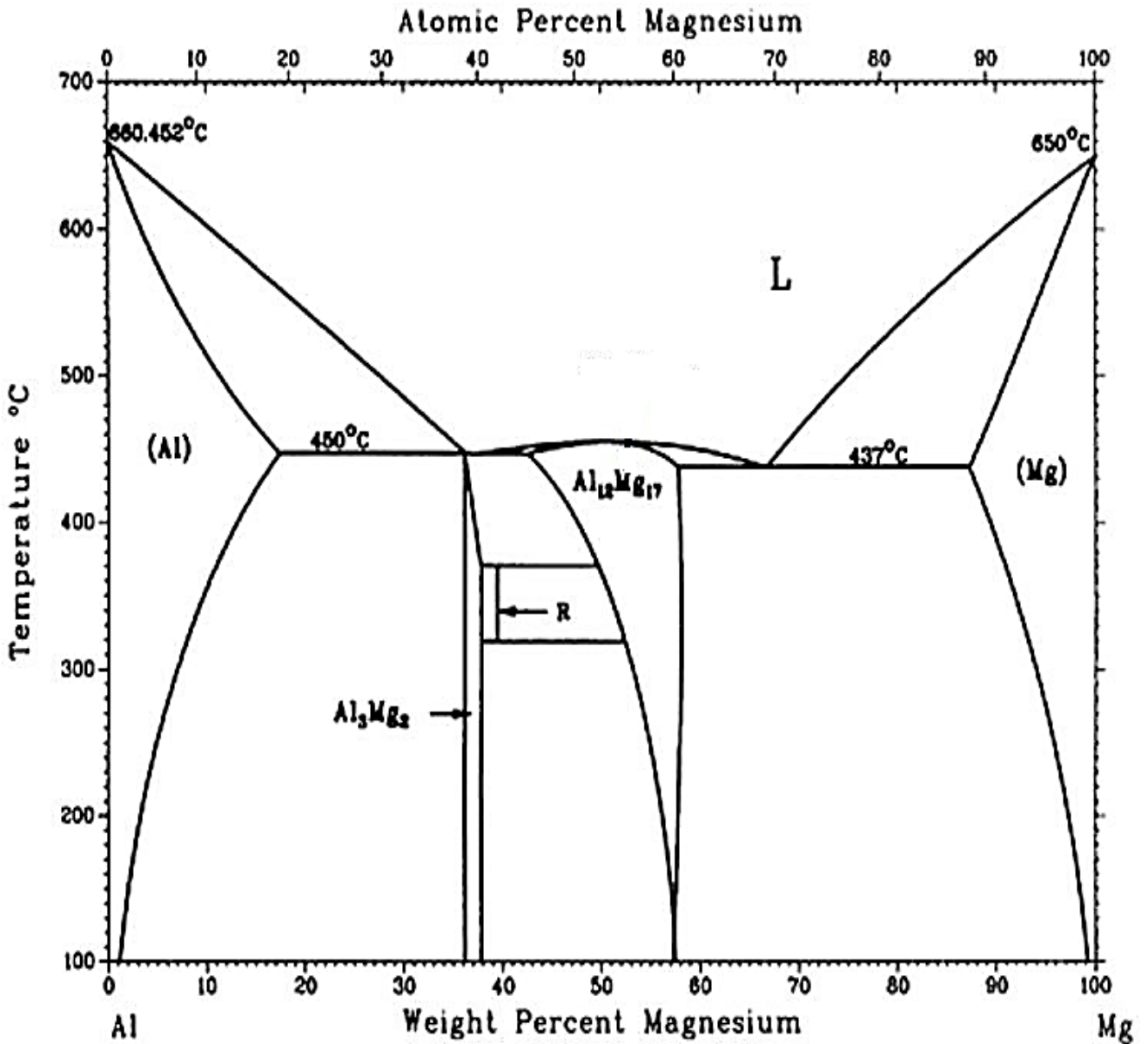


Fig. 4.26 Al-Mg binary phase diagram (Murray 1982)

4.2.8 Micro hardness of the CMT welded A6061-T6 and A6082-T6 joint using ER5356 filler material

Fig. 4.27 shows Vickers micro hardness profiles of the weld joint. The BMs exhibit maximum hardness among all the zones. At both the interfaces, microhardness value has gradually increased from WMZ towards the BMs. During welding, the weld pool attains a high temperature that causes loss of Mg by burning and evaporation (Liang et al. 2018). This significantly reduces solid solution hardening and the hardening by Mg containing secondary phases such as Al_3Mg_2 and Mg_2Si . This could be the possible reason for the decreased hardness in the WMZ. HAZs on both the sides exhibit lower hardness than the respective BMs. This is quite expected as in precipitation hardened alloys the phenomena such as coarsening and over ageing of precipitates occur in HAZ due to the weld thermal cycle. Cao et al (Cao et al. 2013a) have also reported similar type of trend in the A6061 side of dissimilar CMT weld joint. Moreover, PMZs exhibit lower hardness than the BMs and HAZs. This may be attributed to the presence of thin liquid film at the GBs.

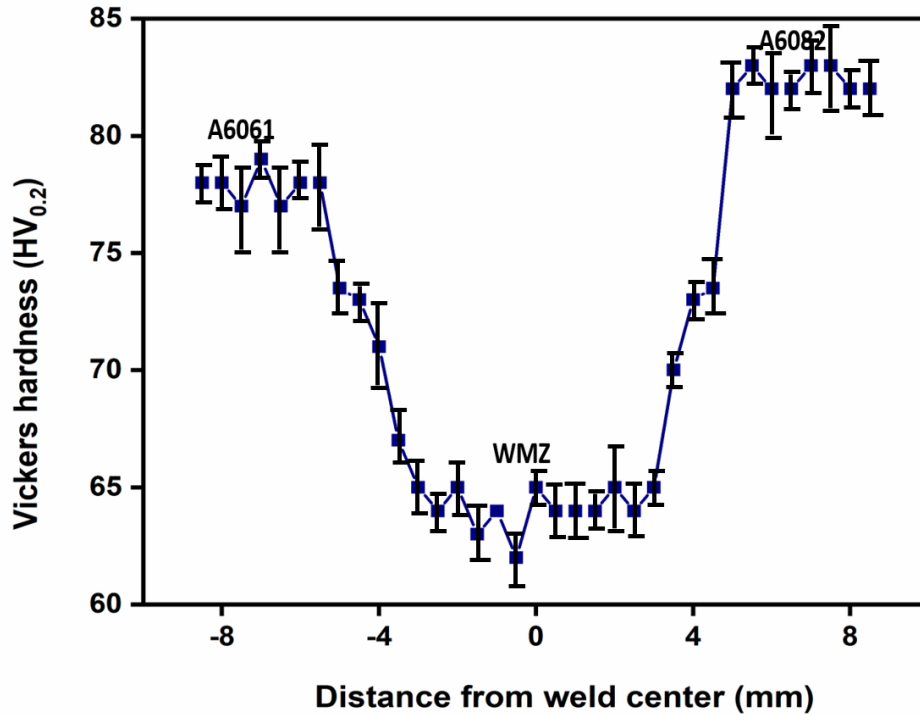


Fig. 4.27 Vickers micro hardness profiles of the CMT welded A6061-T6 and A6082-T6 joint using ER5356 filler wire

4.2.9 Tensile properties of the CMT welded A6061-T6 and A6082-T6 joint using ER5356 filler material

Tensile properties of BMs and weld regions are presented in Fig. 4.28. The tensile values are reported in Table 4.5. As can be seen from the Table 4.5, BMs A6061 and A6082 show yield strength (YS) and ultimate tensile strength (UTS) of 281 MPa, 284 MPa and 321 MPa, 327 MPa, respectively. The YS of WMZ, A6061 interface and A6082 interface are 110 MPa, 171 MPa and 195 MPa, respectively. UTS of WMZ, AA6061-T6 interface and A6082 interface are 180 MPa, 250 MPa and 290 MPa, respectively. It is evident that among

the regions, WMZ exhibits the lowest yield and tensile strengths. The A6082 interface shows higher yield and tensile strength than the A6061 interface.

According to previous research work EQZ is a preferential zone for tensile fracture in weld Al alloys (Li et al. 2007). The mechanical and corrosion properties are deteriorated by the eutectic constituents at GBs of EQZ (Dev et al. 2008). The significant increase in strength of the A6082 interface can be related to the absence of EQZ and consequent reduction in liquation cracks. In contrast, a significant number of liquation cracks are present in EQZ of A6061. Under tensile load, these liquation cracks at GBs propagate and failure occurs. As a result, relatively poor YS and UTS are exhibited by the A6061 interface. HAZ of A6061 contains rod shape precipitates (β' phase) and very few spherical shape precipitates (Fig. 4.22 (a)). The rod shape precipitating phases are absent in HAZ of A6082 (Fig. 4.22 (b)). The HAZ of A6082 contains more spherical shape precipitates (Fig. 4.22 (b)). It is reported that spherical precipitates in Al-Mg-Si alloys have a stronger interaction with the dislocations (Yuan et al. 2007). As the number of precipitates increases there is an increase in dislocation pinning points in each slip plane. Due to the high number of spherical shape precipitates in HAZ of A6082 interface, dislocation pinning points are more thereby increases its strength than the A6061 interface. Due to the presence of significant liquation at GBs of EQZ, a greater number of liquation cracks are exhibited in A6061 interface [Fig. 4.21(a)]. It may, therefore, be inferred that the higher strength of the A6082 interface in comparison to the A6061 interface is a combined result of the absence of EQZ (thereby fewer liquation cracks) and the presence of more spherical shape precipitates in HAZ of A6082.

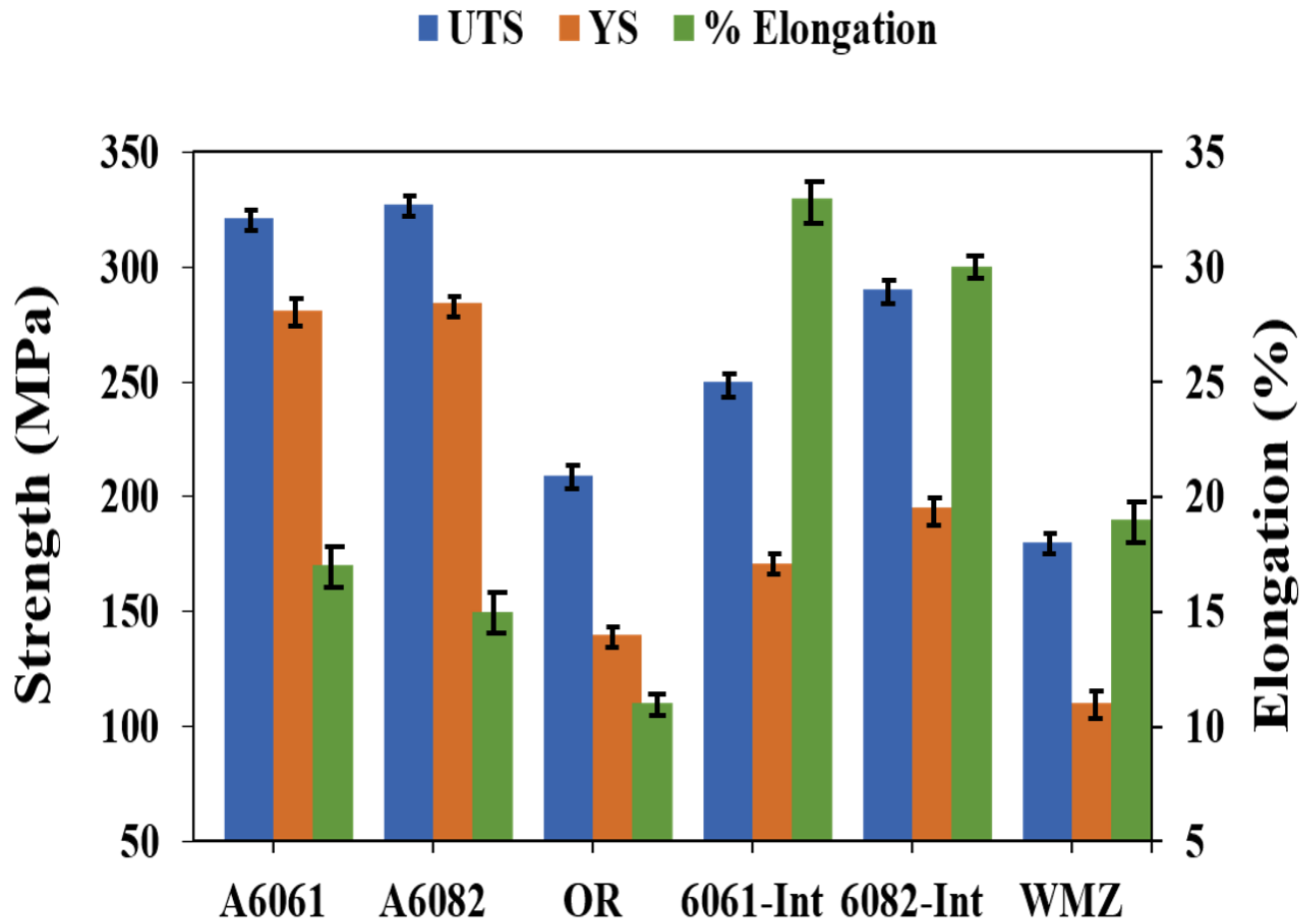


Fig. 4.28 Tensile properties of BMs and CMT welded A6061-T6 and A6082-T6 joint using ER5356 filler wire (OR-over all weld region, Int-Interface and WMZ- weld metal zone; Gauge length of BMs & OR is 25 mm and gauge length of interfaces and WMZ is 5 mm)

Table 4.5 Tensile properties of the BMs and different regions of the CMT welded A6061-T6 and A6082-T6 joint using ER5356 filler wire

Sample	UTS (MPa)	YS (MPa)	Elongation (%)
A6061	321	281	17
A6082	327	284	15
CMT weld joint (OR)	209	140	11
CMT weld joint (6061-T6 int.)	250	171	33
CMT weld joint (6082-T6 int.)	290	195	30
CMT weld metal zone	180	110	19

4.2.10 SEM fractography of the CMT welded A6061-T6 and A6082-T6 joint using ER5356 filler material

Fig 4.29 shows the fractography images of over-all weld joint. Defects such as intergranular microcracks and cavities are present on the fracture surface. Tear planes are also observed. Along with these brittle features, shallow and equiaxed dimples are predominantly exhibited, which confirms the mixed mode of ductile and brittle fracture in the weld joint. The fractography images of A6061 and A6082 interface regions are shown

in Fig. 4.30 (a) and (b), respectively. Interface regions of A6061 and A6082 show cracks in the fracture surface.

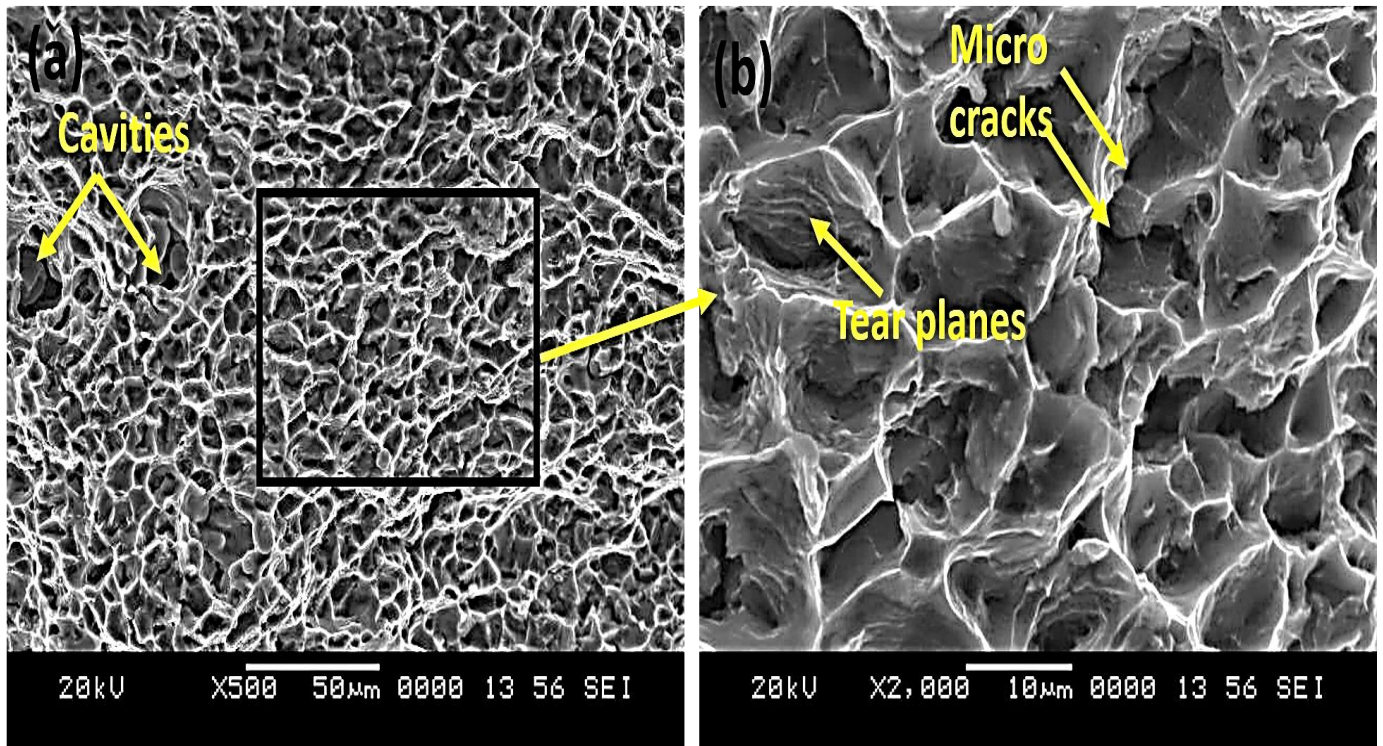


Fig. 4.29 Fractography images of CMT welded A6061-T6 and A6082-T6 joint using ER5356 filler wire: (a) low magnification and (b) high magnification

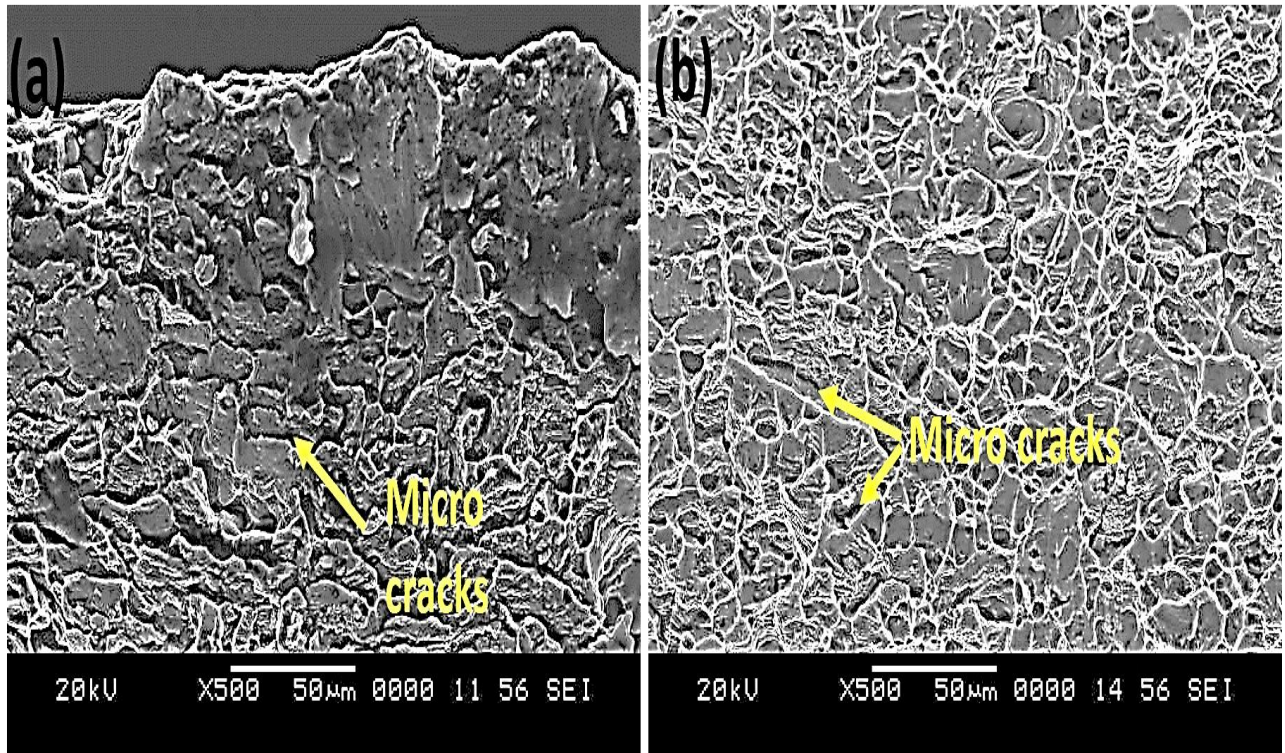


Fig. 4.30 Fractography images of CMT welded A6061-T6 and A6082-T6 joint using ER5356 filler wire: (a) A6061 and (b) A6082

4.3 Cold metal transfer (CMT) welding of dissimilar A5754-H111 and A5083-H111 using ER4043 filler wire

4.3.1 Surface appearance and macrostructure of the CMT welded A5754-H111 and A5083-H111 joint using ER4043 filler wire

Fig. 4.31 and 4.32 show surface appearance and macrostructures, respectively, of transverse section of joint. Both indicate that the weld does not have any defects and full penetration is achieved.

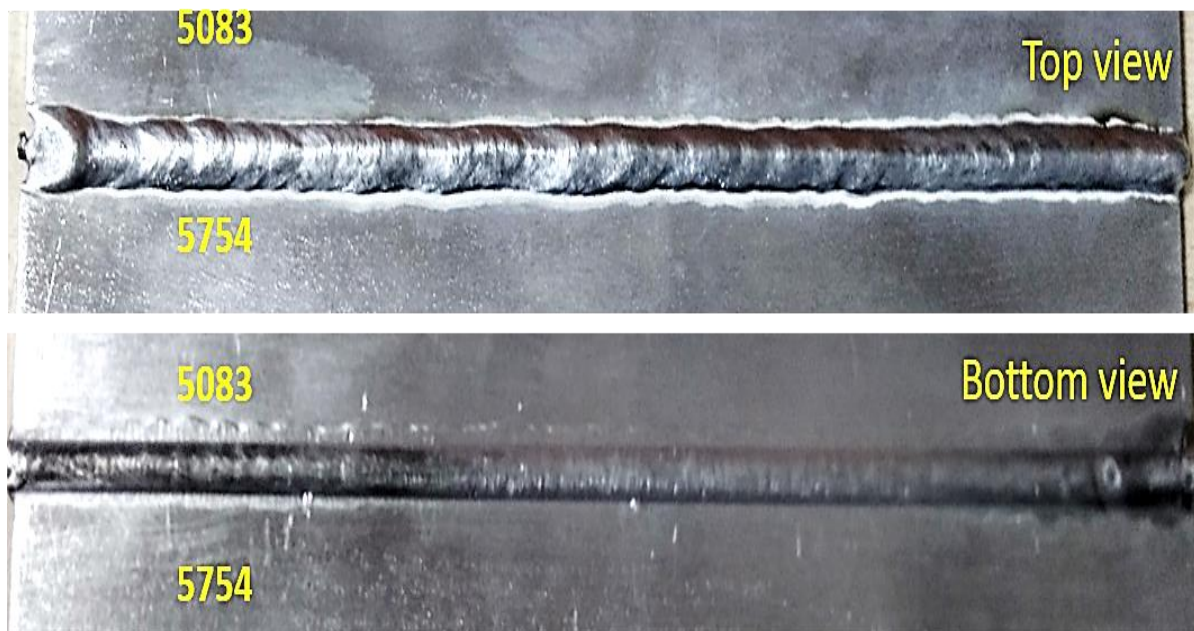


Fig. 4.31 Surface appearance of the CMT welded A5754-H111 and A5083-H111 joint using ER4043 filler wire

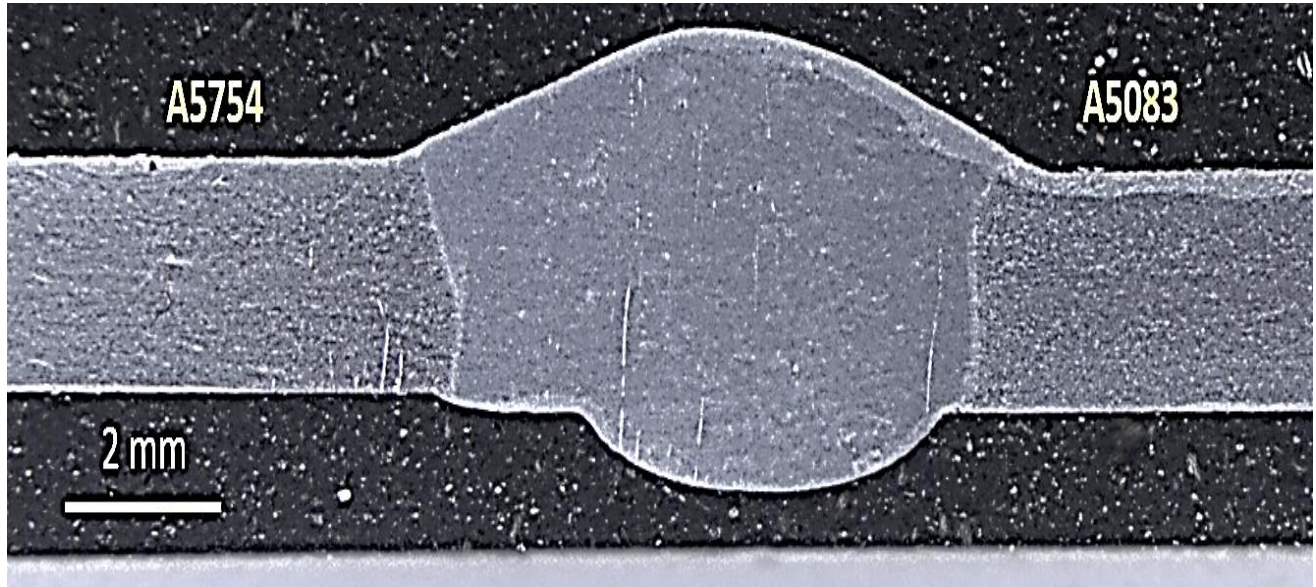


Fig. 4.32 Macrostructure of transverse section of the CMT welded A5754-H111 and A5083-H111 joint using ER4043 filler wire

4.3.2 Optical microstructures of interfaces and WMZ center in CMT welded A5754-H111 and A5083-H111 joint using ER4043 filler wire

Fig. 4.33(a-b) shows optical microstructures of interface regions of weld joint. EQZ appears at the interface of the weldment and it is located between PMZ and WMZ. Dendrites of WMZ at A5754 interface are coarser than the dendrites of WMZ at A5083 interface. The newly evolved EQZ at interfaces is different from the equiaxed zone at the center of WMZ. At the center of WMZ the microstructure exhibits equiaxed dendritic structure [Fig. 4.34(a-b)], whereas EQZ at the interface is equiaxed non-dendritic [Fig.

4.33(a-b)]. The non-dendritic equiaxed grains is formed due to the high nucleation rate near the fusion boundary (Reddy et al. 1998).

The GBs of EQZ at both the interfaces are completely covered by a continuous layer of solidified Si films. This confirms that the GBs of EQZ are completely wetted by a Si melt phase. This type of complete wetting of GBs by liquid phase is reported in Al-Sn alloys (Straumal et al. 1995). Si films are comparatively less and distributed in a non-continuous manner in GBs of PMZ. The non-continuous layer of Si films indicates that the GBs of PMZ are partially wetted by Si melt phase. Moreover, PMZ of A5083 exhibits a greater number of secondary phase particles than the PMZ of A5754.

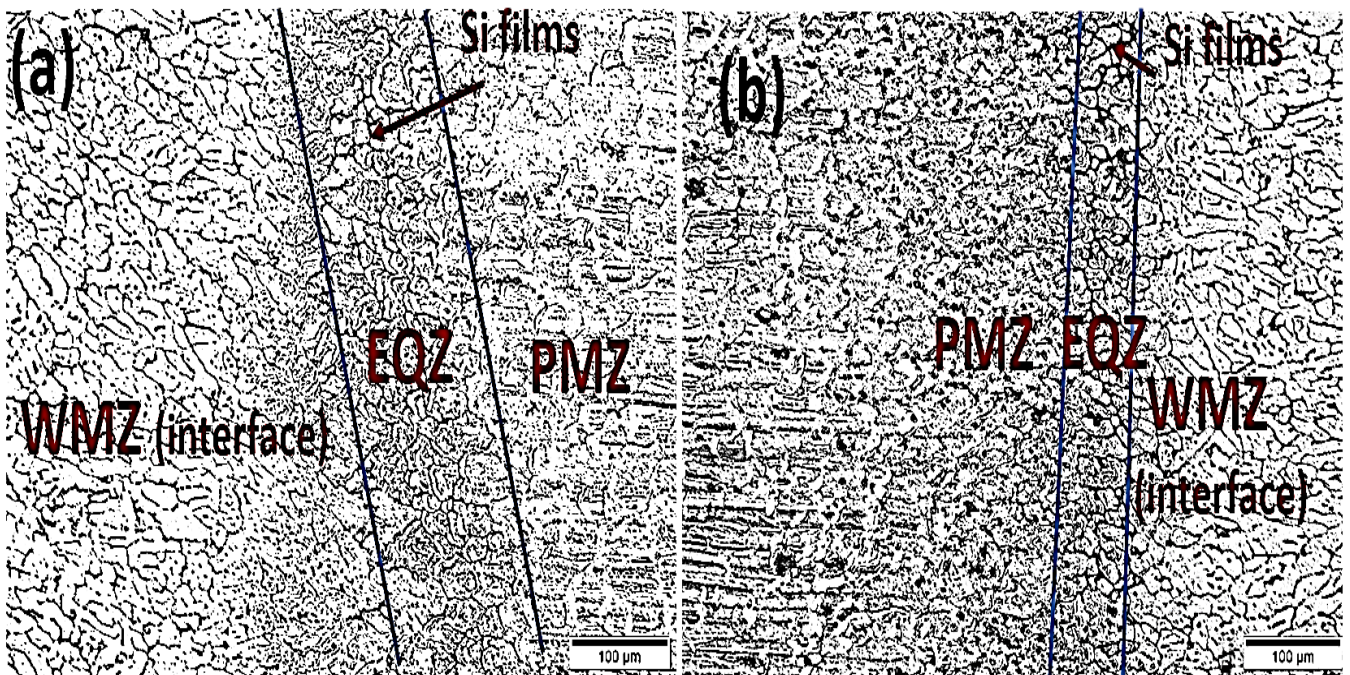


Fig. 4.33 Optical images of CMT welded A5754-H111 and A5083-H111 joint using ER4043 filler wire (a) A5754 interface and (b) A5083 interface

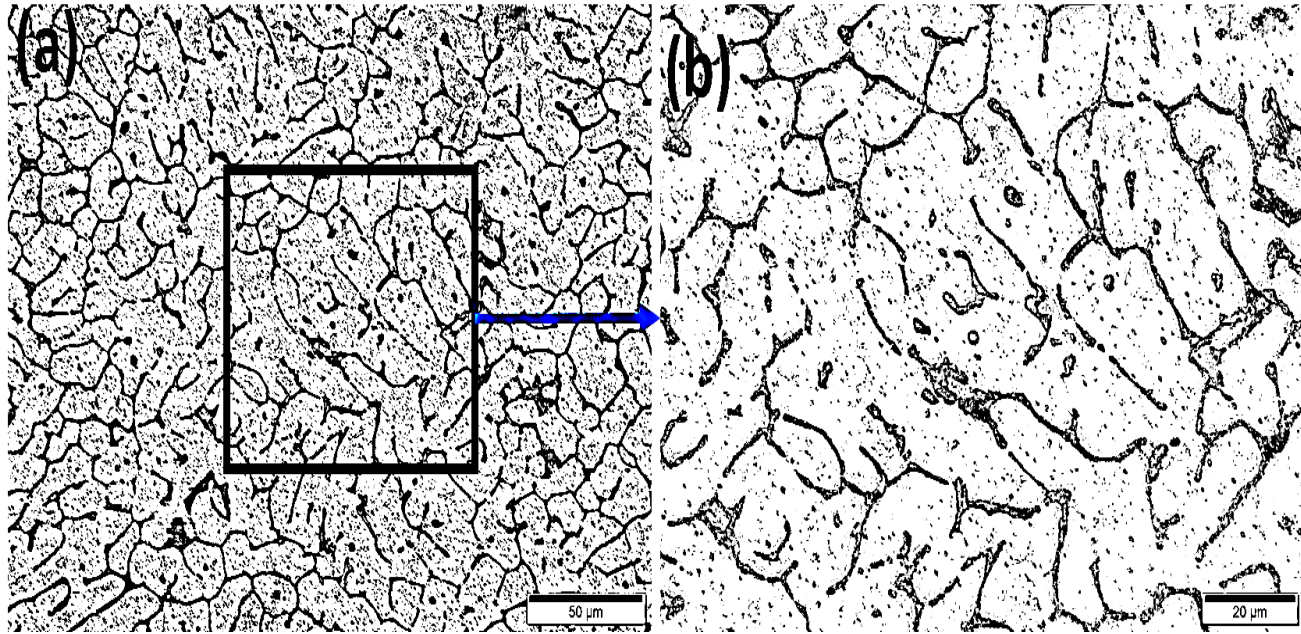


Fig. 4.34 Optical images of WMZ center in CMT welded A5754-H111 and A5083-H111 joint using ER4043 filler wire: (a) Low magnification and (b) High magnification

4.3.3 Schematic diagram of zone evolution

Fig. 4.35(a) shows the schematic diagram of typical zone evolution in conventional Al alloys fusion welded structures viz. HAZ, PMZ and WMZ. Fig. 4.35(b) represents the schematic diagram of zone evolution in the fusion welds of present study. Unlike typical zones, fusion welds of present study exhibit newly evolved EQZ at both the interfaces. This type of unique EQZ is mostly reported in Al-Li alloys and scarcely reported in other type Al alloys (Dev et al. 2008; Ning et al. 2017; Reddy et al. 1998).

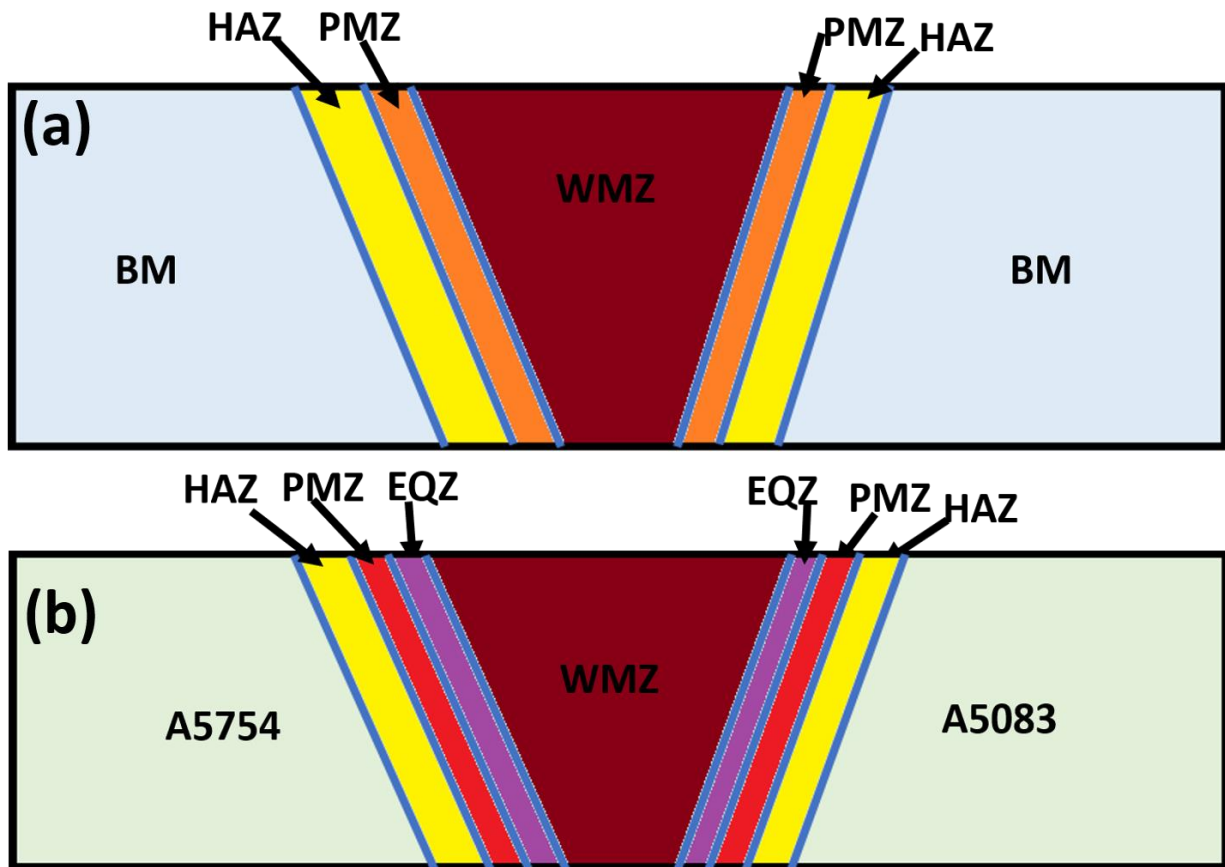


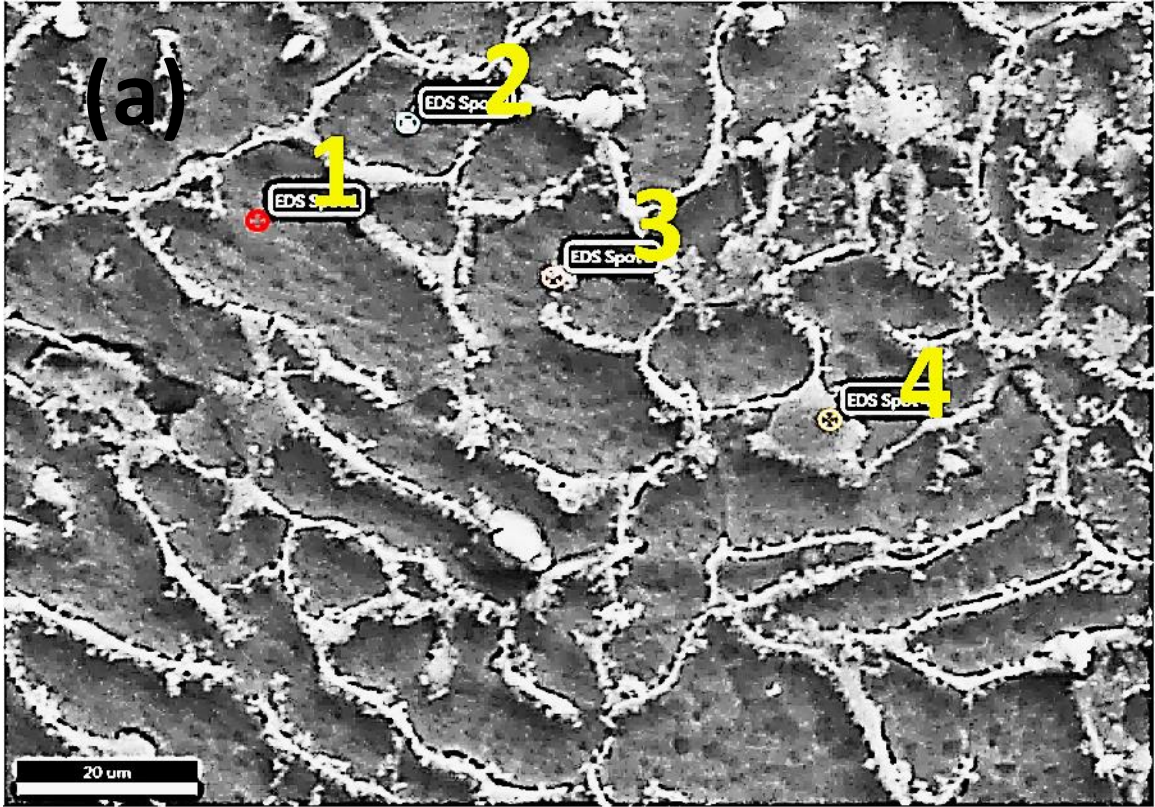
Fig. 4.35 Typical zones in fusion welds: (a) conventional Al alloys (b) present study (CMT welded A5754-H111 and A5083-H111 joint using ER4043 filler wire) showing unique EQZ at both interfaces

During solidification of weld joint contraction occurs in WMZ and PMZ. However, the degree of contraction varies in different zones. The volume of the liquid metal in WMZ is much higher than in other zones, which indicates that the degree of contraction is more in WMZ than in the other zones. In general, liquation cracks are formed, once the magnitude of shrinkage stress reaches a value which is greater than the magnitude of binding force between adjacent grains (Yan et al. 2017). Liquation in the EQZ lowered the binding force

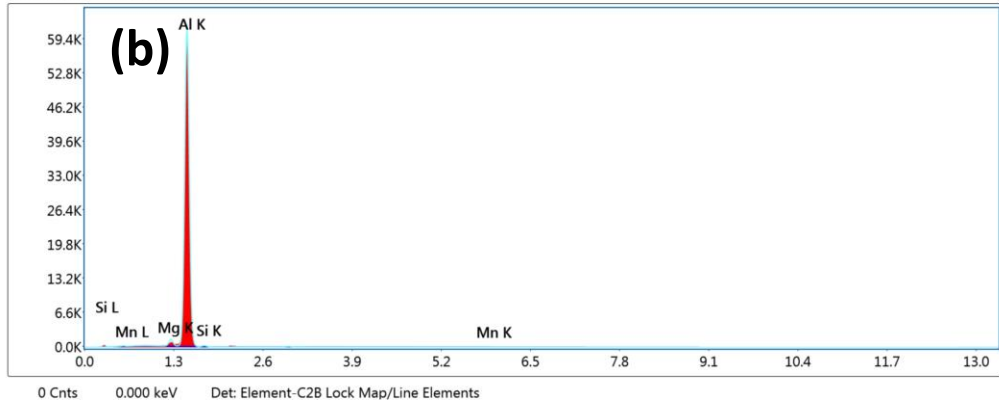
between the adjacent grains. The absence of any liquation crack at both the interfaces implies that the magnitude of shrinkage stress is not greater than magnitude of binding force between adjacent grains. The presence of Ti promotes nucleation of new grains by decreasing the interfacial tension of the solid liquid interface (Yunjia et al. 1989). Both the base metals (BMs) contain trace amounts of Ti that leads to influence EQZ formation in the weldment. Laser beam welding influences the formation of EQZ due to its lower heat input and higher welding speed (Ning et al. 2017). The CMT technique, being also a joining technique with low heat input and high welding speed, is likely to influence the formation of EQZ. Thus, both BM composition and CMT process are the possible reasons for the formation of EQZ. The EQZ width is greater at the A5754 interface than at the A5083 interface. Thermal conductivity of A5754 alloy (130 W/m. K) is significantly higher than the A5083 alloy (120 W/m. K) (Derazkola and Simchi 2019; Ding et al. 2018). Thus, the solute mixing and diffusion of solute elements are easier in A5754, thereby leading to a higher EQZ width. Moreover, the grains in EQZ of A5083 are finer than those in EQZ of A5754. A5083 alloy contains higher amounts of Mg and Mn than A5754 alloy. Due to this, the degree of supercooling at A5083 interface is higher than at A5754 interface. Higher degree of supercooling induces a larger temperature gradient in the liquid metal in front of the solid/liquid interfaces. Thus, the grains of EQZ are finer in A5083 interface than in A5754 interface.

4.3.4 SEM-EDS of WMZ center in CMT welded A5754-H1111 and A5083-H1111 joint using ER4043 filler wire

Fig. 4.36(a) shows the EDS spot analysis of the WMZ center. The corresponding EDS spectra for the spots at WMZ center are shown in Fig. 4.36(b-e). Table 4.6 lists the chemical composition of elements at the spots. The spot 1 EDS analysis was taken from the matrix region. Other than the Al element, this region shows significant quantities of Mg and Mn. The ER4043 filler material contains lower amounts of Mg (0.05%) and Mn (0.05%) in its composition [Table 3.1]. The Mg (1.9%) and Mn (0.3) contents have increased in WMZ center. Both the BMs contain Mg as a primary alloying element and Mn as a secondary alloying element and these have migrated from BMs to the center of WMZ by dilution effect. The analysis of spots 2 and 3 EDS was made on the white color spherical shaped secondary phase particles. The analysis reveals that these phases are possibly Mg_2Si phases which is supported by the previous research work (Lakshminarayanan et al. 2009). EDS spot analysis on segregated layer (spot 4) confirms that the layer is dominated by Si element.



12-4-19 | New Sample | Area 28 | EDS Spot 1



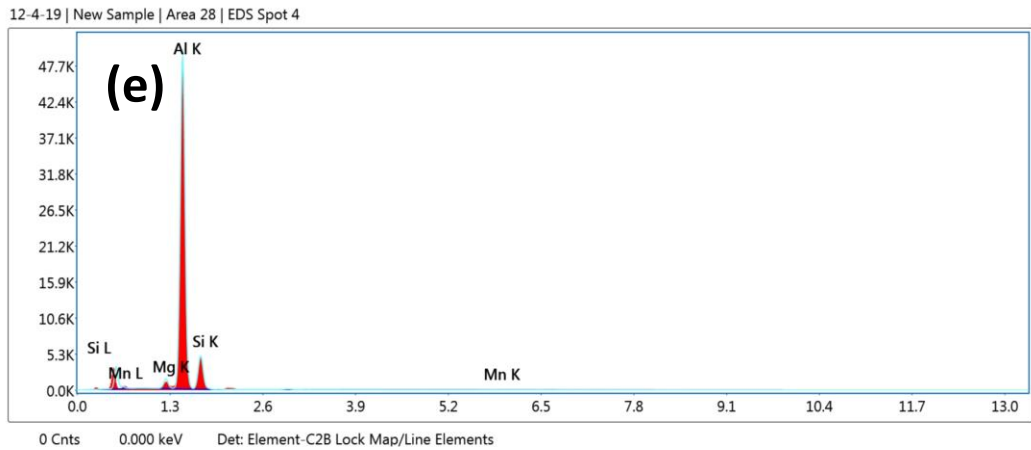
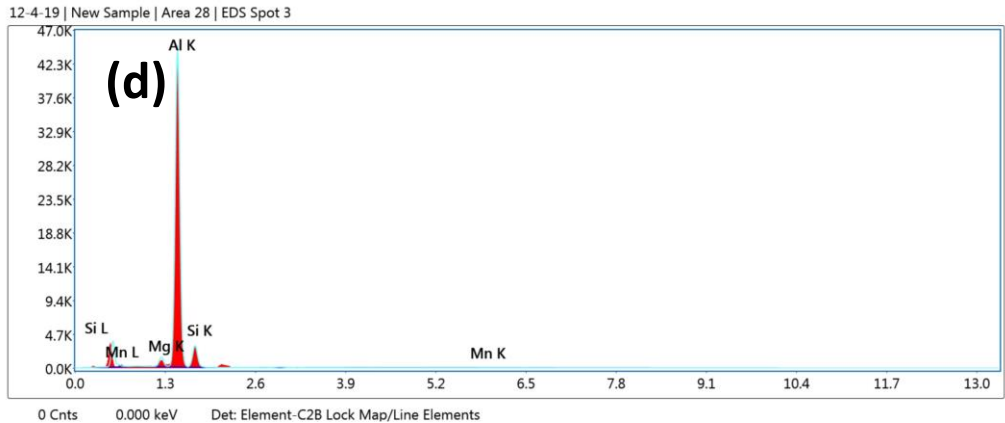
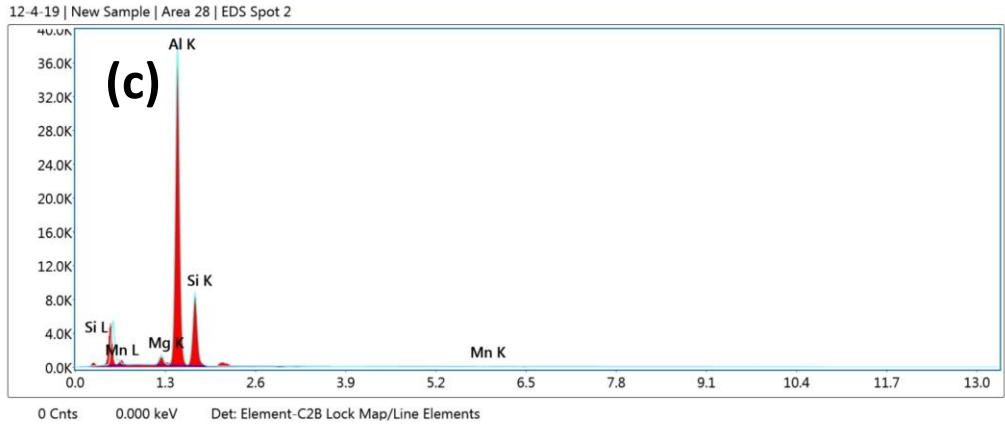


Fig. 4.36 (a) EDS spot analysis of WMZ center in CMT welded A5754-H111 and A5083-H111 joint using ER4043 filler wire and (b-e) EDS spectra for corresponding spots

Table 4.6 SEM-EDS spot analysis of different phases in WMZ center of CMT welded A5754-H111 and A5083-H111 joint using ER4043 filler wire

Spots	(wt. %)				(at. %)			
	Al	Mg	Si	Mn	Al	Mg	Si	Mn
Spot 1	Bal.	1.91	0.96	0.31	Bal.	2.12	0.93	0.15
Spot 2	Bal.	1.87	31.65	0.40	Bal.	2.11	30.78	0.20
Spot 3	Bal.	2.28	14.08	0.36	Bal.	2.54	13.59	0.18
Spot 4	Bal.	2.08	18.68	0.36	Bal.	2.33	18.07	0.18

4.3.5 SEM of HAZ in CMT welded A5754-H111 and A5083-H111 joint using ER4043 filler wire

Fig. 4.37(a-b) shows the SEM images of heat affected zone (HAZ) of A5754 and A5083. Secondary phase particles are more in the HAZ of A5083 interface than at the A5754 interface.

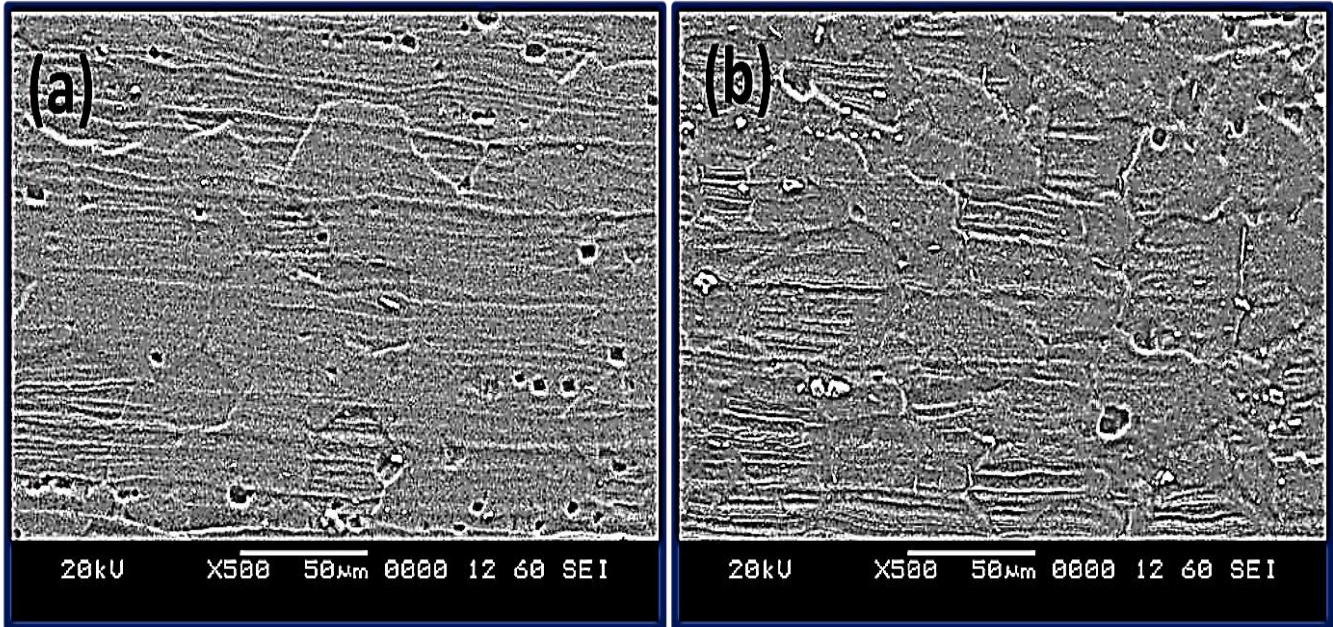


Fig. 4.37 SEM images of HAZ in CMT welded A5754-H111 and A5083-H111 joint using ER4043 filler wire: (a) A5754 interface and (b) A5083 interface

4.3.6 SEM-EDS of interface regions and WMZ center in CMT welded A5754-H111 and A5083-H111 joint using ER4043 filler wire

Fig. 4.38 and Fig. 4.39 show the elemental maps of the interface regions of the weld joint. Mg is low in WMZ, but once it crosses WMZ its quantity has increased. No significant difference is identified in the distribution of Mn. As compared to other regions, Si segregation is more at EQZ and a plentiful of bright (white color) Si-rich particles are visible in this region. It is also noticed that nearer to the columnar crystal zone (CCZ) Si concentration is higher at EQZ and somewhat less nearer to the PMZ. Fig. 4.40 shows elemental maps of WMZ at the center of the weld joint. Si is distributed at dendrite boundaries. Fig. 4.41 shows EDS spectra for mapping images of A5754 interface [Fig.

4.41(a)], A5083 interface [Fig. 4.41(b)], and WMZ at center [Fig. 4.41(c)]. Table 4.7 shows EDS mapping results of the A5754-H111, A5083-H111 interface regions and WMZ center.

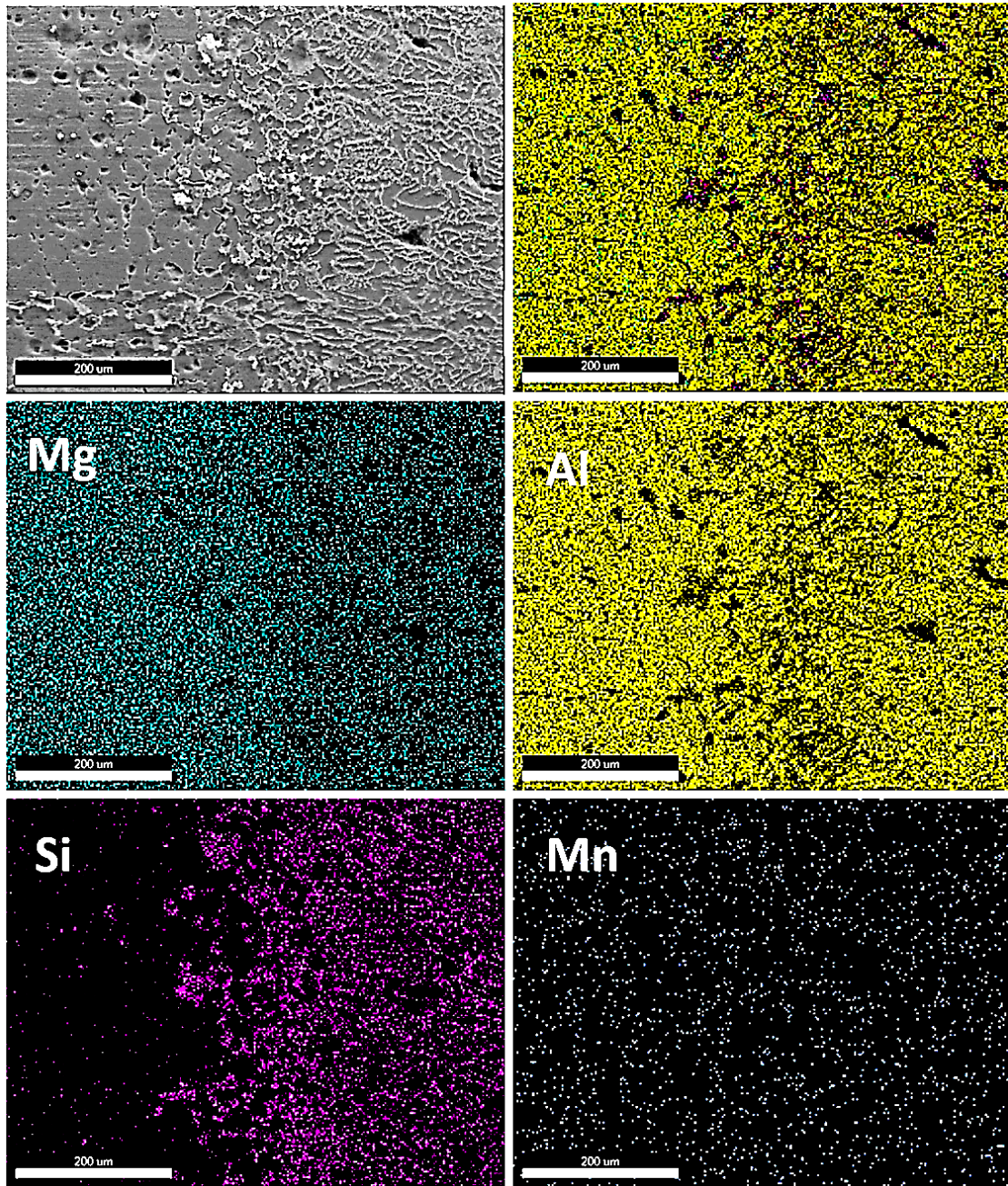


Fig. 4.38 Elemental maps showing distribution of elements at the 5754 interface in CMT welded A5754-H111 and A5083-H111 joint using ER4043 filler wire

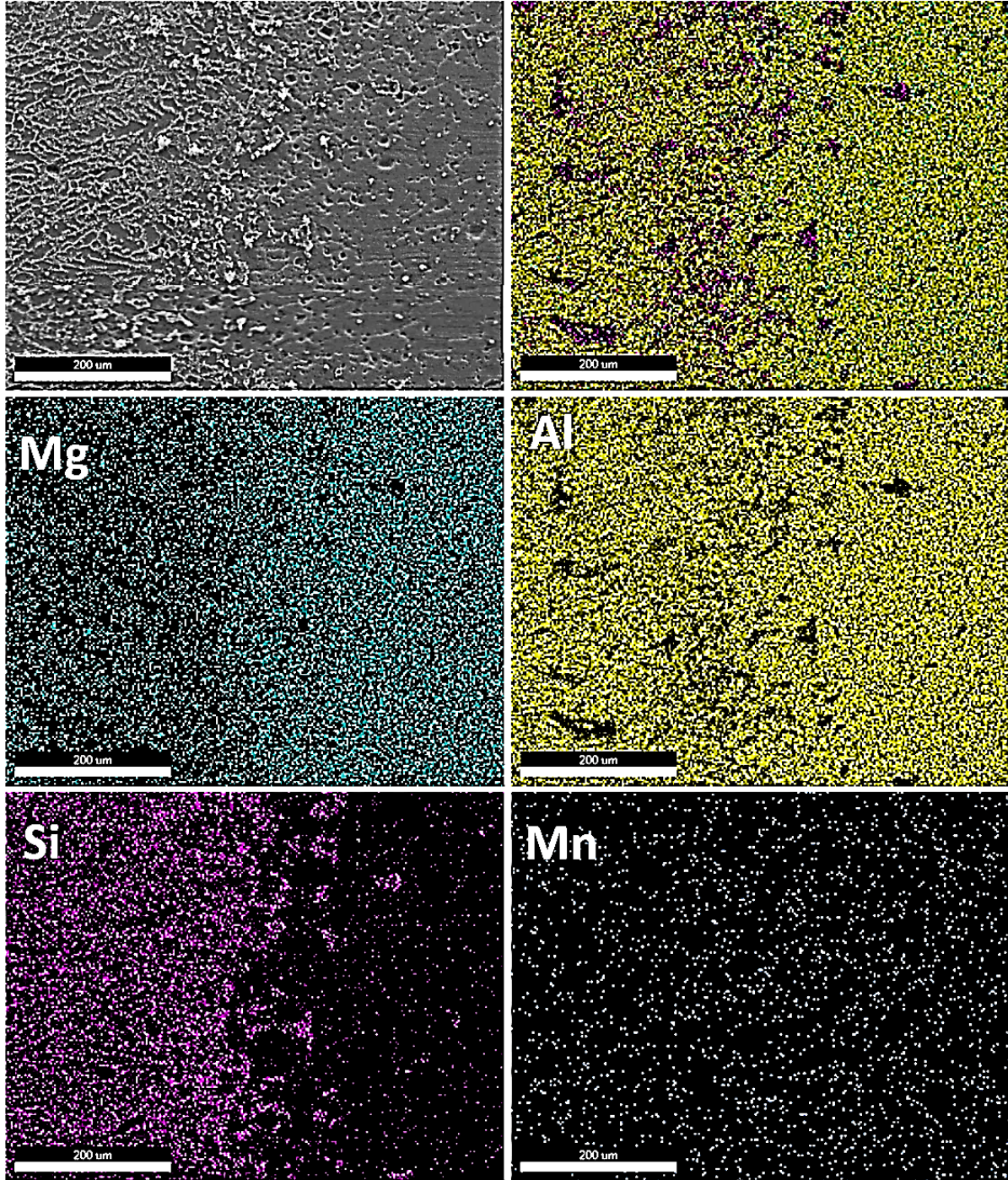


Fig. 4.39 Elemental maps showing distribution of elements at the A5083 interface in CMT welded A5754-H111 and A5083-H111 joint using ER4043 filler wire

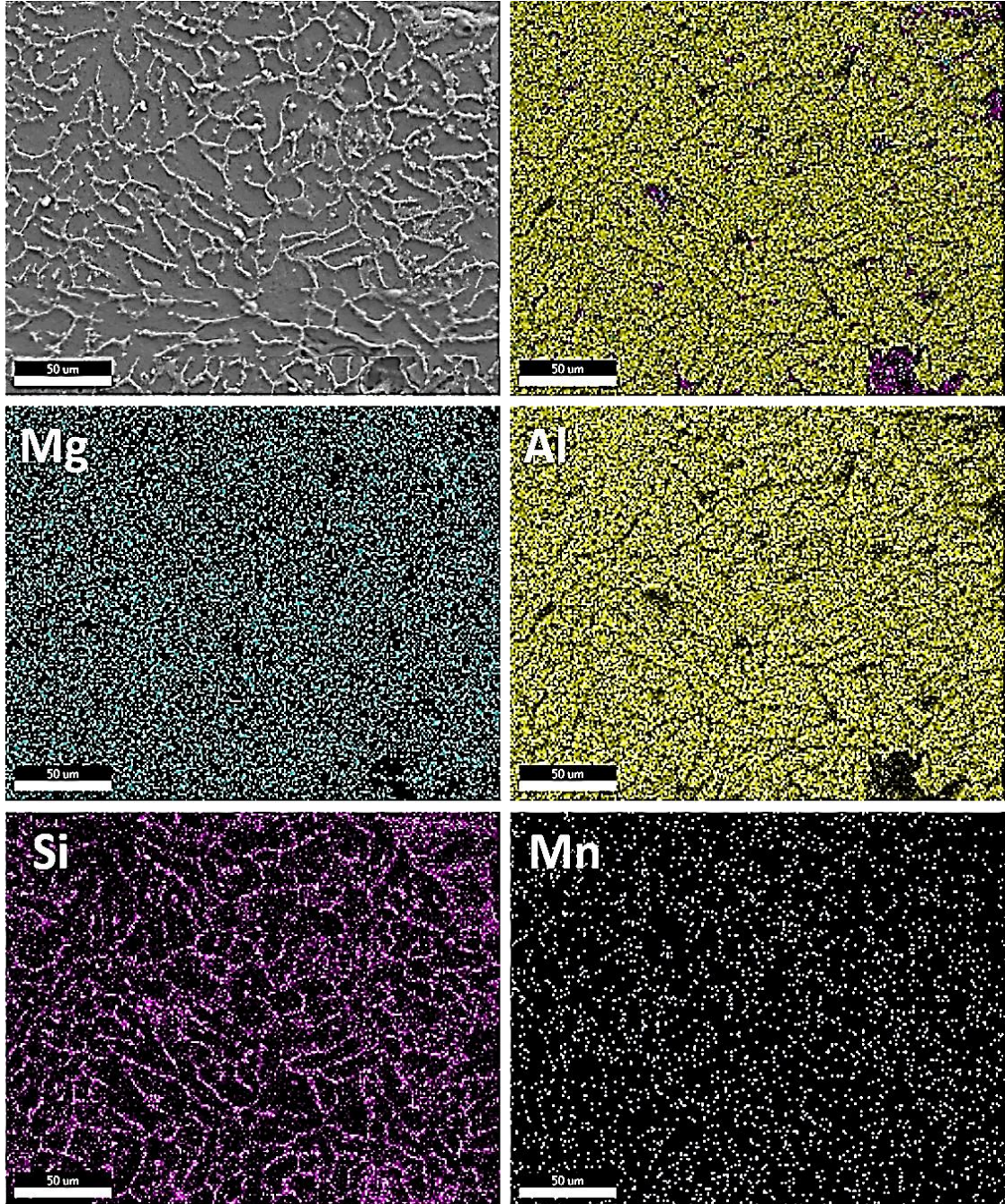


Fig. 4.40 Elemental maps showing distribution of elements at the center of WMZ in CMT welded A5754-H111 and A5083-H111 joint using ER4043 filler wire

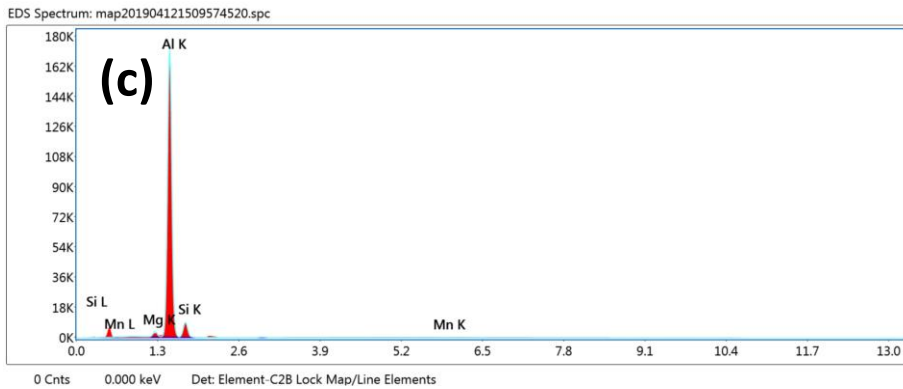
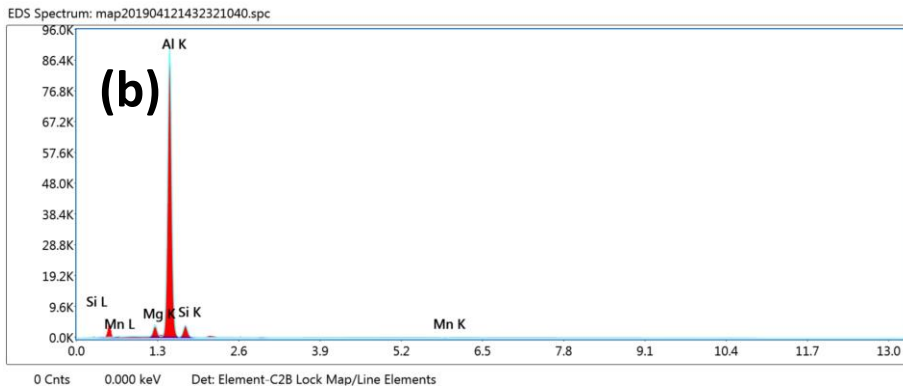
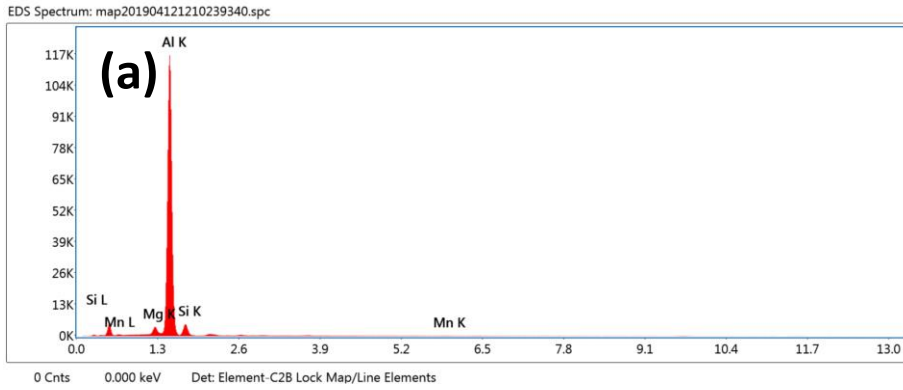


Fig. 4.41 EDS spectra mapping images of the CMT welded A5754-H111 and A5083-H111 joint using ER4043 filler wire: (a) A5754 interface; (b) A5083 interface and (c) WMZ center

Table 4.7 EDS mapping results of the CMT welded A5754-H111 and A5083-H111 joint using ER4043 filler wire

Interface	Al	Mg	Si	Mn	Al	Mg	Si	Mn
	(wt. %)				(at. %)			
A5754	Bal.	2.86	8.96	0.38	Bal.	3.18	8.63	0.19
A5083	Bal.	3.46	7.28	0.32	Bal.	3.84	7	0.16
WMZ	Bal.	1.64	11.57	0.26	Bal.	1.83	11.16	0.13

4.3.7 Microhardness of the CMT welded A5754-H111 and A5083-H111 joint using ER4043 filler wire

Fig. 4.42 displays Vickers micro hardness profiles of the weld joint. The BMs exhibit maximum hardness among all the zones. HAZs and PMZs on both the sides exhibit lower hardness than the respective BMs. Due to the presence of Si films in the PMZ grains, this region exhibits lower hardness than the BMs. The BMs of 5xxx series dissimilar joint contain a significant quantity of Mg and Mn [Table 3.1]. So the amount of migrating Mg and Mn from BM to the center of WMZ due to dilution effect can be more. This is confirmed by EDS spot analysis on the matrix [spot 1 in Table 4.6]. Therefore, solid

solution strengthening effects provided by Mg and Mn have significantly contributed to the hardness increment in WMZ. The presence of Mg_2Si secondary phase particles is confirmed by the EDS spot analysis on the white coloured spherical particles [spot 2 and 3 in Table 4.6]. Thus, secondary phase particle hardening effect provided by Mg_2Si phases is also another possible reason for the increased hardness in WMZ. From the observed results, it is evident that solid solution strengthening by Mg, Mn and secondary phase particles strengthening by Mg_2Si phases have played a decisive role in hardness improvement in WMZ of the welded joint.

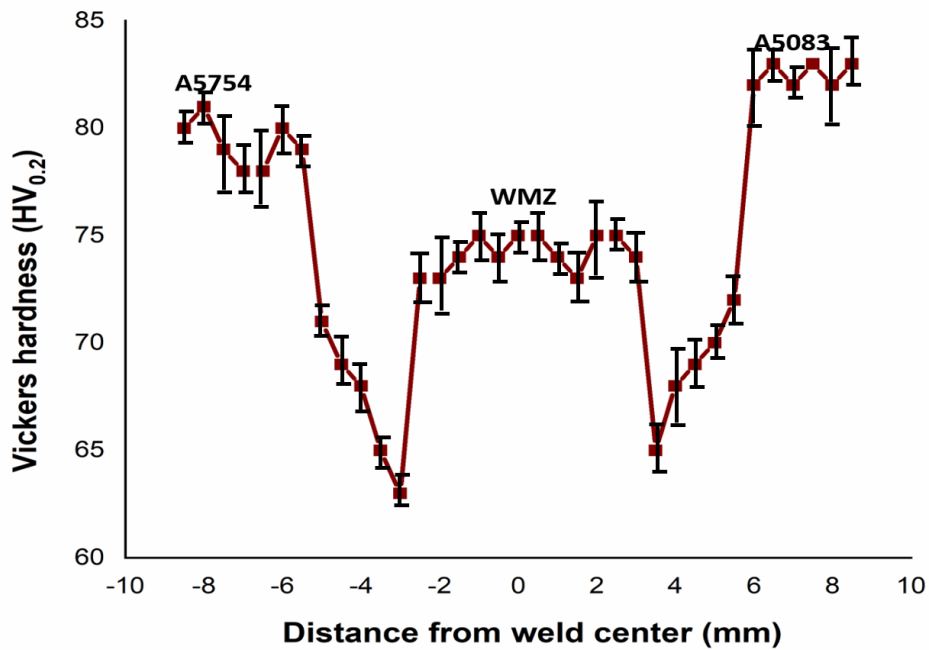


Fig. 4.42 Vickers micro hardness profiles of the CMT welded A5754-H111 and A5083-H111 joint using ER4043 filler wire

4.3.8 Tensile results of the CMT welded A5754-H111 and A5083-H111 joint using ER4043 filler wire

Tensile properties of BMs and weld regions are shown in Fig 4.43. The tensile data of BMs and different regions of welded samples are summarized in Table 4.8. The interface regions show lower strength values than the WMZ. The presence of EQZ is the main reason for the reduction in strength values in interfaces than the WMZ. Si segregation is more at GBs of EQZ at both the interfaces. According to a published research work, the phenomenon of solute segregation at GBs of EQZ reduces the mechanical properties (Dev et al. 2008). Among the interface regions A5754 interface exhibit lower strength values than the A5083 interface. The EQZ width is greater at the A5754 interface than at the A5083 interface and the grains in EQZ of A5754 are coarser than the grains in EQZ of A5083. Apart from these, dendrites of WMZ at A5754 interface are also coarser than the dendrites of WMZ at A5083 interface. The above-mentioned features in A5754 interface have significantly reduced its strength. The presence of lower amounts of secondary phase particles in PMZ and HAZ is also responsible for the decrease of strength of the A5754 interface region.

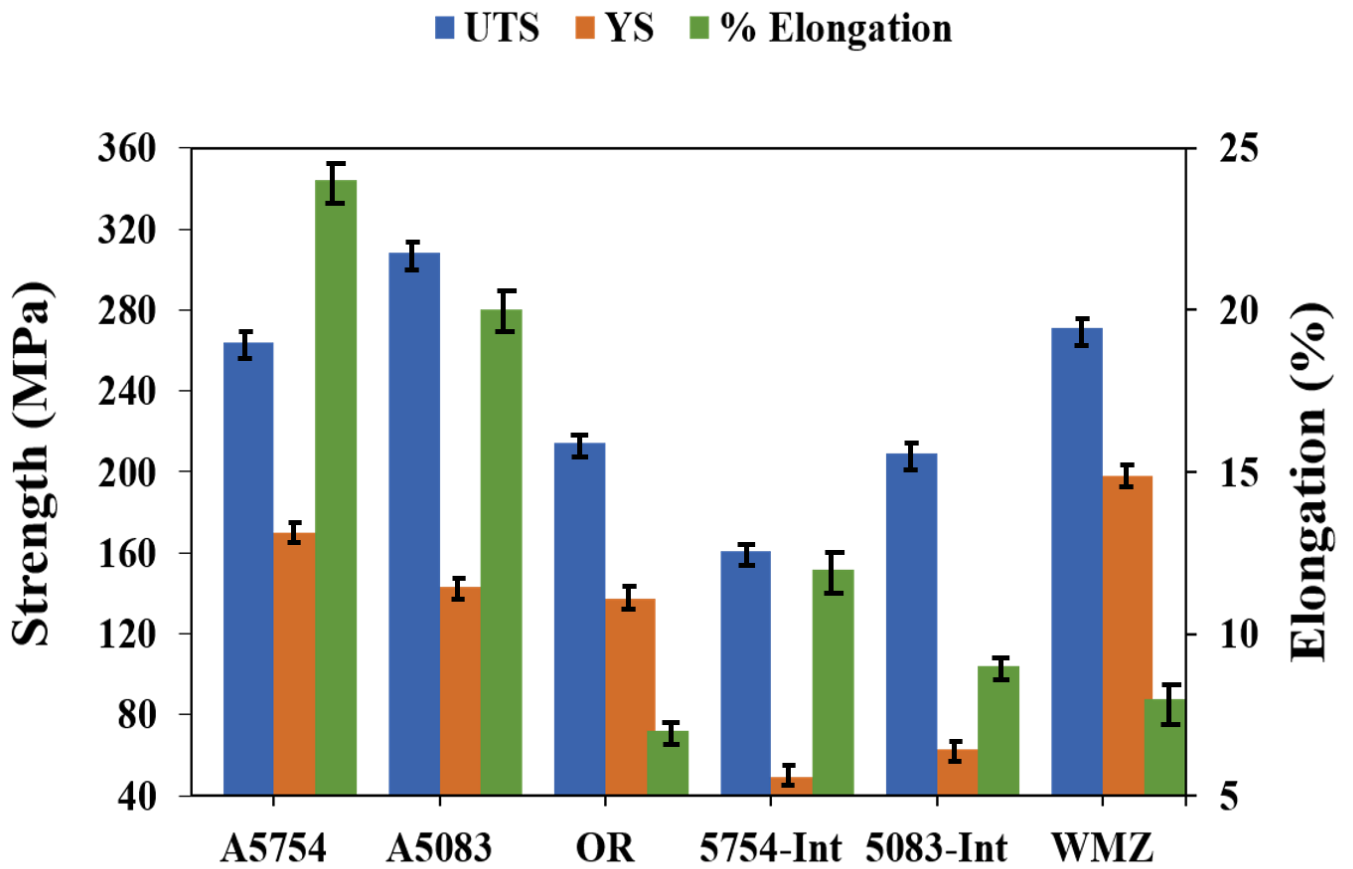


Fig. 4.43 Tensile properties of BMs and welded regions of the CMT welded A5754-H111 and A5083-H111 joint using ER4043 filler wire (OR-over all weld region, Int-Interface and WMZ- weld metal zone; Gauge length of BMs & OR is 25 mm and gauge length of interfaces and WMZ is 5 mm)

Table 4.8 Tensile properties of the base alloys and different regions of CMT welded A5754-H111 and A5083-H111 joint using ER4043 filler wire

Sample	UTS (MPa)	YS (MPa)	Elongation (%)
A5754	264	170	24
A5083	308	143	20
CMT weld joint (A5754 int.)	161	49	12
CMT weld joint (A5083 int.)	209	63	9
CMT weld joint (WMZ)	271	198	8
CMT weld joint (OR)	214	137	7

4.3.9 SEM images of fracture surface in CMT welded A5754-H111 and A5083-H111 joint using ER4043 filler wire

Fig 4.44(a-d) represents SEM images of fractured surface of the A6061 and A6082 interface regions of the weld joints, respectively. The A6061 interface region displays intergranular microcracks on the fracture surface. Presence of dimples is observed on the fracture surface of A6082 interface region. Fig 4.44(e-f) shows SEM images of fractured

surface of over-all weld joint. It can be seen that the fracture surface of over-all weld sample displays predominant presence of dimples.

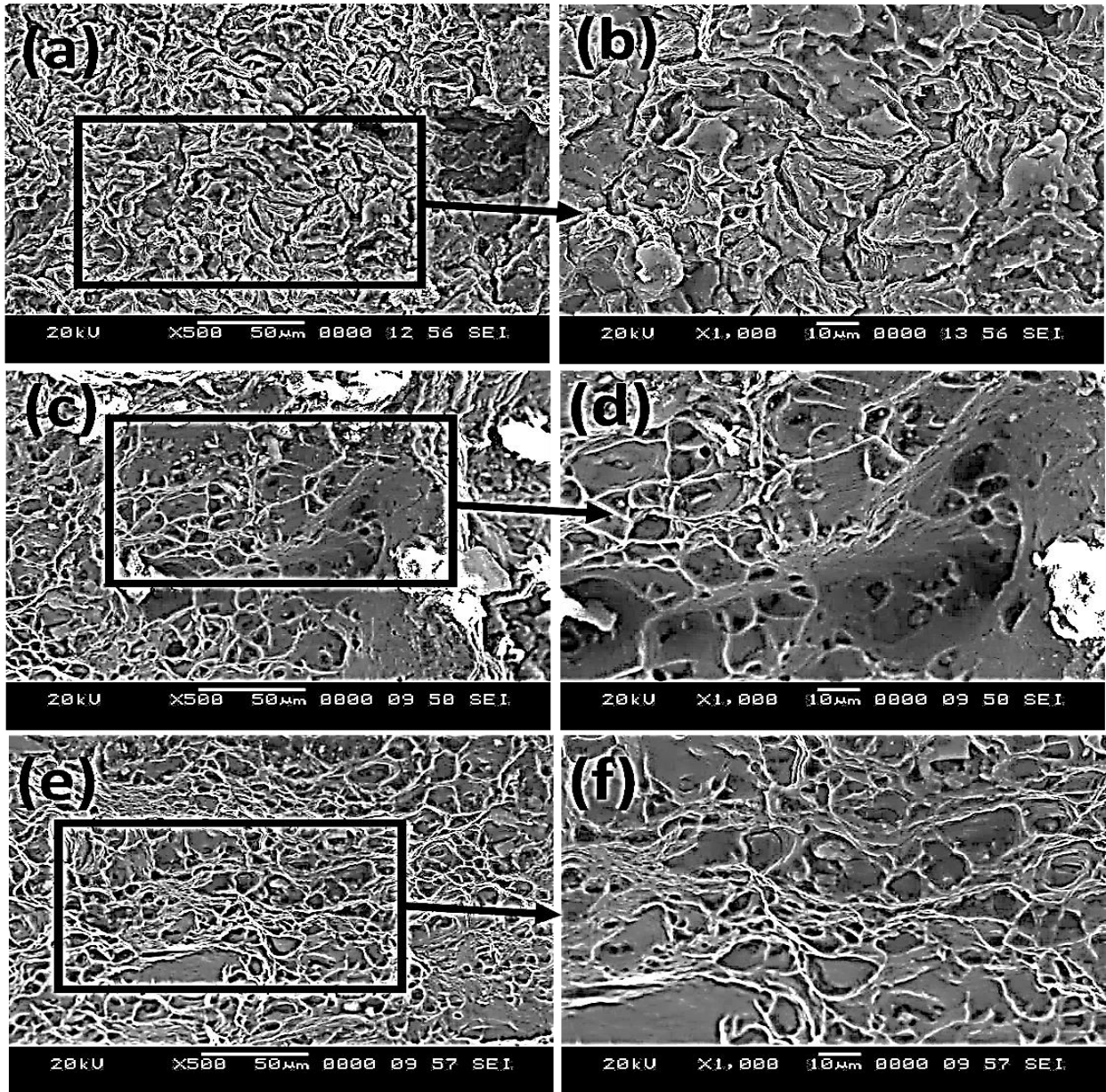


Fig 4.44 SEM images of fractured surfaces of the CMT welded A5754-H111 and A5083-H111 joint using ER4043 filler wire: (a-b) A6061 interface; (c-d) A6082 interface and (e-f) Over all weld region

4.4 Cold metal transfer (CMT) welding of dissimilar A5754-H111 and A5083-H111 using ER5356 filler wire

4.4.1 Surface appearance and macrostructure of the CMT welded A5754-H111 and A5083-H111 joint using ER5356 filler wire

The visual appearance of the CMT welded joint is shown in Fig. 4.45 (a-b). It is observed that the surface appearance does not exhibit any spatter, cracks and undercut defects. As shown in Fig. 4.45 (b), complete penetration of the weld joint is obtained. Fig. 4.46 shows a macroscopic cross-sectional view of the dissimilar A5754-A5083 joint. The cross section of the joint displays good weld profiles without any defect. Complete penetration is observed. The WMZ in the joint is brighter than the other zones owing to the addition of external ER5356 filler material in the weld joint.

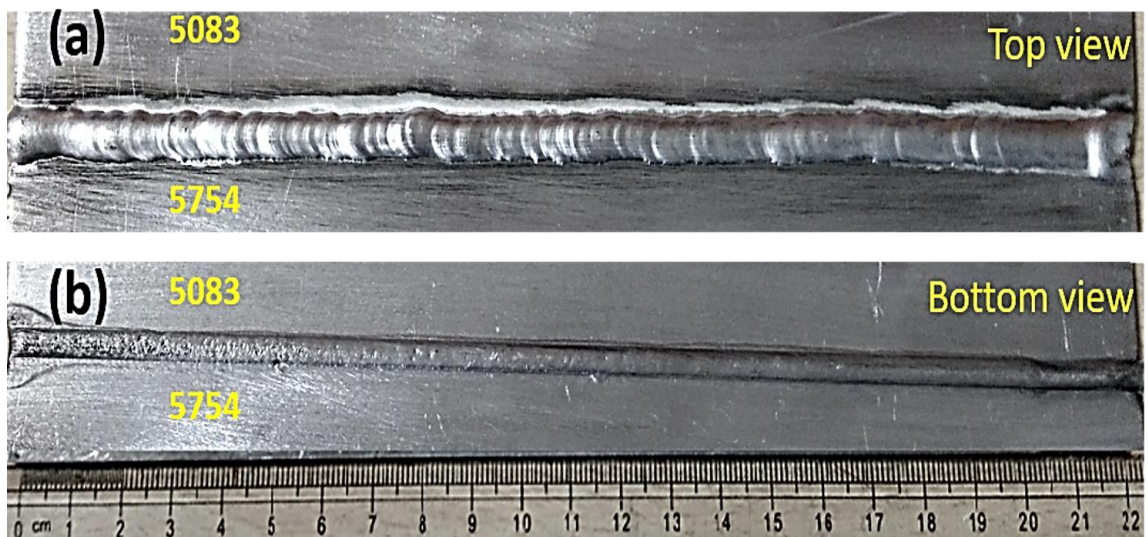


Fig. 4.45 Top and bottom views of the CMT welded A5754-H111 and A5083-H111 joint using ER5356 filler wire

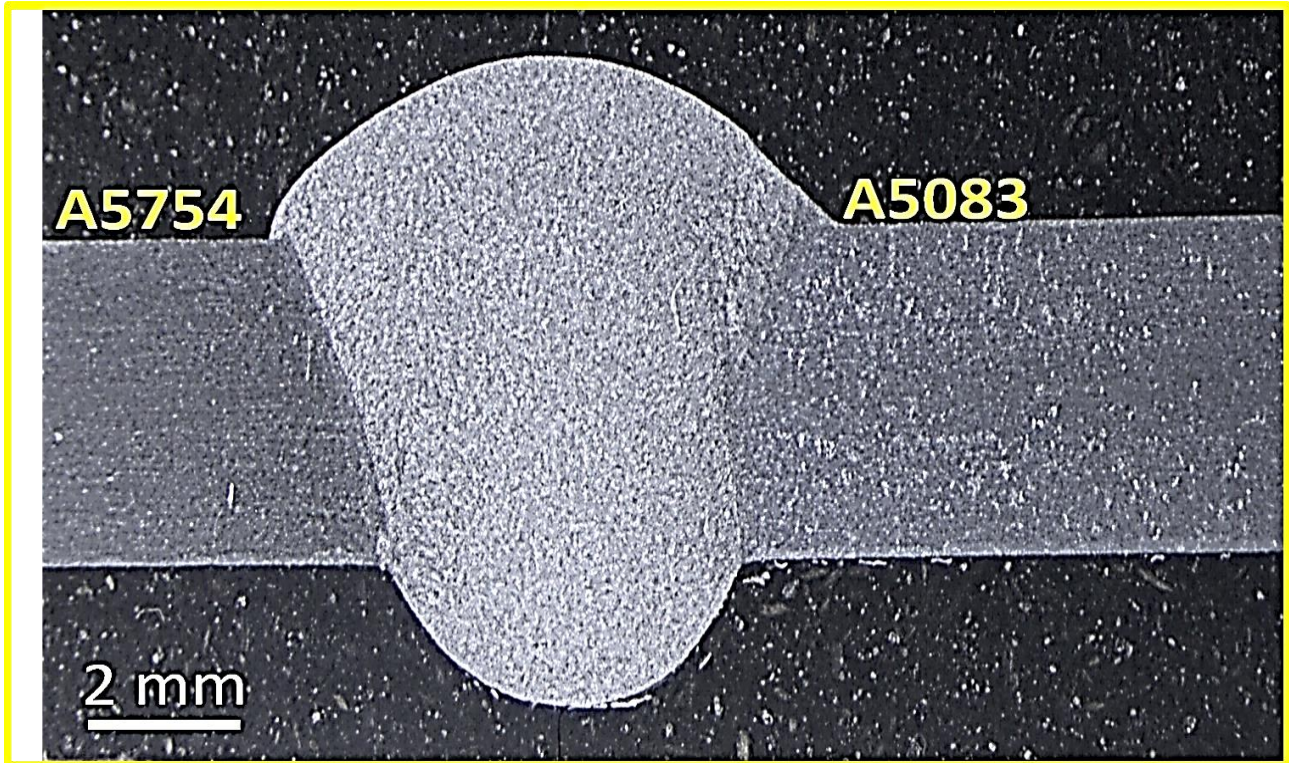


Fig. 4.46 Macroscopic cross-sectional view of the CMT welded A5754-H111 and A5083-H111 joint using ER5356 filler wire

4.4.2 SEM of interface regions of the CMT welded A5754-H111 and A5083-H111 joint using ER5356 filler wire

Fig. 4.47 (a-c) and Fig. 4.48 (a-c) show SEM images of interface regions of the weld joint. In general, weld aluminium alloys show a variation in the microstructure at the fusion boundary. As can be seen from Fig. 4.47 (a) and Fig. 4.48 (a), epitaxial columnar dendrites have grown from the PMZ towards the center of the fusion zone, which is denoted by columnar crystal zone (CCZ). The epitaxial growth can be achieved with minimal degree of undercooling. The temperature increase towards the weld center suppresses the

formation of fine grains, and subsequently columnar grains grow epitaxially from the PMZ. At the PMZ of the interfaces, the base alloys are melted partially and mixed with the elements of the filler material.

The fusion zone (WMZ) center shows equiaxed dendritic microstructure [Fig. 4.47(b) and Fig. 4.48(b)]. At the center of WMZ the under-cooling effect is more that aids the formation of equiaxed fine dendrites. The grains of HAZ are recrystallized at both the interfaces [Fig. 4.47(c) and Fig. 4.48(c)]. This implies that both the HAZs attained temperatures higher than the annealing temperatures of the respective BMs. The existence of recrystallized grains at HAZ indicates that the strengthening due to strain hardening is partially lost. It is observed that the recrystallized grains at HAZ of A5754 is significantly coarser than the recrystallized grains at HAZ of A5083. The size of the secondary phase particles is also affected. As can be seen from Fig. 4.47(c) and Fig. 4.48(c), the secondary phase particles in HAZ of A5083 interface are qualitatively finer and higher than in the HAZ of A5754.

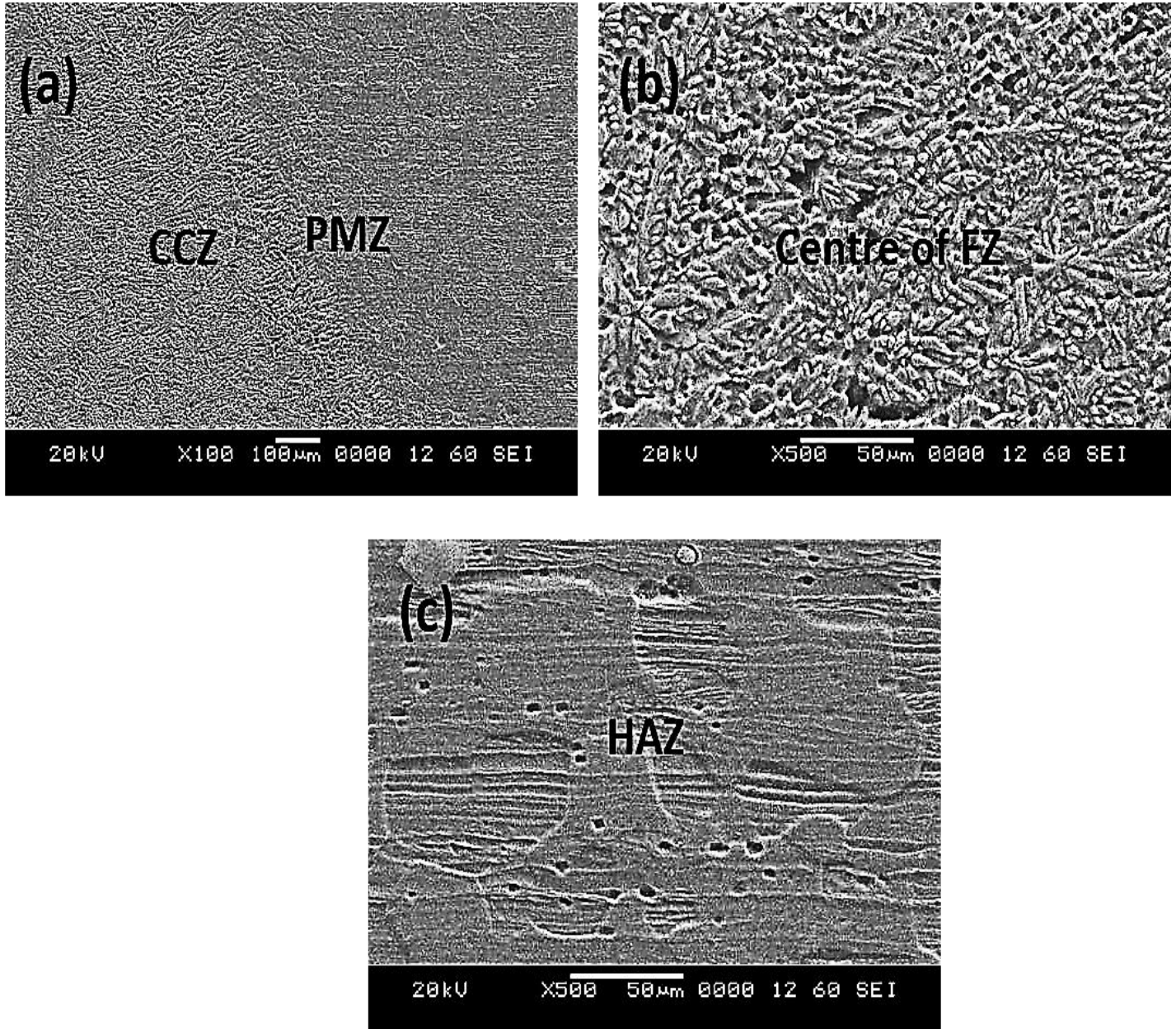


Fig. 4.47 (a-c) SEM images of A5754 interface regions in CMT welded A5754-H111 and A5083-H111 joint using ER5356 filler wire

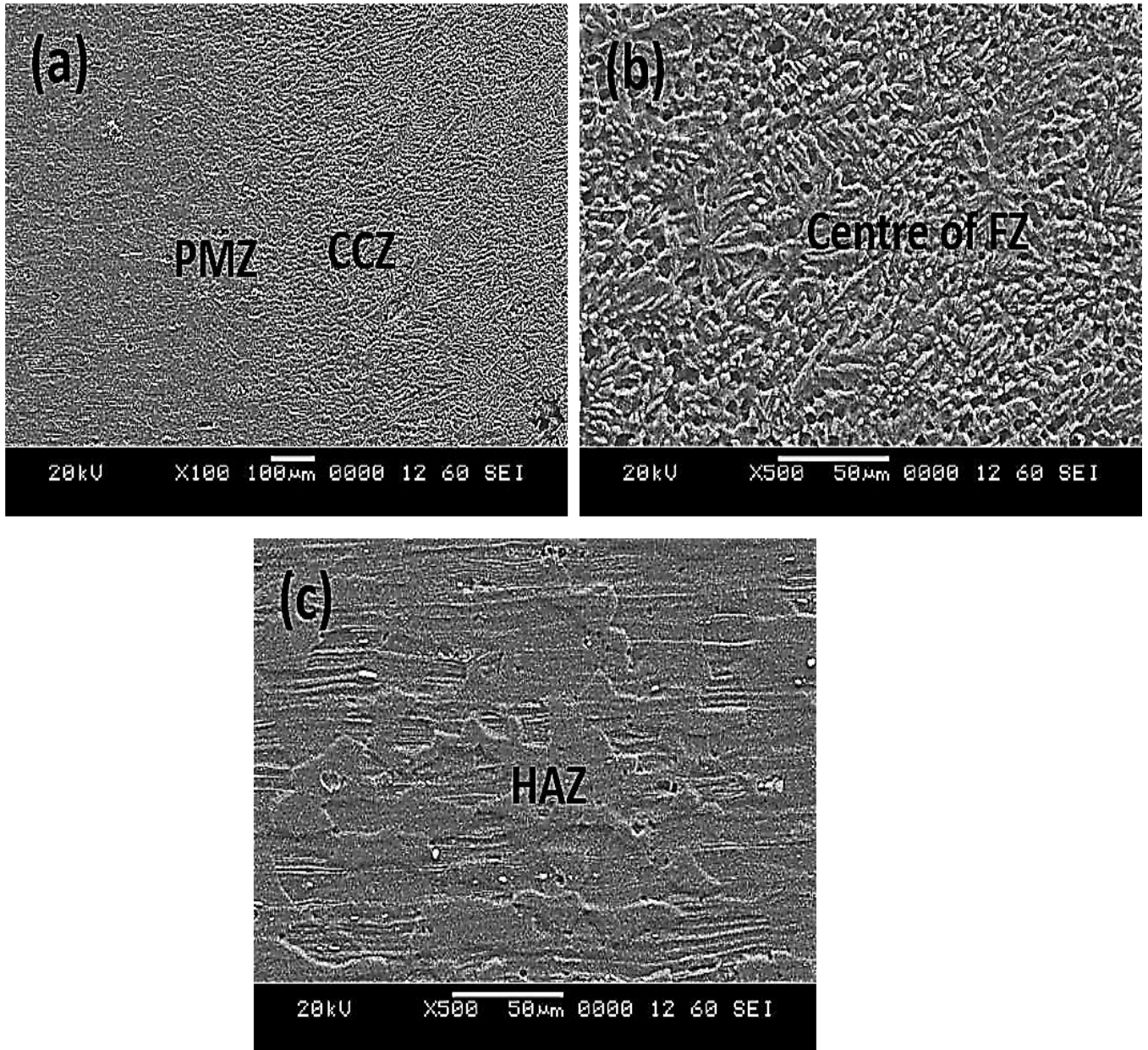


Fig. 4.48 (a-c) SEM images of A5083 interface region in CMT welded A5754-H111 and A5083-H111 joint using ER5356 filler wire

4.4.3 SEM-EDS of the interface regions of CMT welded A5754-H111 and A5083-H111 joint using ER5356 filler wire

Fig. 4.49 and Fig. 4.50 show elemental maps of the interface regions of the weld joint. The composition of the elements at the interface regions is listed in Table 4.9. As can be seen from Fig. 4.50, Mg element variation in different zones at the 5083-interface region is not discernible. This is expected, as the BM (5083) and ER5356 filler materials have almost the same weight percentage of Mg. In contrast, the variation in Mg element at the 5754-interface region (Fig. 4.49) of the joint is clearly visible, as the BM (5754) contains lower quantity of Mg compared to the filler material.

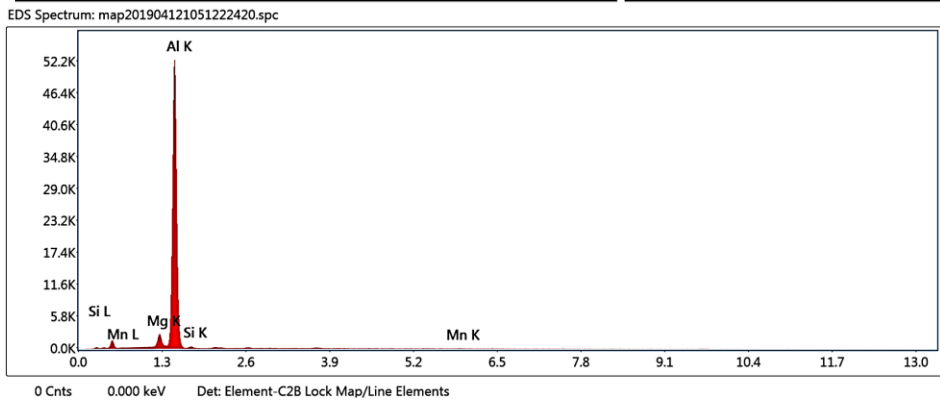
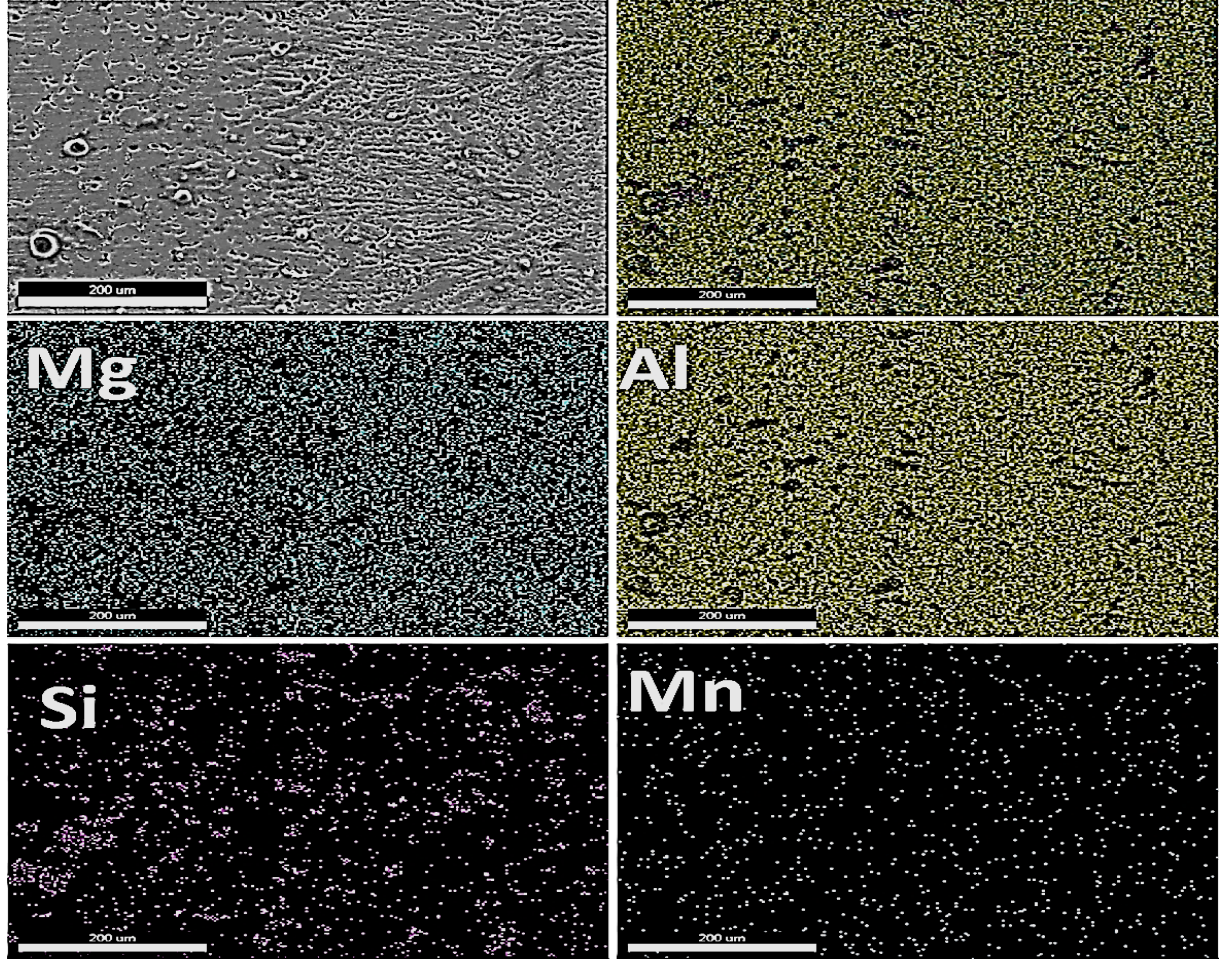


Fig. 4.49 Elemental maps and its EDS spectra at 5754 interface in CMT welded A5754-H111 and A5083-H111 joint using ER5356 filler wire

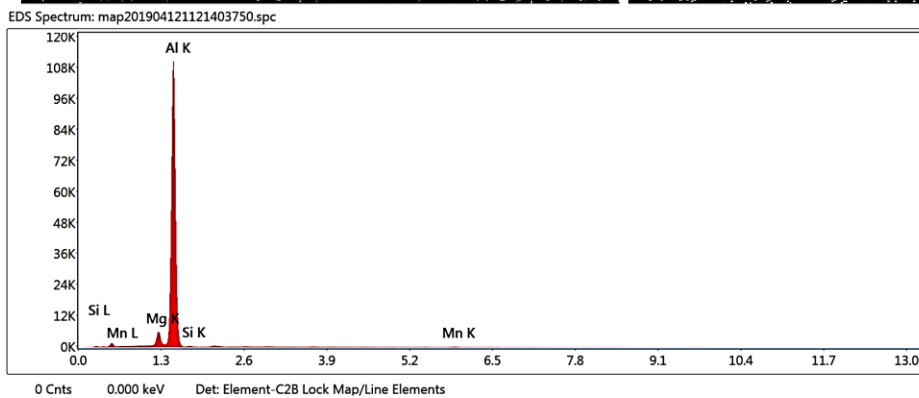
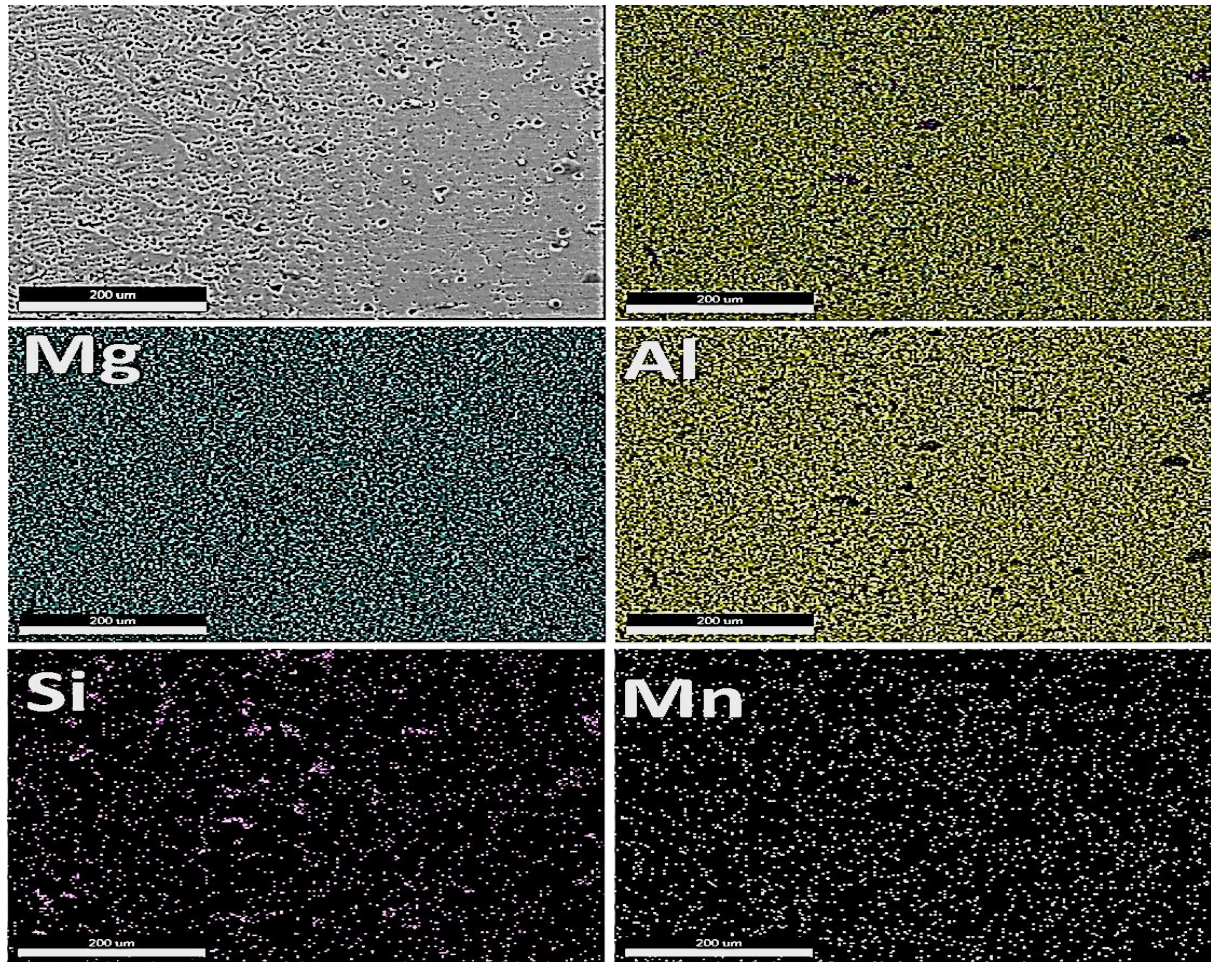


Fig. 4.50 Elemental maps and its EDS spectra of A5083 interface in CMT welded A5754-H111 and A5083-H111 joint using ER5356 filler wire

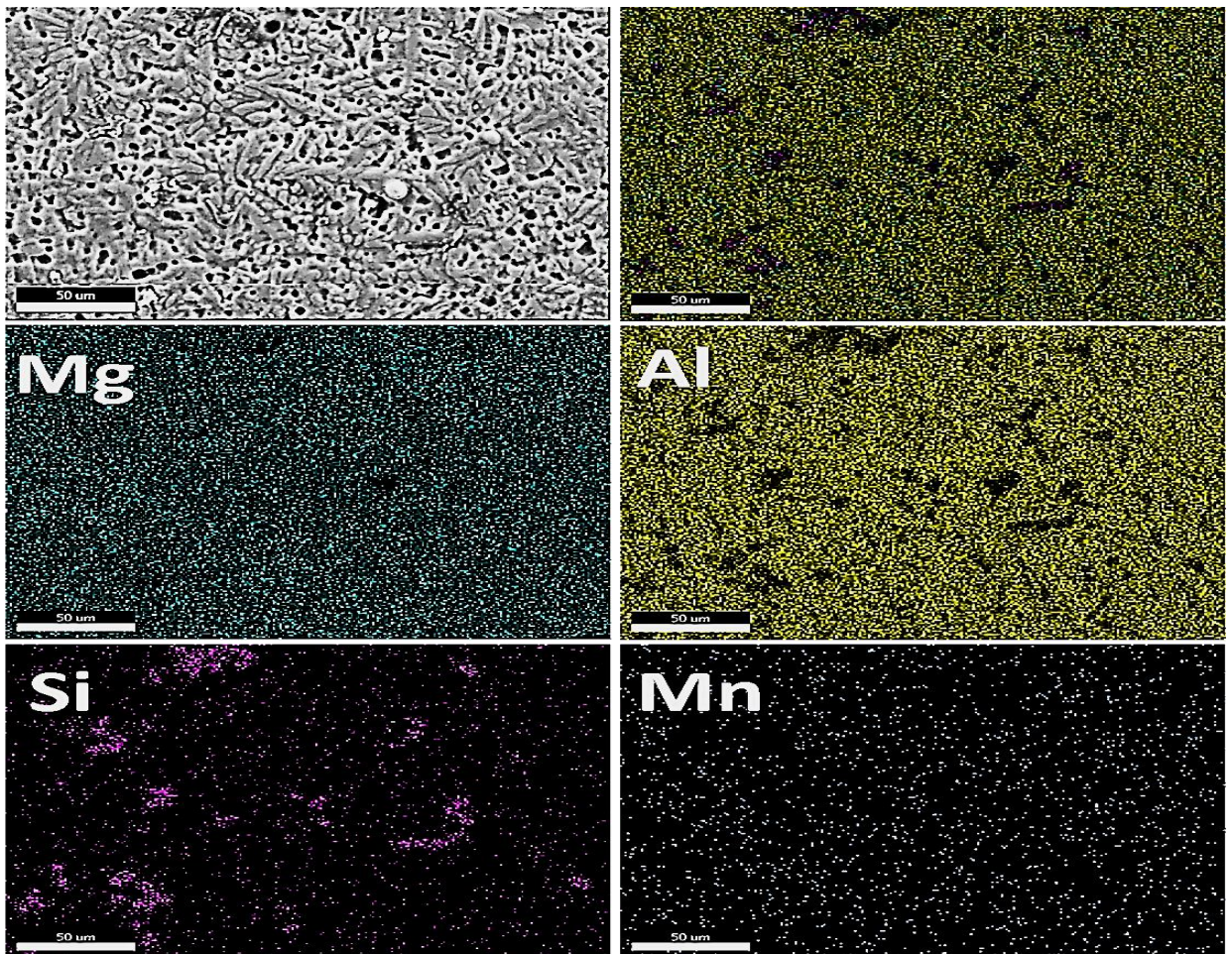
Table 4.9 EDS mapping results of the interface regions in CMT welded A5754-H111 and A5083-H111 joint using ER5356 filler wire

Interface	(wt. %)				(at. %)			
	Al	Mg	Si	Mn	Al	Mg	Si	Mn
A5754	Bal.	4.62	1.23	0.46	Bal.	5.11	1.18	0.23
A5083	Bal.	4.90	0.54	0.72	Bal.	5.43	0.52	0.35

4.4.4 SEM-EDS of WMZ center in CMT welded A5754-H111 and A5083-H111 joint using ER5356 filler wire

Fig. 4.51 presents elemental maps of the center of the WMZ, and the composition of the elements is summarized in Table 4.11. The dendrite boundaries display eutectic phases and secondary phase particles. The dendrite boundaries as well as the inter-dendritic arm spacings are enriched in Mg. Segregation of Si phases is evident from the mapping images. Si (1.09%) and Mn (0.47) contents are increased in the center of the WMZ (Table 4.11). This can be attributed to the migration of Si and Mn from the BMs to the center of the WMZ due to dilution effect. The picture is different for Mg distribution. Both the BMs contain Mg as a main alloying element, and thus like Si and Mn elements, Mg also gets migrated from the BM to the centre of the WMZ due to dilution effect. Therefore, a higher

amount of Mg is expected at the center of the WMZ, but the amount of Mg at the center of the WMZ is (4.66%) less than the amount of Mg in the filler material (5%). This can be explained in the following way. Compared to Al, the vaporizing rate of magnesium is two orders higher (Block-Bolten and Eagar 1984; Zhao and Debroy 2001). Thus, Mg is readily vaporized resulting in a loss of Mg element in the weld pool. Even though some Mg is lost, the amount of Mg in the WMZ is still nearly equal to the amount of Mg in the filler material which implies that the loss is negligible.



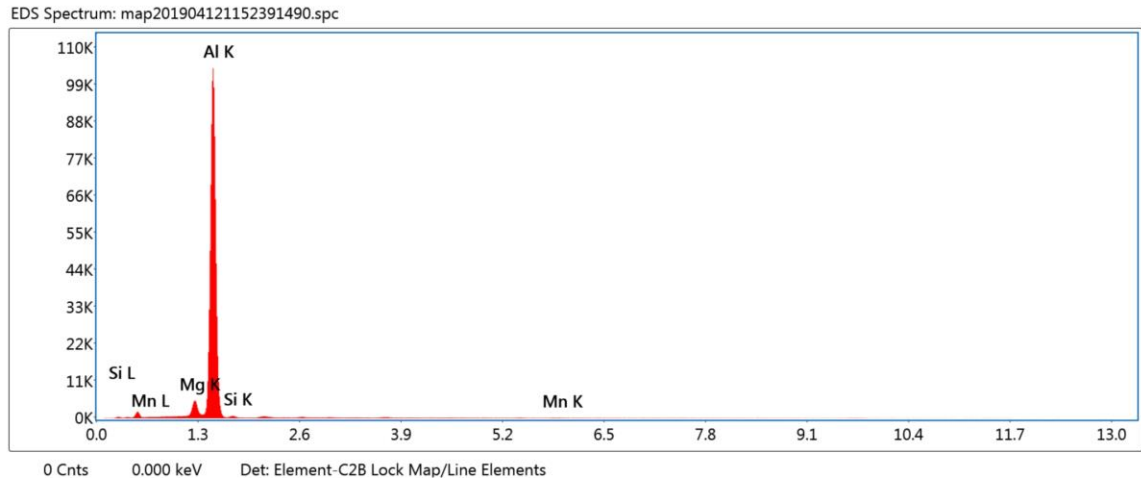
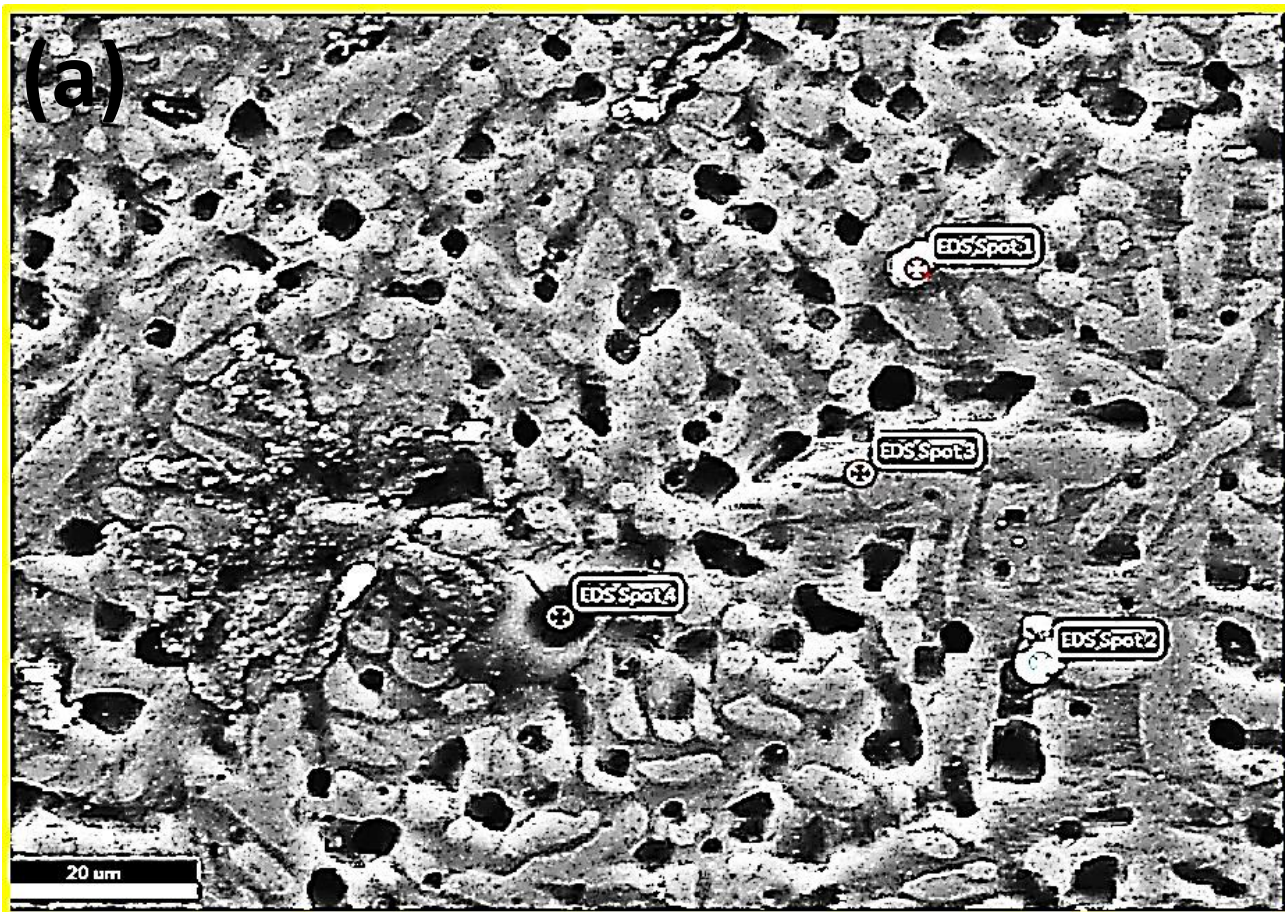


Fig. 4.51 Elemental maps and its EDS spectra of the WMZ center in CMT welded A5754-H111 and A5083-H111 joint using ER5356 filler wire

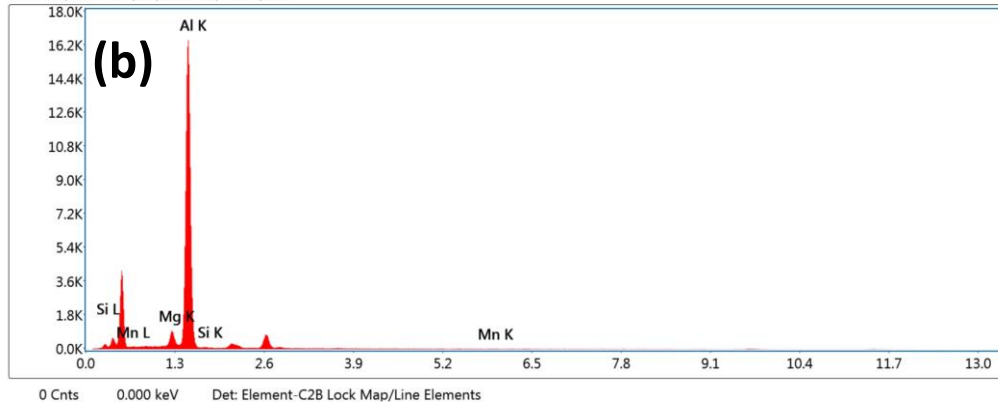
4.4.5 SEM-EDS of WMZ center in CMT welded A5754-H111 and A5083-H111 joint using ER5356 filler wire

Fig. 4.52 shows SEM-EDS spot analysis at the center of the WMZ and the composition of elements is summarized in Table 4.10. The composition confirms that this region contains Al rich matrix and secondary eutectic phases. The secondary eutectic phases are exhibited as spherical and smaller rods in shape that are distributed in the dendrite branches. The spot EDS analysis was made on the white coloured spherical shaped secondary phase particles. The analysis reveals that the phases are Al-Mg intermetallic phases [spots 1 and 2] that also contain some quantities of Si and Mn. These phases are possibly Al_3Mg_2 intermetallic phases. According to Al-Mg phase diagram the maximum solubility of Mg at the eutectic temperature (450°C) is 17.1 wt.%, and the solubility decreases to 1.7 wt.% at the room temperature. Since ER5356 filler contains 5 wt.% Mg, it is expected to contain α -Al (solid

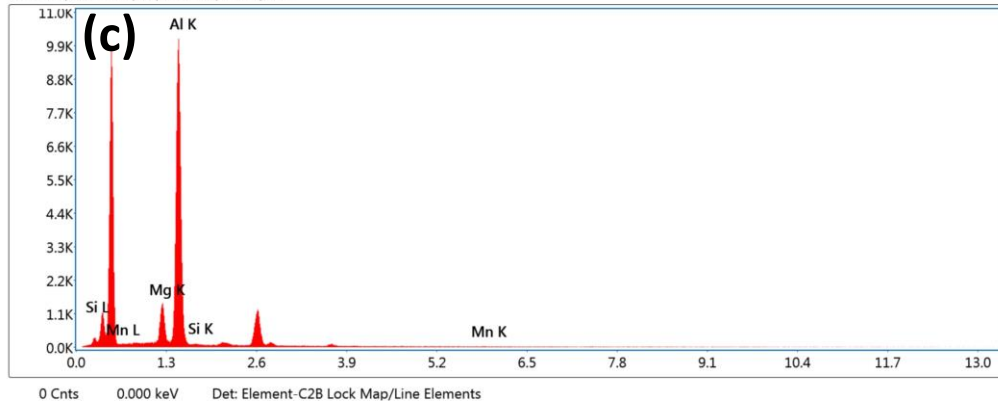
solution of Al and Mg) and β phases (Al_3Mg_2) at room as supported by literature (Mishra 2018). A considerable amount of Mn is detected at spot 4 besides Al and Mg. This could possibly be Al_6Mn phase, as reported by some authors (McShane et al. 1990; Svensson et al. 2000). The dilution effect leads to an increase in the amount of Mn in the WMZ, as a result of which Al_6Mn phase forms at the center of the WMZ. EDS analysis of the eutectic phase (spot 4) exhibits a composition that is nearly equal to the composition of the filler material.



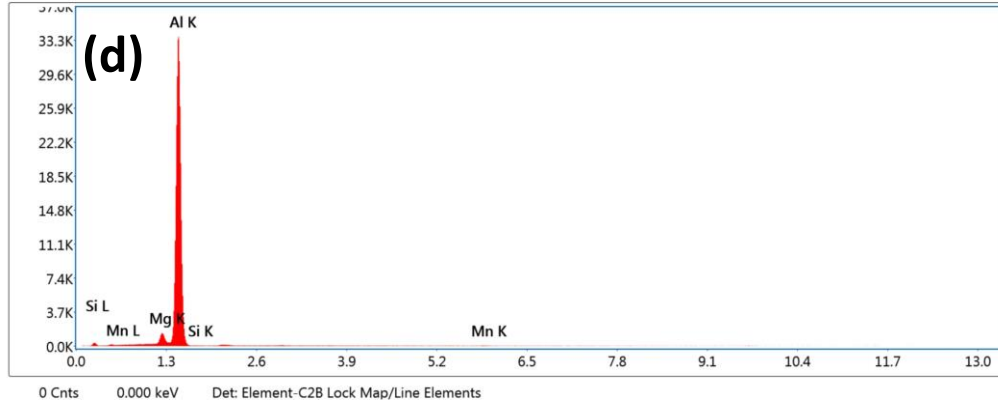
12-4-19 | New Sample | Area 13 | EDS Spot 1



12-4-19 | New Sample | Area 13 | EDS Spot 2



12-4-19 | New Sample | Area 13 | EDS Spot 3



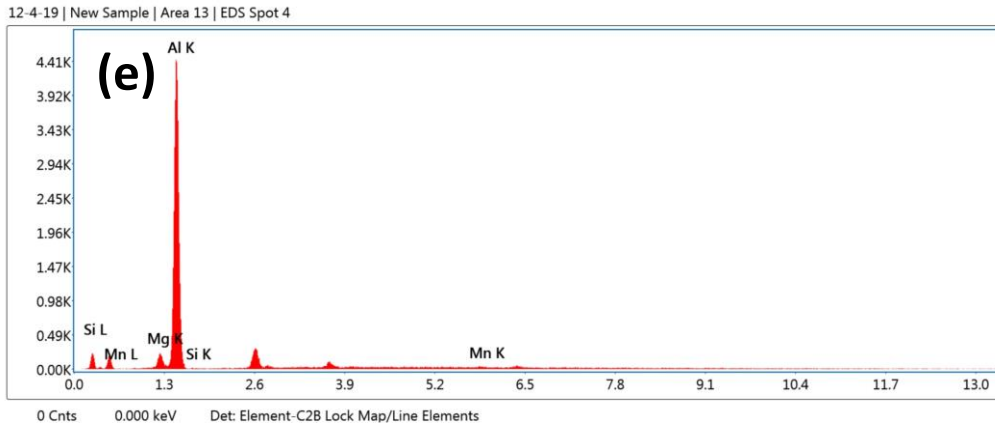


Fig. 4.52(a-e) SEM-EDS spot analysis and its EDS spectra at the center of WMZ in CMT welded A5754-H111 and A5083-H111 joint using ER5356 filler wire

Table 4.10 SEM-EDS spot analysis of different phases in WMZ of the CMT welded A5754-H111 and A5083-H111 joint using ER5356 filler wire

Spots	Al	Mg	Si	Mn	Al	Mg	Si	Mn
	(wt. %)				(at. %)			
Spot 1	Bal.	5.22	0.59	0.62	Bal.	5.78	0.57	0.30
Spot 2	Bal.	10.98	0.87	0.66	Bal.	12.09	0.83	0.32
Spot 3	Bal.	4.18	0.08	0.56	Bal.	4.63	0.08	0.27
Spot 4	Bal.	4.98	0.56	2.76	Bal.	5.57	0.54	1.37

The elemental mapping images at the PMZ of interfaces are shown in Fig. 4.53 and Fig. 4.54. The composition of elements in PMZ is summarized in Table 4.11. It is noticed that compared to PMZ of A5754 interface region, the segregation of Si is less at the PMZ of 5083 interface regions. As the interface of A5083 solidifies faster, the available time for diffusion of solute elements is less. Due to this, the segregation of Si is lower at the A5083 interface than in the other. Moreover, the thermal conductivities of the BMs could also have influenced Si segregation at the interfaces. The amount of Si is similar in the BMs, but due to higher thermal conductivity of A5754 alloy, the diffusion of Si can be faster in this interface than in the other. Consequently, Si segregation is higher at the A5754 interface. The elemental distribution of Mg and Mn is higher at the PMZ of 5083 interface regions compared to the PMZ of A5754 interface [Fig. 4.53 and Fig. 4.54]. The etchant has corroded the secondary phase particles revealing tiny holes in the microstructures of both the alloys. Similar observations have been reported for other 5xxx alloys (Engler et al. 2017). The greater number of secondary phase particles in A5083 alloy can be related to the presence of higher amount of Mg and Mn.

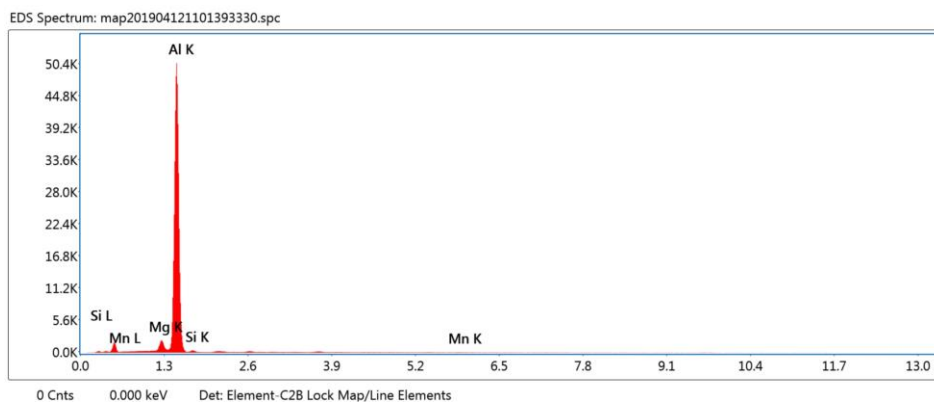
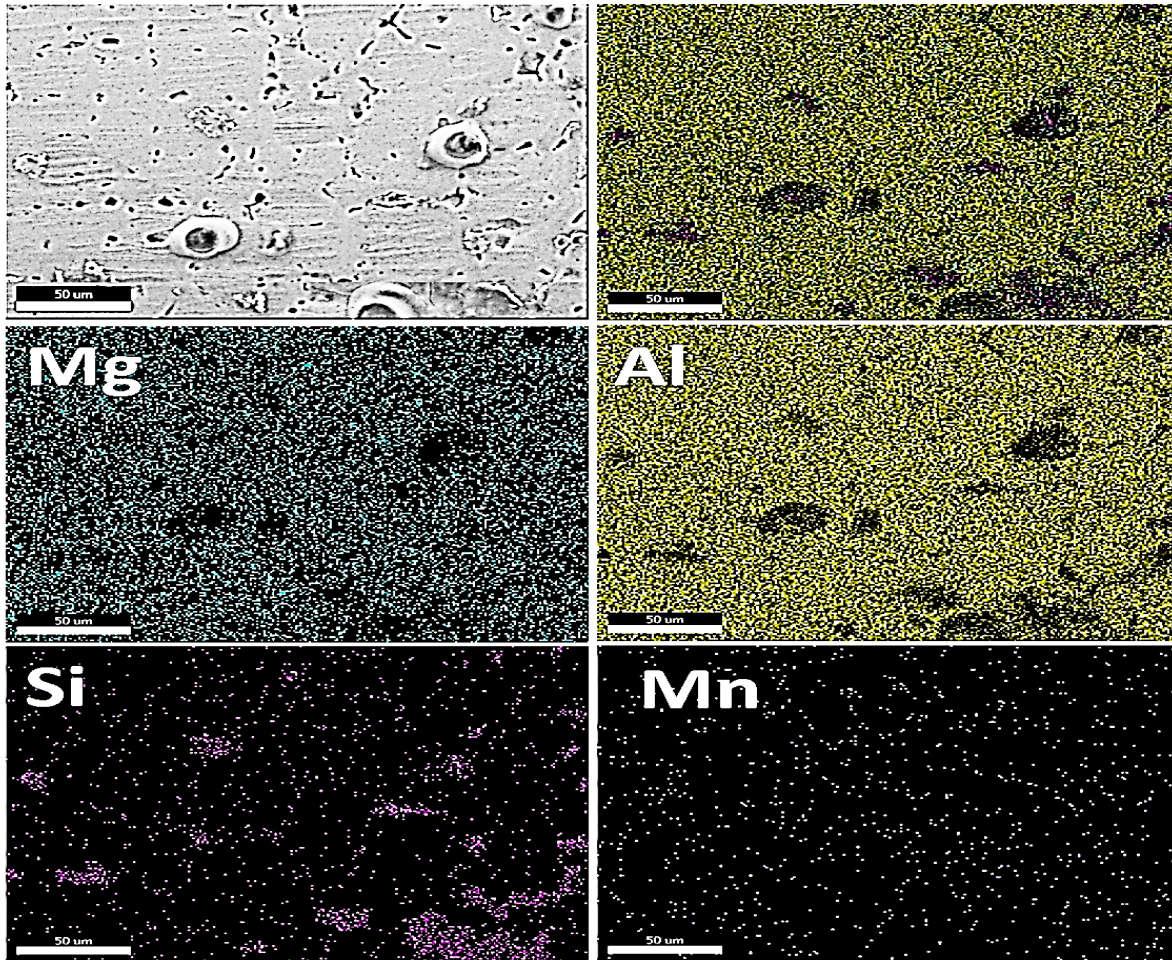


Fig. 4.53 Elemental maps and its EDS spectra at PMZ of 5754 interface in CMT welded A5754-H111 and A5083-H111 joint using ER5356 filler wire

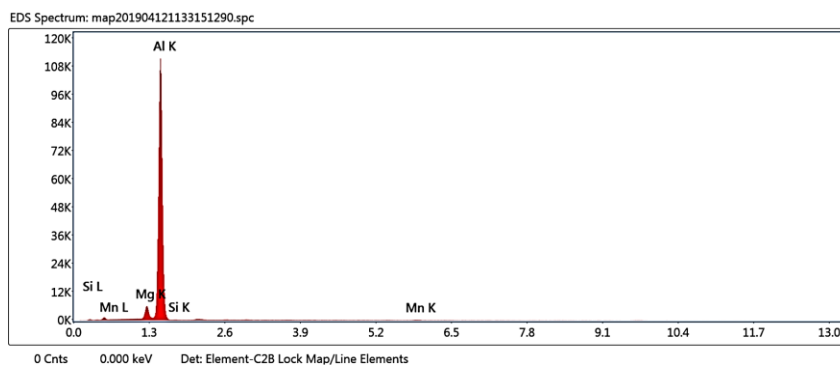
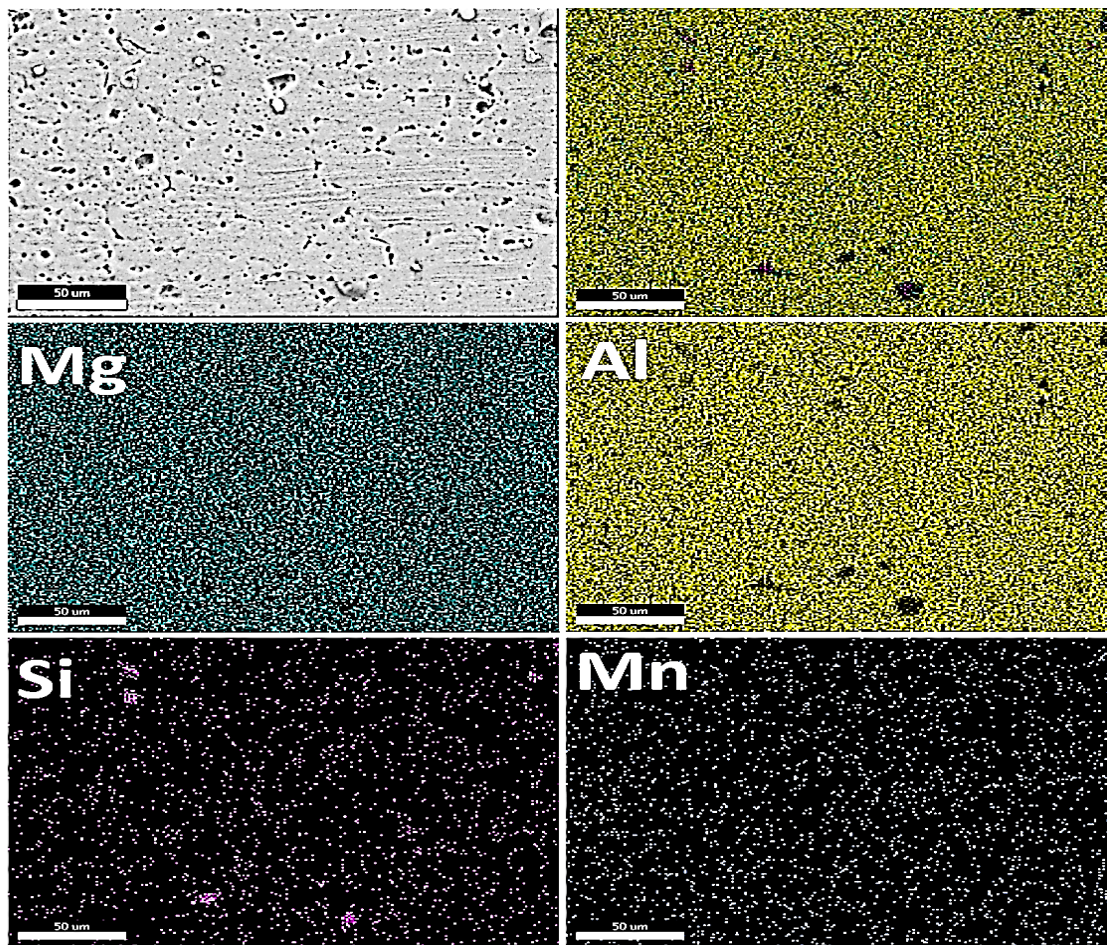


Fig. 4.54 Elemental maps and its EDS spectra at PMZ of 5083 interface in CMT welded A5754-H111 and A5083-H111 joint using ER5356 filler wire

Table 4.11 EDS mapping results of the PMZ of interface regions and WMZ in CMT welded A5754-H111 and A5083-H111 joint using ER5356 filler wire

Interface	Al	Mg	Si	Mn	Al	Mg	Si	Mn
	(wt. %)				(at. %)			
A5754 (PMZ)	Bal.	4.05	1.31	0.50	Bal.	4.48	1.26	0.25
A5083 (PMZ)	Bal.	4.94	0.13	0.68	Bal.	5.47	0.12	0.33
WMZ(Center)	Bal.	4.66	1.09	0.47	Bal.	5.16	1.04	0.23

4.4.6 Microhardness of the CMT welded A5754-H111 and A5083-H111 joint using ER5356 filler wire

Vickers micro hardness distribution of the weld joint is shown in Fig. 4.55. The hardness of the BMs is higher than the respective HAZ and PMZ. The hardness of the BM, HAZ and PMZ on A5083 side is higher than the respective zones in A5754 side. The lower hardness of the HAZ adjacent to the PMZ than the HAZ nearer to the BM on both sides can be attributed mainly to the difference in temperature gradients of the weld thermal cycle. During welding the HAZs experience a temperature which is higher than the recrystallization temperature of the BMs. Due to this, recrystallization and/or grain growth

in these zones lowers the work hardening effect partially in the BMs and, consequently, the hardness decreases. As discussed in the microstructural analysis section, the recrystallized grains and secondary phase particles at the HAZ of A5754 are significantly coarser and lower in amount than on the other side. Consequently, the HAZ of A5754 exhibits lower hardness value than the HAZ of other side.

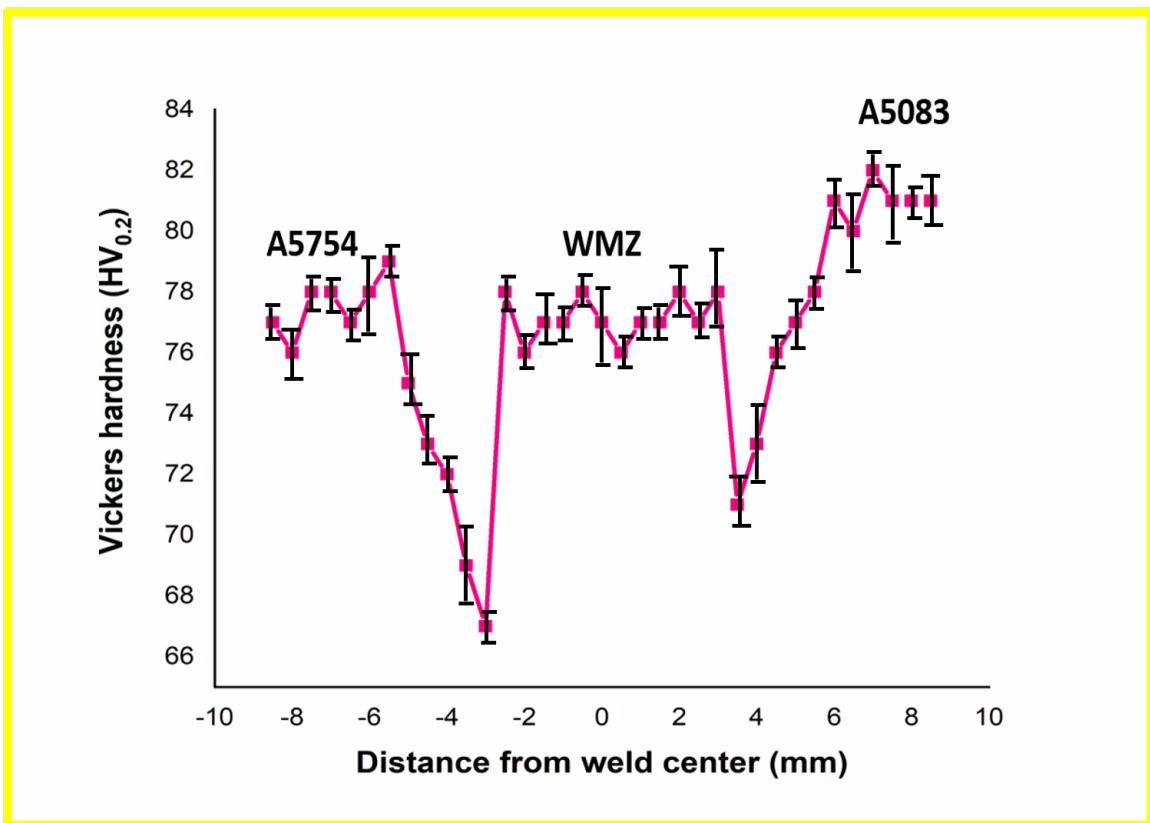


Fig. 4.55 Microhardness profile of the CMT welded A5754-H111 and A5083-H111 joint using ER5356 filler wire

Since there is no variation in Mg distribution at the A5083 interface, the decrease in hardness at PMZ and HAZ cannot be attributed to the Mg content. In contrast, the A5754 interface has shown higher Mg content in the WMZ and lower Mg content at the PMZ and

HAZ. Since Mg is the main strengthening element, the lower hardness of the PMZ and HAZ at the A5754 side is also related to the reduced Mg element in these zones. The EDS spot analysis of two spots reveals Al and Mg in significant quantities and Si and Mn in some quantity [Table 4.10 point 1 and 2]. These phases are Al_3Mg_2 intermetallic phases which gets support from literature (Mishra 2018). According to Al-Mg phase diagram the maximum solubility of Mg at the eutectic temperature (450°C) is 17.1 wt.%, and the solubility decreases to 1.7 wt.% at the room temperature. Since ER5356 filler contains 5 wt.% Mg, it is expected to have α -Al (solid solution of Al and Mg) and β phase (Al_3Mg_2) at room temperature, which gets support from literature (Mishra 2018). EDS spot analysis of another spot reveals that Al and Mn in significant quantities [Table 4.10 point 4]. These phases are Al_6Mn intermetallic phases, which gets support from literature (McShane et al. 1990; Svensson et al. 2000). The presence of Al_3Mg_2 and Al_6Mn secondary phases significantly increases the hardness of WMZ. Moreover, the increased amount of Si in WMZ increases solid solution strengthening effect that increases the hardness of WMZ.

4.4.7 Tensile properties of the CMT welded A5754-H111 and A5083-H111 joint using ER5356 filler wire

Fig. 4.56 shows tensile properties of BMs and different regions of the weld joint. Table 4.12 lists yield strength (YS), ultimate tensile strength (UTS) and % of elongation values. For Al-Mg alloys, an increase in the amount of Mg by 1% leads to an increase of the tensile strength by ~ 34 MPa (Davis and others 1993). Because of the higher Mg content A5083 alloy shows higher strength than A5754 alloy. The A5083 interface region has displayed higher strength than that of A5754 that can be correlated to the presence of a greater amount

of fine secondary phase particles at the HAZ of A5083. The nature and composition of the particles have been discussed earlier in context of EDS analysis.

The WMZ exhibits higher YS than both the BMs, slightly higher UTS than A5754 but lower UTS than A5083. In macro tensile testing, the weld samples have fractured at the interface region of A5754 side, which indicates that the WMZ is stronger. This has been achieved due to the presence of equiaxed dendrite structure as well as minimal loss of Mg alloying element. Mg vaporization in the WMZ has been reported to lower the mechanical properties and increase the hot cracking tendency in the weldment (Cieslak and Fuerschbach 1988). Also, the presence of equiaxed dendrite structure in the WMZ has been reported to have reduced the possibility of solidification cracking tendency resulting in better strength, fatigue life and toughness of the weldment (Cui et al. 2012; Kou 2003).

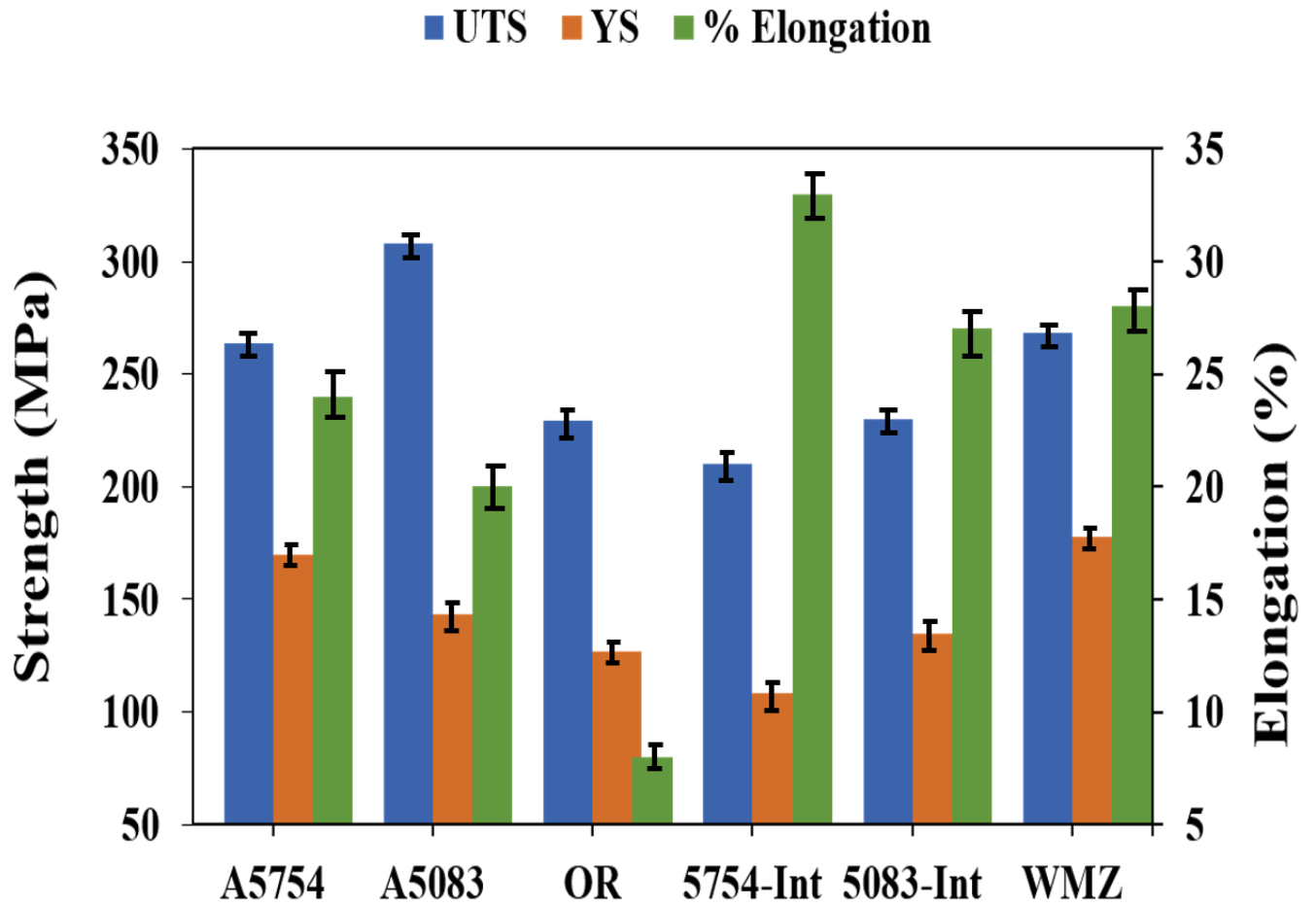


Fig. 4.56 Tensile properties of BMs and weld regions of the CMT welded A5754-H111 and A5083-H111 joint using ER5356 filler wire (OR-over all weld region, Int-Interface and WMZ- weld metal zone; Gauge length of BMs & OR is 25 mm and gauge length of interfaces and WMZ is 5 mm)

Table 4.12 Tensile properties of the CMT welded A5754-H111 and A5083-H111 joint using ER5356 filler wire

Sample	UTS (MPa)	YS (MPa)	Elongation (%)
A5754	264	170	24
A5083	308	143	20
CMT weld joint (OR)	229	127	8
CMT weld joint (WMZ)	268	178	28
CMT weld joint (A5754 int.)	210	108	33
CMT weld joint (A5083 int.)	230	135	27

As discussed earlier, the migration of Mg, Mn and Si from the BM to the WMZ has raised the amount of these elements in the WMZ compensating the loss of secondary phase strengthening as well as solid solution strengthening effects. Micro porosities can be generated in fusion welding of aluminium alloys due to the greater solubility of hydrogen in liquid aluminium and evaporation of alloying elements such as magnesium (Alshaer et al. 2014; Atabaki et al. 2014). Porosities such as hydrogen pores, pores due to loss of alloying elements and shrinkage pores have not been observed in the WMZ. All these are

possible reasons for the increased strength of the WMZ, because of which the fracture has not taken place in this zone in macro tensile testing and a sound weld joint is achieved.

4.4.8 SEM of fracture surface in CMT welded A5754-H111 and A5083-H111 joint using ER5356 filler wire

The fracture surfaces of interface regions and over-all weld region are shown in Fig. 4.57(a-c). Numerous tiny dimples are distributed on the fracture surface indicating the mode of fracture to be ductile. The A5754 interface region exhibits larger dimples than the A5083 interface region, which corroborates with the observations of Shang et al (Shang et al. 2020) that the dimple size is directly related to grain size.

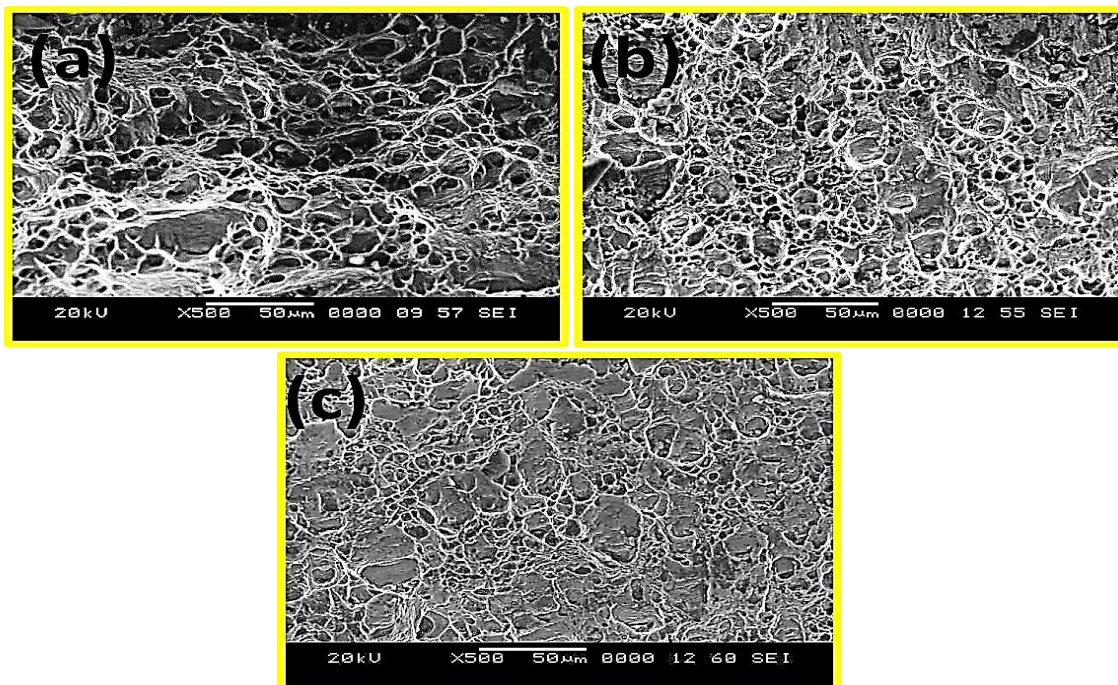


Fig. 4.57 Fracture surface of the interface regions of CMT welded A5754-H111 and A5083-H111 joint using ER5356 filler wire: (a) A5754 side and (b) A5083 side and (c) over-all weld joint

4.5 Tungsten inert gas (TIG) welding of dissimilar A6061-T6 and A6082-T6 using ER4043 filler wire

4.5.1 Surface appearance and macrostructure of the TIG welded A6061-T6 and A6082-T6 joint using ER4043 filler wire

Fig. 4.58 and 4.59 show surface appearance and macrostructures of transverse section of joint, respectively. Both indicate that the weld does not have any defects and full penetration is achieved.

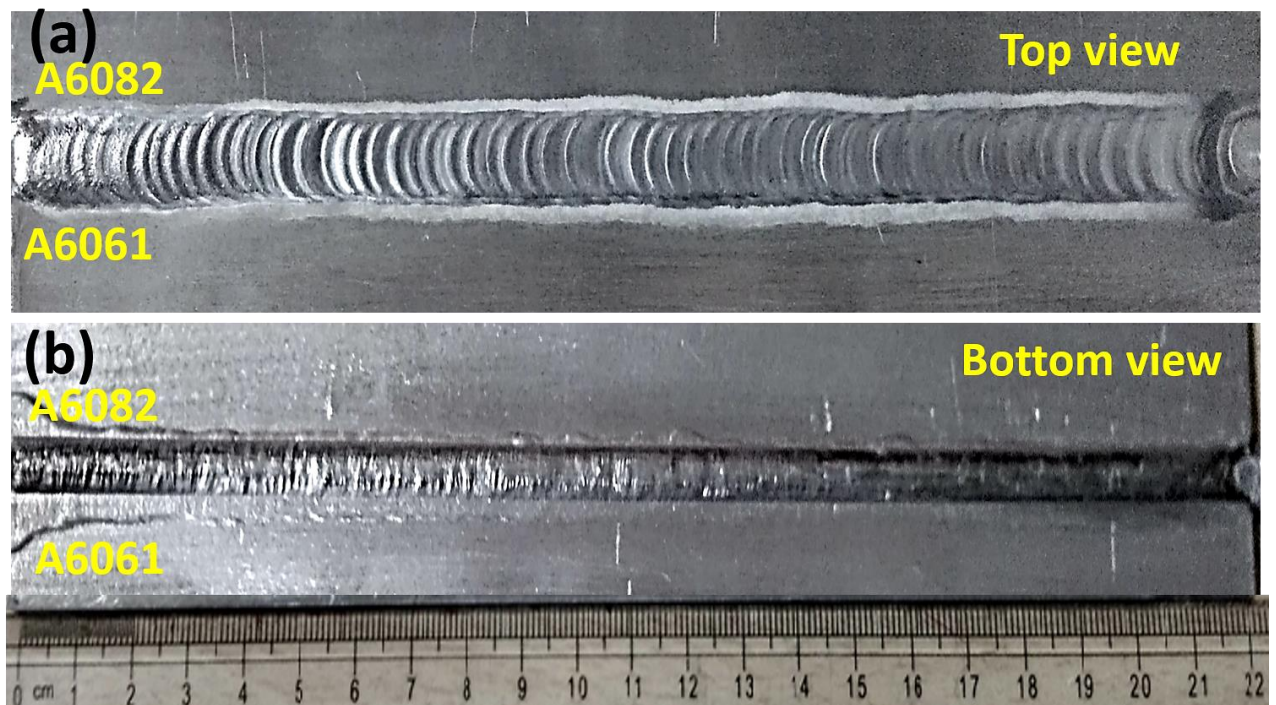


Fig. 4.58 Surface appearance of the TIG welded A6061-T6 and A6082-T6 joint using ER4043: (a) Top view and (b) Bottom view

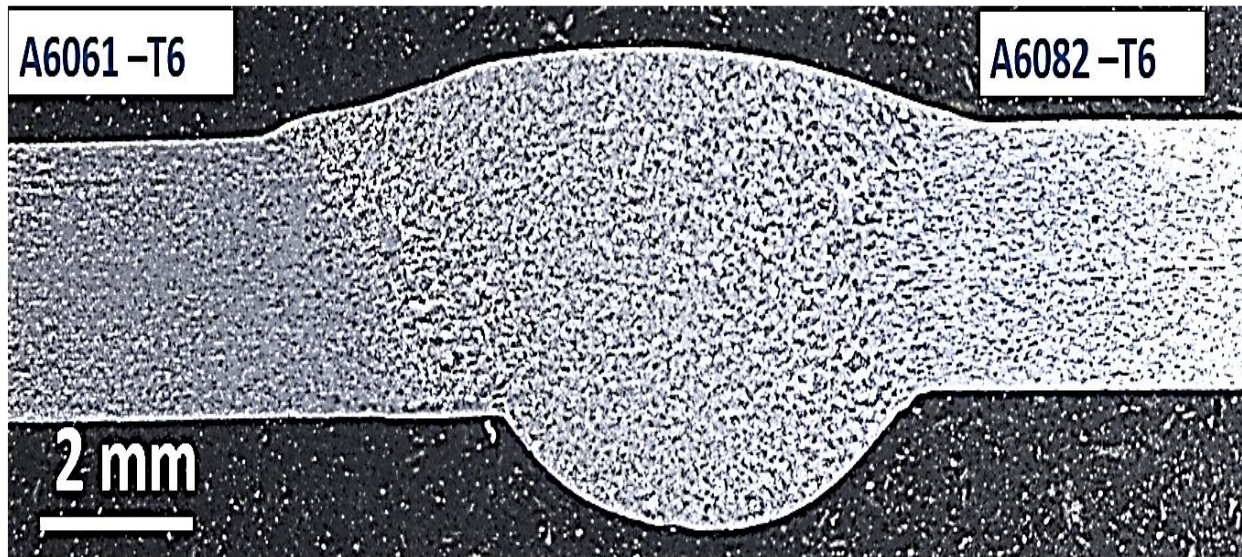


Fig. 4.59 Macrostructure of transverse section of the TIG welded A6061-T6 and A6082-T6 joint using ER4043

4.5.2 SEM microstructure and EDS of WMZ center in TIG welded A6061-T6 and A6082-T6 joint using ER4043 filler wire

Fig. 4.60 shows SEM microstructure of weld joint at WMZ center. The microstructure of WMZ center exhibits equiaxed dendritic feature. This zone shows solid solution of aluminium (α -Al) matrix, seeming dark grey, and Al-Si eutectic phases at the dendrite boundaries appearing light grey. Since ER4043 filler contains 5 wt.% Si, it falls within the hypoeutectic region according to Al-Si phase diagram (Murray and McAlister 1984). During solidification, due to low solubility of Si in Al, a small fraction of Si dissolves with the Al matrix and a solid solution of Al (α -Al) is formed. A large fraction of Si and other minor alloying elements in front of solid liquid interface provides constitutional supercooling that refines the dendrites and forms equiaxed dendrite structure at the center

of WMZ. It is worth mentioning that solidified Al-Si eutectic is distributed as a continuous layer in most of the dendrite boundaries (DBs) at the center of WMZ. The continuous distribution of Al-Si eutectic phases suggests that the DBs of WMZ center are completely wetted by Al-Si eutectic melt phase. Such a GB wetting transition phenomenon is reported in Cu-In and Al-Sn systems (Straumal et al. 1992, 1995). Fig. 4.61 (a-c) shows SEM-EDS spot analysis of WMZ at the center and its composition is listed in Table 4.13. The EDS analysis of secondary phases (spots 2 and 3) shows a considerable amount of Si and Mg elements. This confirms that these phases are Mg_2Si phases. Lakshminarayanan et al. (Lakshminarayanan et al. 2009) have also reported the presence of Mg_2Si phases in WMZ while welding A6061-T6 alloy with ER4043 filler material.

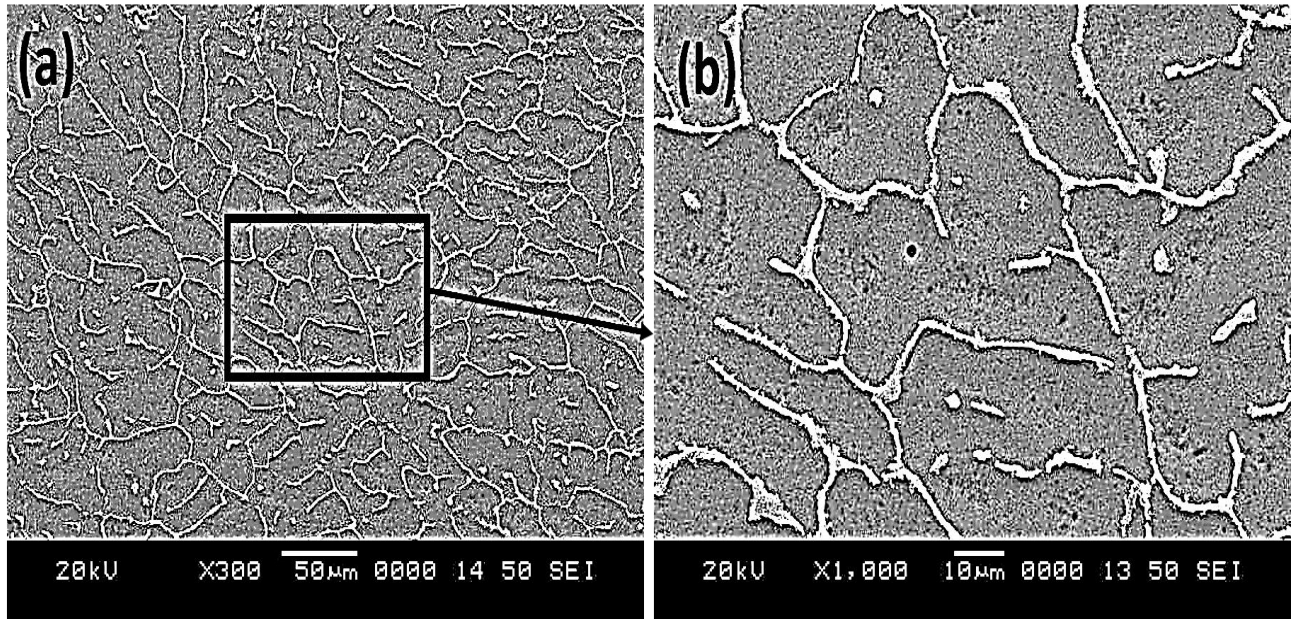
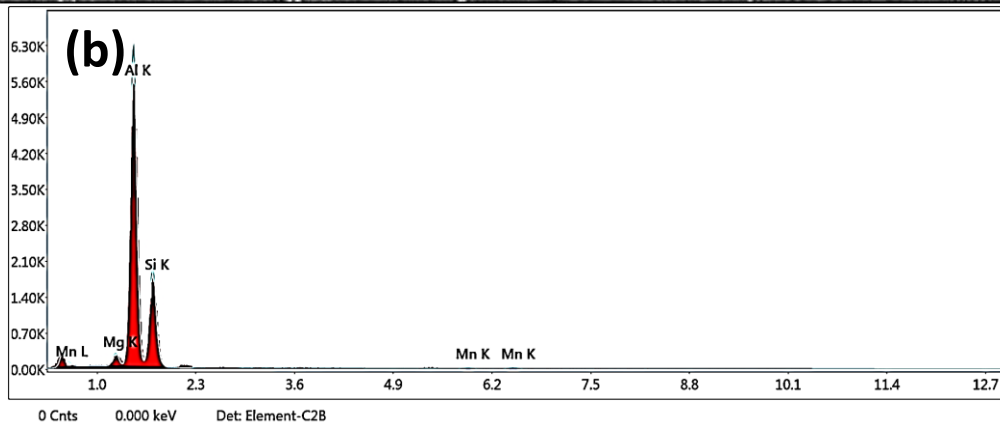
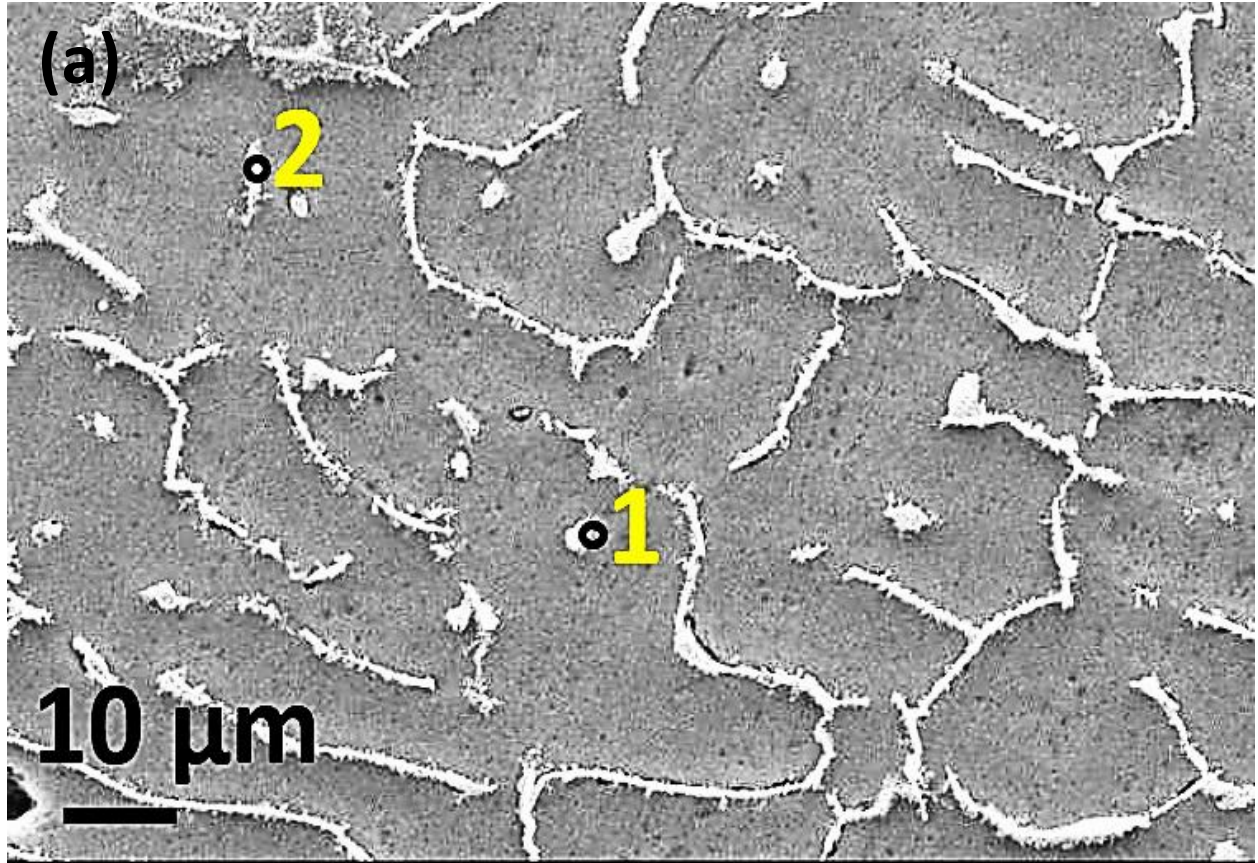


Fig. 4.60 SEM microstructure of WMZ center in TIG welded A6061-T6 and A6082-T6 joint using ER4043: (a) low magnification image and (b) high magnification image



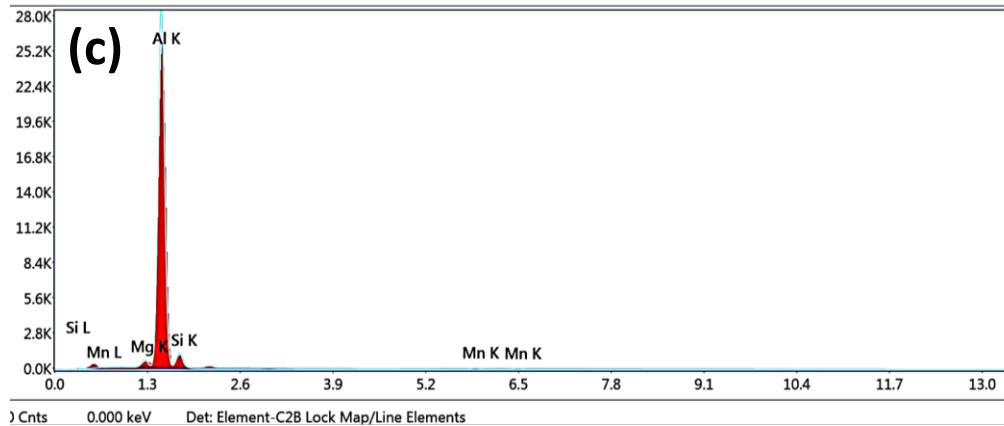


Fig. 4.61 (a) SEM-EDS spot analysis of WMZ center in TIG welded A6061-T6 and A6082-T6 joint using ER4043 (b) EDS spectra of spot 1 and (c) EDS spectra of spot 2

Table 4.13 EDS analysis on precipitates present at WMZ center in TIG welded A6061-T6 and A6082-T6 joint using ER4043

	Al	Mg	Si	Mn		Al	Mg	Si	Mn
	(wt. %)					(at. %)			
Point 1	Bal.	2.3	36.7	0.7		Bal.	2.6	35.8	0.4
Point 2	Bal.	1.9	9.4	0.5		Bal.	2	9	0.3

4.5.3 SEM microstructure of interface regions of the TIG welded A6061-T6 and A6082-T6 joint using ER4043 filler wire

SEM microstructures of A6061 and A6082 dissimilar weld joint interfaces are shown in Fig. 4.62 and Fig. 4.63, respectively. Unlike WMZ center, a varied microstructure is observed near the fusion line of both the interfaces. It can be seen that A6061 interface

consists of CCZ, EQZ, PMZ and HAZ. At the same time, EQZ is completely absent at the A6082 interface. Normally, in the case of fusion weld of Al alloys columnar grains grow from PMZ. In the present research also, similar phenomenon is observed at A6082 interface. However, at A6061 interface columnar grains have grown from EQZ. It has been reported that in Al-Li alloy TIG welds, the amount of Zr and Li influences the formation of EQZ and its width (Lin et al. 2003). Other researchers have also found that the addition of Zr and Ti can decrease the interfacial tension of the solid liquid interface, thereby promoting nucleation of new grains (Yunjia et al. 1989). The BMs do not contain Zr, whereas minor amounts of Ti are present in both the BMs (Table 3.1). The amount of Ti in A6061-T6 is a little higher than in A6082-T6. EQZ zone formation is attributed to the high nucleation rate near the fusion boundary (Reddy et al. 1998). Due to the higher amount of Ti (0.15 wt.%) at A6061-T6, solid liquid interfacial tension can be reduced significantly that provides faster cooling next to the fusion boundary and, correspondingly, the nucleation rate increases. As a result, non-dendritic EQZ is formed at the A6061-T6 interface. At the same time, the amount of Ti (0.1 wt.%) present in A6082-T6 is insufficient to form an EQZ. It is worth mentioning that Al-Si eutectic phases along the GBs of EQZ are distributed as discontinuous fine particles. The presence of EQZ in Al-Li alloys is reported to have induced solidification cracking (Kostrivas and Lippold 2006). However, no such cracking is observed in the EQZ in the present study.

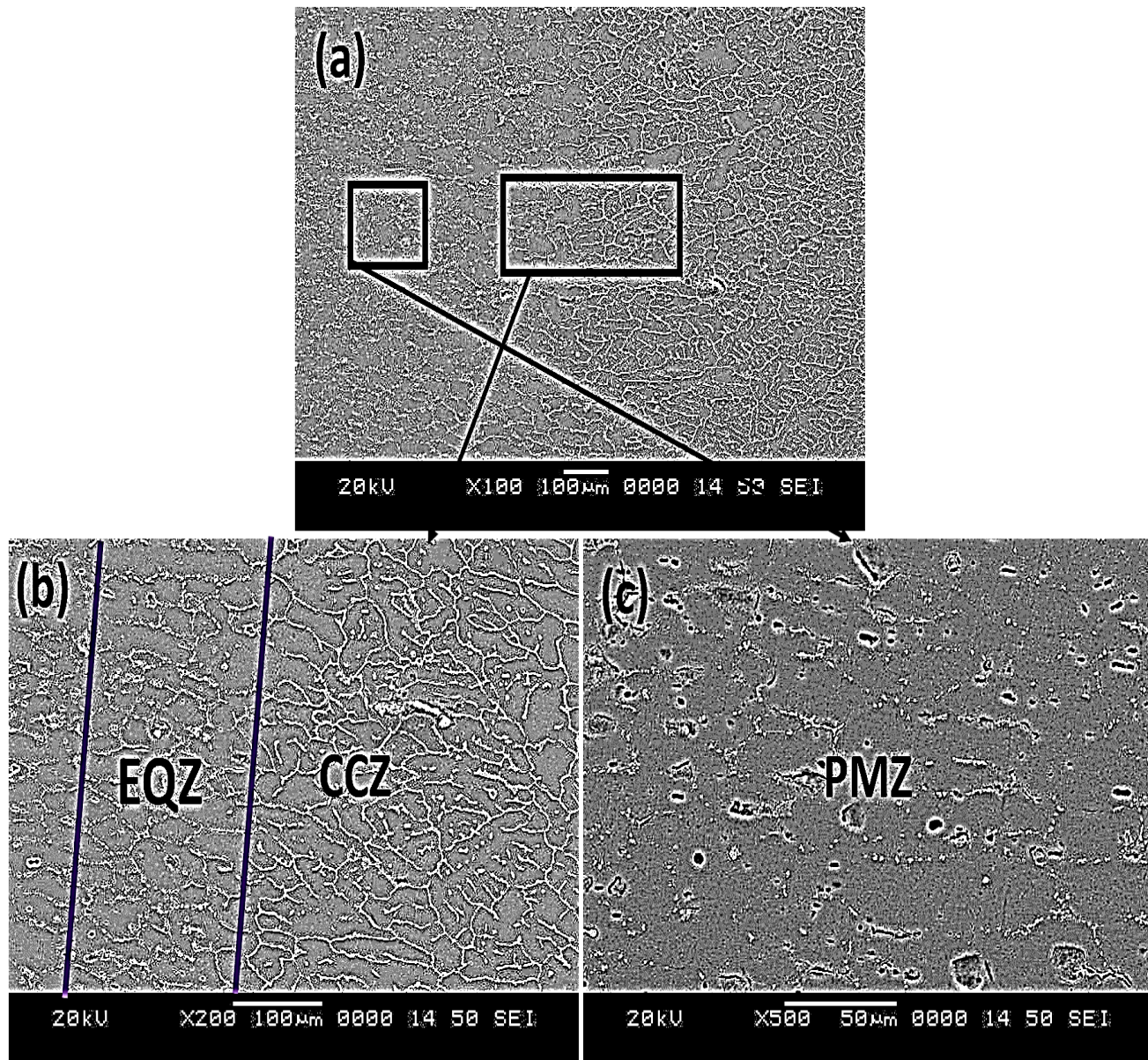


Fig. 4.62. SEM microstructure of TIG welded A6061-T6 and A6082-T6 joint using ER4043: (a) low magnification image of interface region of A6061-T6 (c) high magnification image of interface region of A6061-T6 (d) PMZ of A6061-T6

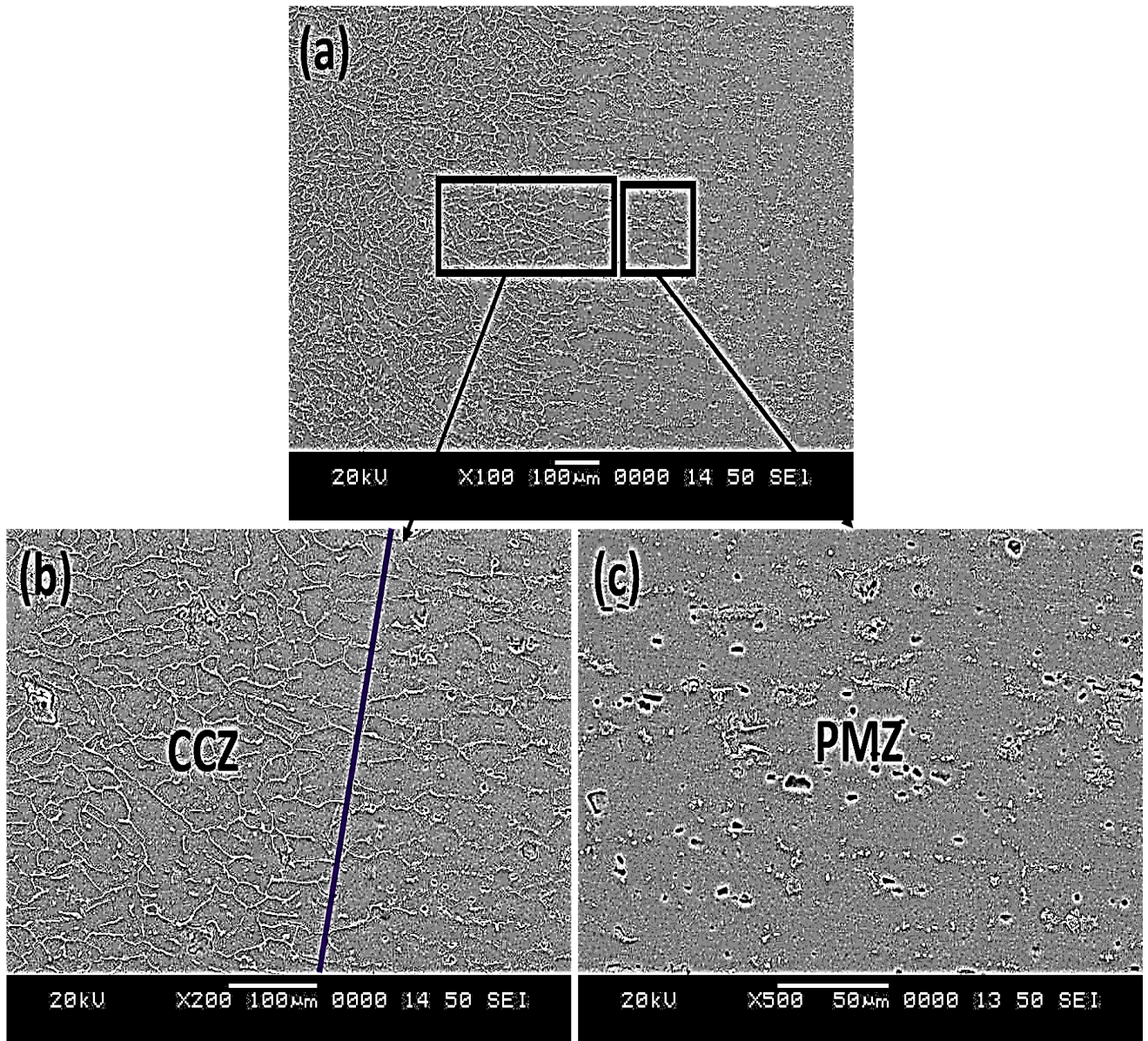


Fig. 4.63. SEM microstructure of TIG welded A6061-T6 and A6082-T6 joint using ER4043: (a) low magnification image of interface region of A6082-T6 (c) high magnification image of interface region of A6082-T6 (d) PMZ of A6082-T6

The microstructures of PMZs of the dissimilar joint interfaces are shown in Fig. 4.62 (c) and Fig. 4.63 (c). Like EQZ, Al-Si eutectic phase particles are present in a discontinuous manner at both the PMZs. Moreover, the Al-Si eutectic phase particles at the PMZ of A6082-T6 are finer than those at the PMZ of A6061-T6. The discontinuous distribution of Al-Si eutectic phase particles suggests that the GBs of EQZ and PMZ are partially wetted by the Al-Si eutectic melt phase. Similar phenomenon of GB wetting by solid secondary phase particles is reported in Al-Mg alloys (Straumal et al. 2010).

4.5.4 SEM-EDS of weld interface in TIG welded A6061-T6 and A6082-T6 joint using ER4043 filler wire

The SEM-EDS mapping images of A6061 and A6082 interfaces of the dissimilar weld joint is shown in Fig. 4.64 and 4.65 respectively. The amount of Si has gradually decreased at both the interfaces from WM to HAZ. The mapping images of A6061 interface clearly show the distribution of Si elements at dendrite boundaries (DBs) of WMZ interface and GBs of EQZ. The amount Si eutectic phases is higher at DBs of WMZ at interface than the GBs of EQZ. Table 4.14 shows percentage (at. % and wt.%) of the elements present in the A6061- T6 and A6082- T6 interface regions.

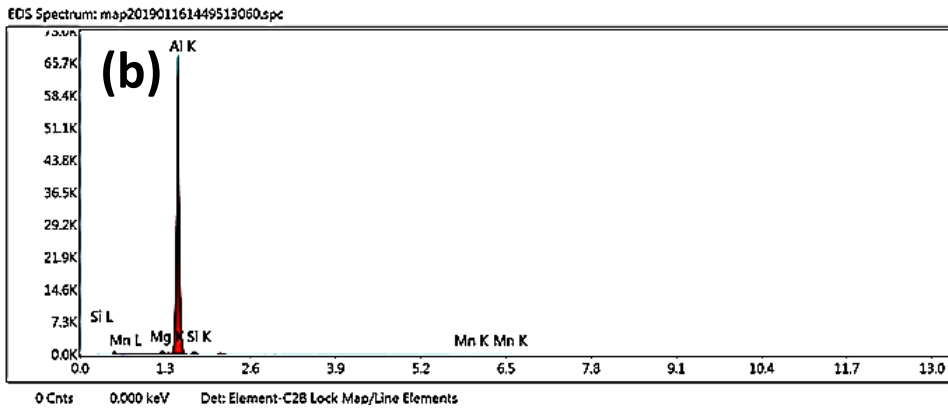
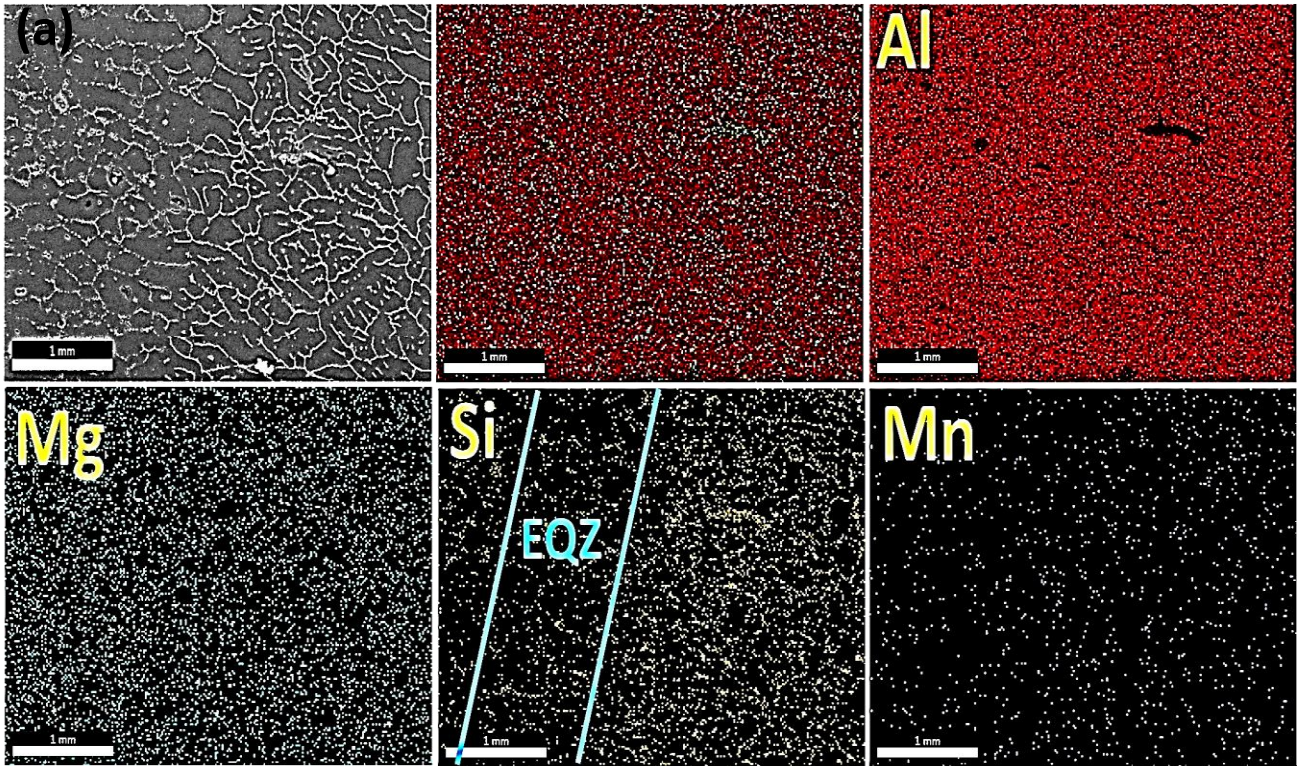


Fig. 4.64 (a-b) SEM-EDS mapping images and its EDS spectra of A6061-T6 interface in TIG welded A6061-T6 and A6082-T6 joint using ER4043

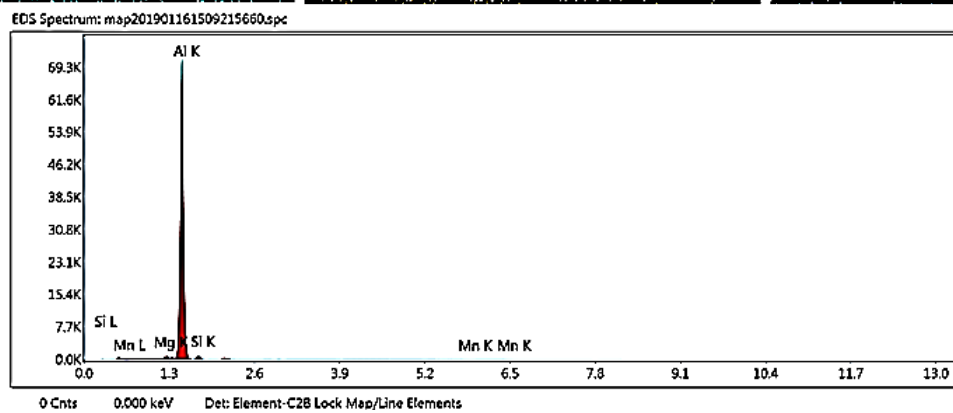
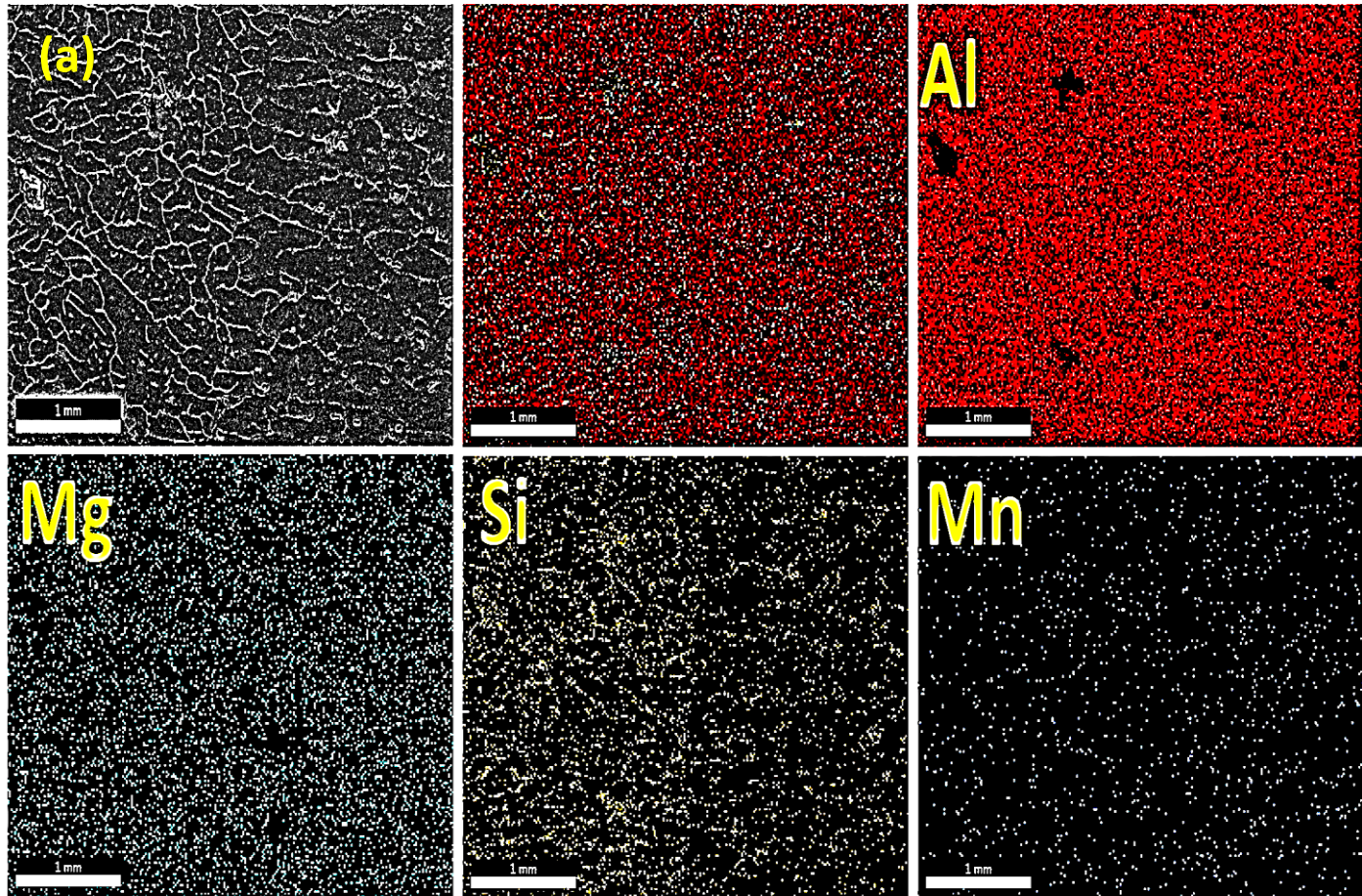


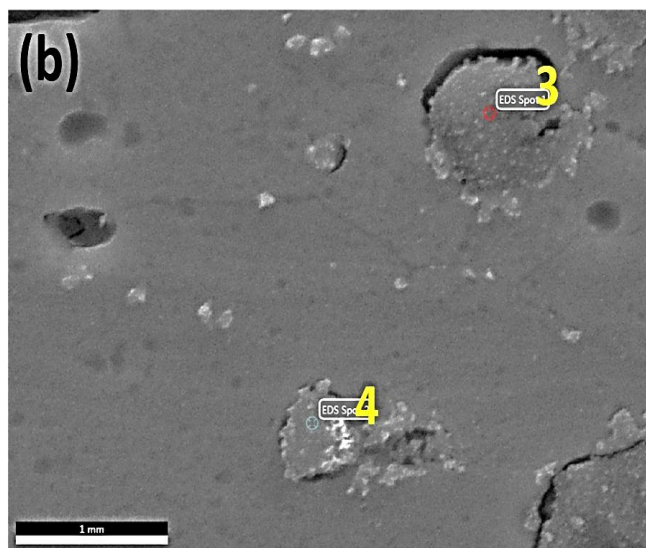
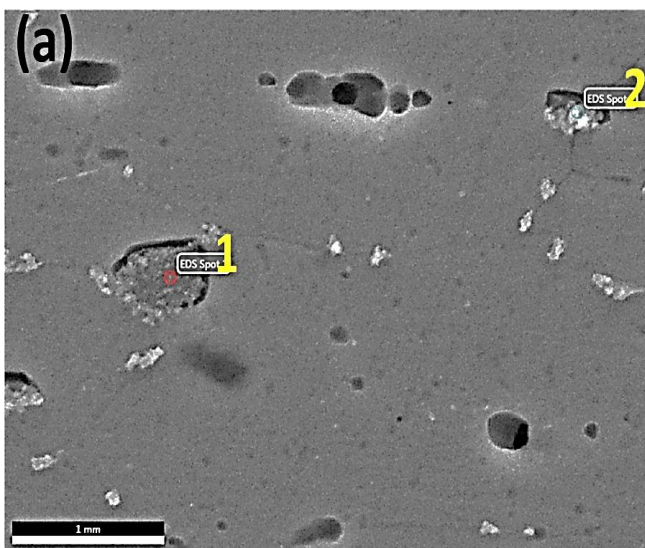
Fig. 4.65 (a-b) SEM-EDS mapping images and its EDS spectra of A6082-T6 interface in TIG welded A6061-T6 and A6082-T6 joint using ER4043

Table 4.14 EDS mapping results of interface regions in TIG welded A6061-T6 and A6082-T6 joint using ER4043

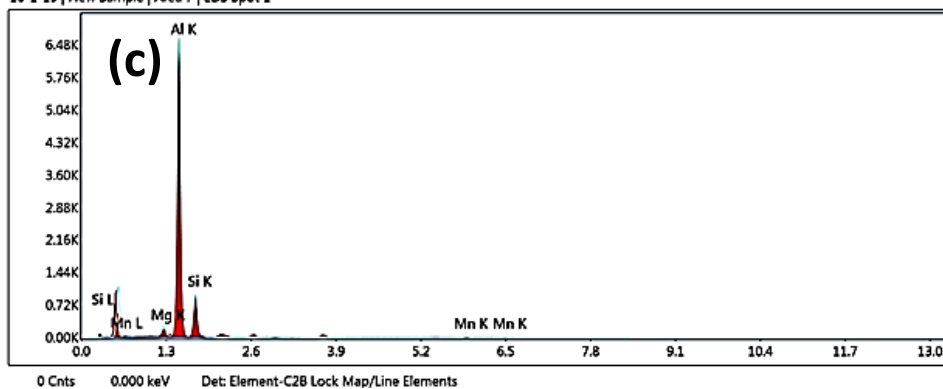
Interface	(wt. %)				(at. %)			
	Al	Mg	Si	Mn	Al	Mg	Si	Mn
A6061-T6	Bal.	1.5	3.2	0.5	Bal.	1.7	3.1	0.2
A6082-T6	Bal.	1.5	3.4	0.7	Bal.	1.7	3.3	0.3

4.5.5 SEM-EDS analysis of PMZ and HAZ precipitates in TIG welded A6061-T6 and A6082-T6 joint using ER4043 filler wire

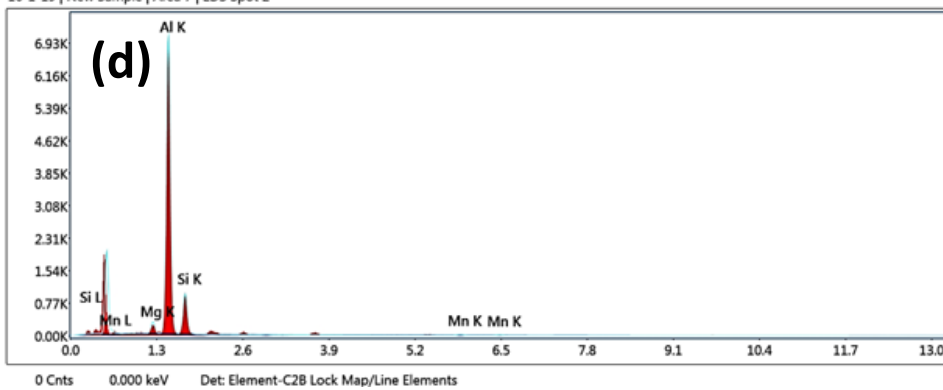
Fig. 4.66 and 4.67 show EDS results of the precipitates at PMZs and HAZs of the interfaces. The chemical compositions of precipitates present at PMZ and HAZ of interfaces are summarized in Tables 4.15 and 4.16. The precipitates at PMZs, HAZs of both the alloys mainly contain Si in a significant quantity. It is worth noting that the quantity of Si in the precipitates at HAZs of both the alloys is nearly double the Si present in the precipitates at PMZs of both the alloys.



16-1-19 | New Sample | Area 7 | EDS Spot 1



16-1-19 | New Sample | Area 7 | EDS Spot 2



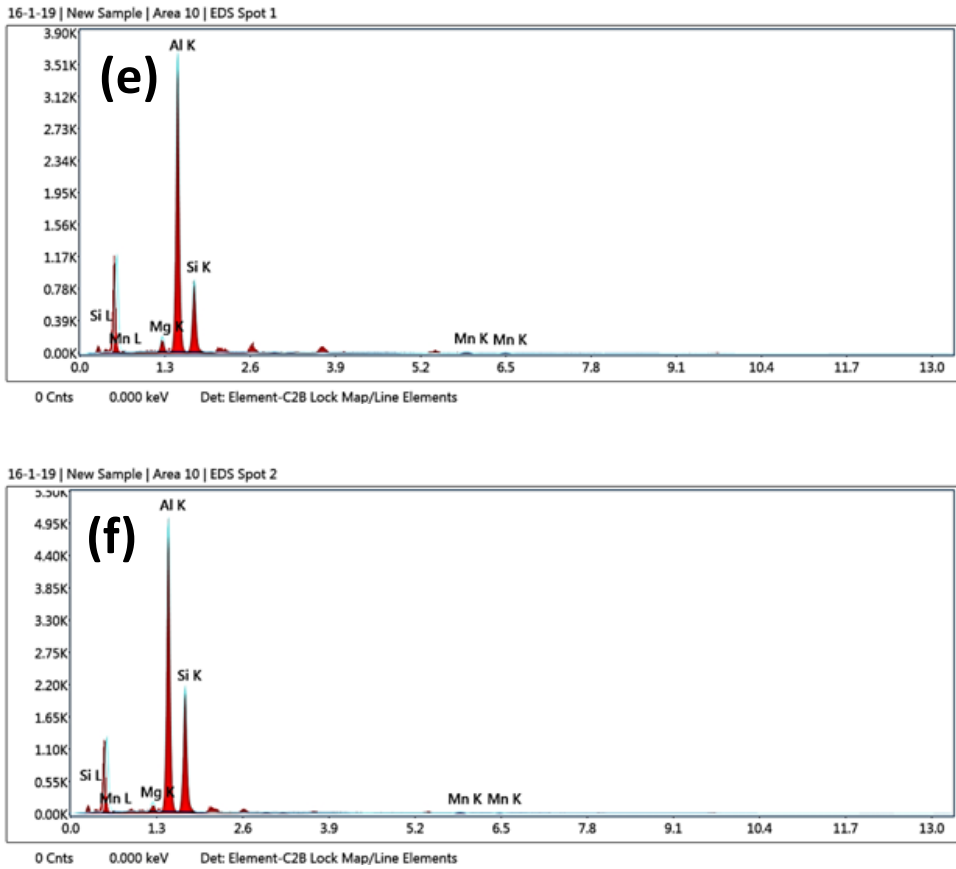
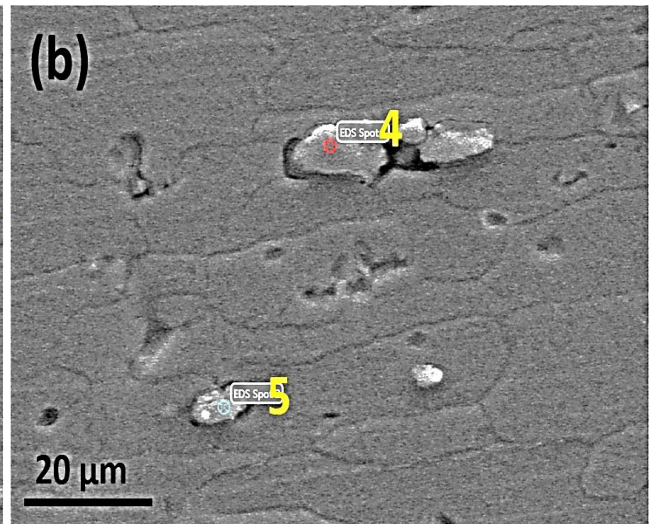
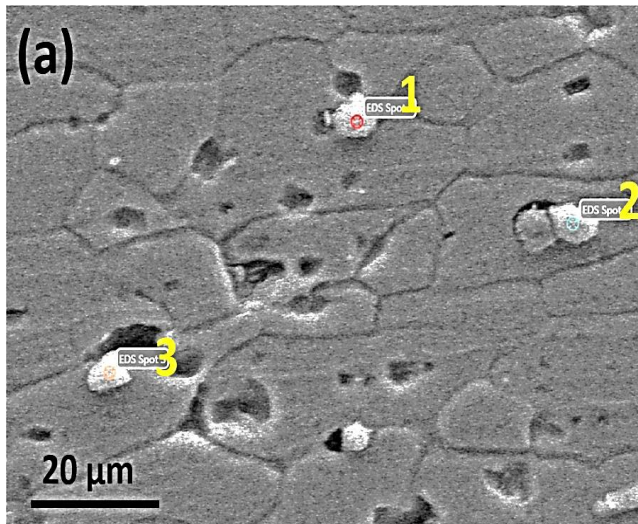


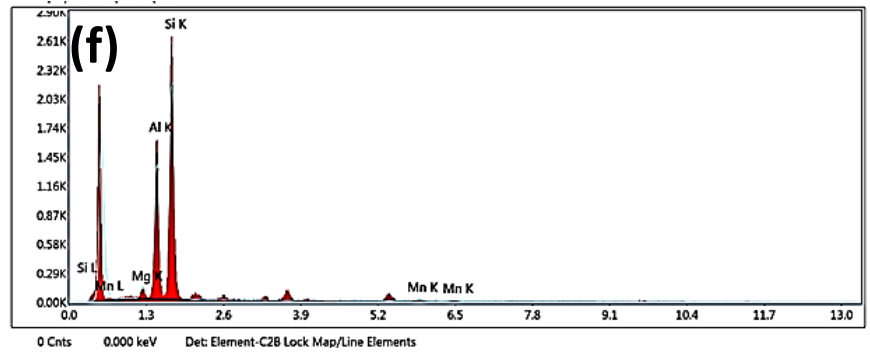
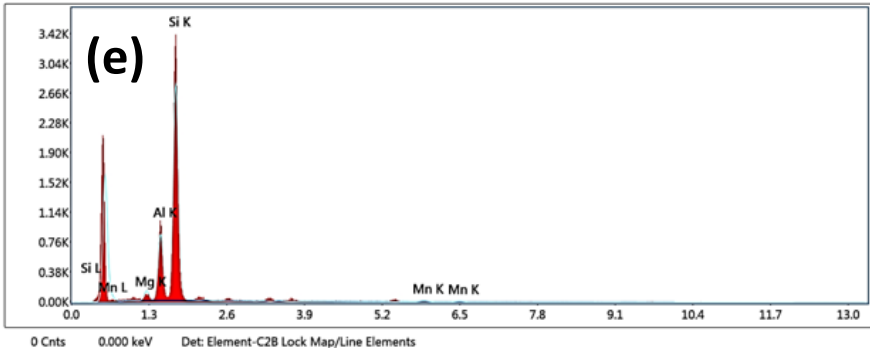
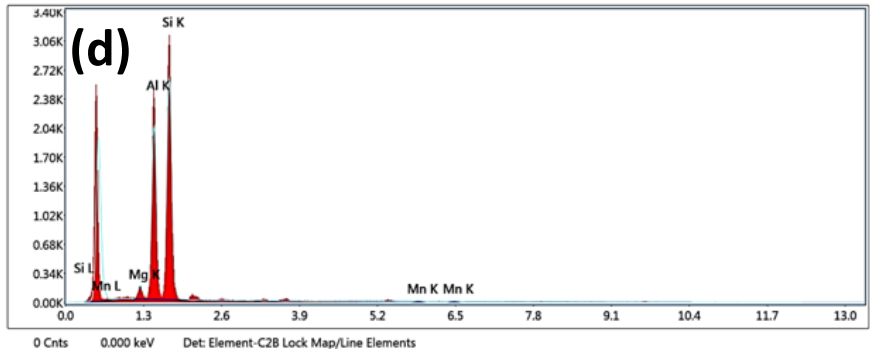
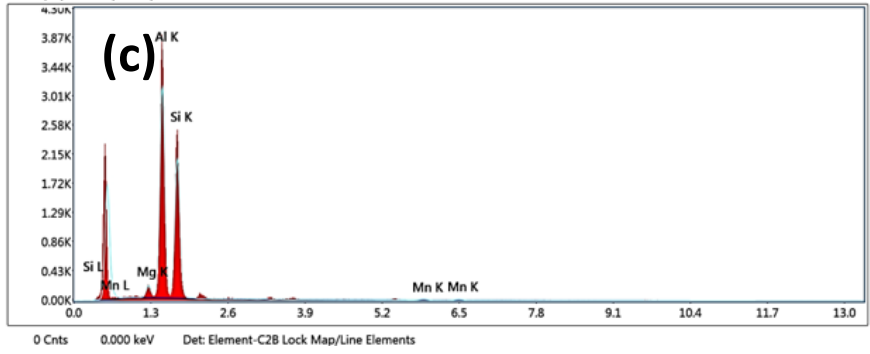
Fig. 4.66 SEM-EDS analysis of precipitates present at PMZ of interface in TIG welded A6061-T6 and A6082-T6 joint using ER4043 (a) A6061-T6 and (b) A6082-T6 (c-d) EDS spectra for precipitates present at PMZ of A6061-T6 (e-f)) EDS spectra for precipitates present at PMZ of A6082-T6

Table 4.15 EDS analysis of precipitates present at PMZ of interfaces in TIG welded A6061-T6 and A6082-T6 joint using ER4043

	Al	Mg	Si	Mn		Al	Mg	Si	Mn
	(wt. %)					(at. %)			
Point 1	Bal.	2.4	24	0.8		Bal.	2.7	23.3	0.4
Point 2	Bal.	2.7	23.4	1		Bal.	3	22.7	0.5
Point 3	Bal.	3	32	1.7		Bal.	3.4	31.3	0.8
Point 4	Bal.	1.6	43.9	1.1		Bal.	1.8	43	0.6



27-12 | 5 | Area 16 | EDS Spot 1



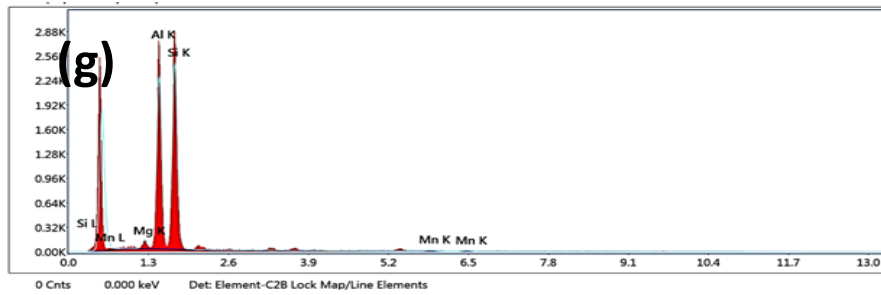


Fig. 4.67 SEM-EDS analysis of precipitates present at HAZ of interfaces in TIG welded A6061-T6 and A6082-T6 joint using ER4043 (a) HAZ of A6061-T6 and (b) HAZ of A6082-T6; (c-e) EDS spectra for precipitates present at HAZ of A6061-T6; (f-g) EDS spectra for precipitates present at HAZ of A6082-T6

Table 4.16 EDS analysis of precipitates present at HAZ of interfaces in TIG welded A6061-T6 and A6082-T6 joint using ER4043

	Al	Mg	Si	Mn	Al	Mg	Si	Mn
	(wt. %)				(at. %)			
Point 1	Bal.	2.5	50	1	Bal.	2.9	49.5	0.5
Point 2	Bal.	2.5	62.5	1	Bal.	2.9	61.7	0.5
Point 3	Bal.	1.9	60	1.1	Bal.	2.1	59.2	0.5
Point 4	Bal.	2.7	76.5	1.6	Bal.	3	76.1	0.8
Point 5	Bal.	2.6	65.7	1.8	Bal.	3	65.2	0.9

4.5.6 Microhardness of the TIG welded A6061-T6 and A6082-T6 joint using ER4043 filler wire

Fig. 4.68 shows Vickers micro hardness profiles of the weld joint. Since both the alloys are precipitation hardened alloys, phenomena such as coarsening and over ageing of precipitates occur in HAZ during welding due to weld thermal cycle. This can lead to reduce the hardness of HAZs at the respective interface. The WMZ exhibits maximum hardness among all the zones. The Mg and Si contents are 1.1 wt.% and 0.7 wt%, respectively, in A6061 base and 0.8 wt.% and 1.1 wt%, respectively, in A6082 base metal . Due to this, the amount of Mg and Si migrated from the BM to the center of the WMZ can be increased due to dilution effect. As discussed earlier, according to Al-Si binary phase diagram, a fraction of Si dissolves in the Al matrix and forms a solid solution of Al (α -Al) during solidification. Moreover, Al-Si eutectic along the equiaxed dendrites is observed in WMZ due to the addition of ER4043 filler. Additionally, Mg_2Si phases are observed in WMZ center. Thus, improved hardness in WMZ is attributed to the solid solution strengthening effects provided by Mg and Si and secondary phase particles strengthening provided by Mg_2Si , eutectic Al-Si along the equiaxed dendrites.

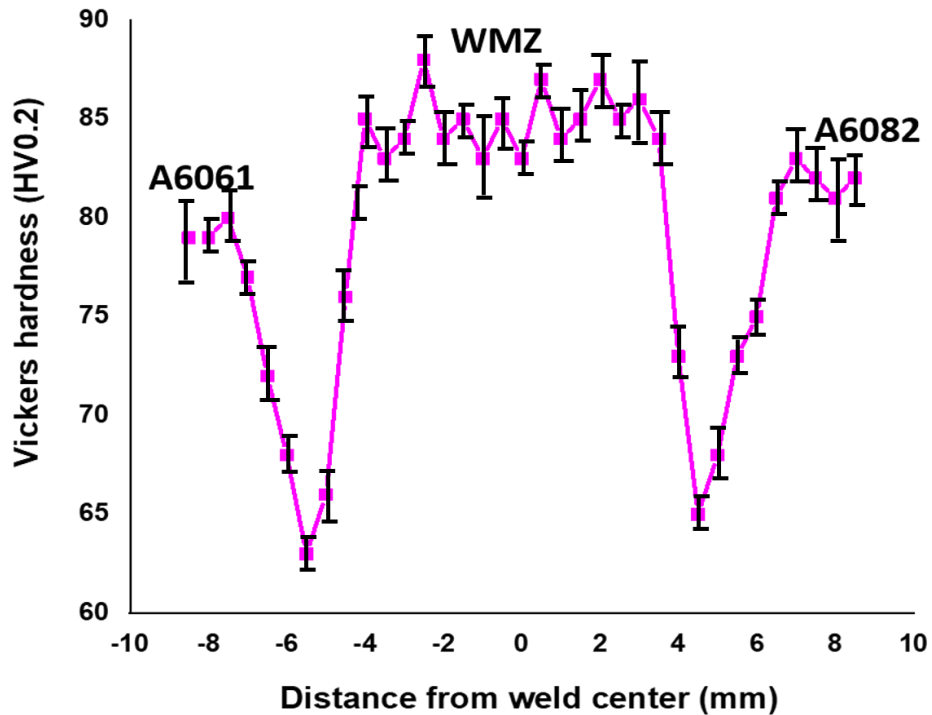


Fig. 4.68 Vickers microhardness profile of the TIG welded A6061-T6 and A6082-T6 joint using ER4043

4.5.7 Tensile properties of the TIG welded A6061-T6 and A6082-T6 joint using ER4043 filler wire

Fig. 4.69 shows tensile properties of the BMs and weld regions. Tensile properties of BMs, TIG weld joint (over all region), TIG weld joint (WMZ at center), TIG weld joint (6061-T6 interface region) and TIG weld joint (6082-T6 interface region) are listed in Table 4.17. It can be observed that 6082-T6 region shows higher strength than the 6061-T6 interface region. It is reported that severe segregation of elements at GBs of EQZ and continuous network of eutectic phases along GBs of EQZ have a detrimental effect on mechanical

properties of the weld joint (Dev et al. 2008). The present study does not show severe segregation at GBs of EQZ. Moreover, the eutectic phase along GBs of EQZ is also distributed in a discontinuous manner. Because of the above mentioned features, it is expected that the mechanical properties of the interfaces would not vary much. In contrast, significant reduction in strength has been noticed at the A6061-T6 interface compared to the A6082-T6 interface. The distribution of finer Al-Si eutectic phase particles at PMZ and the presence of finer dendrites of CCZ at 6082-T6 interface could be the possible reasons for the improvement in its mechanical properties. The finer dendrites in CCZ makes the material more tough, hence during solidification of the WM the shrinkage strain can be accommodated by the material. Thus, the weld tensile residual stresses can be reduced significantly in the 6082-T6 interface than in the 6061-T6 interface. The absence of EQZ can also be a reason for the improved strength of 6082-T6 interface. The WMZ does not show any porosities or solidification cracks in its microstructure. In WMZ, solid solution strengthening effect is provided by Si and secondary phase particles strengthening provided by Mg_2Si phases. Due to the above-mentioned reasons the strength of WMZ is increased in a significant manner.

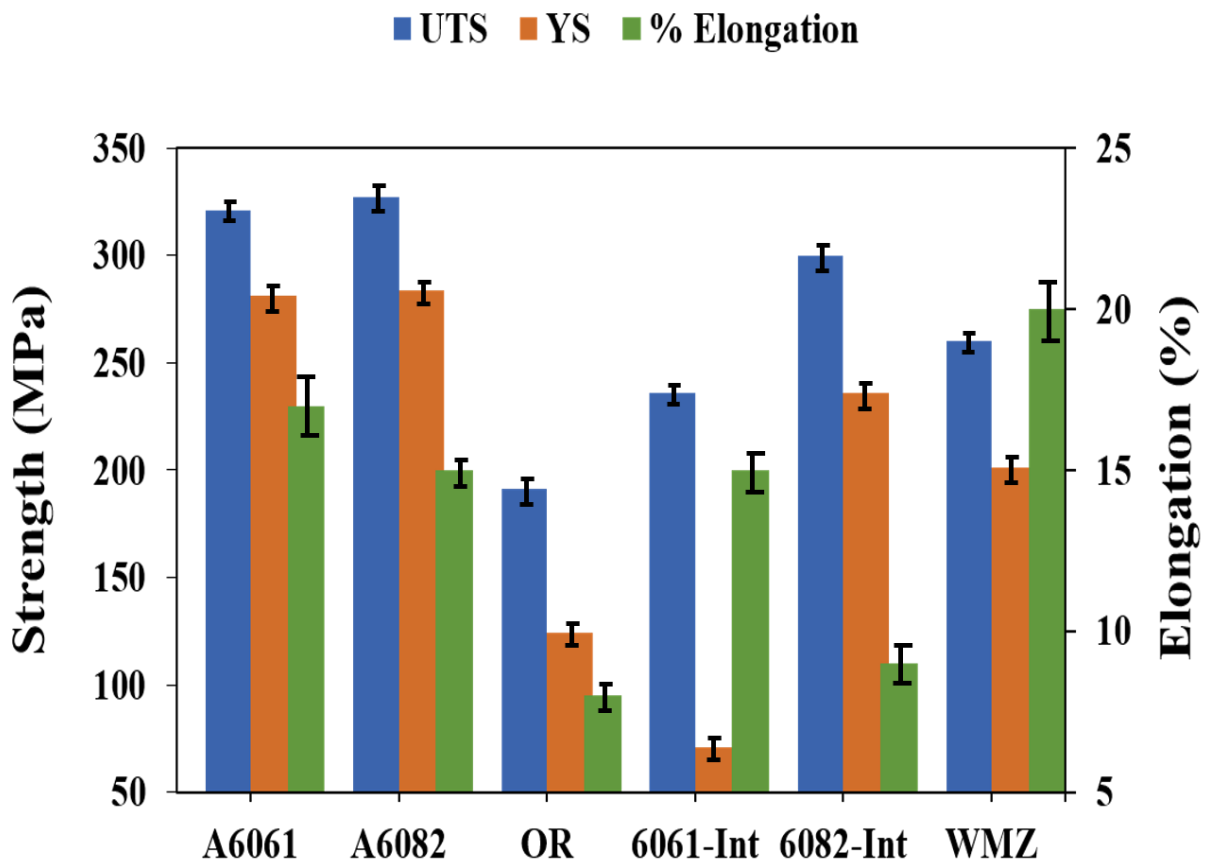


Fig. 4.69 Tensile properties of the BMs and different regions of TIG welded A6061-T6 and A6082-T6 joint using ER4043 (OR-over all weld region, Int-Interface and WMZ- weld metal zone; Gauge length of BMs & OR is 25 mm and gauge length of interfaces and WMZ is 5 mm)

Table 4.17 Tensile properties of the BMs and different regions of TIG welded A6061-T6 and A6082-T6 joint using ER4043

Sample	UTS (MPa)	YS (MPa)	Elongation (%)
A6061	321	281	17
A6082	327	284	15
TIG weld joint (OR)	191	124	8
TIG weld joint (6061-T6 int.)	236	71	15
TIG weld joint (6082-T6 int.)	300	236	9
TIG (WMZ)	260	201	20

4.5.8 Fractography analysis of TIG welded A6061-T6 and A6082-T6 joint using ER4043 filler wire

Fig 4.70(a-f) represents SEM images of fractured surfaces of the A6061, A6082 interface regions and over-all weld regions of the joints. It can be seen that presence of dimples is predominant on the fracture surface of all the three regions. This indicates the mode of failure to be ductile.

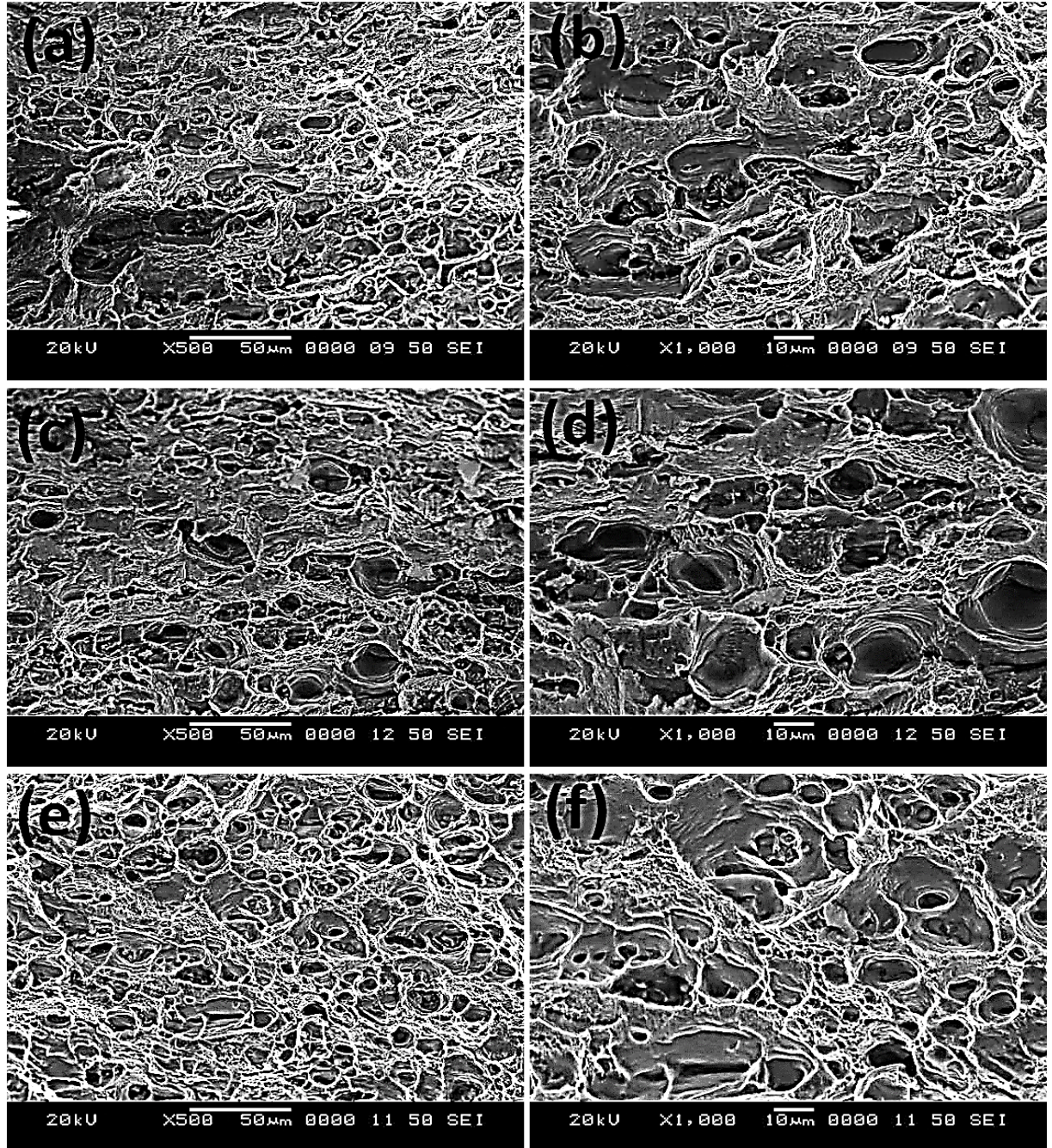


Fig. 4.70 SEM images of fracture surface of the different regions of TIG welded A6061-T6 and A6082-T6 joint using ER4043: (a-b) A6061 interface region; (c-d) A6082 interface region and (e-f) over-all weld joint

4.6 Tungsten inert gas (TIG) welding of dissimilar A6061-T6 and A6082-T6 using ER5356 filler wire

4.6.1 Surface appearance of TIG welded A6061-T6 and A6082-T6 joint using ER5356 filler wire

Fig. 4.71(a-b) shows the surface appearance of TIG welded A6061-T6 and A6082-T6 dissimilar joint produced using ER5356 filler wire. Visual examination confirms that there are no defects on the surface. The joint does not exhibit cracks and spatter in the weldment. The ripples are consistent and uniform. The back side of the dissimilar joint does not show any lack of fusion, and full penetration is achieved with the used parameters. The joint shows white color oxide regions nearer to the weld toes. These have been identified to be Al_2O_3 (white color) (Guojin et al. 2018).

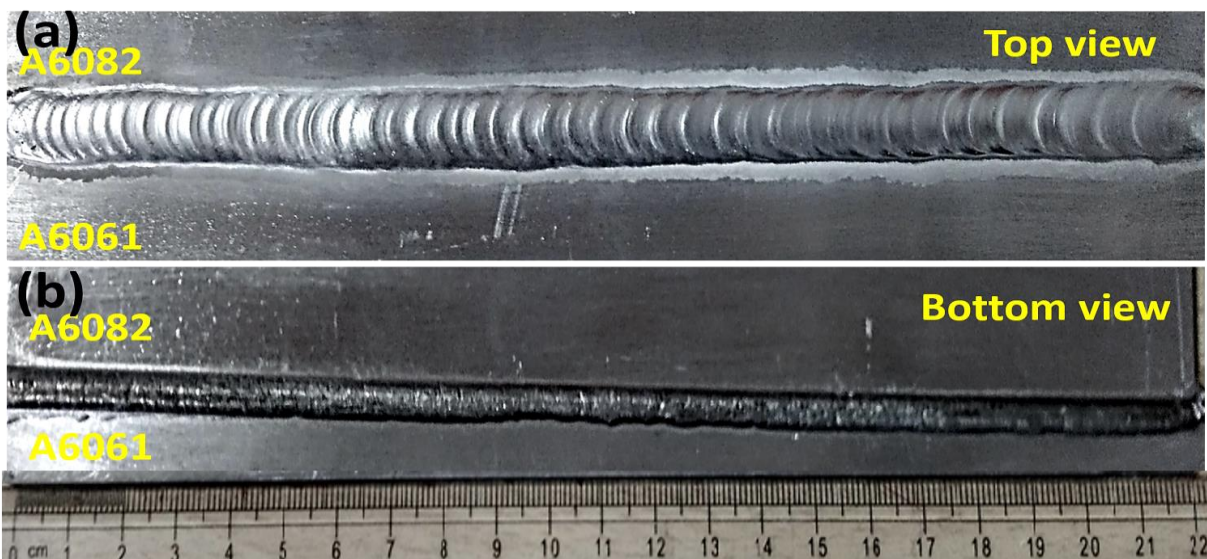


Fig. 4.71 Surface appearance of the TIG welded A6061 and A6082 joint using ER5356 (a)

Top view and (b) Bottom view

4.6.2 Macrostructure of transverse section of the TIG welded A6061-T6 and A6082-T6 joint using ER5356 filler wire

Fig. 4.72 shows macrostructure of transverse section of the TIG welded A6061-T6 and A6082-T6 dissimilar joint. The joint exhibits a weld without any defect. Complete depth of penetration is achieved in the joint. It is observed that WMZ exhibits white color and other regions are grey in color. This color contrast has occurred due to the addition of external ER5356 filler material in the weld joint. With the addition of filler material, compositional changes take place in the weld fusion zones, particularly at WMZ. The reactivity of the zones with the applied etchant varies and that makes the color difference.

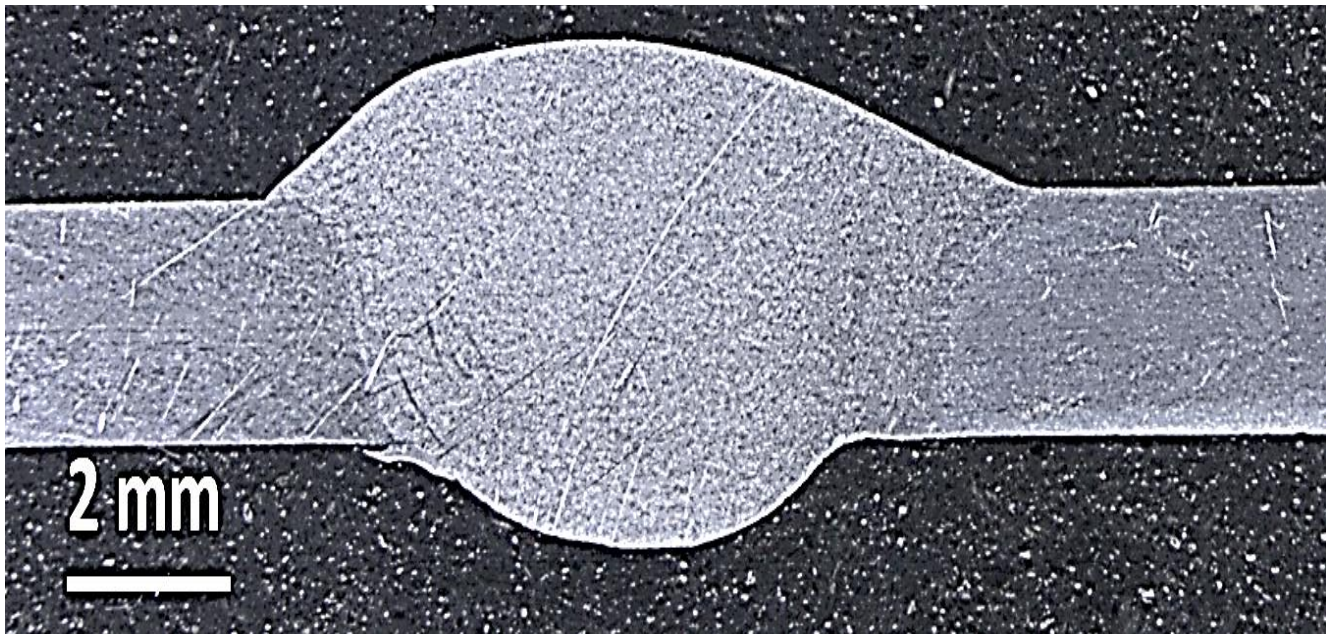


Fig. 4.72 Macrostructure of transverse section of the TIG welded A6061 and A6082 joint using ER5356

4.6.3 Optical microstructure of WMZ center in TIG welded A6061-T6 and A6082-T6 joint using ER5356 filler wire

Fig. 4.73 shows optical microstructure of WMZ center. This zone exhibits an equiaxed dendritic microstructure. The ER5356 filler contains 5 wt.% Mg. Because of the low solubility of Mg in Al (1.7 wt.%), only a small amount of Mg forms solid solution with Al and Al_3Mg_2 phases are also formed at room temperature (Mishra 2018). Thus, a significant quantity of Mg and other minor alloying elements accumulate in front of solid liquid interface that induces constitutional supercooling at the WMZ center. As a result, equiaxed grains are formed in the WMZ center. The equiaxed dendrite formation can also be related to the presence of liquid film along the PMZ grains (S. Kou 1986). Liquid films are observed to be present in the GBs of PMZ at both the interfaces in the present study. These grains are loosely attached to each other and get detached due to weld pool convection. If the detached grains survive till they reach the weld pool, they can act as nucleating sites, and subsequently fine equiaxed dendrites are formed at center of the WMZ. The eutectic phases are distributed almost uniformly. However, at a few places these phases are agglomerated.

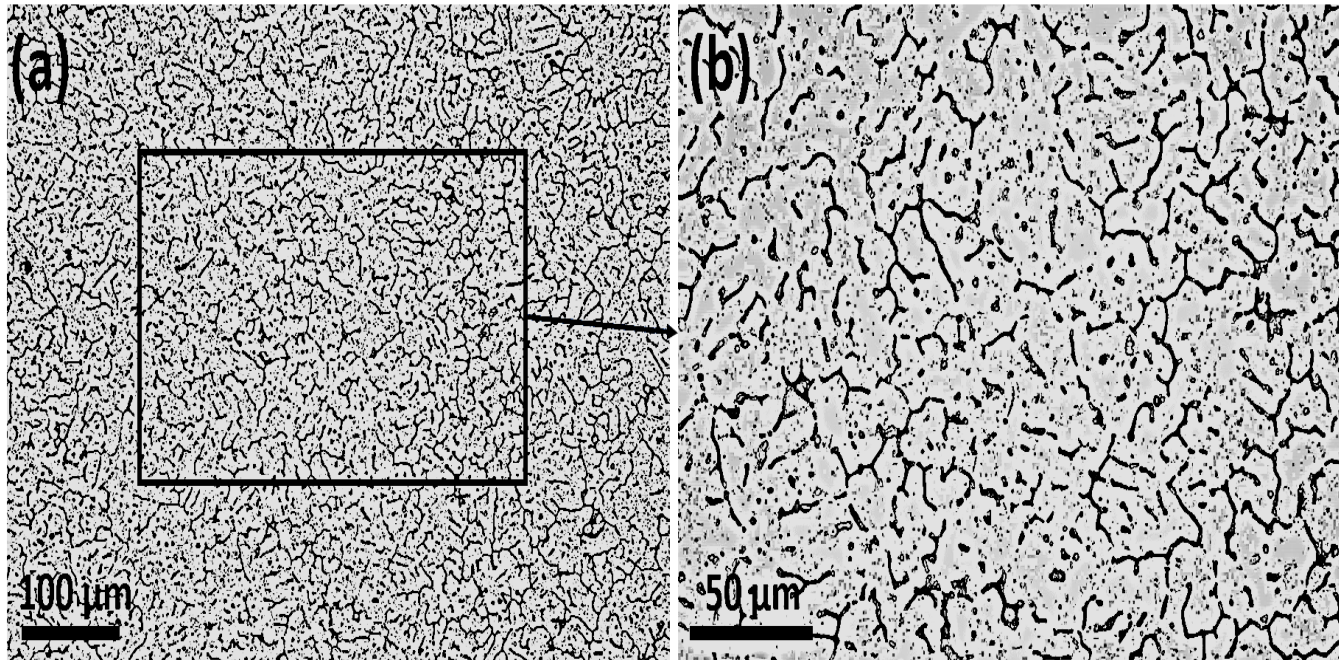


Fig. 4.73 Optical microstructure of WMZ center in TIG welded A6061 and A6082 joint using ER5356: (a) low magnification and (b) high magnification

4.6.4 Optical microstructure of weld interface regions of the TIG welded A6061-T6 and A6082-T6 joint using ER5356 filler wire

Figs. 4.74 and 4.75 show optical microstructures of the weld interface regions of 6061-T6 and 6082-T6, respectively. Five zones, viz. heat affected zone (HAZ), partially melted zone (PMZ), non-dendritic equiaxed zone (EQZ), columnar crystal zone (CCZ) and equiaxed dendritic zone (at WMZ center) are observed to extend from base metal towards weld in 6061-T6. Four zones, viz. heat affected zone (HAZ), partially melted zone (PMZ), columnar crystal zone (CCZ) and equiaxed dendritic zone(at WMZ center) are observed

to extend from base metal towards weld in 6082-T6. The newly evolved EQZ at 6061-T6 exhibits equiaxed non-dendritic feature which is different from the equiaxed dendritic structure at the center of WMZ. Liquation is observed at most of the GBs in EQZ. Fig. 4.75(c-d) shows CCZ of 6061-T6 and 6082-T6 interfaces. It can be seen that the dendrite size in CCZ of 6061-T6 interface is somewhat coarser than the dendrite size in CCZ of 6082-T6 interface. The difference in thermal conductivity of the individual alloys influences the dendrite size in CCZs. The thermal conductivity of A6082-T6 alloy is higher than that of A6061-T6 alloy (Hamilton et al. 2008). Due to the higher thermal conductivity of A6082-T6, the cooling rate during solidification is larger at the 6082-T6 interface than at the 6061-T6 interface. Thus, the dendrites of CCZ at 6082-T6 interface are finer than the dendrites of CCZ at 6061-T6 interface.

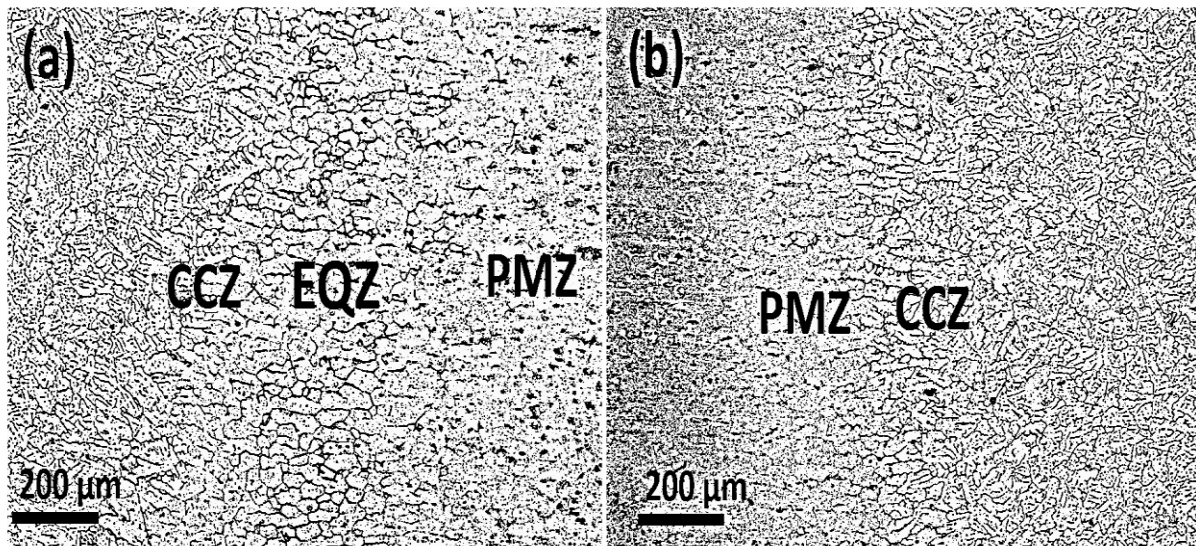


Fig. 4.74 Optical microstructure of interface regions of the TIG welded A6061 and A6082 joint using ER5356 (a) A6061-T6 and (b) A6082-T6

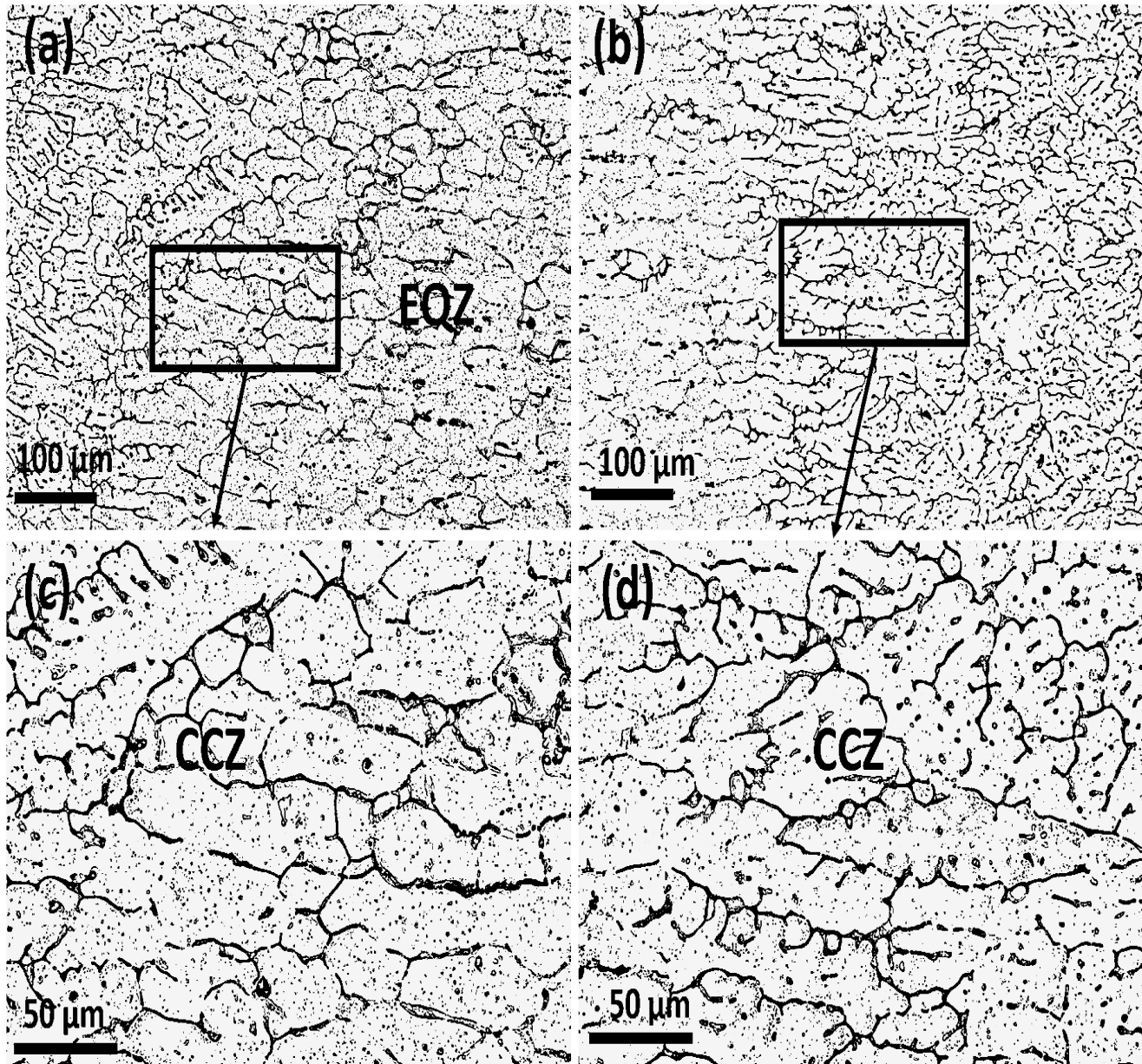


Fig. 4.75 Optical microstructure of interface regions of the TIG welded A6061 and A6082 joint using ER5356 (a&c) A6061-T6 and (b&d) A6082-T6

4.6.5 SEM microstructure of PMZs in TIG welded A6061-T6 and A6082-T6 joint using ER5356 filler wire

Fig. 4.76(a-b) displays SEM microstructure of the PMZ at weld interface regions of 6061-T6 and 6082-T6. GB liquation is noticed in PMZs of both the interfaces. While some liquation is noticed in PMZ of A6061 interface, it is almost insignificant in the PMZ of A6082. The liquation at grain interiors is completely absent in PMZs of both the interfaces.

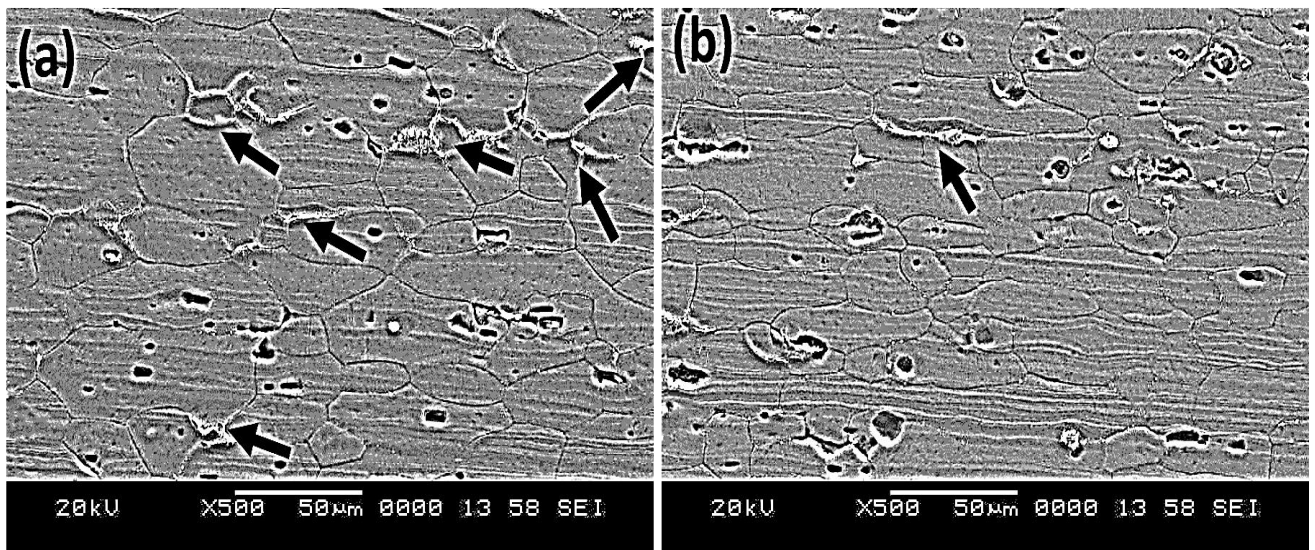
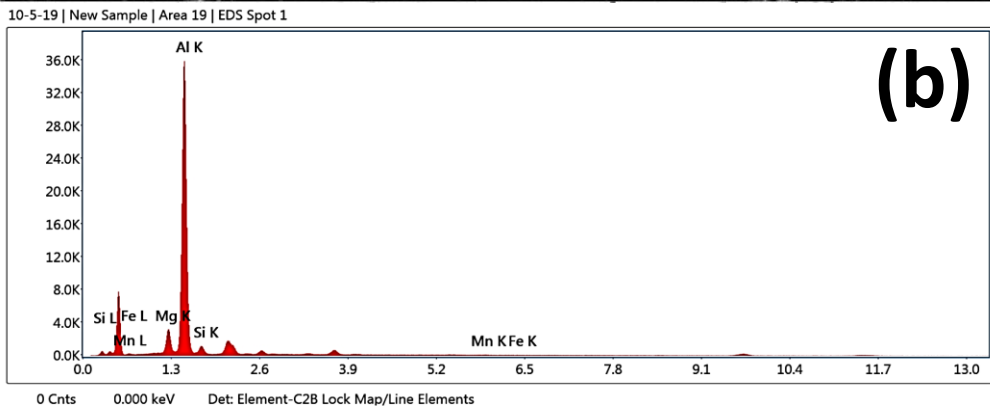
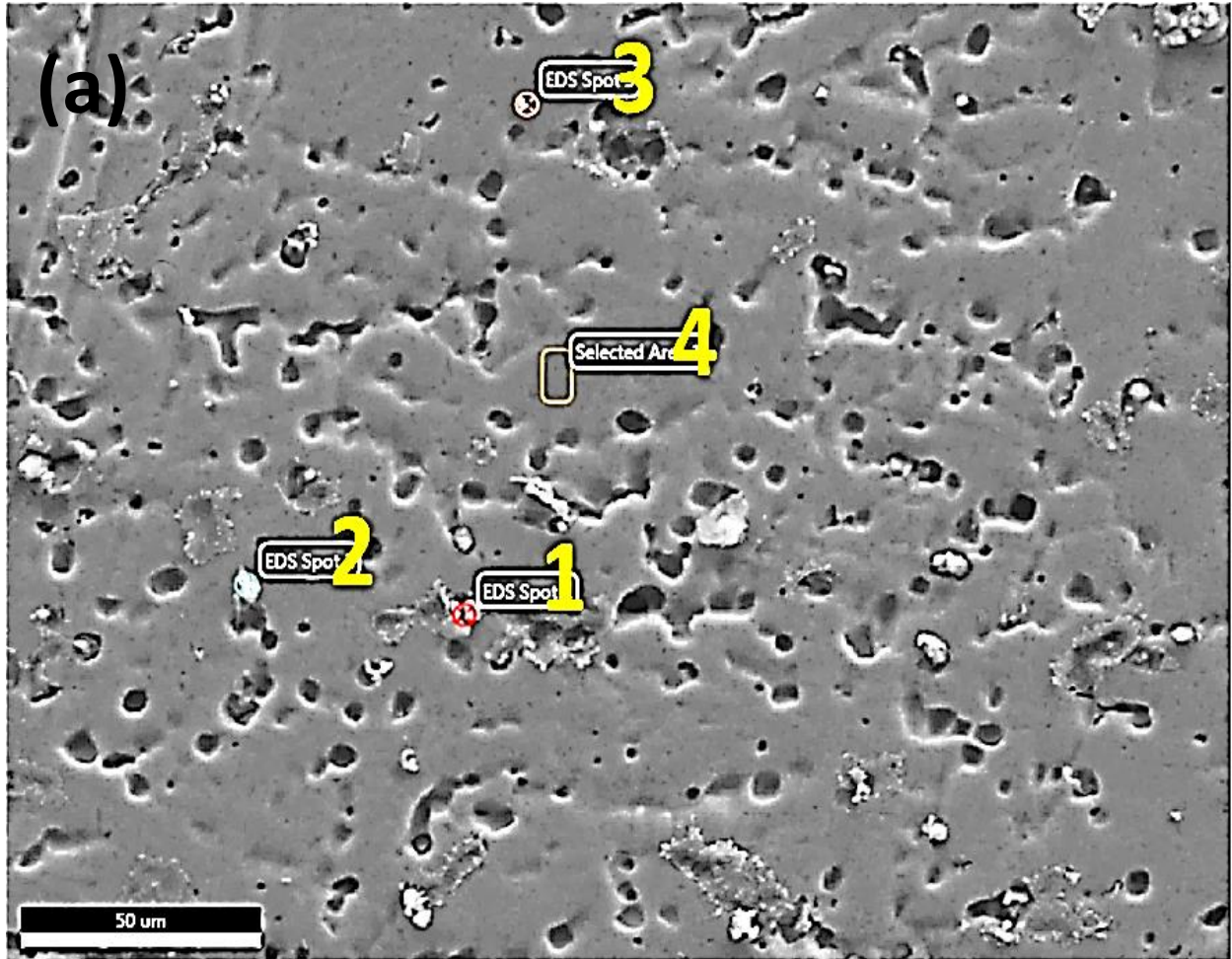


Fig. 4.76 SEM microstructure of PMZ (black arrow indicates GB liquation) in TIG welded A6061 and A6082 joint using ER5356 (a) A6061-T6 and (b) A6082-T6

4.6.6 SEM-EDS analysis of WMZ center in TIG welded A6061-T6 and A6082-T6 joint using ER5356 filler wire

The SEM-EDS spot analysis at the center of the WMZ and its corresponding EDS spectra is shown in Fig. 4.77. The elemental compositions are listed in Table 4.18. The composition

of a particle (spot 1) shows that this region is composed of Mg and Si in a significant quantity, which is possibly Mg_2Si phase. EDS analysis of spot 2 confirms the presence of Al_3Mg_2 phase, which is supported from the Al-Mg phase diagram and a previous work employing an Al-5 wt.% filler material (Mishra 2018). A significant quantity of Mn is found at spot 3 confirming the presence of Al_6Mn phase, which gets support from a previous work (McShane et al. 1990; Svensson et al. 2000). The migration of Si and Mn by dilution effect leads to an increase in the amount of Mn and Si in the WMZ, as a result of which Mg_2Si and Al_6Mn phases are formed at the center of the WMZ. The selected area of EDS analysis on the matrix (spot 4) shows a composition that is nearly equal to the composition of the filler material.



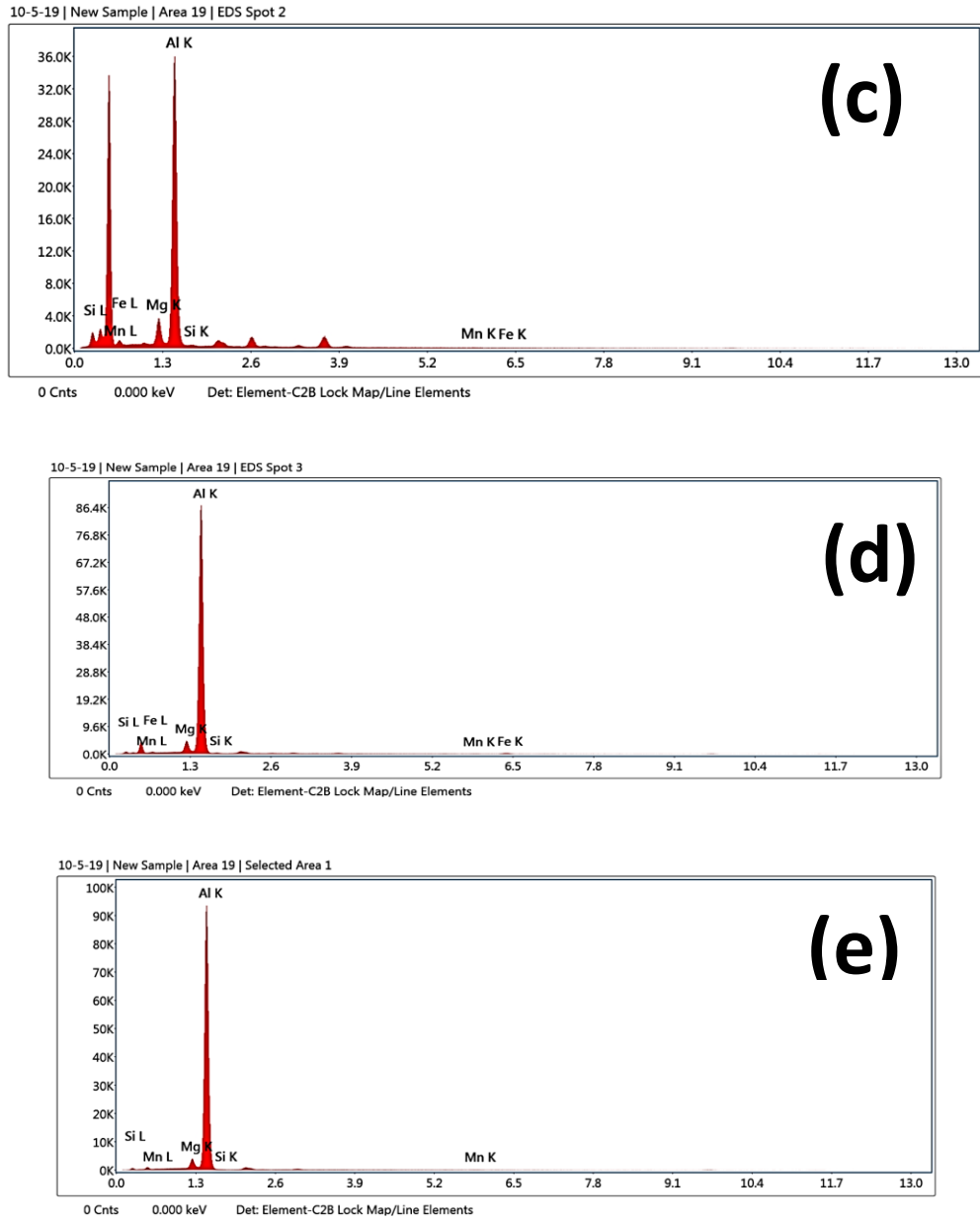


Fig. 4.77(a-e) EDS spot analysis and its EDS spectra at WMZ center of the TIG welded A6061 and A6082 joint using ER5356

Table 4.18 EDS analysis of precipitates present at WMZ center of the TIG welded A6061 and A6082 joint using ER5356

	Al	Mg	Si	Mn	Fe	Al	Mg	Si	Mn	Fe
	(wt. %)					(at. %)				
Point 1	Bal.	7	5.9	0.6	0.4	Bal.	7.8	5.6	0.3	0.2
Point 2	Bal.	8.2	0.8	0.6	0.3	Bal.	9	0.7	0.3	0.1
Point 3	Bal.	4.7	0.4	0.4	1.3	Bal.	5.3	0.4	0.2	0.6
Point 4	Bal.	4.1	0.05	0.4	-	Bal.	4.6	0.05	0.2	-

4.6.7 SEM microstructure and SEM-EDS analysis of HAZ precipitates in TIG welded A6061-T6 and A6082-T6 joint using ER5356 filler wire

Fig. 4.78 shows SEM microstructure of HAZ (a) A6061-T6; (b) A6082-T6. The HAZ of A6061-T6 interface is composed of rod shaped precipitates as seen from Fig 4.78(a). Other than the few rod shapes β' precipitates, a considerable amount of spherical shaped Si rich precipitates appearing dark grey in colour is also found in the HAZ of A6082 interface [Fig 4.78(b)]. No such dark grey appearing spherical particles have been observed in HAZ of A6061 interface. The EDS analysis of precipitates at the HAZs is shown in Fig. 4.79(a-b). As can be seen from Table 4.19, all the precipitates contain high amounts of Si.

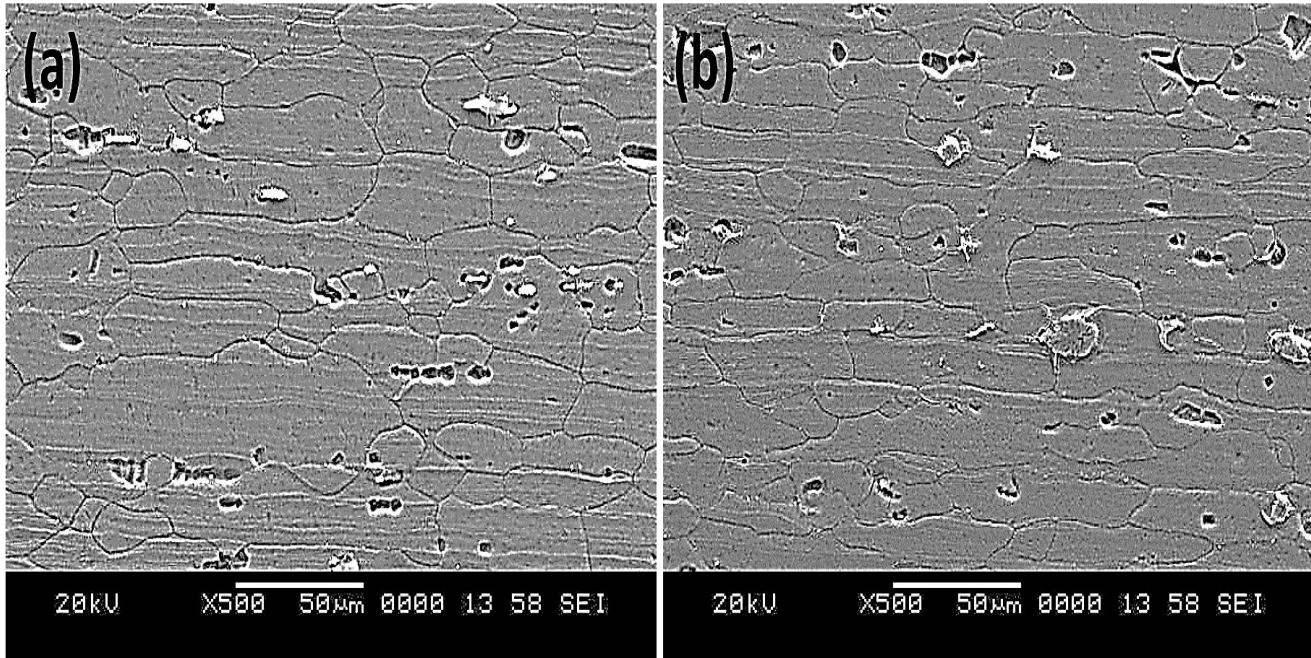
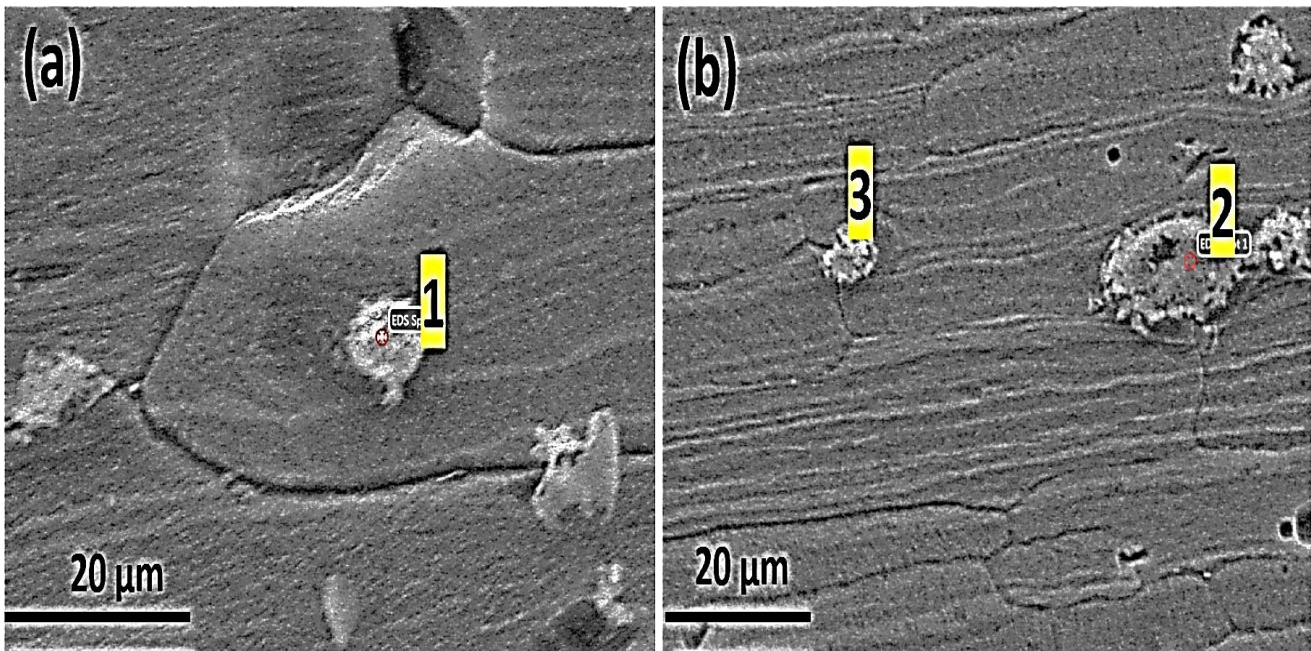


Fig. 4.78 SEM microstructure of HAZ of the TIG welded A6061 and A6082 joint using ER5356: (a) A6061-T6; (b) A6082-T6



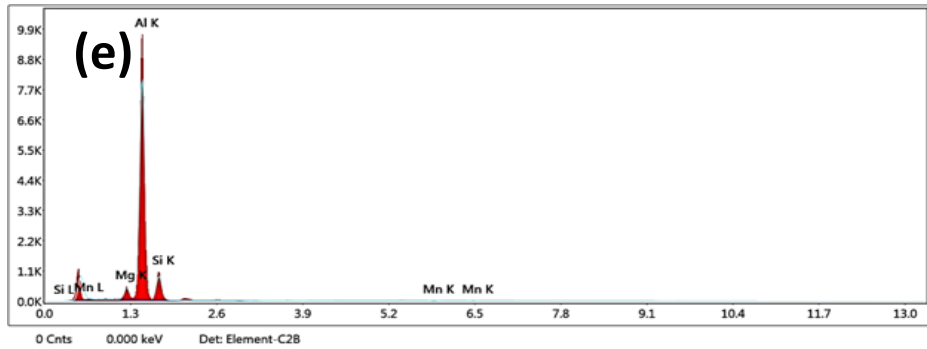
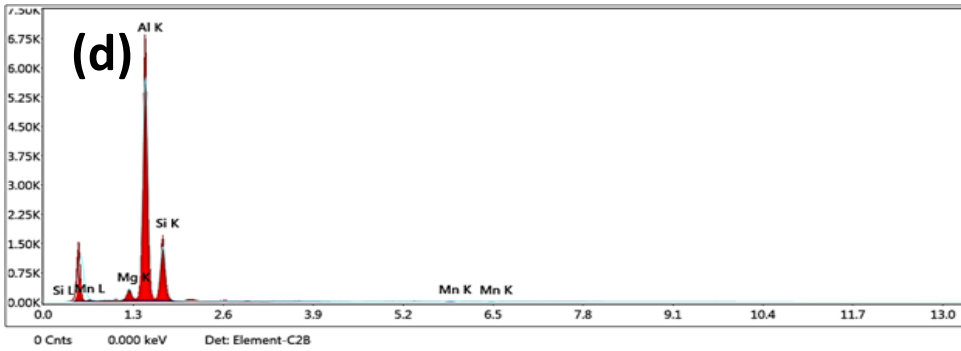
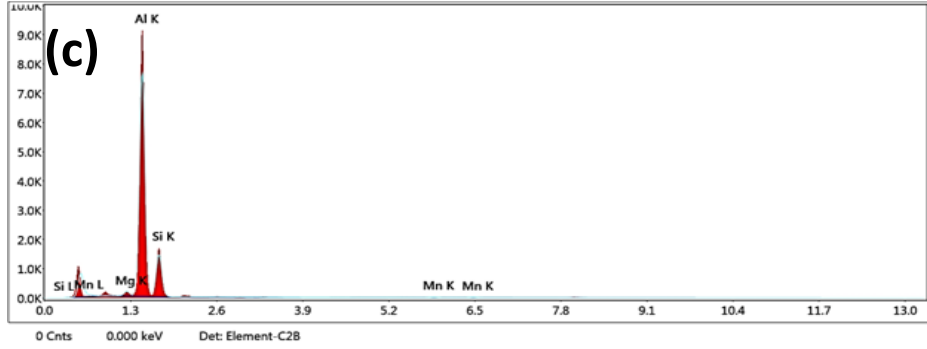


Fig. 4.79 SEM-EDS spot analysis of HAZs and its EDS spectra in TIG welded A6061 and A6082 joint using ER5356: (a) A6061-T6; (b) A6082-T6; (c) EDS spectra of spots in A6061-T6 and (d-e) EDS spectra of spots in A6082-T6

Table 4.19 EDS analysis of precipitates present at HAZ of the TIG welded A6061 and A6082 joint using ER5356

	Al	Mg	Si	Mn	Al	Mg	Si	Mn
	(wt. %)				(at. %)			
Point 1	Bal.	1.4	28.1	0.6	Bal.	1.6	27.3	0.3
Point 2	Bal.	3.2	31.4	0.8	Bal.	3.6	30.6	0.4
Point 3	Bal.	3.7	18.7	0.7	Bal.	4.2	18	0.3

4.6.8 Microhardness of the TIG welded A6061-T6 and A6082-T6 joint using ER5356 filler wire

Vickers microhardness profile of the weld joint is shown in Fig. 4.80. The readings are taken from the middle portion of the cross section. The Al-Mg-Si series alloys are precipitation hardened alloys and these precipitates are obtained through ageing treatment. In general, the precipitation sequence in Al-Mg-Si alloys is reported as follows; α -SSS \rightarrow G.P zone \rightarrow β'' precipitates (needle shaped precipitates) \rightarrow β' precipitates (rod shaped meta stable precipitates) \rightarrow β precipitates (stable precipitates) (Tsao et al. 2006). In the case of artificially aged Al-Mg-Si alloys, fine needle shaped β'' precipitates are the main strengthening phases (Myhr et al. 2001). The presence of rod shaped β' precipitates in HAZs indicates that the temperature rise in HAZ leads to transform β'' precipitates to β'

precipitates. This phenomenon leads to reduce hardness of HAZs than the BMs. The lower hardness in PMZs is attributed to the presence of a thin liquid film at the GBs of PMZs. The temperature at PMZ was very high that led to the dissolution of the precipitates. The reprecipitation phenomenon has not occurred in PMZ due to insufficient time during cooling. No precipitation was observed in the cooled samples, taking into consideration the limitations of the SEM facility. An earlier research work has reported that for a 6xxx series alloy, the PMZ became partially solution treated zone where some of the precipitates got dissolved because of high prevailing temperature (Gungor et al. 2014b). The dissolution of precipitates at PMZ also decreases the hardness of the zone. The WMZ has exhibited maximum hardness among all the zones. The addition of ER5356 filler (Al-5Mg) could have increased the Mg content of the solid solution and also the amount of Al_3Mg_2 particles. Moreover, the BMs mainly contain Si as an alloying element and some amount of Mn is also present. Migration of these elements from the BM to the center of the WMZ due to dilution effect has taken place during welding. Due to this, secondary phases such as Mg_2Si and Al_6Mn have been formed. This is confirmed by EDS spot analysis. The increased amount of Mg in WMZ increases solid solution strengthening effect and the presence of Al_3Mg_2 , Mg_2Si and Al_6Mn particles increases secondary phase particle strengthening that increases the hardness of WMZ.

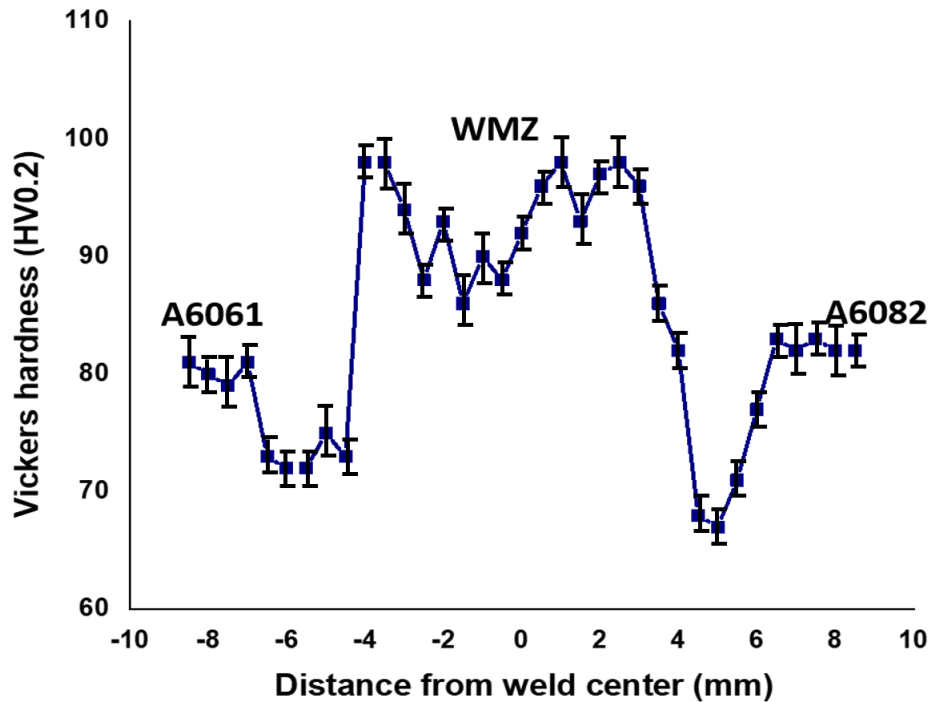


Fig. 4.80 Vickers microhardness profile of the TIG welded A6061 and A6082 joint using ER5356

4.6.9 Tensile properties of the TIG welded A6061-T6 and A6082-T6 joint using ER5356 filler wire

Tensile properties of different regions of dissimilar weld joint are presented in Fig. 4.81. The tensile values are reported in Table 4.20. The entire gage area of miniature samples was prepared from 6061-T6 side consisting of base 6061-T6, HAZ of 6061-T6, PMZ of 6061-T6, and WMZ very next to 6061-T6 fusion boundary. In a similar way, the gage area of miniature samples of 6082-T6 side comprised of base 6082-T6, HAZs of 6082-T6, PMZ of 6082-T6 and WMZ very next to 6082-T6 fusion boundary. The gage length of over- all

weld region consisted of BMs, HAZs, PMZs of both 6061-T6 as well as 6082-T6 alloys and the whole WM region.

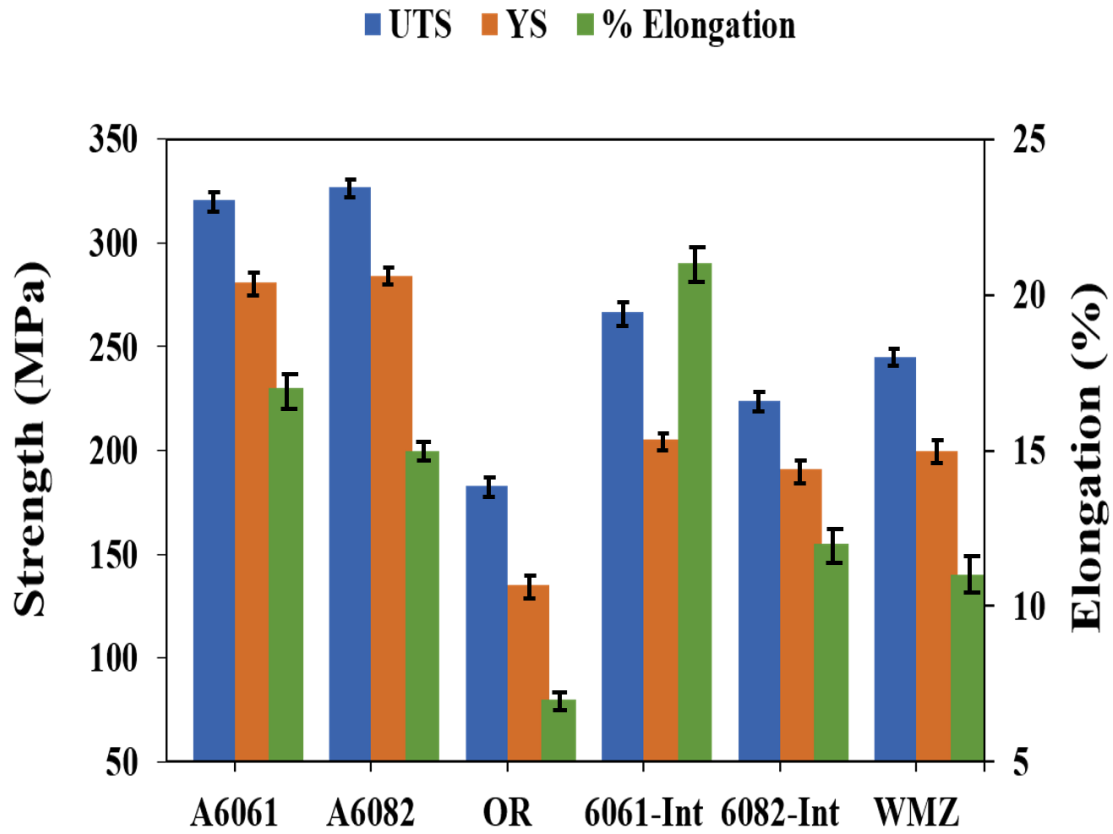


Fig. 4.81 Tensile properties of the BMs and different regions of TIG welded A6061 and A6082 joint using ER5356 (OR-over all weld region, Int-Interface and WMZ- weld metal zone; Gauge length of BMs & OR is 25 mm and gauge length of interfaces and WMZ is 5 mm)

Table 4.20 Tensile properties of the BMs and different regions of TIG welded A6061 and A6082 joint using ER5356

Sample	UTS (MPa)	YS (MPa)	Elongation (%)
A6061	321	281	17
A6082	327	284	15
TIG weld joint (OR)	183	135	7
TIG weld joint (6082-T6 int.)	267	205	21
TIG weld joint (6061-T6 int.)	224	191	12
TIG (WMZ)	245	200	11

GB liquation and weld tensile residual stress play a major role in inducing cracking in PMZ (Ghaini et al. 2009). GB liquation phenomenon is rarely found in the PMZ of 6082-T6 interface. However, it is higher in the PMZ of 6061-T6 interface. This has led to increase the PMZ cracking possibility in A6061-T6 interface, subsequently lowering its strength. The dendrites of CCZ at 6061-T6 interface are somewhat coarser than the dendrites of CCZ at 6082-T6 interface. This may also have decreased the strength of 6061-T6 interface.

Tensile properties of the precipitation hardened alloys mainly depend on the type of precipitates, their size, morphology and distribution. It is found that rod shaped precipitates are present in HAZs of 6061-T6 interface. Apart from a few rod shapes β' precipitates, a considerable amount of spherical shaped Si rich precipitates appearing dark grey is also found in the HAZ of A6082 interface. Moreover, absence of EQZ is noticed in A6082-T6 interface. Such structural variations can account for the increased strength of 6082-T6 interface as compared to 6061-T6 interface.

4.6.10 Fractography of the TIG welded A6061-T6 and A6082-T6 joint using ER5356 filler wire

Fig 4.82 shows SEM images of fractured surface of interface regions and the over-all weld region. The presence of dimples on the fracture surface of all the regions confirms that the mode of fracture is ductile in the weld joint.

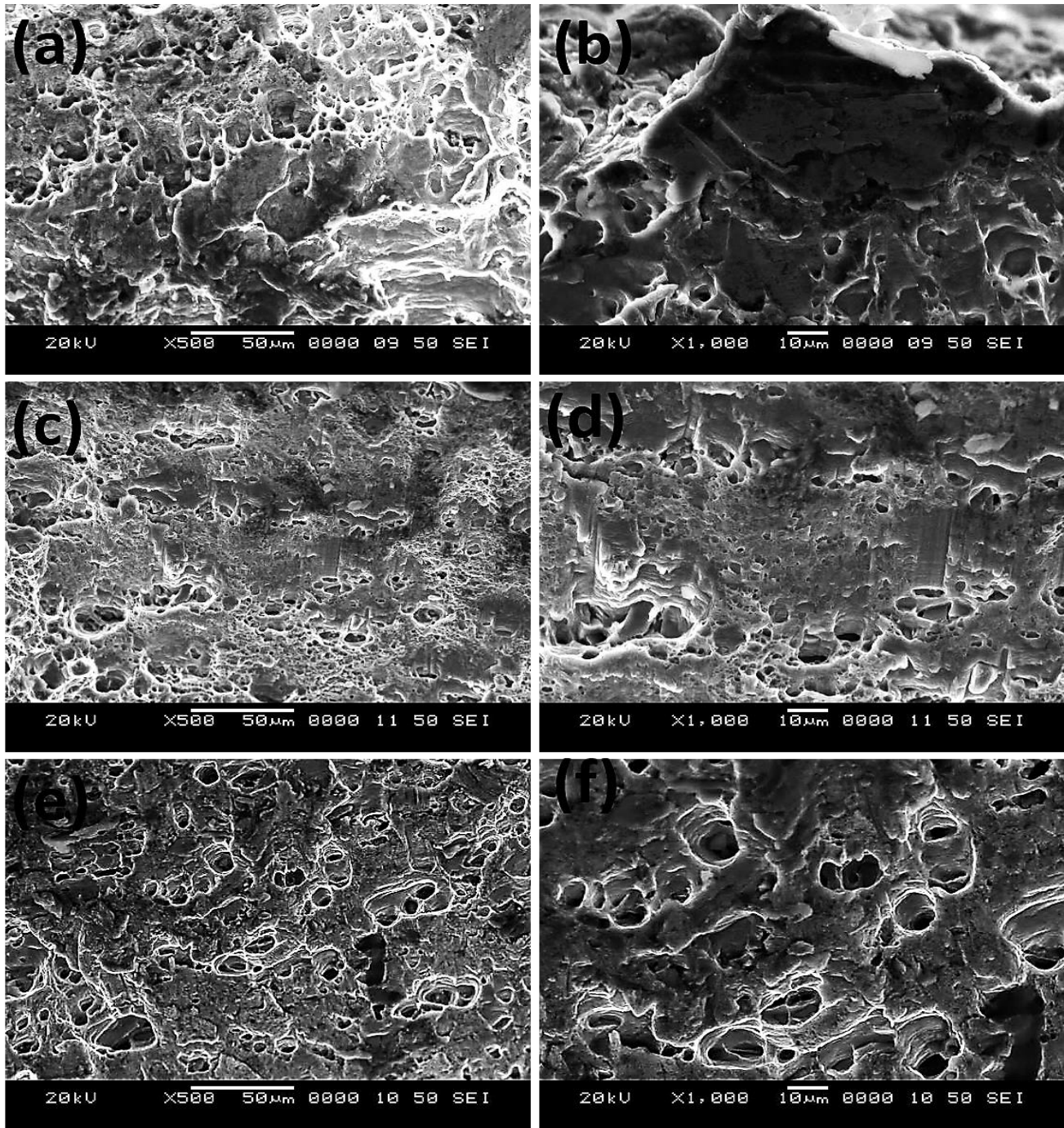


Fig. 4.82 Fracture surface of the TIG welded A6061 and A6082 joint using ER5356 (a) A6061 interface region; (b) A6082 interface region and (c) over-all weld joint

4.7 Tungsten inert gas (TIG) welding of dissimilar A5754-H111 and A5083-H111

using ER4043 filler wire

4.7.1 Surface appearance of the TIG welded A5754-H111 and A5083-H111 joint

using ER4043 filler wire

The surface appearance of the TIG welded joint is shown in Fig. 4.83 (a-b). It can be seen that the top view of surfaces exhibits good bead profiles. No spatter is noticed on its surface. Also, no cracks are present on the surface. The bottom view of surfaces indicates that full penetration is achieved.

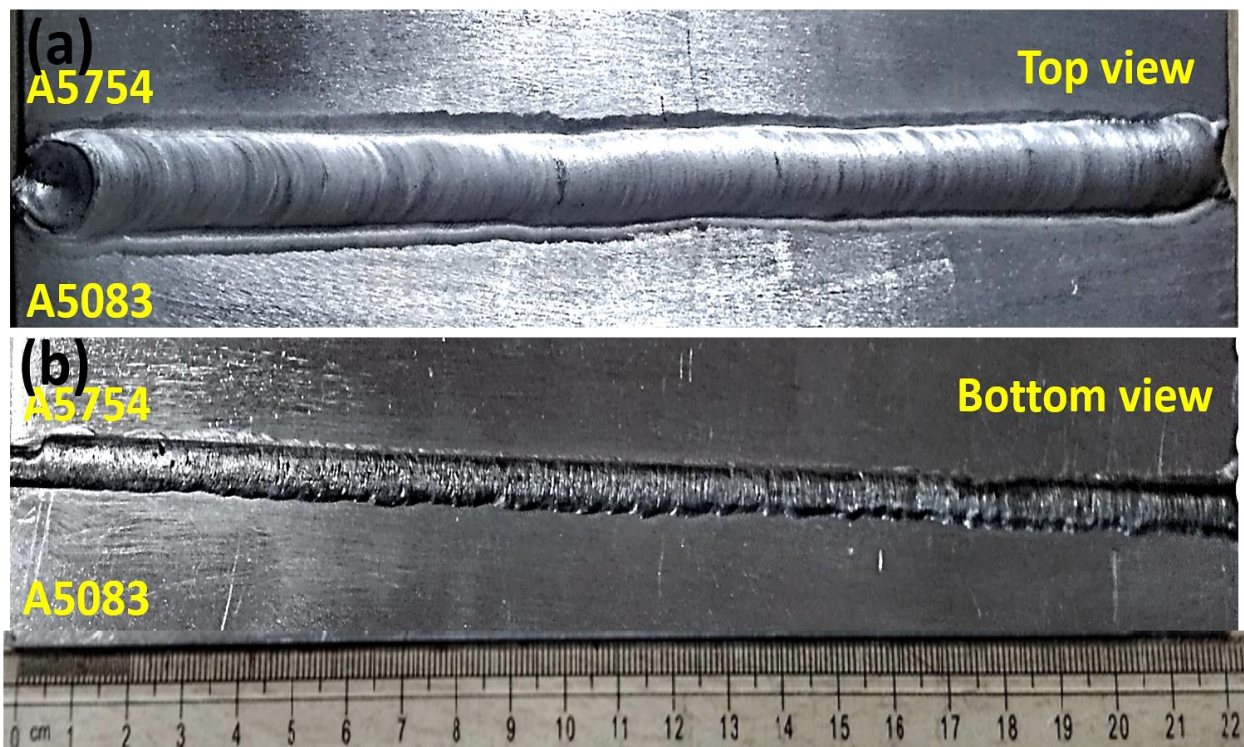


Fig. 4.83 Surface appearance of the TIG welded A5754-H111 and A5083-H111 joint using

ER4043: (a) Top view and (b) Bottom view

4.7.2 Macrostructure of transverse section of the TIG welded A5754-H111 and A5083-H111 joint using ER4043 filler wire

Fig. 4.84 shows a macroscopic cross-sectional view of the dissimilar A5754-A5083 joint. The cross section of the joint displays good weld profiles without any defect. Complete penetration is observed. The WMZ in the joint is brighter than the other zones owing to the addition of external ER4043 filler material in the weld joint.

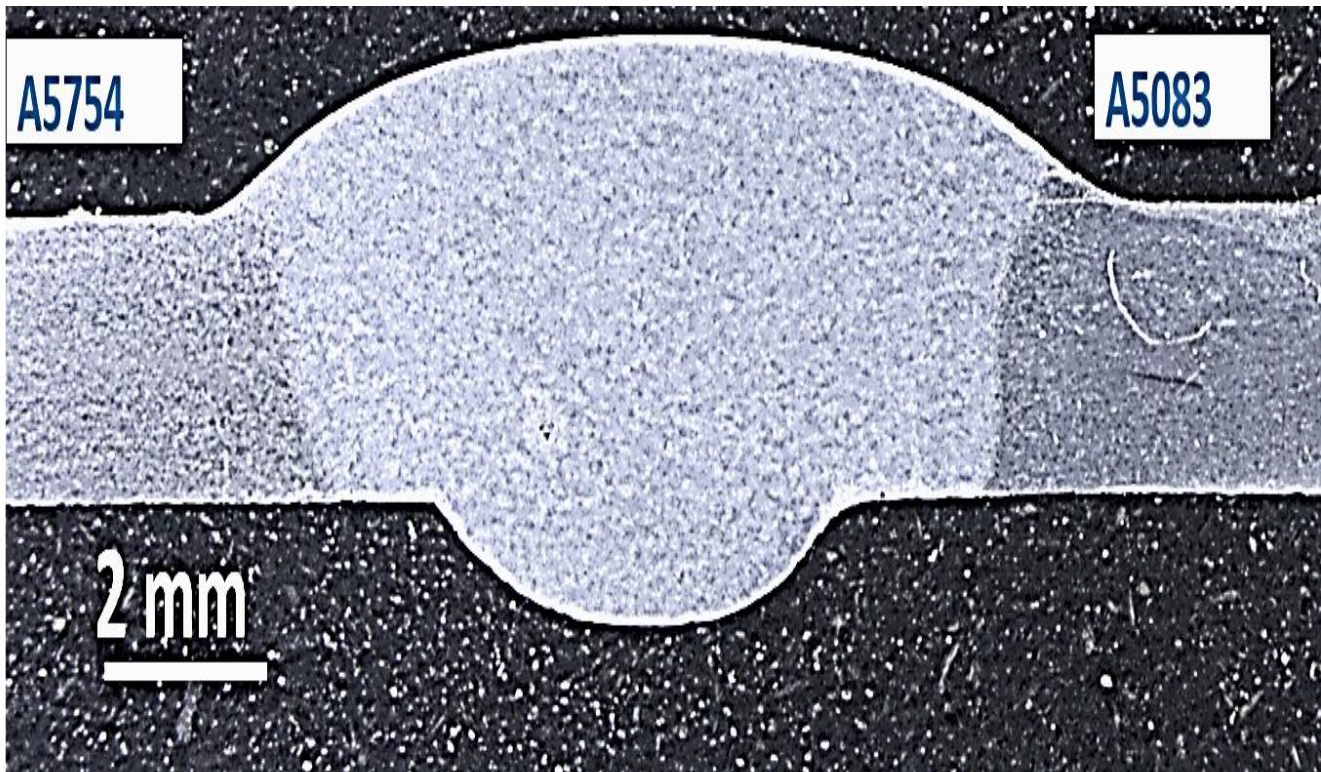


Fig. 4.84 Macrostructure of transverse section of the TIG welded A5754-H111 and A5083-H111 joint using ER4043

4.7.3 SEM of interface regions of the TIG welded A5754-H111 and A5083-H111 joint using ER4043 filler wire

Figs. 4.85 and 4.86 show SEM microstructures of the weld interface regions of A5754 and A5083, respectively. The zones such as heat affected zone (HAZ), partially melted zone (PMZ), non-dendritic equiaxed zone (EQZ), columnar crystal zone (CCZ) have evolved at A5083 side. The EQZ near fusion boundary exhibits non-dendritic feature. However, EQZ has not been noticed in the A5754 interface region.

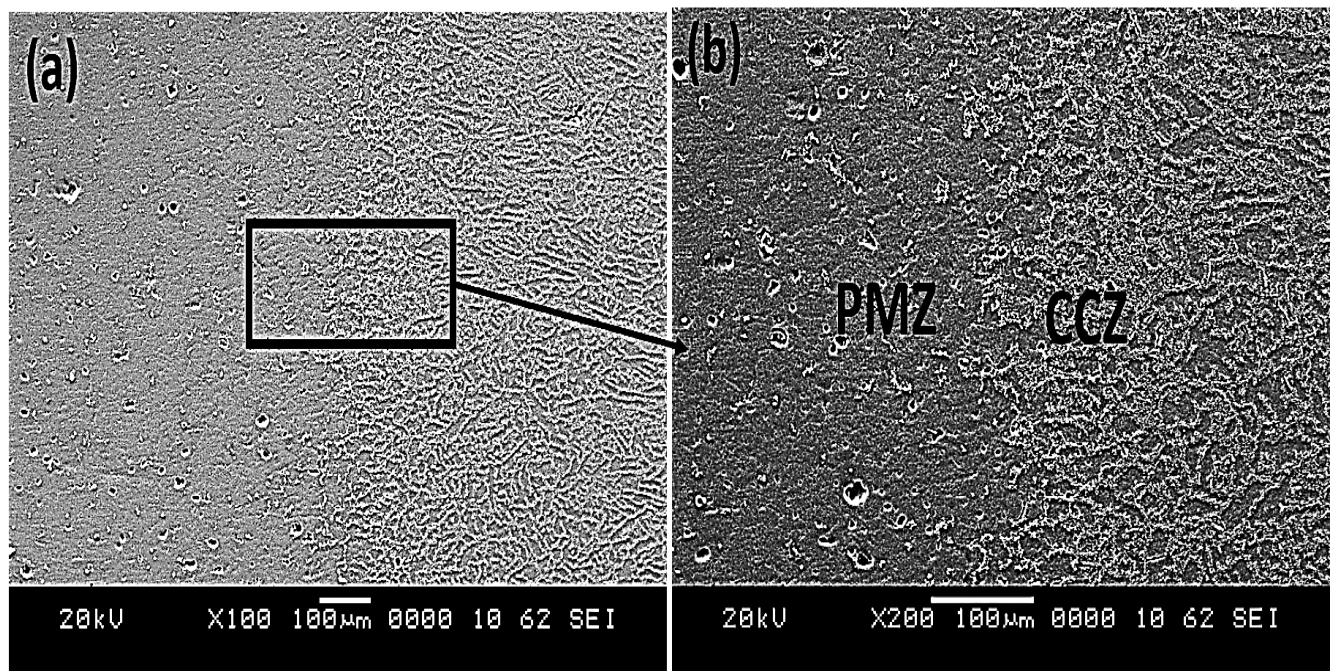


Fig. 4.85 SEM microstructure of the TIG welded A5754-H111 and A5083-H111 joint using ER4043 (a) low magnification image of interface region of A5754 (b) high magnification image of interface region of A5754

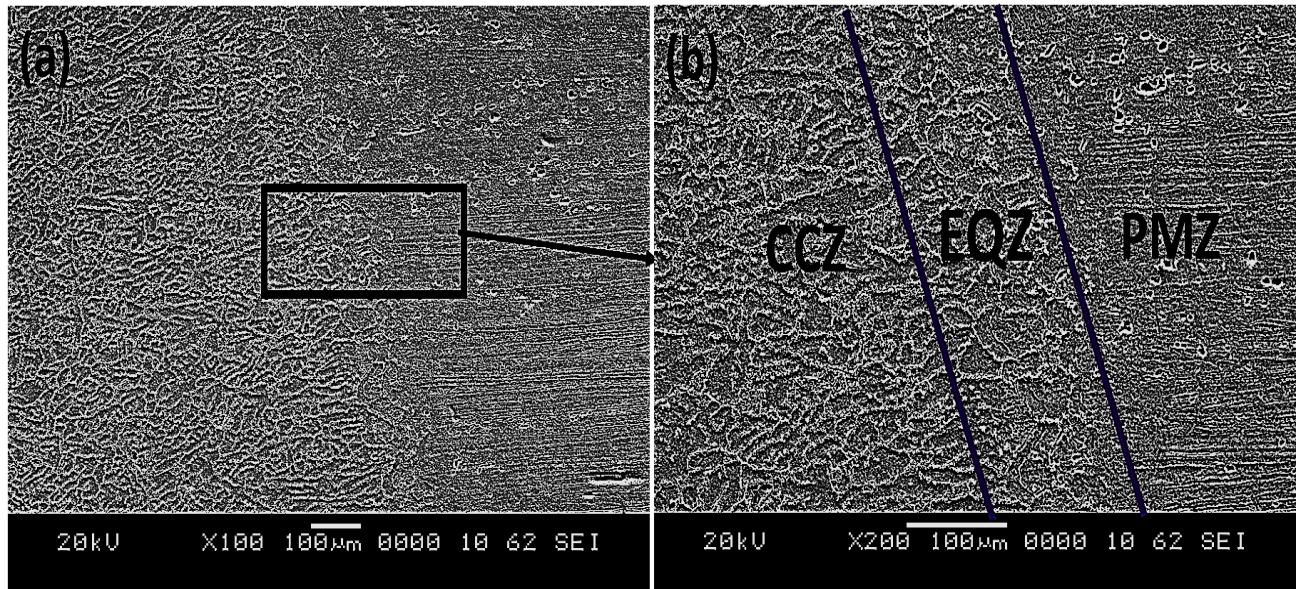


Fig. 4.86 SEM microstructure of the TIG welded A5754-H111 and A5083-H111 joint using ER4043: (a) low magnification image of Interface region of A5083 (b) high magnification image of interface region of A5083

4.7.4 SEM of WMZ and HAZs of the TIG welded A5754-H111 and A5083-H111 joint using ER4043 filler wire

Fig. 4.87 (a) shows SEM microstructure of weld joint at the center of WMZ and Fig. 4.87 (b-c) HAZ of interface regions. It is observed that WMZ center exhibits dendritic feature. During arc welding, BMs get melted and mix with the droplets of filler metal that subsequently solidifies as a weld metal zone (WMZ). Si is segregated at dendrite boundaries in WMZ. The Si enriched strips have been noticed to be continuous at the major portion of dendrite boundaries in WMZ. Dendrite interiors at WMZ consist of dark grey colored secondary phase particles. The amounts of secondary phase particles in HAZ are higher in A5083 interface region than the A5754 interface region.

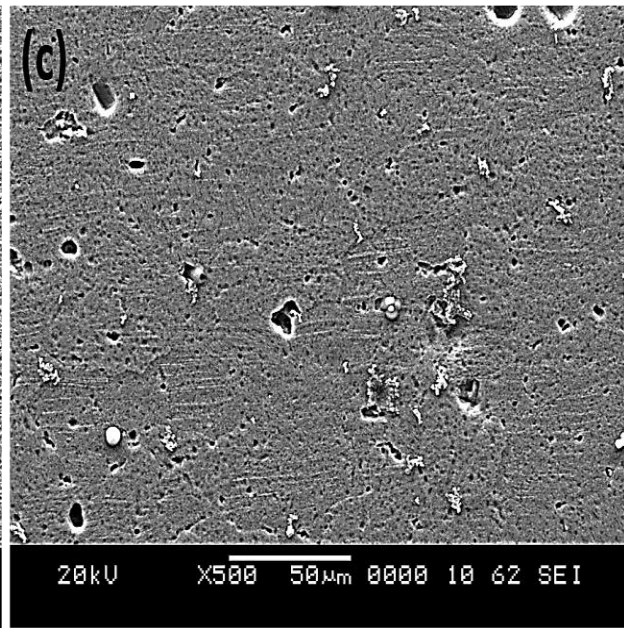
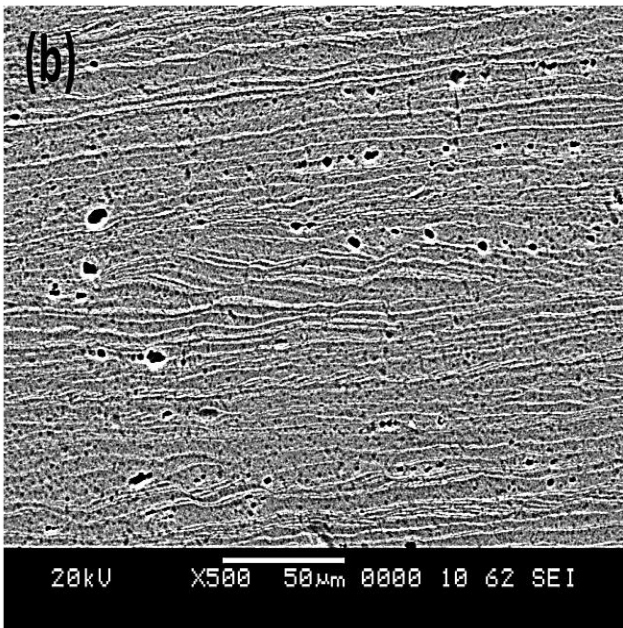
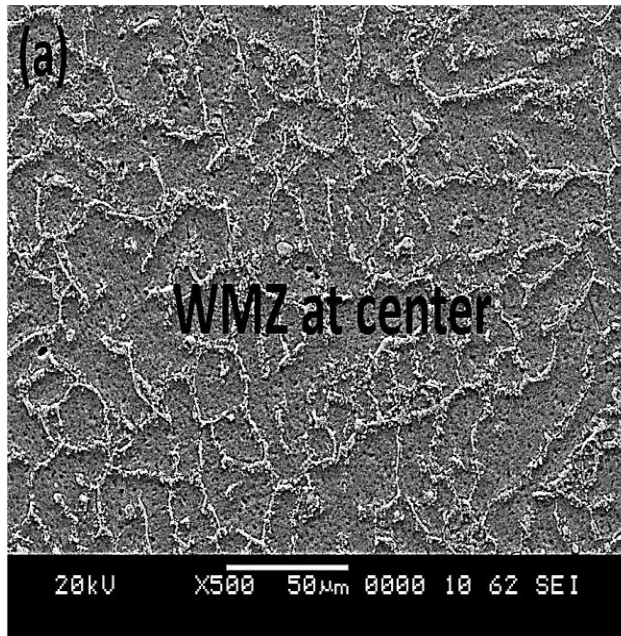
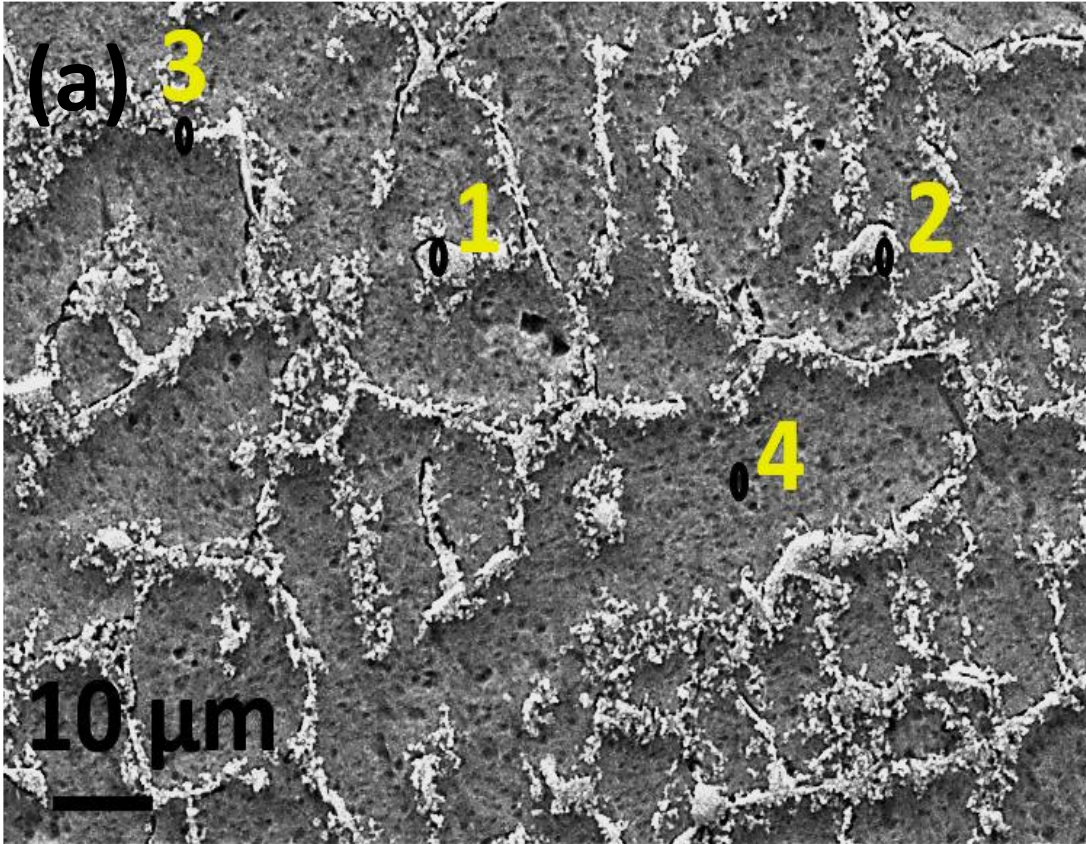


Fig. 4.87 SEM microstructure of the TIG welded A5754-H111 and A5083-H111 joint using ER4043: (a) WMZ center (b) HAZ of A5754 and (c) HAZ of A5083

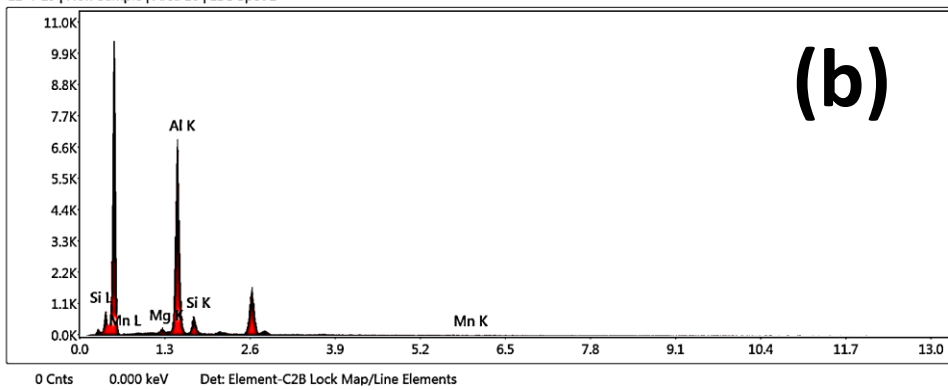
4.7.5 SEM-EDS of WMZ in TIG welded A5754-H111 and A5083-H111 joint using ER4043 filler wire

Fig. 4.88 shows SEM EDS spot analysis of WMZ center and its corresponding EDS spectra. The chemical composition of elements is summarized in Table 4.21. The EDS spot analysis on secondary phase particles (spots 1,2 and 3) confirms that these phases are Mg_2Si particles. A previous research work has also reported the presence of Mg_2Si phases in WMZ when Al alloy is welded using ER4043 filler material (Lakshminarayanan et al. 2009).

The EDS analysis of the matrix region (spot 4) displays significant quantities of Mg and Mn. The Mg content of WMZ center is 2.4% and the Mn content 0.3%. Both the BMs contain Mg as a primary alloying element and Mn as a secondary alloying element. Mn are migrated Their migration from BMs to the center of WMZ by dilution effect has effectively increased their concentration.



12-4-19 | New Sample | Area 16 | EDS Spot 1



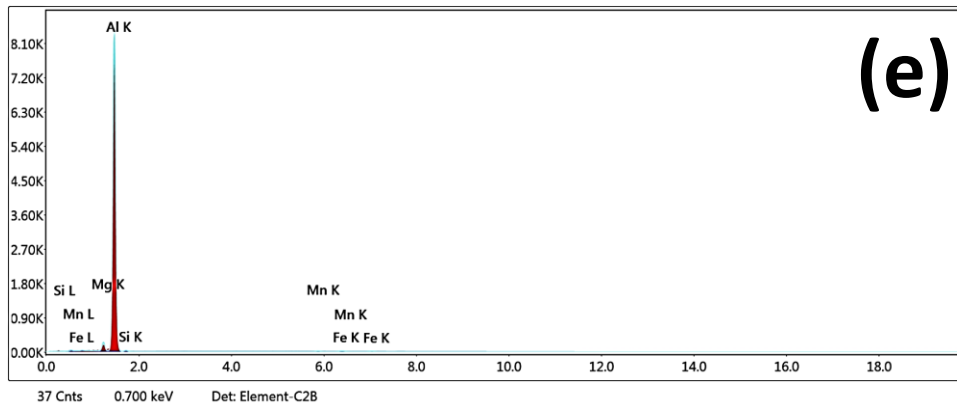
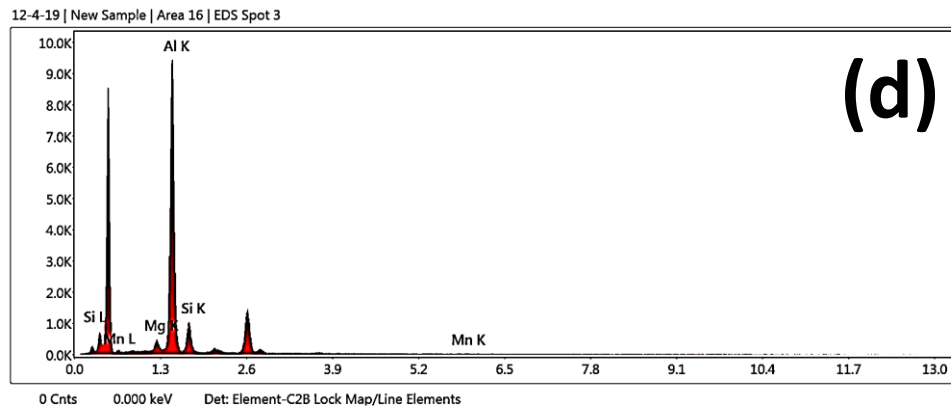
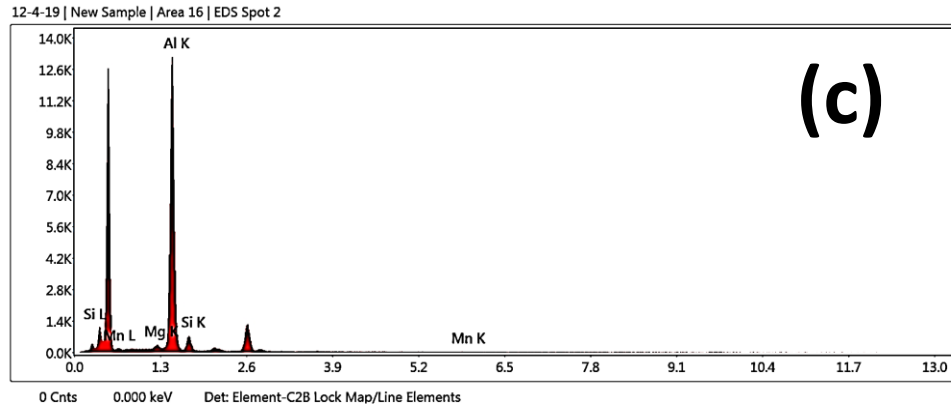


Fig. 4.88(a-e) SEM EDS spot analysis of the WMZ center and its EDS spectra in TIG welded A5754-H111 and A5083-H111 joint using ER4043

Table 4.21 EDS analysis on precipitates present at WMZ center in TIG welded A5754-H111 and A5083-H111 joint using ER4043

	Al	Mg	Si	Mn	Al	Mg	Si	Mn
	(wt. %)				(at. %)			
Point 1	Bal.	3.6	16	1.3	Bal.	4	15.6	0.6
Point 2	Bal.	2.9	10.9	1	Bal.	3.2	10.5	0.5
Point 3	Bal.	4.2	17.7	1.2	Bal.	4.7	17.2	0.6
Point 4	Bal.	2.4	1	0.3	Bal.	2.7	0.9	0.2

4.7.6 SEM-EDS of weld interface regions in TIG welded A5754-H111 and A5083-H111 joint using ER4043 filler wire

The SEM-EDS mapping images of A5754 and A5083 interfaces using ER4043 are shown in Fig. 4.89 and 4.90, respectively. Table 4.22 shows EDS mapping results of the A5754-H111 and A5083-H111 interface regions. The amount of Si has gradually decreased from WM to HAZ at both the interfaces. However, the quantity of Mg and Al has increased. Si has segregated at dendrite boundaries. At A5083 interface, a compositional gradient is noticed between WMZ and EQZ. EQZ is formed next to the fusion line and Si concentration at GBs of EQZ is lower than the DBs of CCZ. However, at A5754 interface near the fusion boundary small Si segregated layers are observed instead of EQZ.

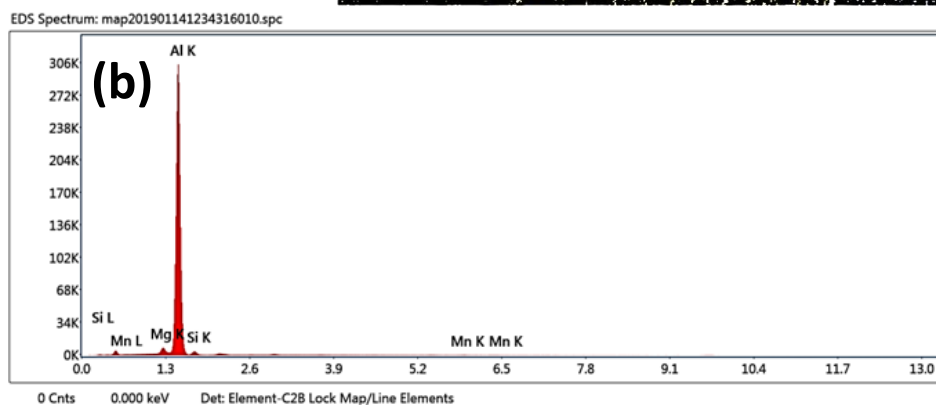
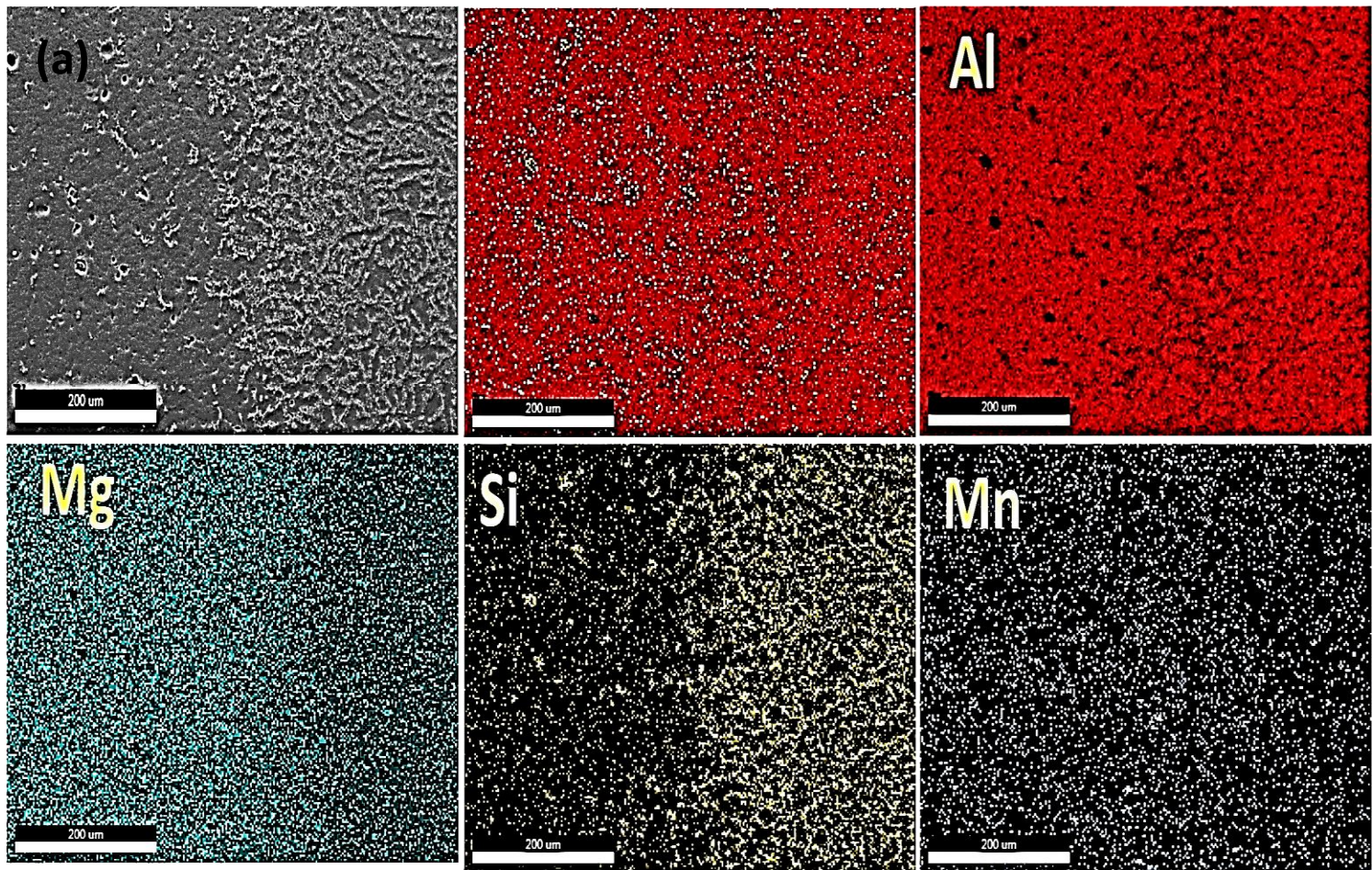
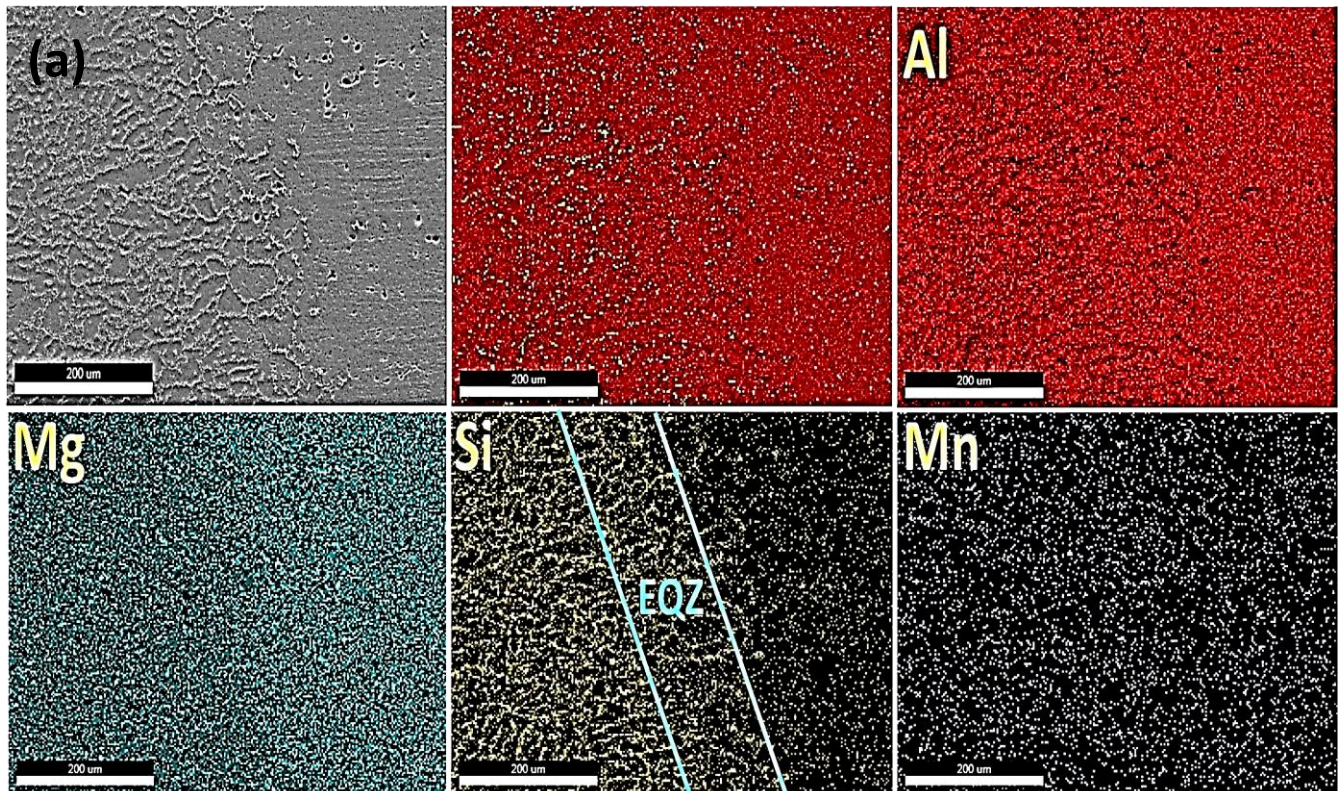


Fig. 4.89(a-b) SEM-EDS mapping images of A5754 interface and its EDS spectra in TIG welded A5754-H111 and A5083-H111 joint using ER4043



EDS Spectrum: map201901141208199080.spc

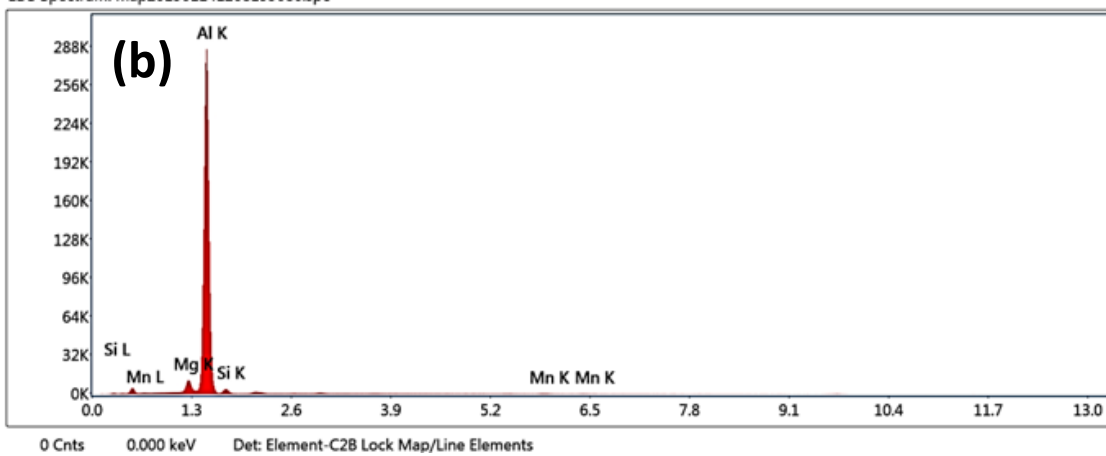


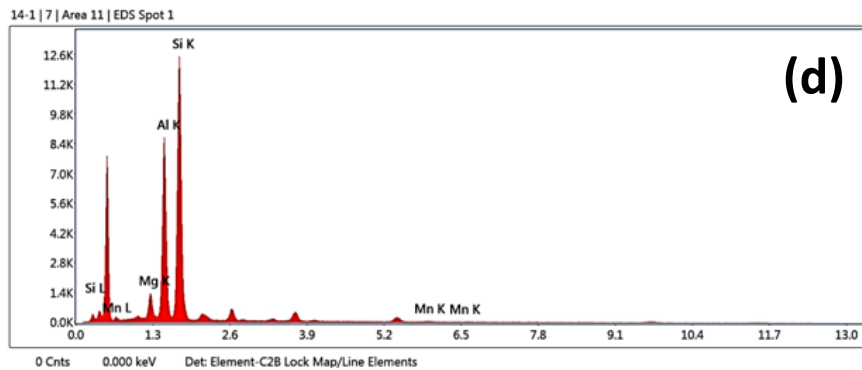
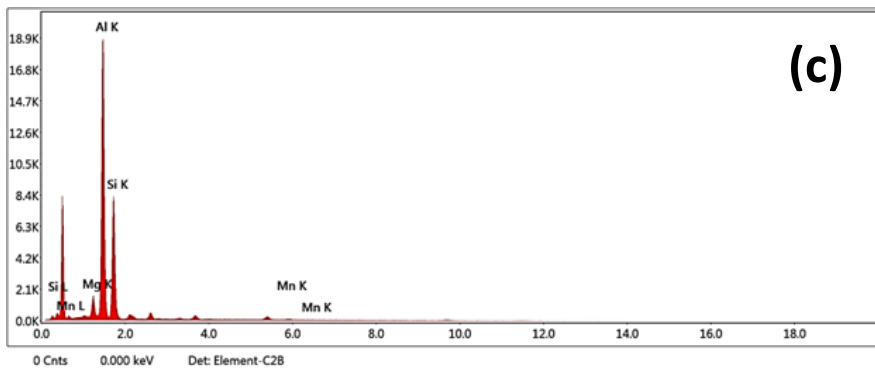
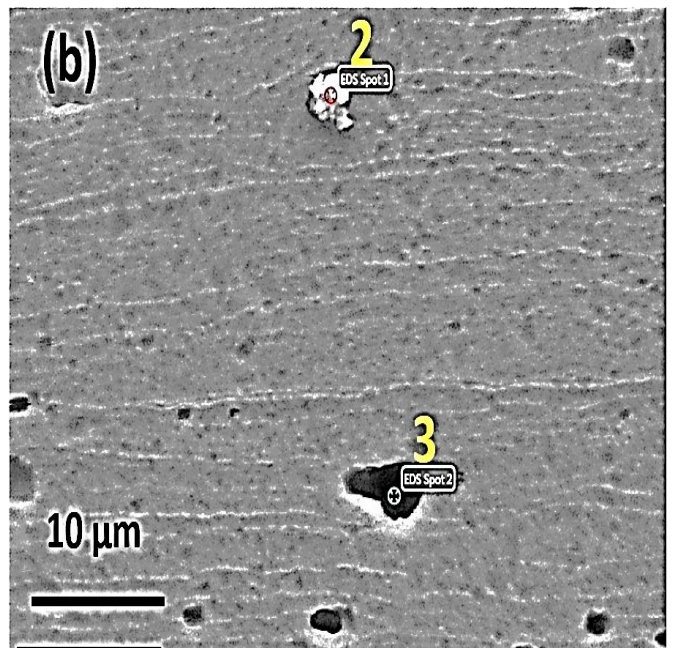
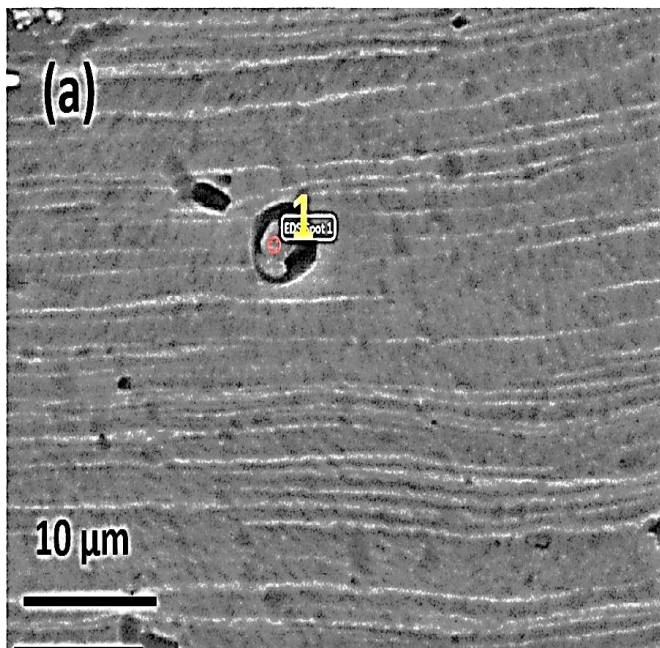
Fig. 4.90(a-b) SEM-EDS mapping images of A5083 interface and its EDS spectra in TIG welded A5754-H111 and A5083-H111 joint using ER4043

Table 4.22 EDS mapping results of interface regions of the TIG welded A5754-H111 and A5083-H111 joint using ER4043

Interface	Al	Mg	Si	Mn	Al	Mg	Si	Mn
	(wt. %)				(at. %)			
A5754	Bal.	2.7	3.1	0.3	Bal.	2.9	3	0.2
A5083	Bal.	3.8	3.3	0.5	Bal.	4.3	3.2	0.3

4.7.7 SEM-EDS analysis of HAZ precipitates in TIG welded A5754-H111 and A5083-H111 joint using ER4043 filler wire

The EDS analysis of precipitates at the HAZ of A5754 and A5083 is shown in Fig. 4.91(a) and Fig. 4.91(b). As can be seen from Table 4.23, the precipitates at spot1 and spot 2 contain high amount of Si whereas spot 3 contain higher amount of Mn. At the same time Mg content is nearly equal in all the precipitates.



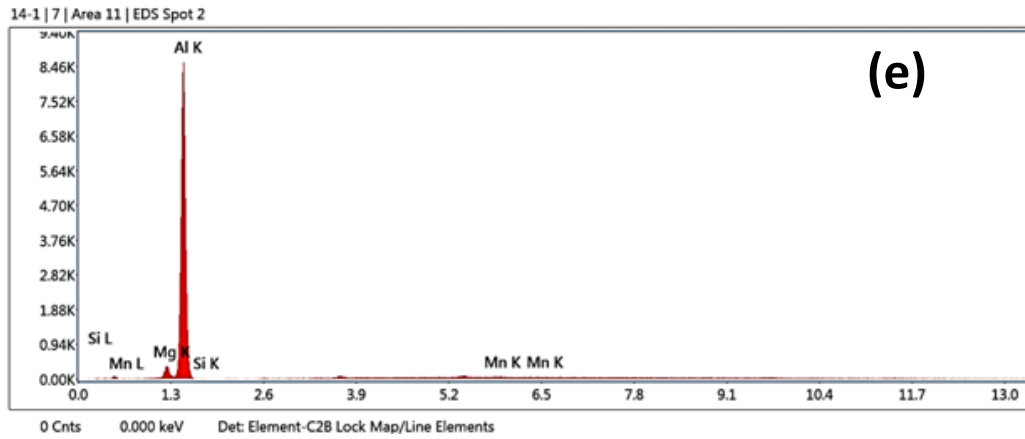


Fig. 4.91 SEM-EDS analysis of precipitates present at HAZ of the TIG welded A5754-H111 and A5083-H111 joint using ER4043 (a) HAZ of A5754 and (b) HAZ of A5083(c) EDS spectra for precipitates present at HAZ of A5754 (d-e) EDS spectra for precipitates present at HAZ of A5083

Table 4.23 EDS analysis on precipitates present at HAZ of the TIG welded A5754-H111 and A5083-H111 joint using ER4043

	Al	Mg	Si	Mn	Al	Mg	Si	Mn
	(wt. %)				(at. %)			
Point 1	Bal.	4.1	42	0.9	Bal.	4.7	41	0.5
Point 2	Bal.	4.6	63	1	Bal.	5.2	63	0.4
Point 3	Bal.	4.1	0.1	2.6	Bal.	4.7	0.1	1.3

4.7.8 Microhardness of the TIG welded A5754-H111 and A5083-H111 joint using ER4043 filler wire

Fig. 4.92 displays distribution of Vickers microhardness in the weld joint. The WMZ shows the highest hardness among all the zones including BMs when ER4043 filler is used. In ER4043 weld, EDS spot analysis on aluminium matrix (α -Al) shows significant quantities of Mg (2.4 wt.%), Si (1 wt.%) and Mn (0.3 wt.%). Since ER4043 filler contains negligible amount of Mg (0.05 wt.%) and Mn (0.05 wt.%), the significant increase of those elements in WMZ is attributed to the migration of Mg and Mn elements from BMs. The BMs of 5xxx series dissimilar joint have a significant quantity of Mg (2.6 wt.%) and Mn (0.5 wt.%) in A5754 and Mg (4.5 wt.%) and Mn (1 wt.%) in A5083. Due to this, Mg and Mn have migrated from BM to the center of the WMZ by dilution effect increasing the concentration of these elements in WMZ, which is confirmed from EDS analysis. So, the solid solution strengthening effect provided by Mg, Mn and Si elements plays a major role in the significant improvement of hardness of WMZ in ER4043 weld. The presence of Mg_2Si is also confirmed from the EDS results. These phases in WMZ have significantly increased its hardness. Additionally, fine eutectic Al-Si distributed along the equiaxed dendrites have also contributed to the improvement in hardness.

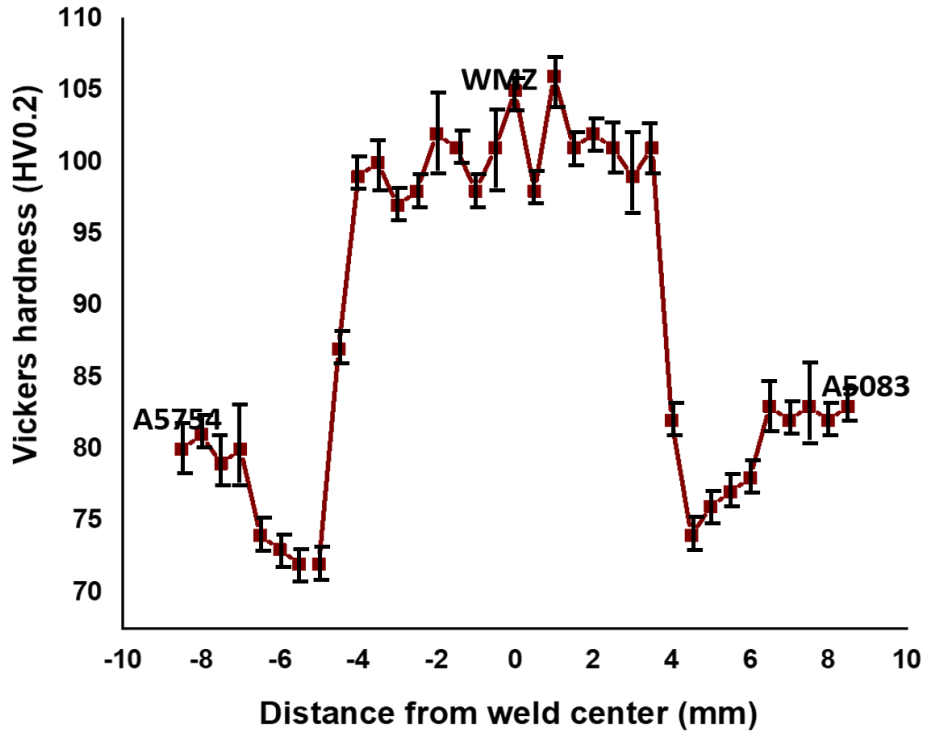


Fig. 4.92 Vickers microhardness distribution of the TIG welded A5754-H111 and A5083-H111 joint using ER4043

4.7.9 Tensile properties of the TIG welded A5754-H111 and A5083-H111 joint using ER4043 filler wire

The tensile properties of the BMs and weld joint are shown in Fig. 4.93. The tensile data of BMs and different regions of the welded samples are summarized in Table 4.24. For Al-Mg alloys, an increase in the amount of Mg by 1% leads to an increase of the tensile strength by ~34 MPa (Davis and others 1993). Because of the higher Mg content A5083 alloy shows higher strength than A5754 alloy. It can be seen that the strength of the

interface regions is lower than that of WMZ. The amount of secondary phase particles is higher at the HAZ of A5083 than at the HAZ of A5754. Thus, a significant improvement in the strength of A5083 than the A5754 is expected. However, A5083 interface shows only a slightly higher strength value than the A5754 interface. The presence of EQZ in A5083 can significantly reduce the strength. The significant improvement in strength of WMZ is attributed to solid solution strengthening effects provided by Mg, Mn and Si. Moreover, the presence of Mg_2Si and fine eutectic Al-Si along the equiaxed dendrites could also improve the strength of the WMZ.

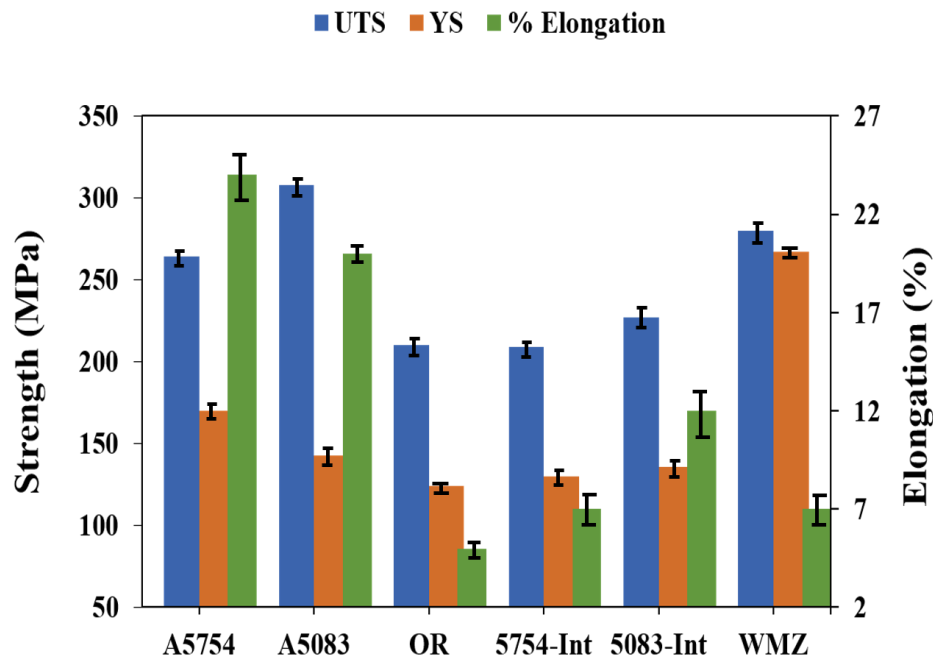


Fig. 4.93 Tensile properties of the BMs and different regions of TIG welded A5754-H111 and A5083-H111 joint using ER4043 (OR--over all weld region, Int—Interface and WMZ-weld metal zone; Gauge length of BMs and OR is 25 mm and gauge length of interfaces and WMZ is 5 mm)

Table 4.24 Tensile properties of the BMs and different regions of TIG welded A5754-H111 and A5083-H111 joint using ER4043

Sample	UTS (MPa)	YS (MPa)	Elongation (%)
A5754	264	170	24
A5083	308	143	20
TIG weld joint (A5754 int.)	209	130	7
TIG weld joint (A5083 int.)	227	136	12
TIG weld joint (WMZ)	280	267	7
TIG weld joint (overall)	210	124	5

4.7.10 Fractography of the TIG welded A5754-H111 and A5083-H111 joint using ER4043 filler wire

Fig 4.94(a-f) shows the fractography images of weld joints. The dimples are predominantly exhibited in all the regions confirming the mode of fracture to be ductile in the weld joint.

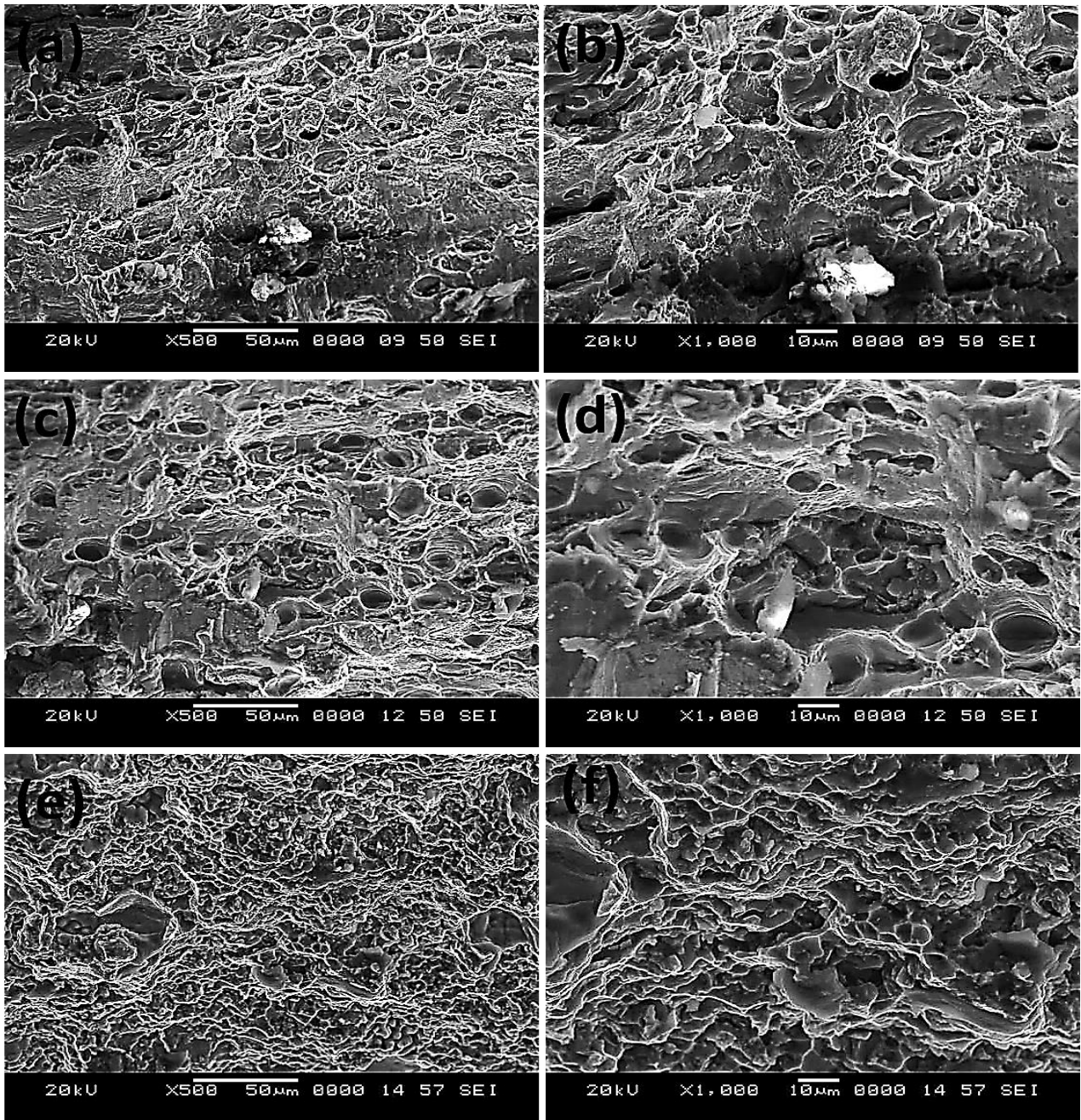


Fig. 4.94 SEM image of fracture surface of the TIG welded A5754-H111 and A5083-H111 joint using ER4043: (a-b) A5754 interface at low and high magnification; (c-d) A5083 interface at low and high magnification and (e-f) Overall weld joint at low and high magnification

4.8 Tungsten inert gas (TIG) welding of dissimilar A5754-H111 and A5083-H111 using ER5356 filler wire

4.8.1 Surface appearance of the TIG welded A5754-H111 and A5083-H111 joint using ER5356 filler wire

Fig. 4.95 shows the surface appearance of TIG welded A5754 and A5083 dissimilar joint using ER5356 filler wire. No defects are present on the surface. There are no cracks and spatter in the weldment. As can be seen from back side of the joint, full penetration is achieved.

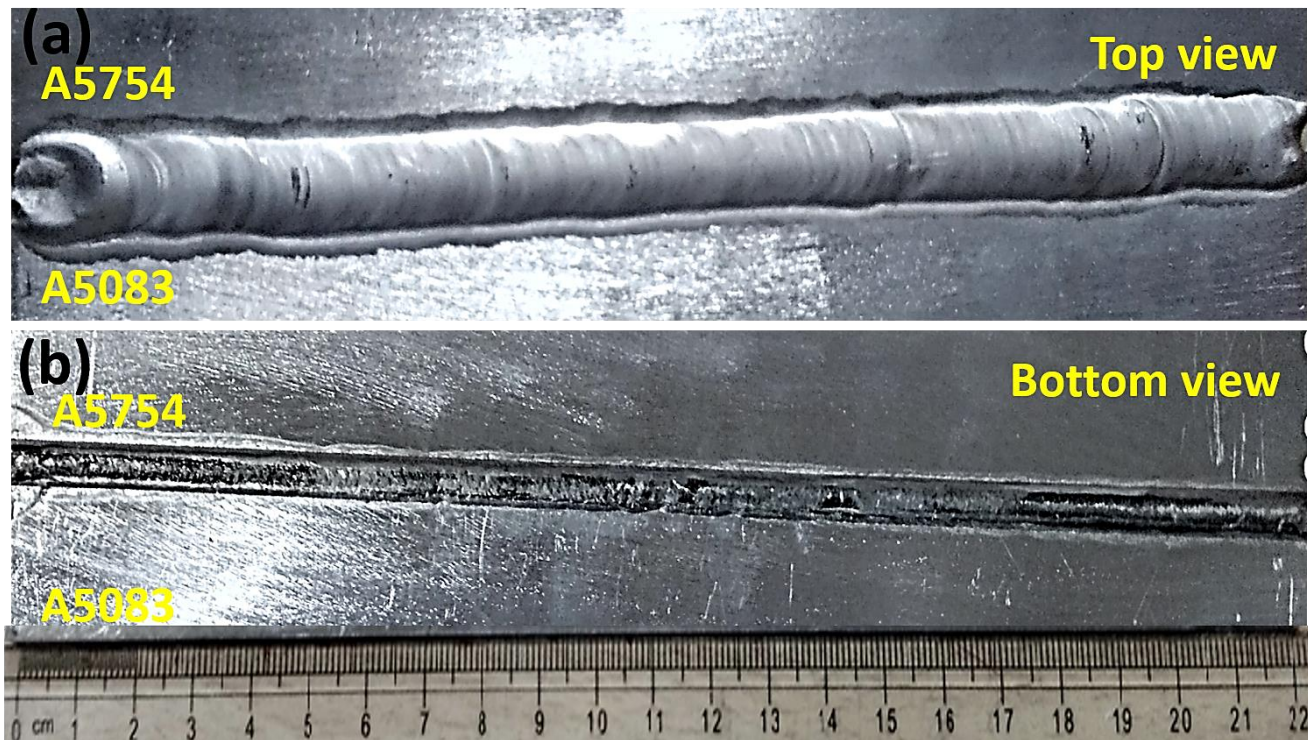


Fig. 4.95 Surface appearance of the TIG welded A5754 and A5083 joint using ER5356:

(a) Top view and (b) Bottom view

4.8.2 Macrostructure of transverse section of the TIG welded A5754-H111 and A5083-H111 joint using ER5356 filler wire

Fig. 4.96 shows macrostructure of transverse section of the joint. This further confirms that complete depth of penetration is achieved. Like surface appearance results, in the macrostructure of the cross section also shows no defects.



Fig. 4.96 Macrostructure of transverse section of the TIG welded A5754-H111 and A5083-H111 joint using ER5356

4.8.3 SEM microstructures of interface regions in TIG welded A5754-H111 and A5083-H111 joint using ER5356 filler wire

SEM images of interface regions of the A5754-A5083 weld joint using ER5356 is shown in Fig. 4.97(a-c) and Fig. 4.98(a-c). Typical zones such as HAZ, PMZ, CCZ are noticed at both interfaces. The interfaces do not show EQZ. The Columnar dendrites have grown from PMZ towards the center of the fusion zone, which is denoted by columnar crystal zone (CCZ). At PMZs, the respective Al base metals (A5754 at interface of A5754 and

A5083 at interface region of A5083) are partially melted and mixed with the Al filler material. The epitaxial growth can be achieved with minimal degree of undercooling. The temperature increase towards the weld center has suppressed the formation of fine grains, and subsequently columnar grains have grown epitaxially from the PMZ.

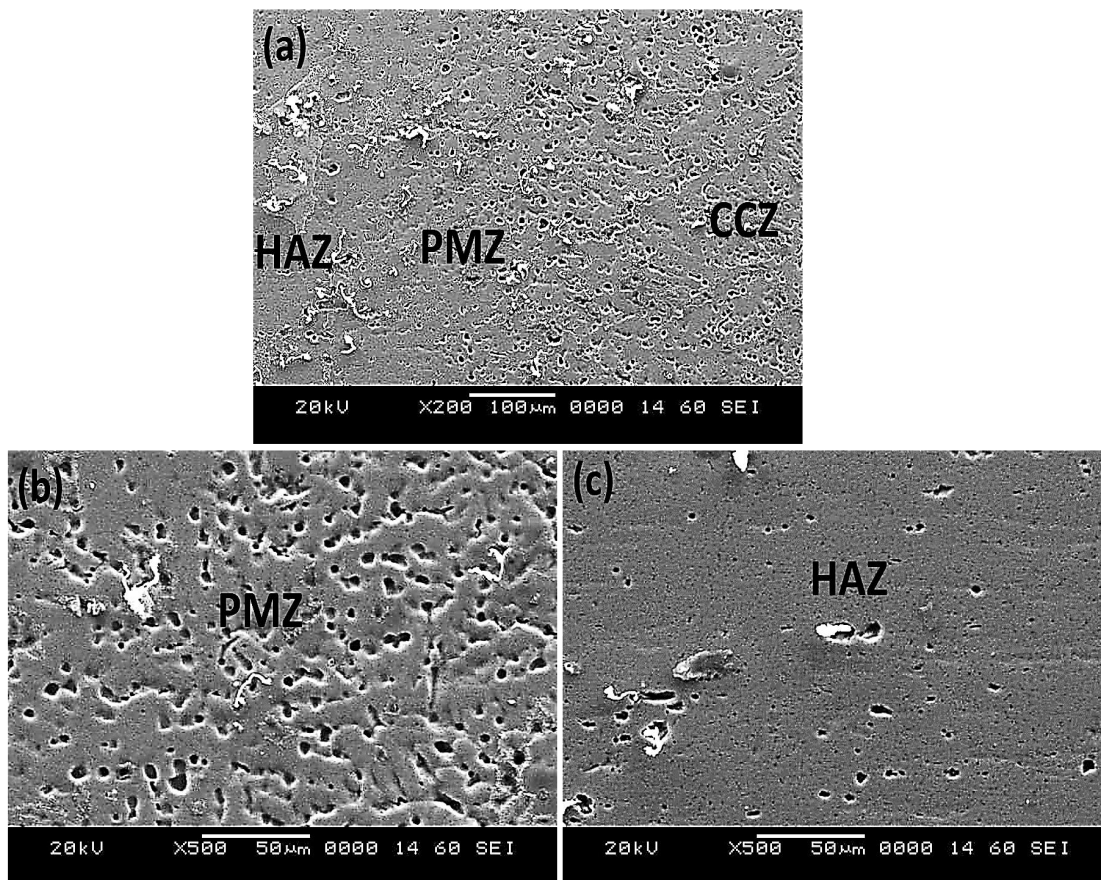


Fig. 4.97 SEM microstructure of weld joint: (a) low magnification image of Interface region of A5754; high magnification image of (b) CCZ of A5754; (c) PMZ of A5754 and (d) HAZ of A5754

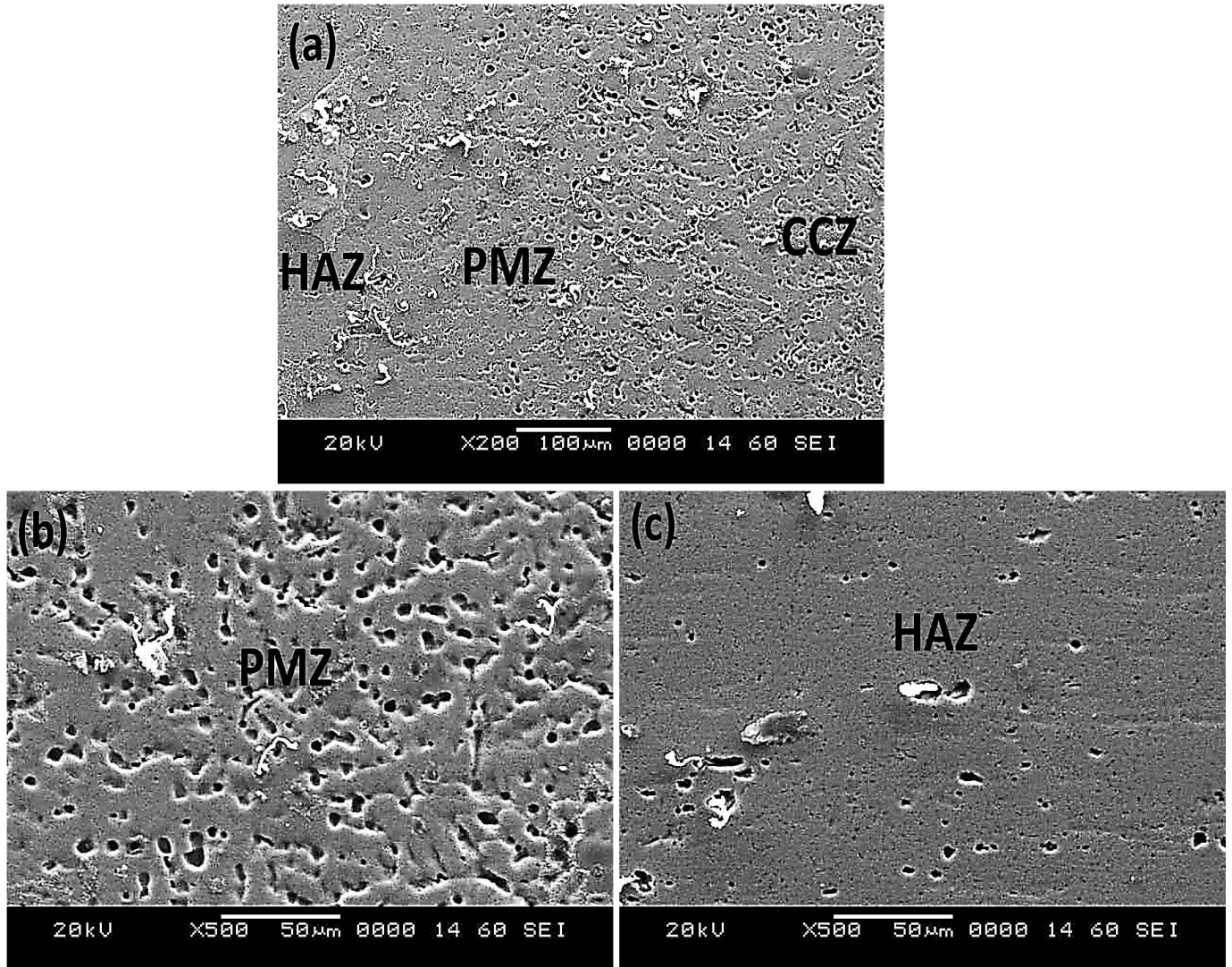


Fig. 4.98 SEM microstructure of the TIG welded A5754-H111 and A5083-H111 joint using ER5356: (a) low magnification image of interface region of A5083; high magnification image of interface region of A5083 (b) PMZ of A5083 and (c) HAZ of A5083

4.8.4 SEM microstructure of WMZ center in TIG welded A5754-H111 and A5083-H111 joint using ER5356 filler wire

Fig. 4.99 shows SEM microstructure of WMZ center. Mg is segregated at the dendrite boundaries in WMZ of Al-Mg filler. Mg enriched strips are non-continuous at dendrite boundaries in WMZ center. The black colored secondary phase particles are observed in WMZ of Al-Mg filler. The dendrites at the WMZ interface are columnar in structure and dendrites at the WMZ center are equiaxed in structure. The microstructure evolution in the molten pool mainly depends on solute concentration (C_0), crystallization rate (R) and temperature gradient (G) in the liquid phase (Wang et al. 2016a). The G/R ratio plays a vital role to identify a solidification mode and microstructure (Wang et al. 2016a). The value of G/R ratio is lower at the weld center, and consequently equiaxed dendrite structure is evolved. At the same time, the higher G/R ratio has led to the formation of columnar dendrites near the fusion line (Fig. 4.97 (a) and Fig. 4.98 (a)).

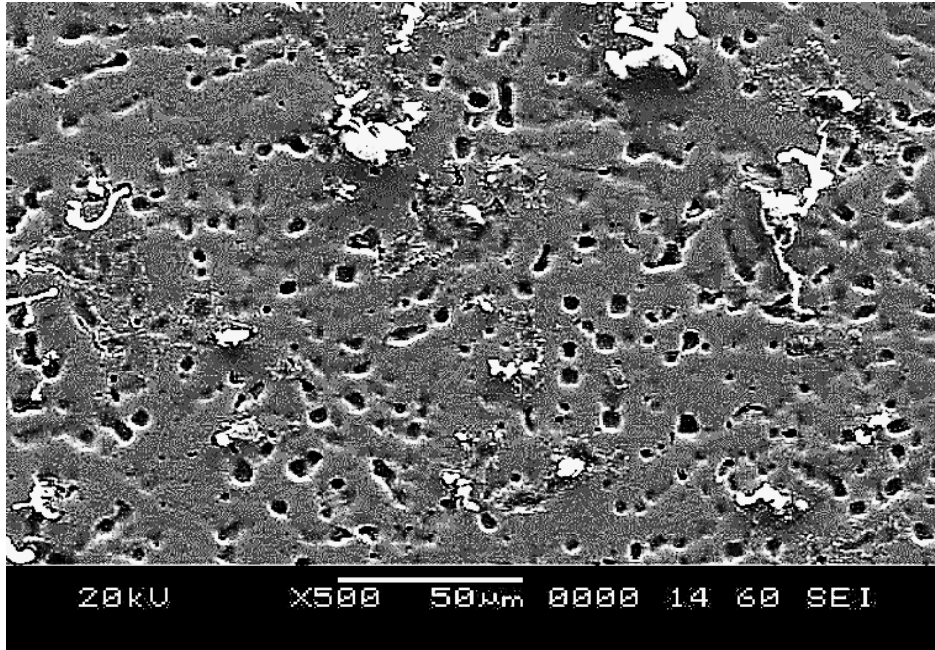
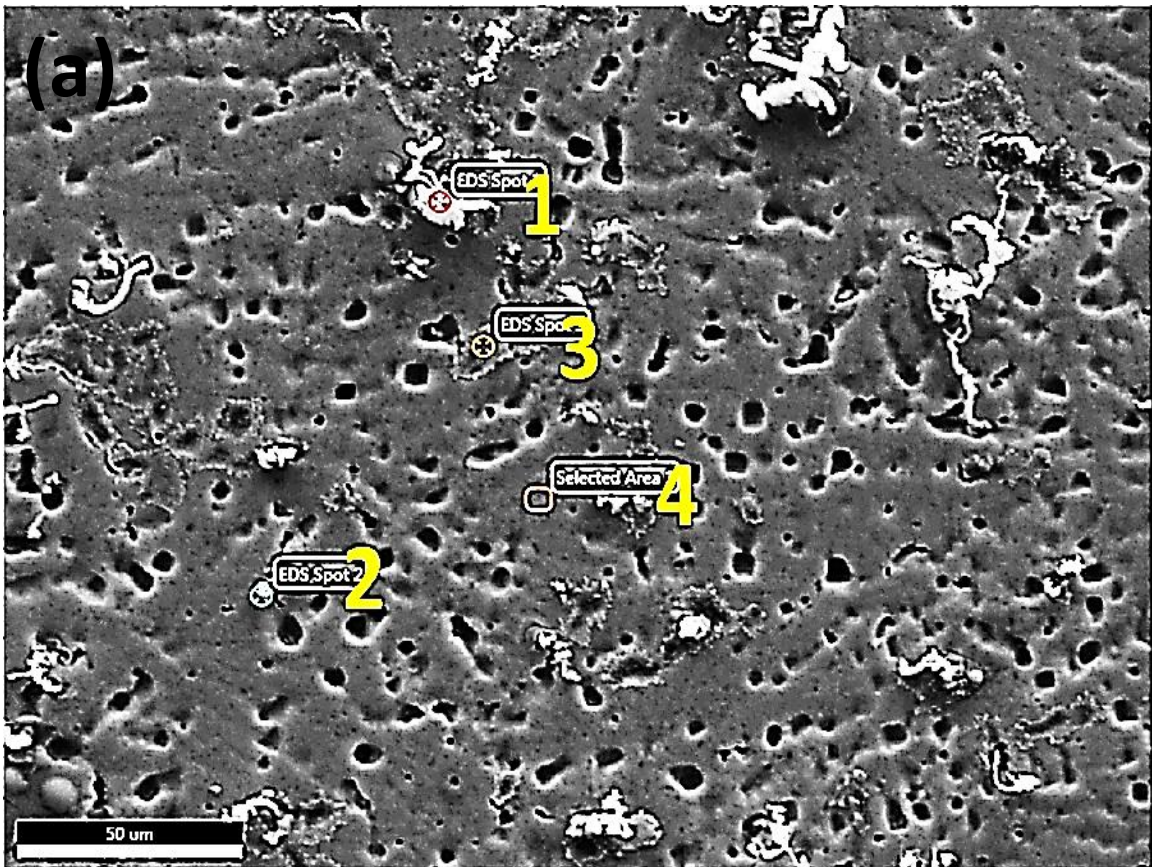


Fig. 4.99 SEM microstructure of WMZ center in TIG welded A5754-H111 and A5083-H111 joint using ER5356

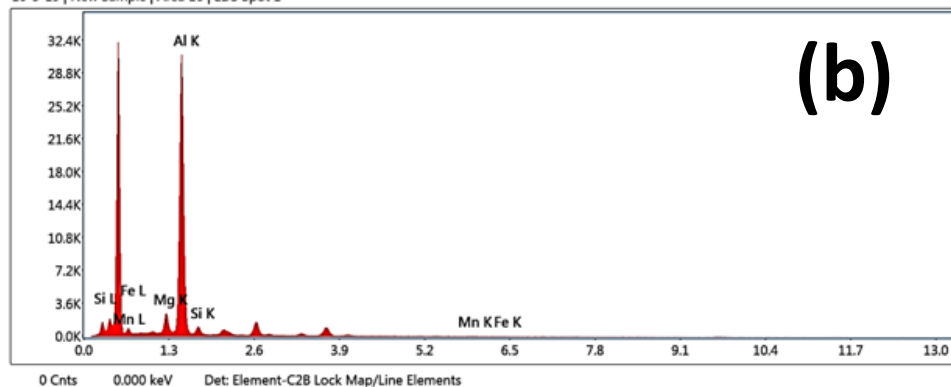
4.8.5 SEM-EDS of WMZ center in TIG welded A5754-H111 and A5083-H111 joint using ER5356 filler wire

Fig. 4.100 shows SEM-EDS spot analysis at the center of the WMZ. The composition of elements is summarized in Table 4.25. The composition confirms that this region contains Al rich matrix and secondary eutectic phases. EDS analysis of spot 4 shows a composition corresponding to that of the filler material. The spot 1 EDS analysis was done on secondary phase particle. The analysis reveals that the phases consist largely of Al and Mg with some quantities of Si and Mn. Thus, this particle is identified as Al_3Mg_2 intermetallic

phases. A previous research work has also reported the presence of Al_3Mg_2 phases (Mishra 2018; Murray et al. 1986). The spot 2 EDS analysis was done on the white coloured spherical shaped secondary phase particle. The analysis reveals that the particles are Mg_2Si particles. The spot 3 EDS analysis was done on the segregated layer in the matrix that has revealed higher amounts of Si in the region.

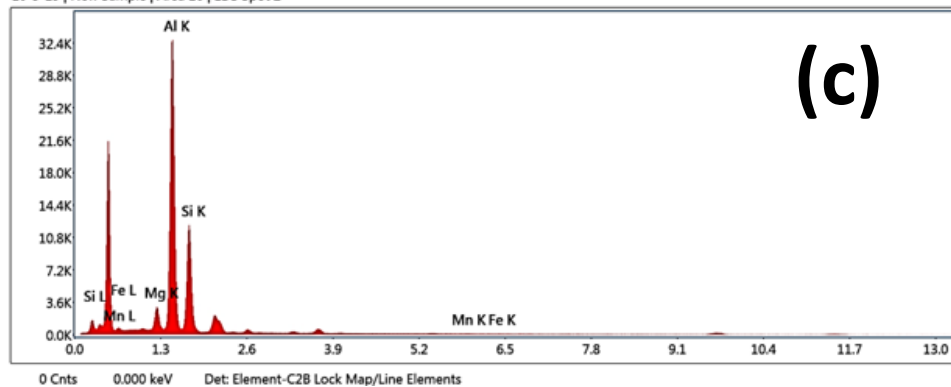


10-5-19 | New Sample | Area 16 | EDS Spot 1



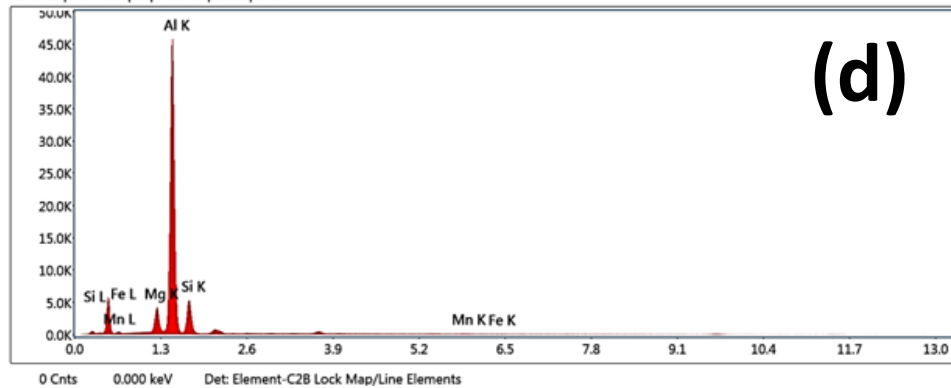
(b)

10-5-19 | New Sample | Area 16 | EDS Spot 2



(c)

10-5-19 | New Sample | Area 16 | EDS Spot 3



(d)

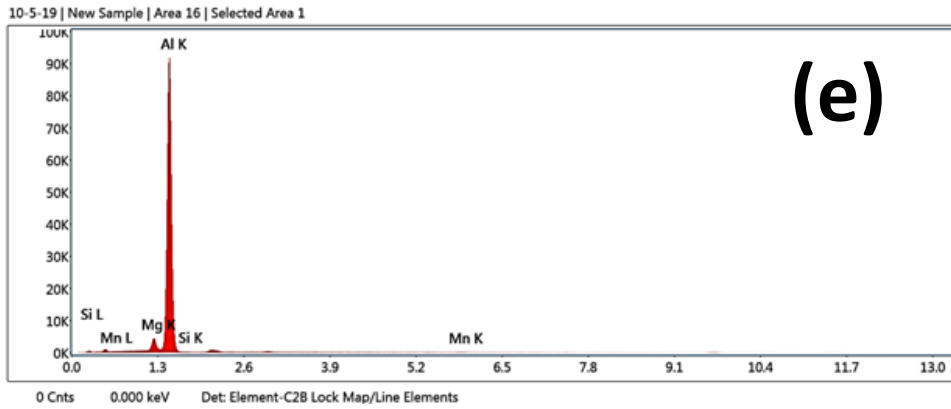


Fig. 4.100 SEM-EDS spot analysis of the TIG welded A5754-H111 and A5083-H111 joint using ER5356: (a) WMZ center; (b-e) EDS spectra of spot analysis

Table 4.25 EDS analysis on precipitates present at WMZ center in TIG welded A5754-H111 and A5083-H111 joint using ER5356

	Al	Mg	Si	Mn	Fe	Al	Mg	Si	Mn	Fe
	(wt. %)					(at. %)				
Point 1	Bal.	6.6	5.7	0.6	0.4	Bal.	7.4	5.5	0.3	0.2
Point 2	Bal.	4.6	37.9	0.4	0.2	Bal.	5.1	36.9	0.2	0.1
Point 3	Bal.	6.3	18.2	0.6	0.3	Bal.	7	17.6	0.3	0.1
Point 4	Bal.	4.6	0.05	0.4	-	Bal.	5.1	0.04	0.2	-

4.8.6 SEM-EDS of WMZ center and interface regions of the TIG welded A5754-H111 and A5083-H111 joint using ER5356 filler wire

The SEM-EDS mapping images of WMZ center are shown in Fig. 4.101. SEM-EDS mapping images of A5754 and A5083 interfaces using ER5356 are shown in Fig. 4.102 and 4.103, respectively. Mg has gradually decreased from WM to HAZ at the A5754 interface. Since the filler and A5083 have almost similar amount of Mg (5%), no difference is noticed in Mg distribution at A5083 interface. Table 4.26 shows EDS mapping results of the interface regions and WMZ.

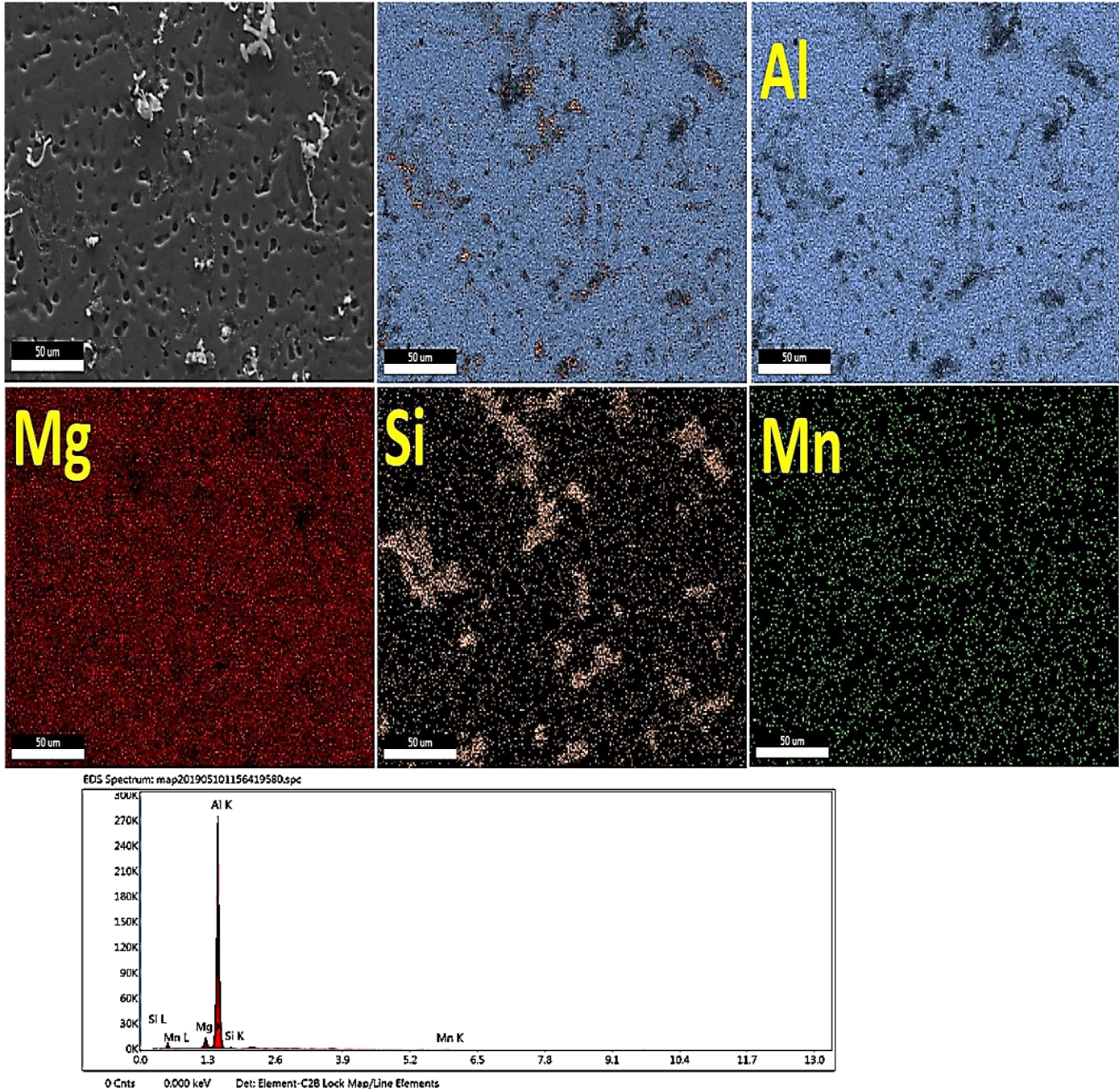


Fig. 4.101 SEM-EDS mapping images and its EDS spectra of WMZ center in TIG welded A5754-H111 and A5083-H111 joint using ER5356

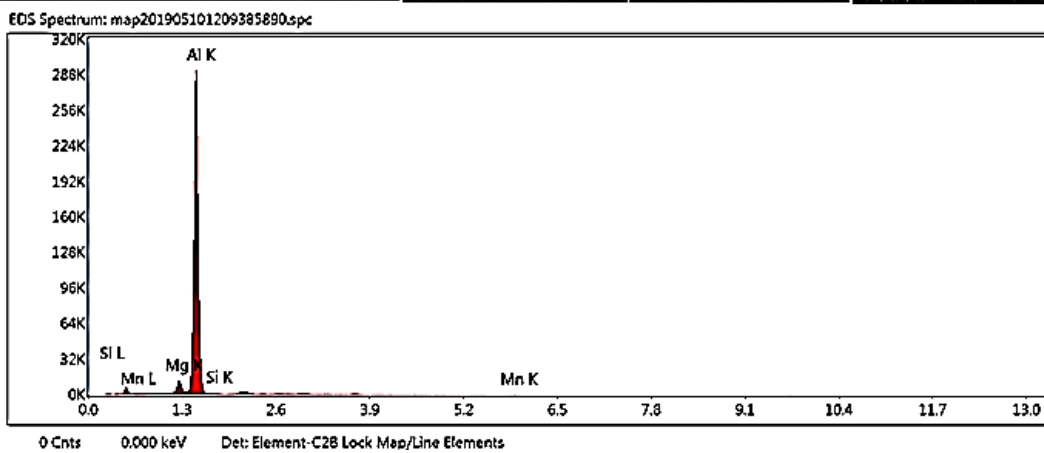
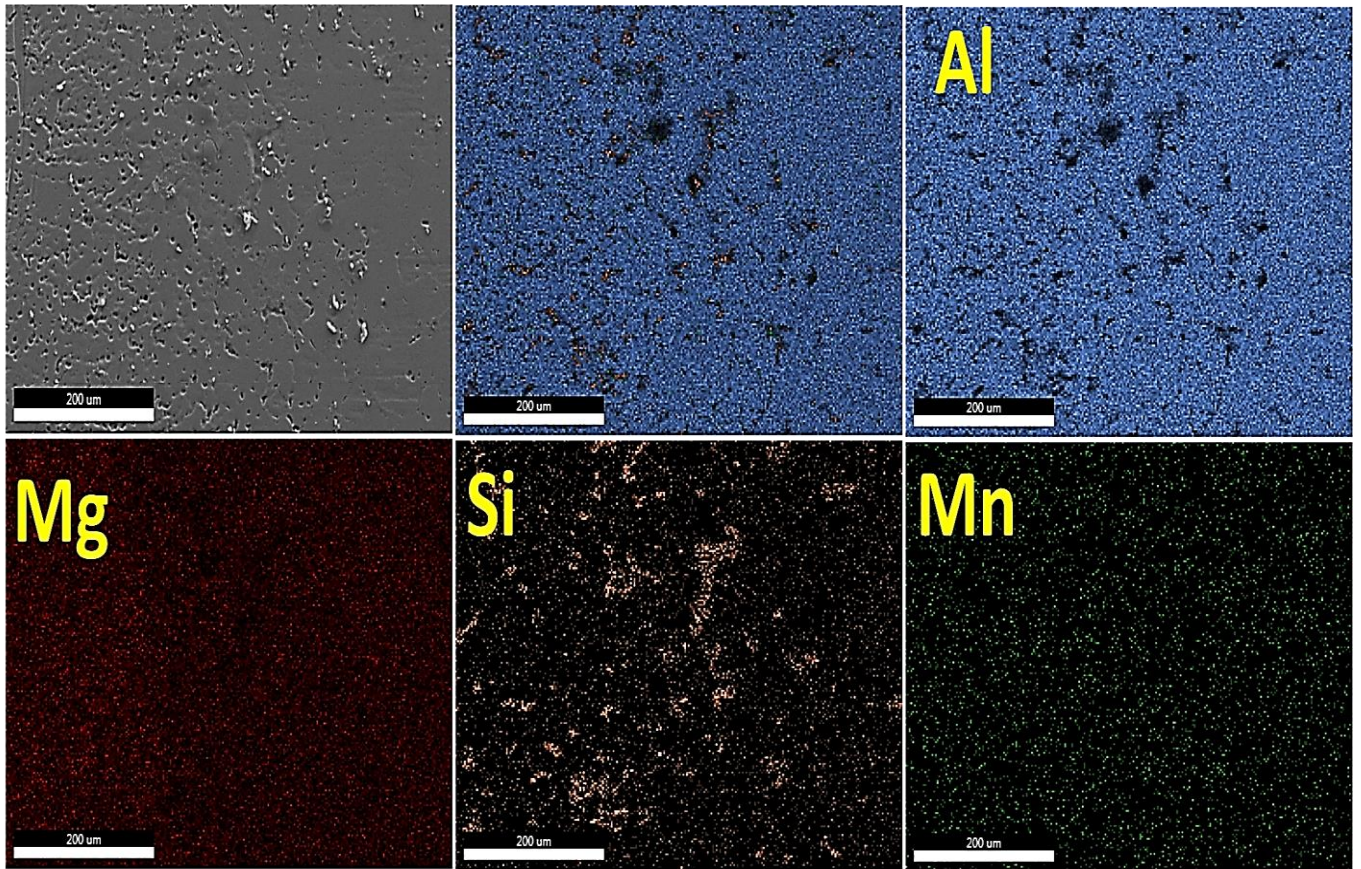


Fig. 4.102 SEM-EDS mapping images and its EDS spectra of A5754 interface in TIG welded A5754-H111 and A5083-H111 joint using ER5356

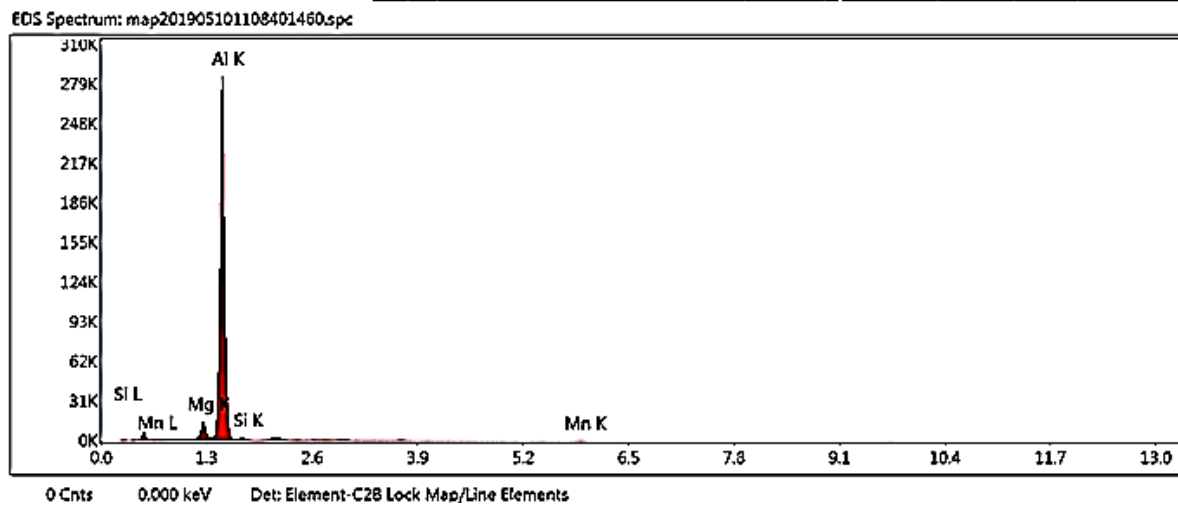
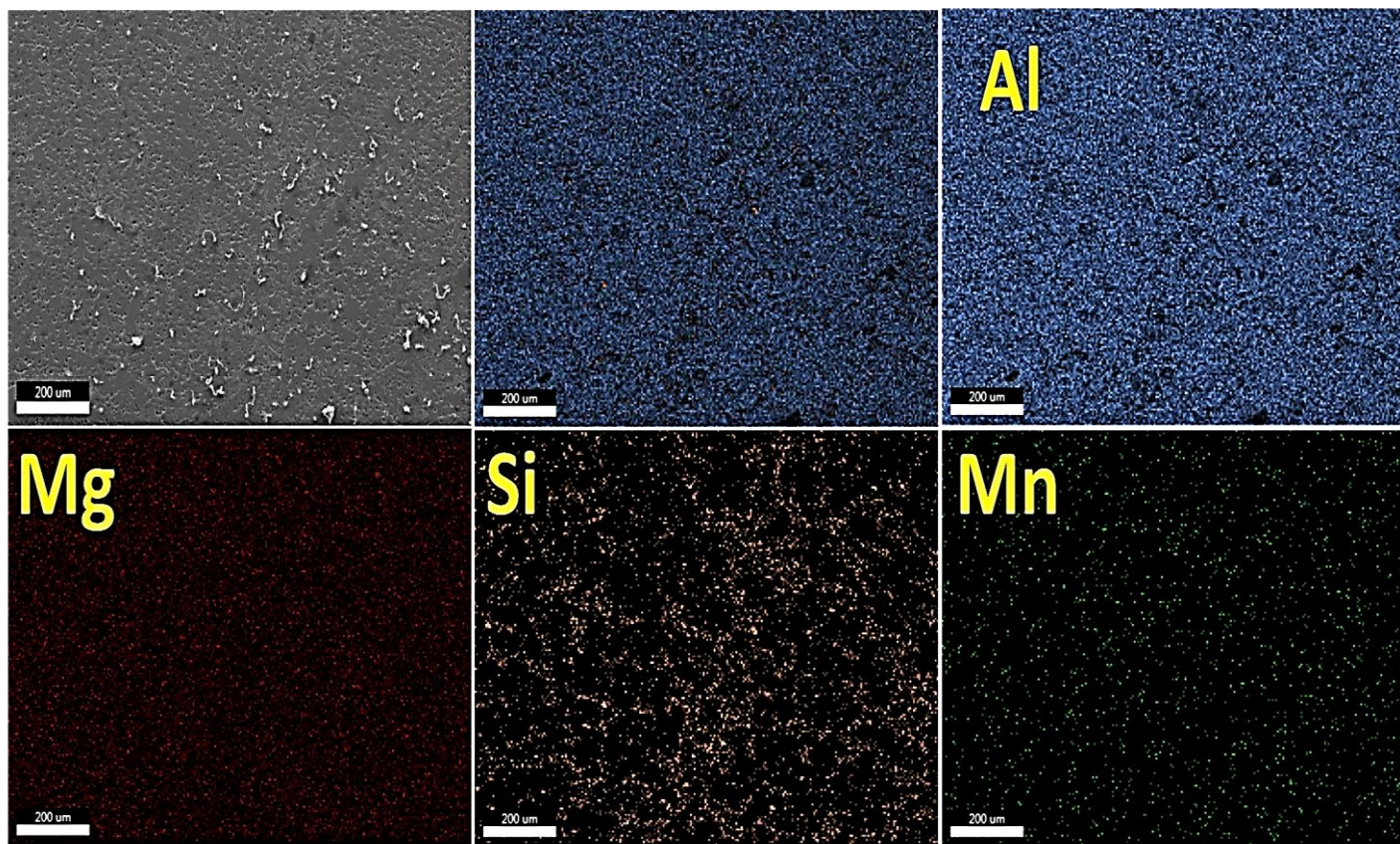


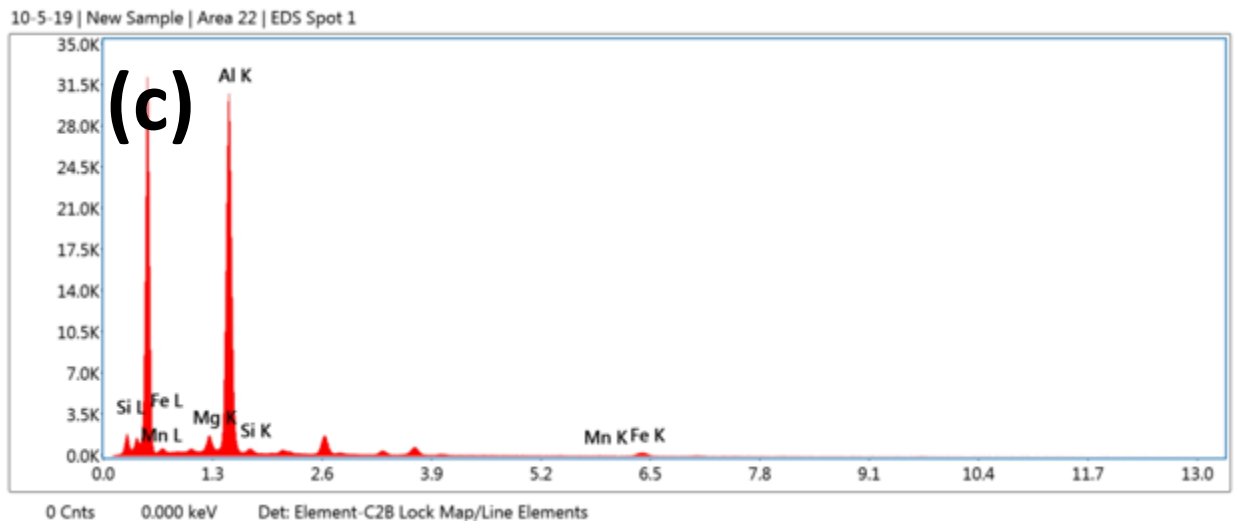
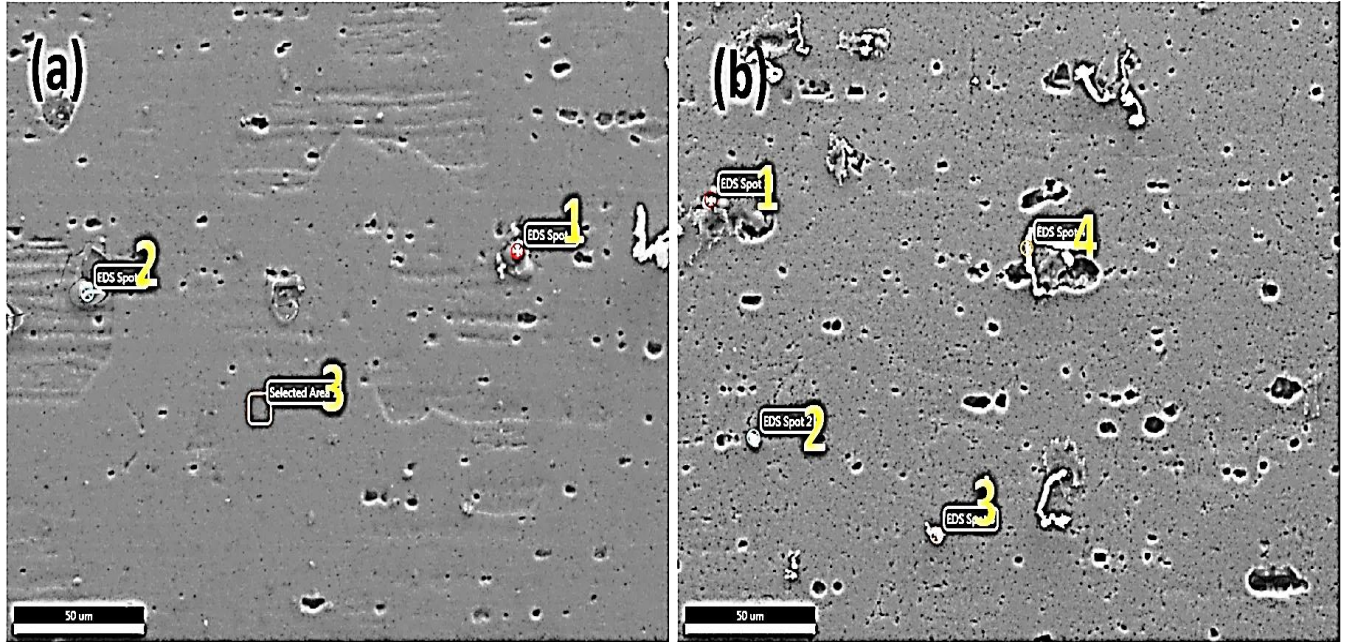
Fig. 4.103 SEM-EDS mapping images and its EDS spectra of A5083 interface in TIG welded A5754-H111 and A5083-H111 joint using ER5356

Table 4.26 EDS mapping results of the interface regions and WMZ center in TIG welded A5754-H111 and A5083-H111 joint using ER5356

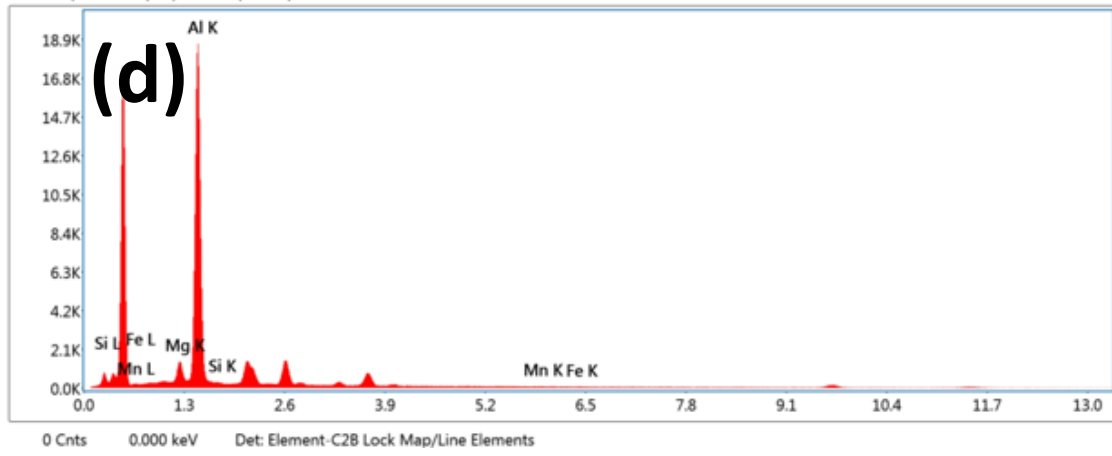
Region	Al	Mg	Si	Mn	Al	Mg	Si	Mn
	(wt. %)				(at. %)			
A5754 (Interface)	Bal.	4.1	1	0.3	Bal.	4.5	0.9	0.1
A5083 (Interface)	Bal.	4.8	1.8	0.5	Bal.	5.3	1.7	0.3
WMZ(Center)	Bal.	4.6	1.5	0.4	Bal.	5.1	1.4	0.2

4.8.7 SEM-EDS of HAZs in TIG welded A5754-H111 and A5083-H111 joint using ER5356 filler wire

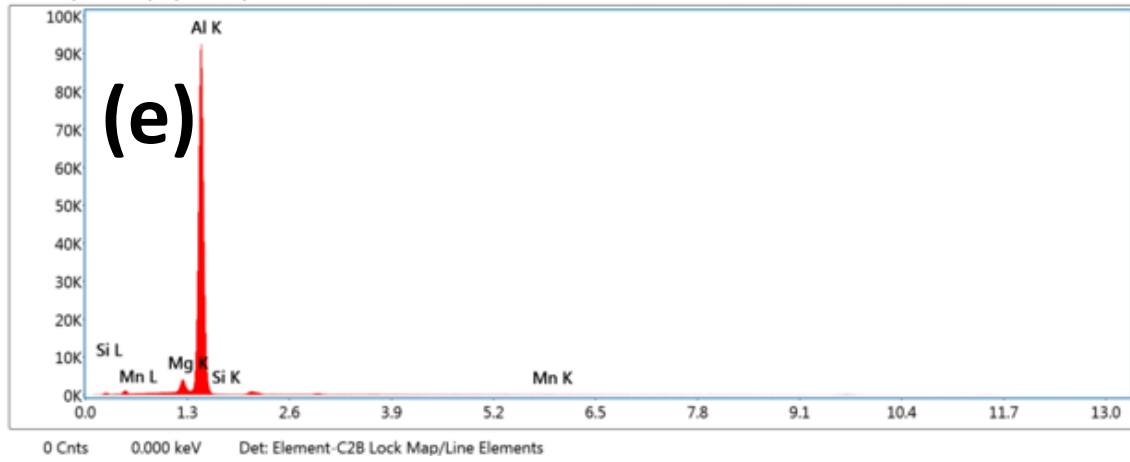
Fig. 4.104 shows SEM-EDS spot analysis at the HAZs of both the sides of the dissimilar joint and the composition of elements is summarized in Table 4.27 and Table 4.28. The spot 1 EDS analysis of A5754 HAZ and spot 2 EDS analysis of A5083 HAZ show Fe in a significant quantity, besides Mn. The analysis reveals that the phases are Al_6MnFe particles. The spot 1 and spot 4 EDS analyses of A5083 HAZ and spot 2 EDS analysis of A5754 HAZ show higher quantities of Mg and Si. These phases are possibly Mg_2Si phases. The spot 3 analyses of A5083 HAZ and A5754 HAZ show Mg in higher quantities, corresponding possibly to Al_3Mg_2 phases.



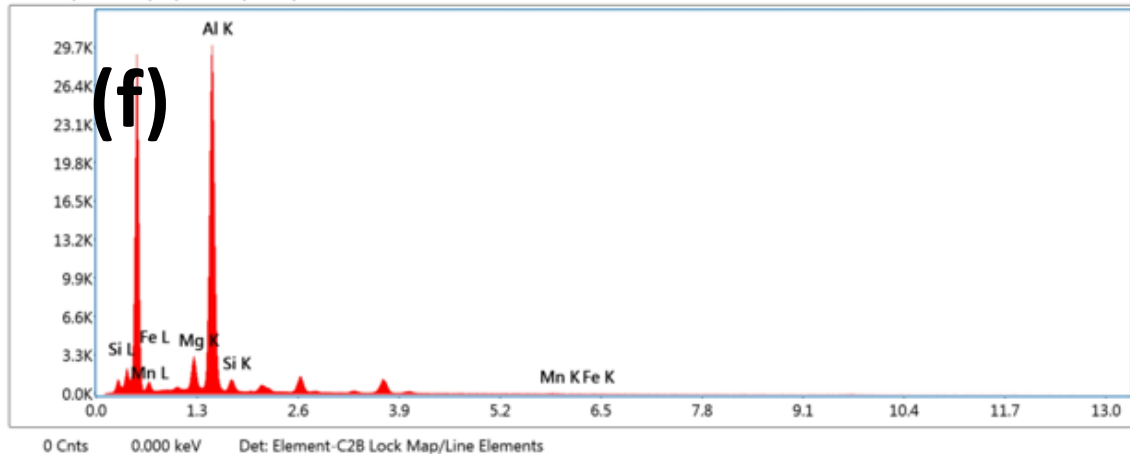
10-5-19 | New Sample | Area 22 | EDS Spot 2



10-5-19 | New Sample | Area 22 | Selected Area 1



10-5-19 | New Sample | Area 13 | EDS Spot 1



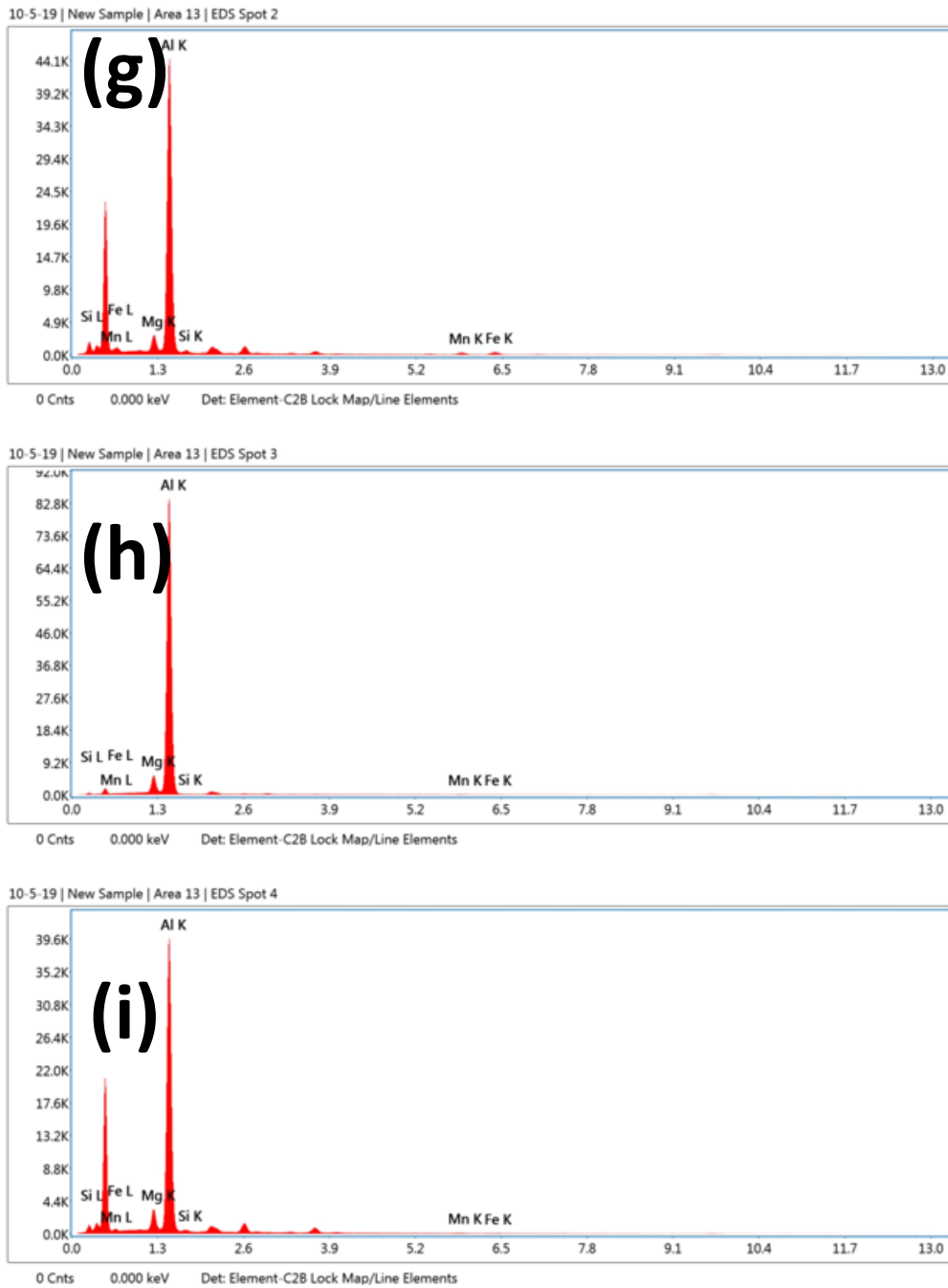


Fig. 4.104 SEM EDS spot analysis of HAZ of the TIG welded A5754-H111 and A5083-H111 joint using ER5356 (a) A5754; (b) A5083; (c-e) EDS spectra for spots on A5754 and (f-i) EDS spectra for spots on A5083

Table 4.27 EDS analysis of precipitates present at HAZ of A5754 in TIG welded A5754-H111 and A5083-H111 joint using ER5356

	Al	Mg	Si	Mn	Fe	Al	Mg	Si	Mn	Fe
	(wt. %)					(at. %)				
Point 1	Bal.	5.4	2.7	0.6	4.7	Bal.	6.1	2.7	0.3	2.3
Point 2	Bal.	7.1	1.7	0.8	0.6	Bal.	7.9	1.6	0.4	0.3
Point 3	Bal.	4.3	0.02	0.3	-	Bal.	4.8	0.02	0.2	-

Table 4.28 EDS analysis of precipitates present at HAZ of A5083 in TIG welded A5754-H111 and A5083-H111 joint using ER5356

	Al	Mg	Si	Mn	Fe	Al	Mg	Si	Mn	Fe
	(wt. %)					(at. %)				
Point 1	Bal.	8.3	6.5	0.9	0.4	Bal.	9.2	6.2	0.4	0.2
Point 2	Bal.	5.3	1.5	2.9	3.7	Bal.	6	1.5	1.4	1.8
Point 3	Bal.	5.8	0.02	0.5	0.2	Bal.	6.5	0.02	0.2	0.08
Point 4	Bal.	6.7	1.5	0.7	0.4	Bal.	7.5	1.4	0.4	0.2

4.8.8 Vickers microhardness of the TIG welded A5754-H111 and A5083-H111 joint using ER5356 filler wire

Fig. 4.105 displays distribution of Vickers microhardness in the weld joint. Hardness adjacent to the WMZ has shown an increase towards the BMs. The BMs exhibit higher hardness than the WMZ, respective PMZ and HAZ. At the same time, WMZ shows maximum hardness among PMZs and HAZs on both the sides. The lower hardness in HAZ is mainly attributed to the difference in temperature gradients of weld thermal cycle. The HAZs have undergone a temperature higher than the recrystallization temperature of the BMs due to weld thermal cycle. This leads to lower the work hardening effect in BMs, subsequently lowering the hardness. The presence of Al_3Mg_2 and Mg_2Si particles significantly increases the hardness of WMZ. Moreover, Mg and Mn form a solid solution with Al in WMZ increasing the solid solution strengthening effect that increases the hardness of WMZ.

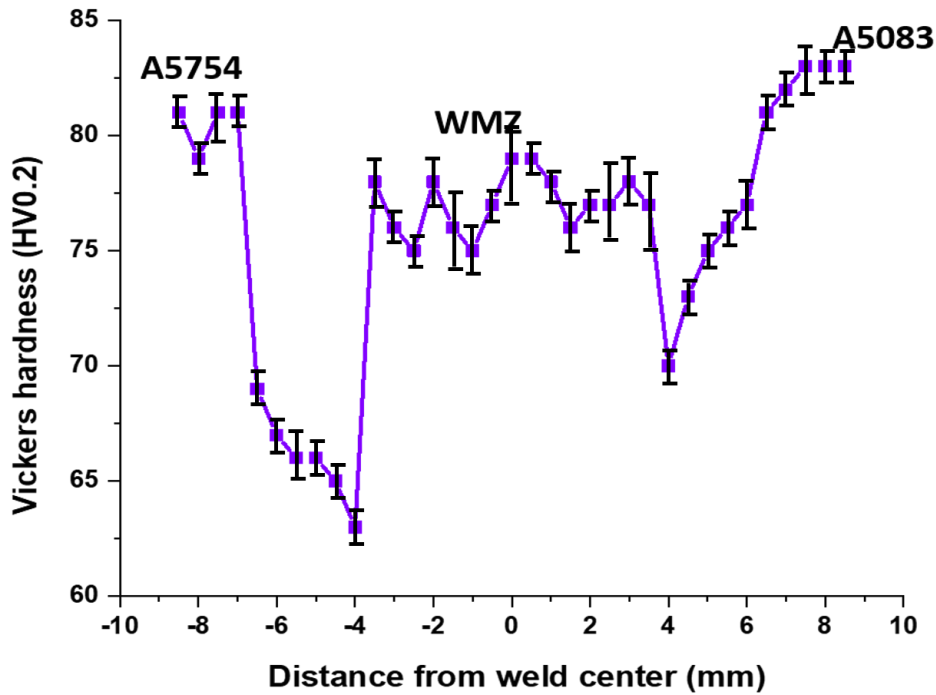


Fig. 4.105 Vickers microhardness distribution of the TIG welded A5754-H111 and A5083-H111 joint using ER5356

4.8.9 Tensile properties of the TIG welded A5754-H111 and A5083-H111 joint using ER5356 filler wire

Fig. 4.106 shows stress-strain curves of the BMs and different regions of the weld joint. Table 4.29 lists yield strength (YS), ultimate tensile strength (UTS) and % of elongation values that are extracted from the tensile test curves. WMZ exhibits higher YS than both the BMs, slightly higher UTS than A5754 but lower UTS than A5083. The presence of equiaxed dendrite structure in WMZ has been reported to reduce the possibility of solidification cracking tendency resulting in better strength, fatigue life and toughness of

the weldment (Cui et al. 2012; Kou 2003). The migration of Mg and Mn from BM to WMZ has raised the amount of these elements in the WMZ compensating the loss of secondary phase strengthening as well as solid solution strengthening effects. Porosities such as hydrogen pores, pores due to loss of alloying elements and shrinkage pores have not been observed in the WMZ. All these are possible reasons for the increased strength of the WMZ.

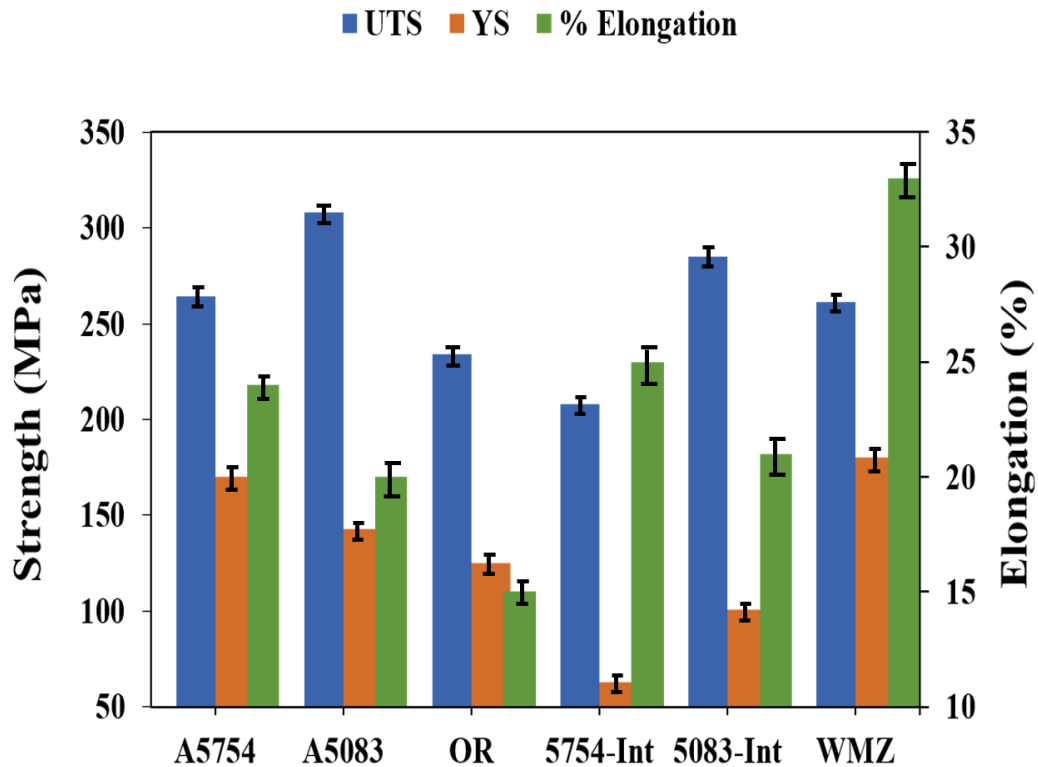


Fig. 4.106 Tensile properties of the BMs and different regions of TIG welded A5754-H111 and A5083-H111 joint using ER5356 (OR-over all weld region, Int-Interface and WMZ-weld metal zone; Gauge length of BMs & OR is 25 mm and gauge length of interfaces and WMZ is 5 mm)

Table 4.29 Tensile properties of the BMs and different regions of TIG welded A5754-H111 and A5083-H111 joint using ER5356

Sample	UTS (MPa)	YS (MPa)	Elongation (%)
A5754	264	170	24
A5083	308	143	20
TIG weld joint (A5754 int.)	208	63	25
TIG weld joint (A5083 int.)	285	101	21
TIG weld joint (WMZ)	261	180	33
TIG weld joint (OR)	234	125	15

4.8.10 Fractography of the TIG welded A5754-H111 and A5083-H111 joint using ER5356 filler wire

The fracture surfaces of weld samples are shown in Fig. 4.107(a-f). Numerous tiny dimples are distributed on the fracture surface of all the regions indicating the mode of fracture to be ductile.

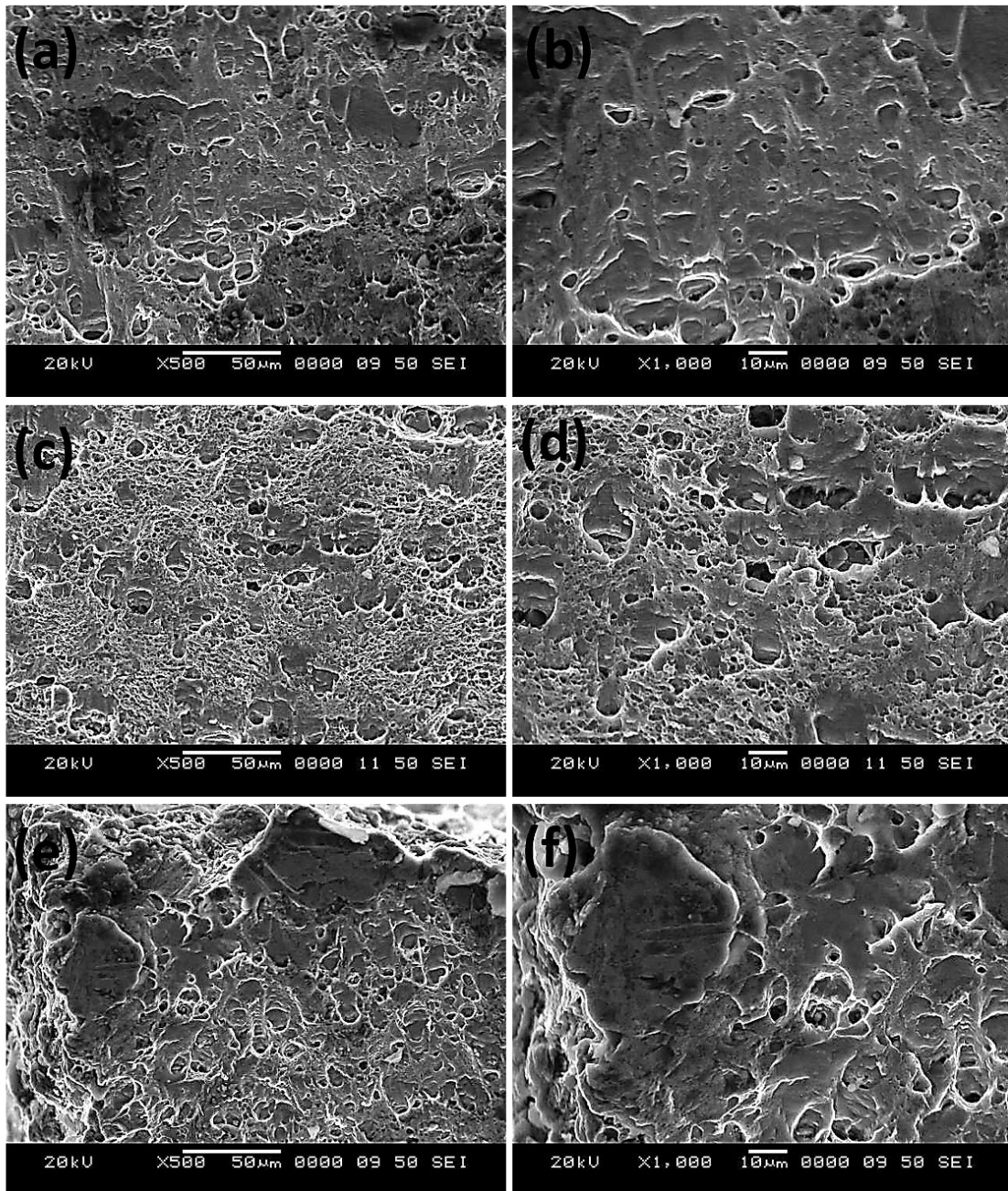


Fig. 4.107 SEM images of fracture surface of the TIG welded A5754-H111 and A5083-H111 joint using ER5356: (a-b) A5754 interface at low and high magnification; (c-d) A5083 interface at low and high magnification and (e-f) Overall weld joint at low and high magnification

4.9 Friction stir welding (FSW) of dissimilar A6061-T6 and A6082-T6

4.9.1 Surface appearance of the FSWed A6061-T6 and A6082-T6

Fig 4.108 shows the surface appearance of the FSWed dissimilar aluminium alloys. There are no defects in the surface and it was smooth. Small flash was observed on both AS and RS. A hole was visible at the end of FSWed weld.

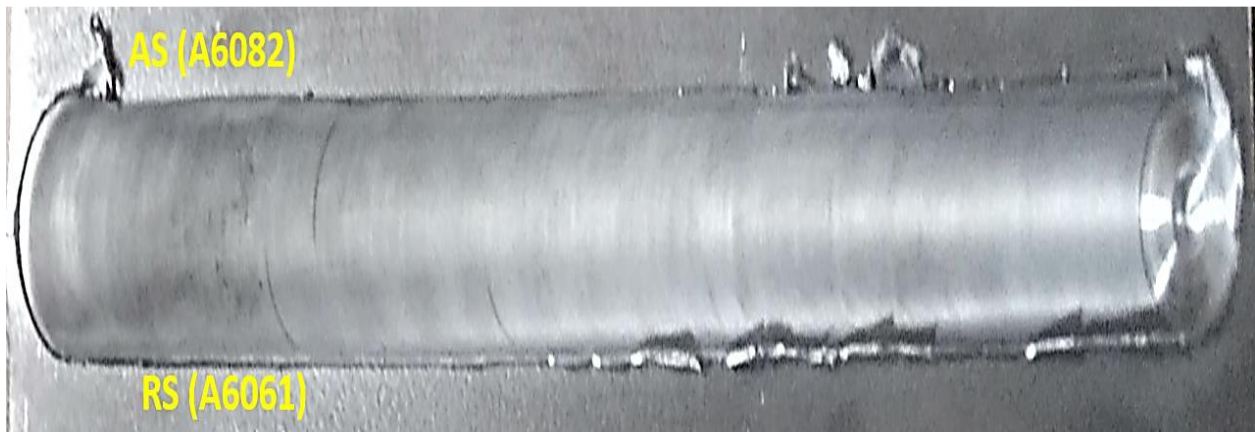


Fig. 4.108 Surface appearances of the FSWed A6061-T6 and A6082-T6 joint

4.9.2 Macrostructure of transverse section of FSWed A6061-T6 and A6082-T6

Fig. 4.109 shows macroscopic appearance of transverse section of FSW A6061-A6082 dissimilar aluminium alloys joint. Penetration of the joint is full. Defects are completely absent in the cross section of the joint. The weld surface appearance and the macro and microstructures have not shown any welding defects indicating thereby that the chosen parameters in the present study have created a balance material flow during FSW and

produced defect free welding. The colour difference is clearly visible between AS (A6082) and RS (A6061). A continuous “S” line (boundary between the two dissimilar aluminium alloys) is observed at the centre of the SZ.

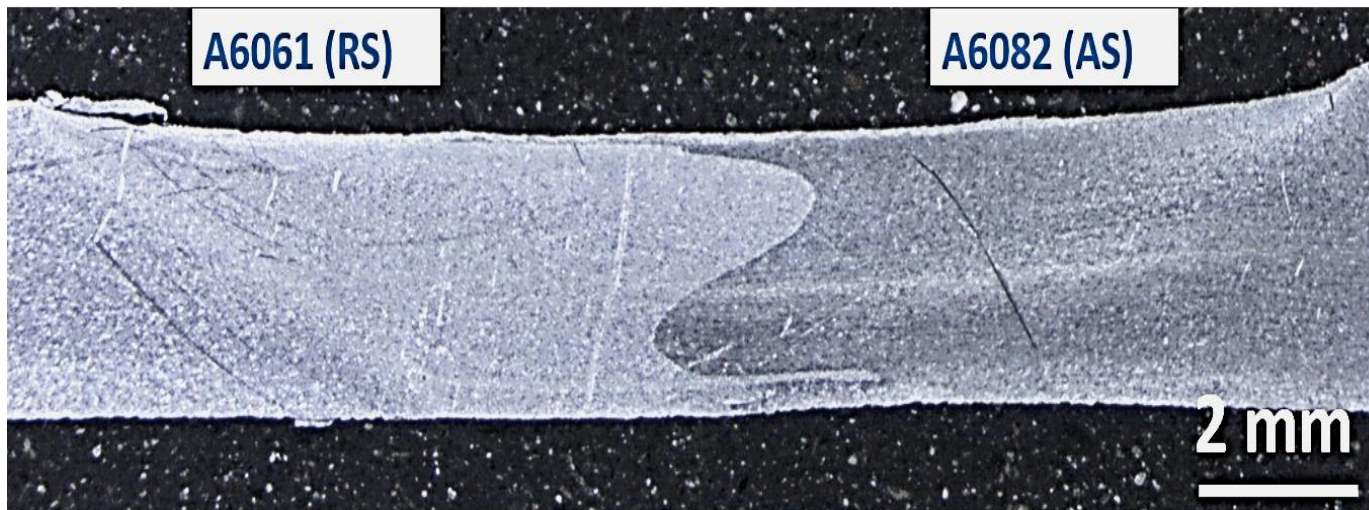


Fig. 4.109 Macrostructure of transverse section of FSWed A6061-T6 and A6082-T6 joint

(AS denotes advancing side and RS denotes retreating side of the weldment)

4.9.3 EBSD maps of BMs and different zones of the FSWed A6061-T6 and A6082-T6

The EBSD maps of BM and different zones of the A6061-T6 (RS) and A6082-T6 (AS) regions are shown in Fig. 4.110(a-d) and Fig. 4.111(a-d), respectively. The orientation triangle shows the color code, color varying with crystallographic direction. It can be seen that grain structures of BM, HAZ, TMAZ and NZ are different. Both the SZ are composed of refined grain structure as shown in Figs. 4.110(d) and 4.111(d).

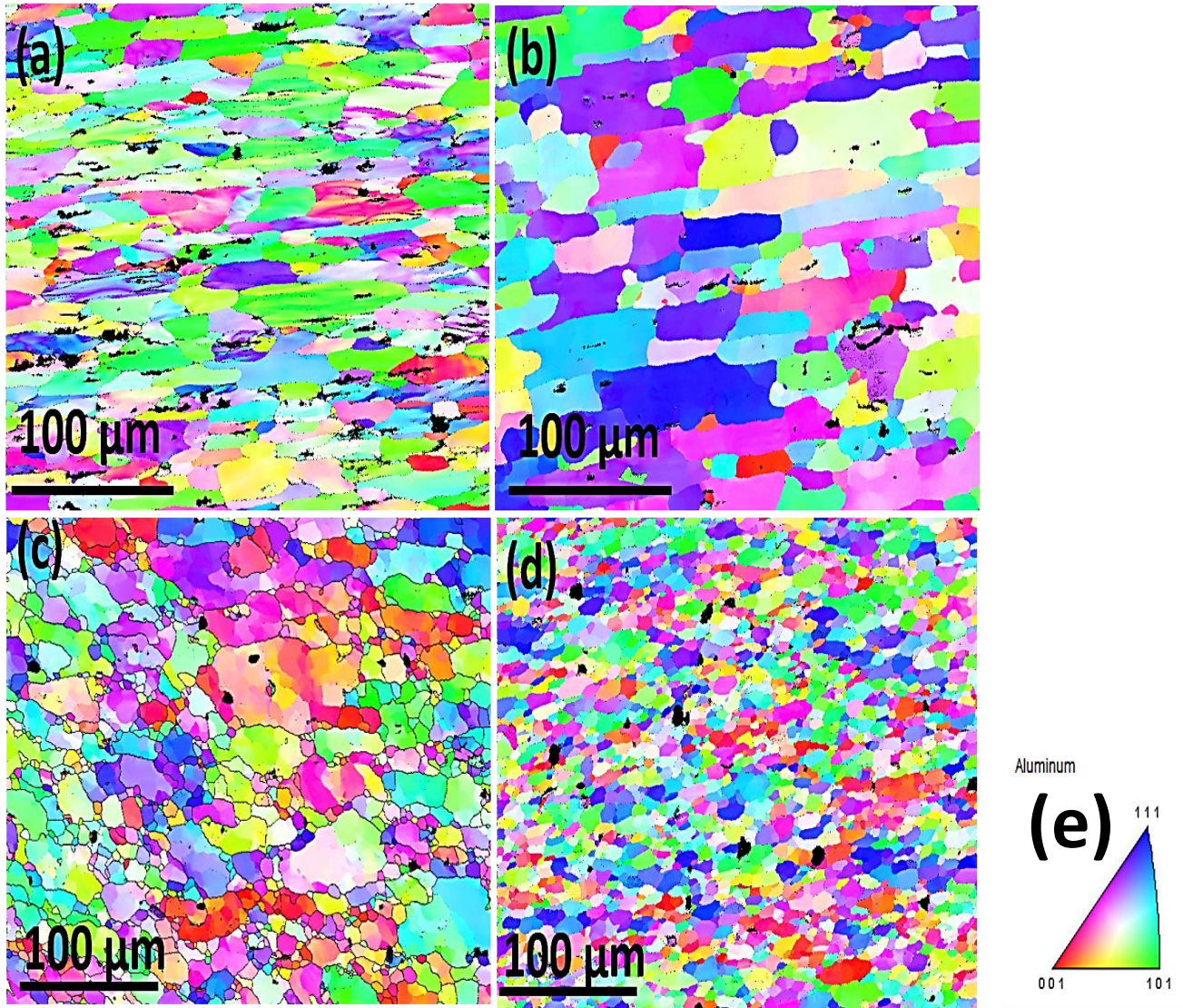


Fig. 4.110 OIM images of retreating side (RS) for A6061-T6 alloy in FSWed A6061-T6 and A6082-T6 joint: (a) BM; (b) HAZ;(c) TMAZ ;(d) SZ and (e) Orientation triangle that shows the correspondence between colors and crystallographic orientations

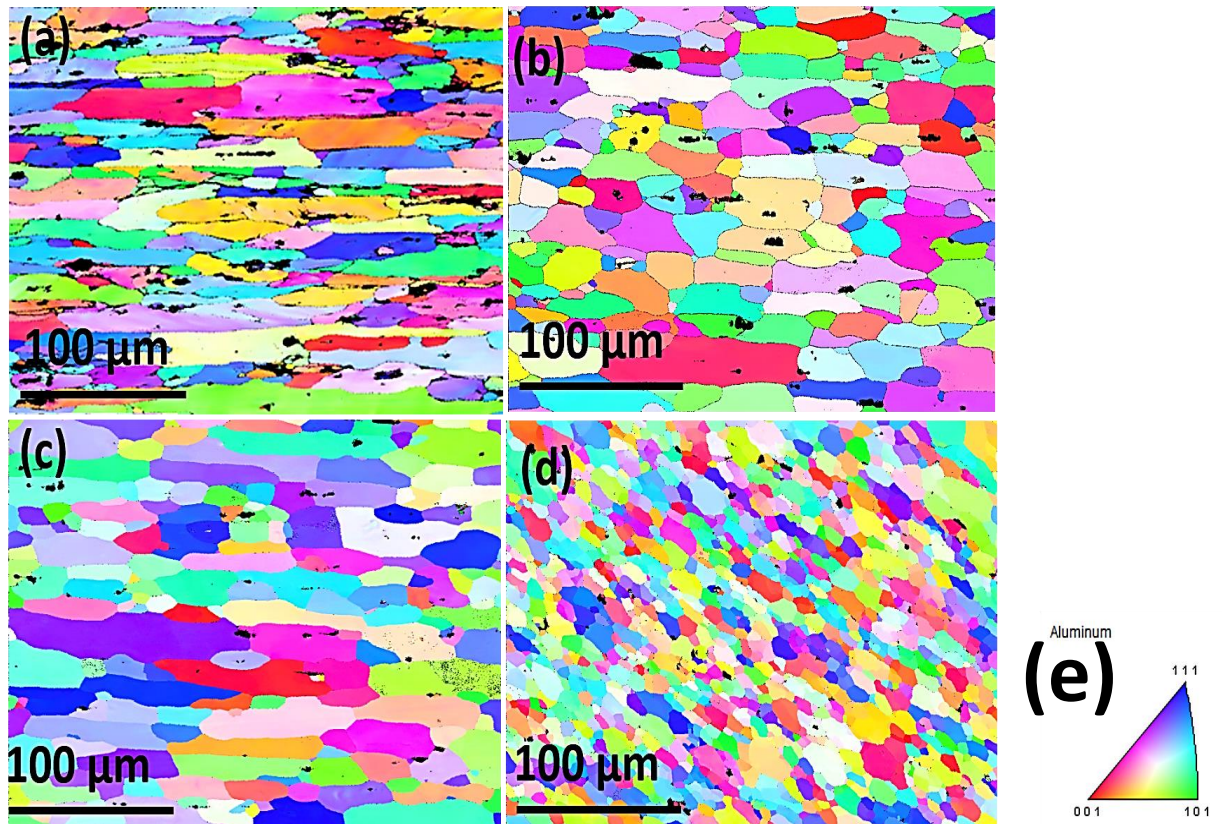


Fig. 4.111 OIM images of advancing side (AS) for A6082-T6 alloy in FSWed A6061-T6 and A6082-T6 joint: (a) BM; (b) HAZ; (c) TMAZ ;(d) SZ and (e) Orientation triangle that shows the correspondence between colors and crystallographic orientations

4.9.4 Grain boundary character maps of BMs and FSWed A6061-T6 and A6082-T6

Grain boundary character maps of A6061-T6 base metal and FSWed regions of A6061-T6 are shown in Fig. 4.112(a-d). Fig. 4.113(a-d) shows grain boundary character maps of A6082-T6 base metal and FSWed regions of A6082-T6. The GB map of A6061-T6 is composed of high density of Low Angle Grain Boundaries (LAGBs) whereas GB map of A6082-T6 is composed of low density of LAGBs. The LAGBs with misorientation angle

range of 2° - 5° are shown in red and LAGBs with misorientation angle range of 5° - 15° are shown in green. The distribution of High Angle Grain Boundaries (HAGBs) of 15° - 65° are shown in blue. The fraction of LAGBs (2° - 15°) for BMs of A6061-T6 and A6082-T6 are 0.3 and 0.7, respectively. The fractions of LAGBs in weld regions HAZ, TMAZ and SZ are 0.3, 0.6 and 0.4, respectively, for A6061-T6 and those for A6082-T6 are 0.08, 0.1 and 0.3, respectively. It is noticed that in A6061-T6 side HAGBs are higher in BM than in SZ. However, in A6082-T6 side HAGBs are higher in SZ than in BM.

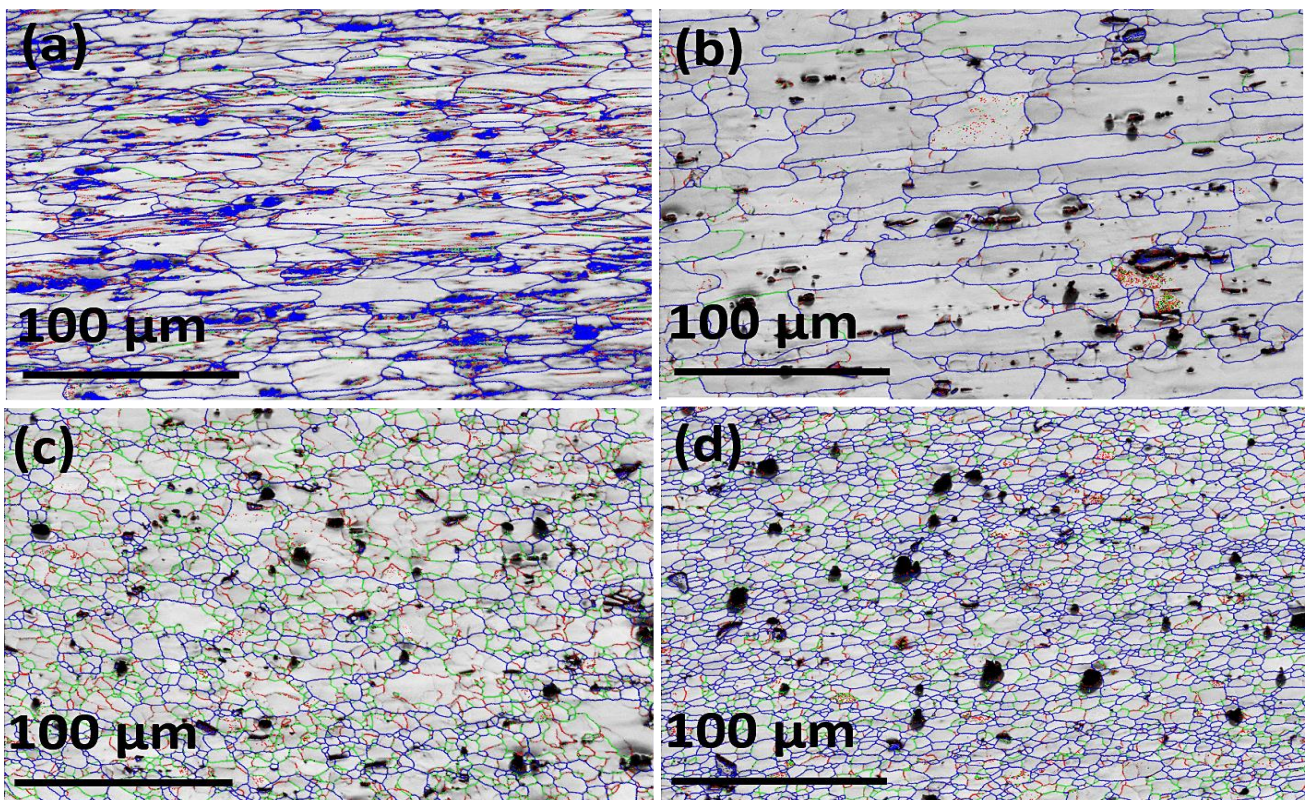


Fig. 4.112 Grain boundary character maps of retreating side (RS) of A6061-T6 alloy in FSWed A6061-T6 and A6082-T6 joint (a) BM; (b) HAZ; (c) TMAZ and (d) SZ

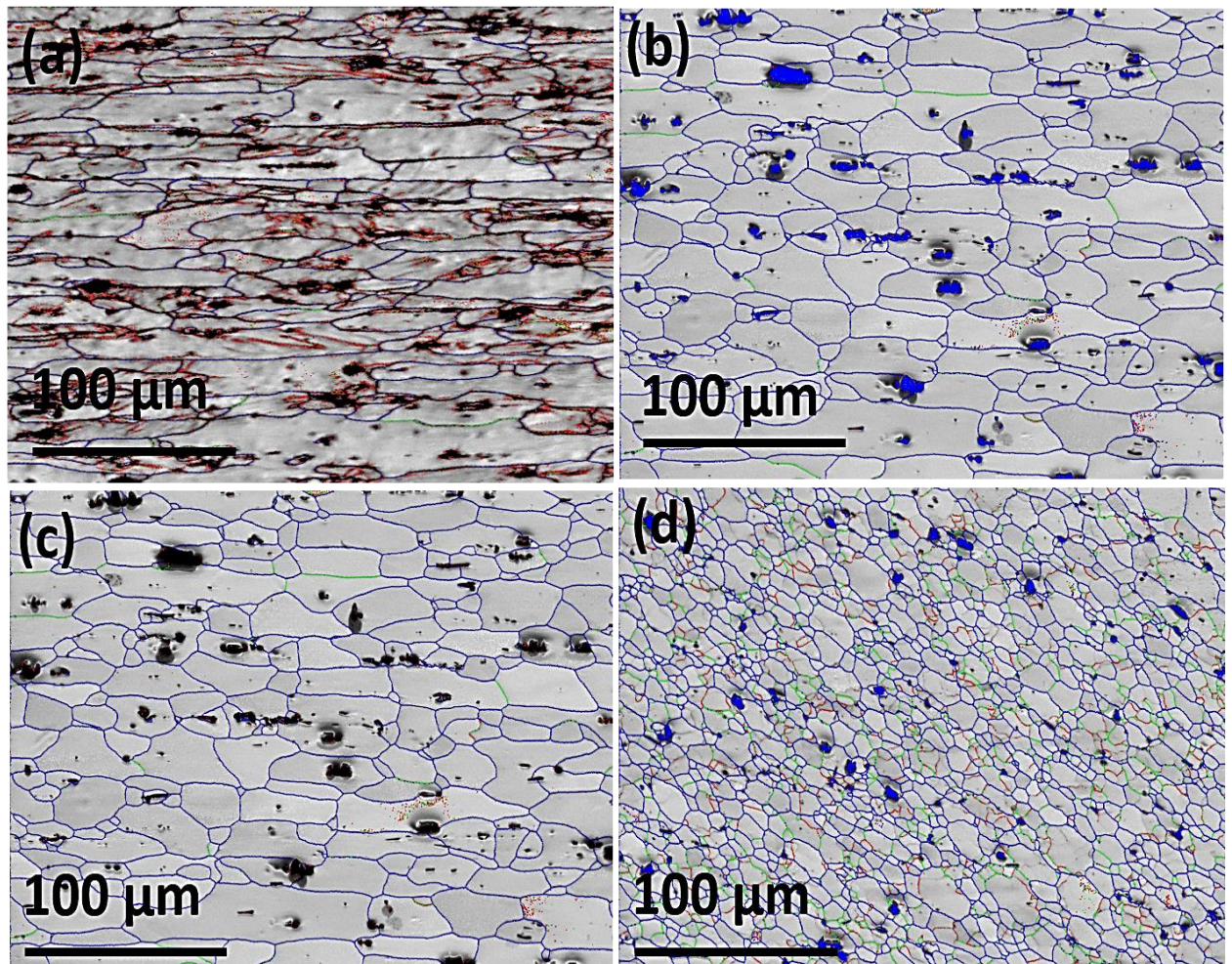


Fig. 4.113 Grain boundary character maps of advancing side (AS) of A6082-T6 alloy in FSWed A6061-T6 and A6082-T6 joint (a) BM; (b) HAZ; (c) TMAZ and (d) SZ

4.9.5 KAM maps of BMs and FSWed A6061-T6 and A6082-T6 joint

Fig. 4.114 and 4.115 show Kernel Average Misorientation (KAM) maps of BMs and FSWed regions. It is easy to distinguish high strain areas and low strain areas from the KAM maps. The high strain areas indicate that the dislocation densities are higher, and it is revealed by green color in the maps. On other hand, low strain areas indicate that the

dislocation densities are lower, and it is revealed by blue color in the maps. Both the BMs display larger green areas that indicates larger prevalence of high strain areas compared to other zones. In both the BMs high strain areas are mostly observed in grain interiors (GIs) rather than at grain boundaries (GBs). At the same time, in SZs of both the alloys high strain areas are mostly observed in GBs rather than at GIs. The dislocations are inhomogeneously distributed at the grain interiors (GIs) of both SZs. Among the SZs, high dislocation density areas are larger in amount at GIs of SZ of A6061-T6, whereas they are confined to fewer regions at GIs of SZ of A6082-T6. The dislocation density around the refined GBs in A6061-T6 SZ is higher than the A6082-T6 SZ. In the case of A6082-T6 SZ, higher dislocation densities are absent around most of the refined GBs suggesting thereby that most of the grains are recrystallized fine grains. However, SZ of A6061-T6 exhibits higher dislocation densities around most of the refined GBs thereby indicating that refined grains are mostly deformed sub grains.

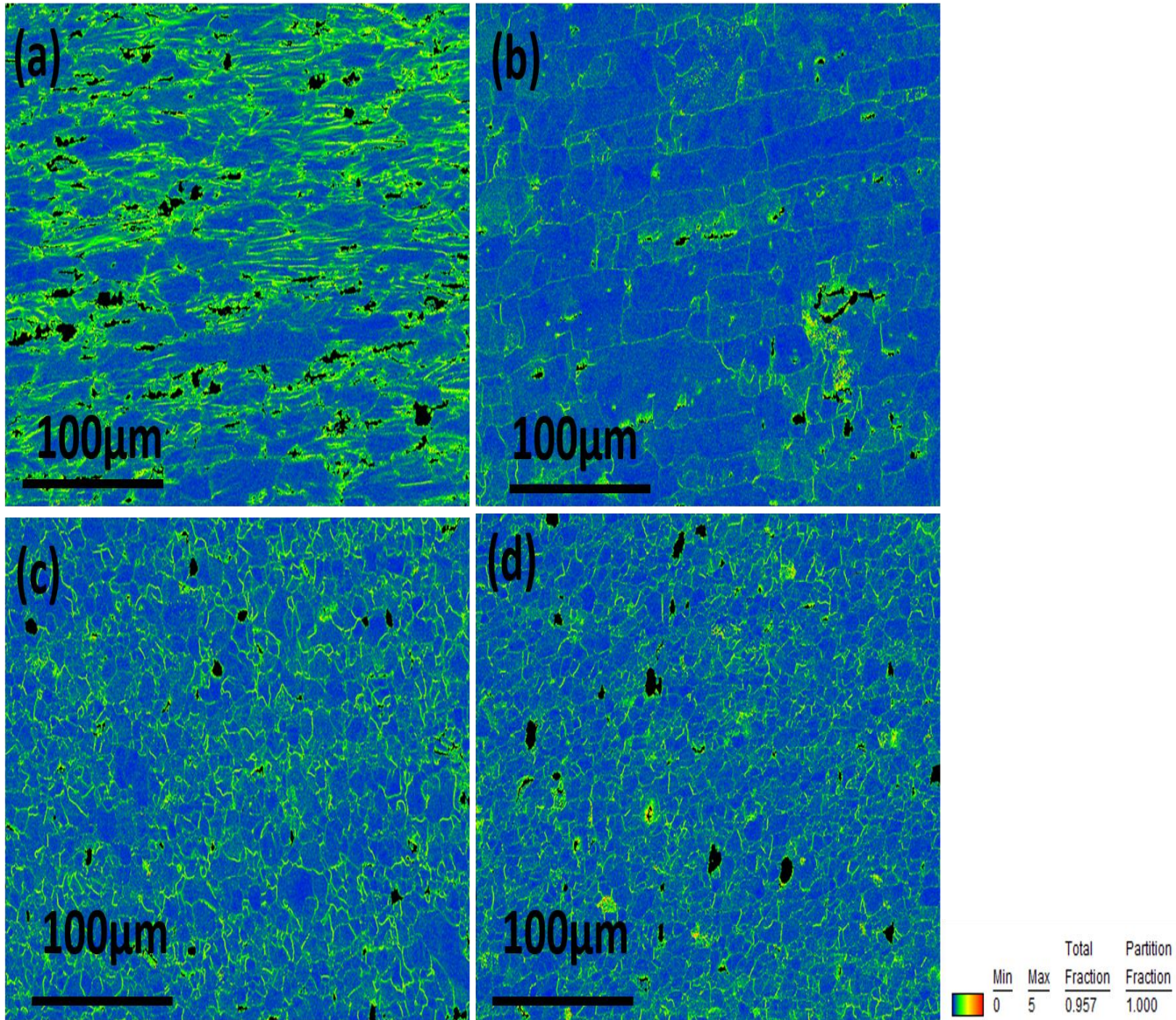


Fig. 4.114 KAM maps of retreating side (RS) of A6061-T6 alloy in FSWed A6061-T6 and A6082-T6 joint (a) BM; (b) HAZ; (c) TMAZ and (d) SZ

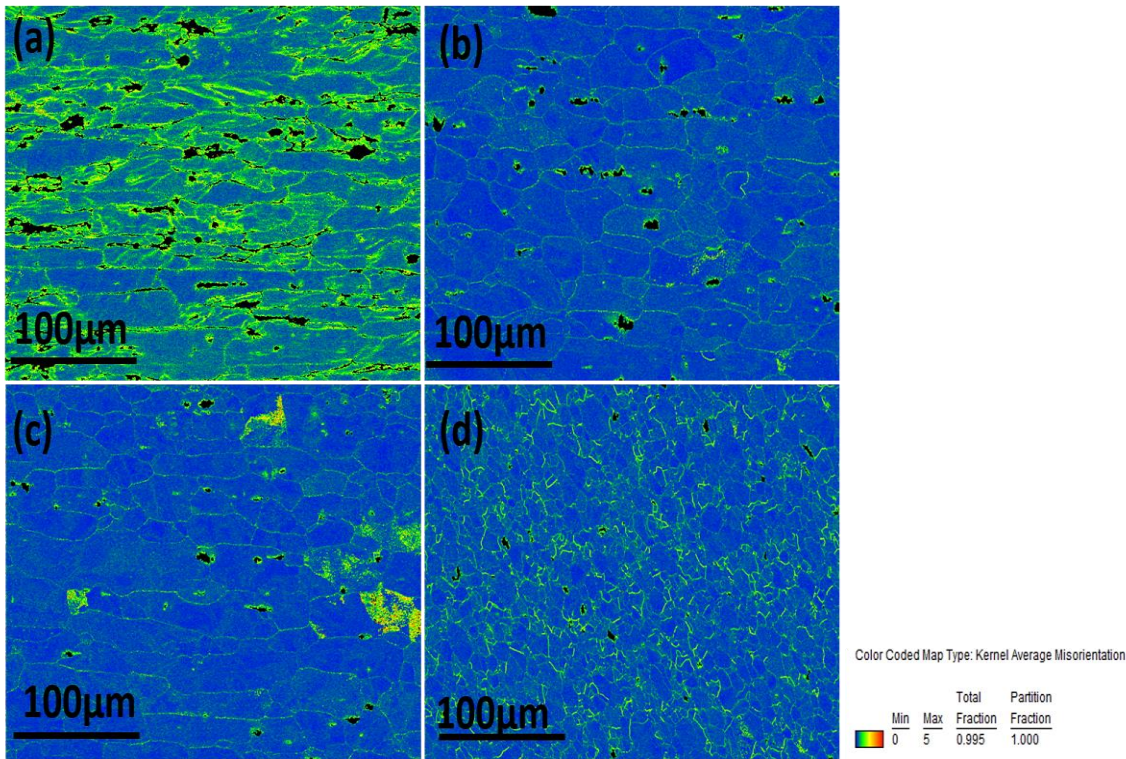


Fig. 4.115 KAM maps of advancing side (AS) of A6082-T6 alloy in FSWed A6061-T6 and A6082-T6 joint (a) BM; (b) HAZ; (c) TMAZ and (d) SZ

4.9.6 GOS maps of BMs and FSWed A6061-T6 and A6082-T6 joint

Fig. 4.116 and 4.117 show GOS maps of BMs and FSWed regions. Generally, GOS values for deformed grains are higher and the GOS values for recrystallized grains are lower (Polkowski et al. 2014). The values of GOS can be used to identify a recrystallized grain. When the material undergoes deformation the grains became distorted resulting in a higher accumulation of dislocations, thus deformed grains lead to high GOS values (Polkowski et al. 2014). On the other hand, recrystallized grains (deformation free) grains exhibit low GOS value close to zero due to lower accumulation of dislocations. The SZs exhibit the

entire range of GOS values. This implies that complete recrystallization has not been achieved in both the SZs.

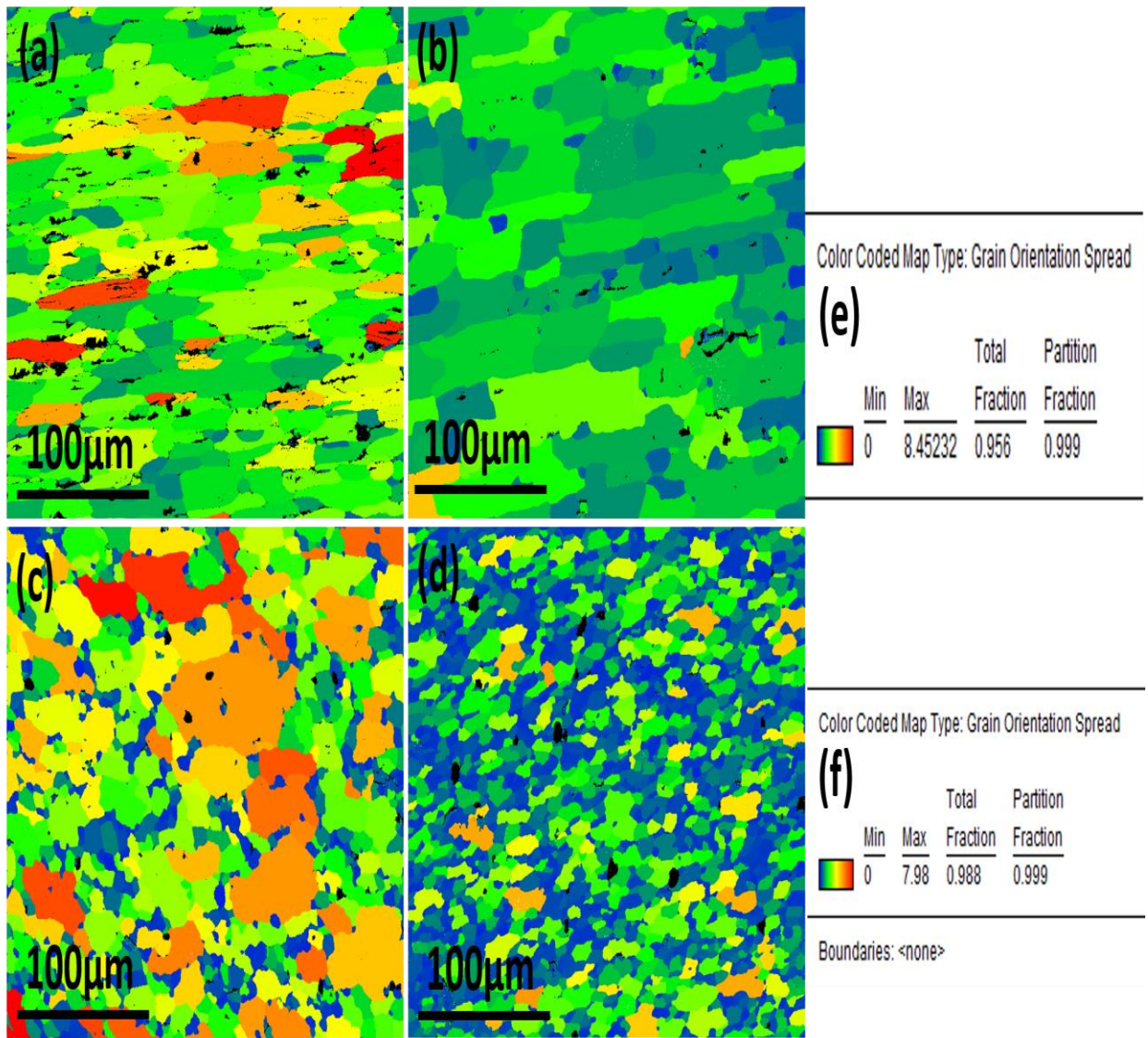


Fig. 4.116 GOS maps of retreating side (RS) of A6061-T6 alloy in FSWed A6061-T6 and A6082-T6 joint (a) BM; (b) HAZ; (c) TMAZ; (d) SZ (e) Color code map for GOS map of BM and (f) Color code map for GOS maps of HAZ, TMAZ and SZ

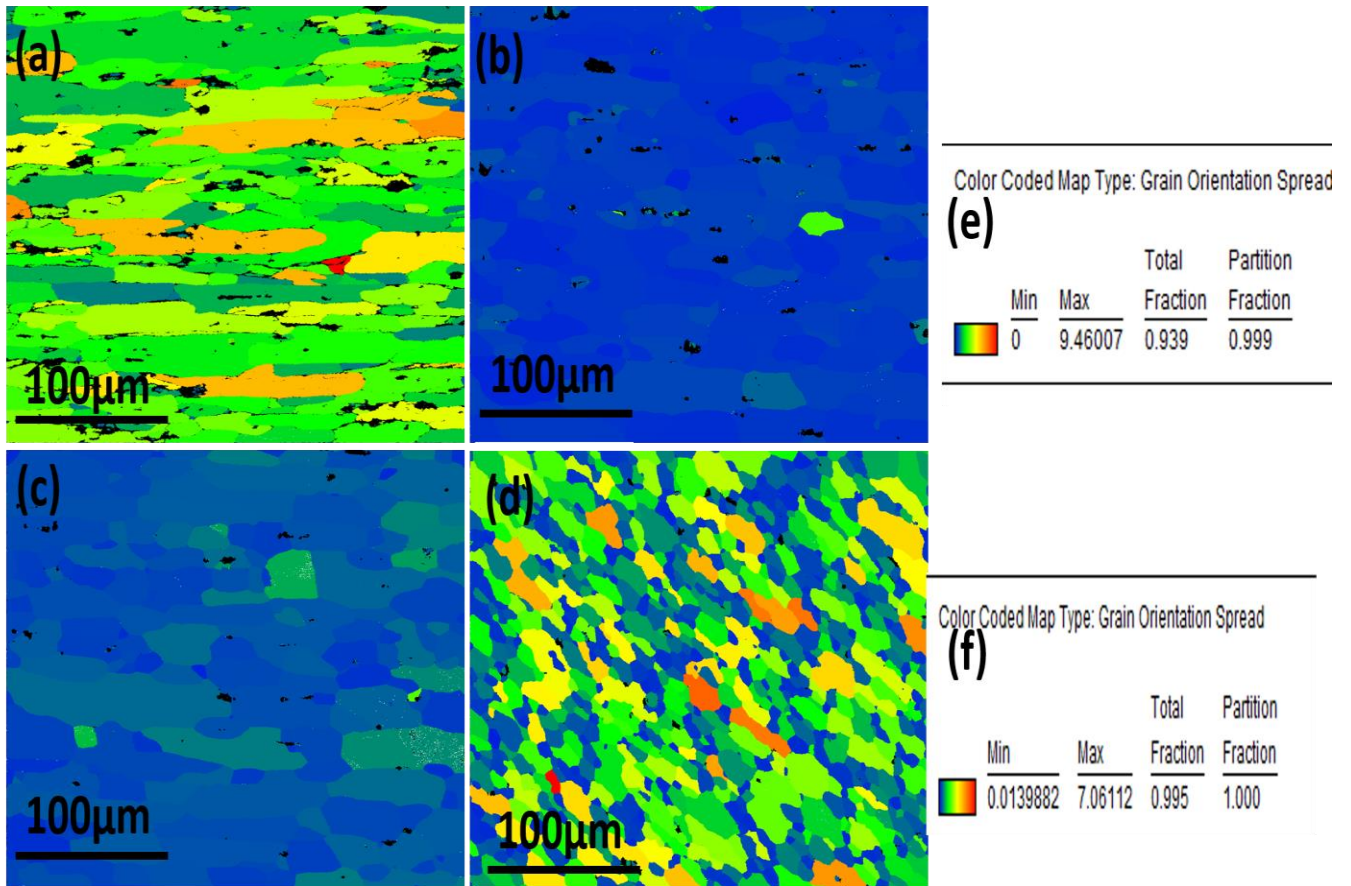


Fig. 4.117 GOS maps of advancing side (AS) of A6082-T6 alloy in FSWed A6061-T6 and A6082-T6 joint (a) BM; (b) HAZ; (c) TMAZ; (d) SZ (e) Color code map for GOS map of BM and (f) Color code map for GOS maps of HAZ, TMAZ and SZ

The presence of higher fraction HAGBs in SZs reveals that continuous activities of formation of sub grains followed by recrystallization phenomenon has occurred, which is usually named as continuous dynamic recrystallization process (Chhangani et al. 2020). Based on this, it is confirmed that the most of refined grains in SZ of A6082-T6 is formed

via continuous dynamic recrystallization process, whereas the refined grains of SZ are mostly deformed sub grains in A6061-T6.

4.9.7 Microhardness analysis of the FSWed A6061-T6 and A6082-T6

Fig. 4.118 shows microhardness profiles that are taken at the mid thickness in the transverse section of welded joints. The SZ of the weld joint has exhibited maximum hardness in the TMAZ and HAZ regions. The average hardness values of 6082-T6 and 6061-T6 base metals are 81 HV and 78 HV, respectively, whereas, the average hardness value of SZ of is 72 HV. The hardness of SZ exhibits ~89 % of BM 6082-T6 alloy and ~92 % of BM 6061-T6 alloy.

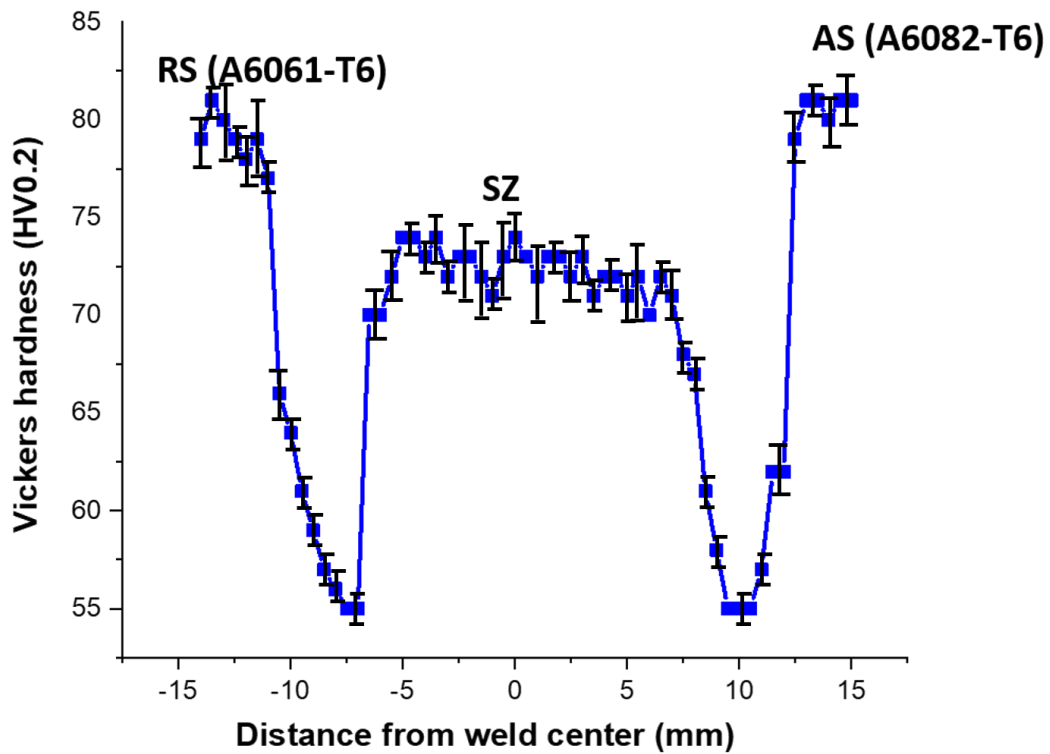


Fig. 4.118 Microhardness profile of the FSWed A6061-T6 and A6082-T6 joint

Since both BMs are precipitation hardened alloys, the hardening of the alloys mainly comes through the presence of fine precipitates. Due to the weld thermal cycles during FSW, peak temperature is much higher at the SZ. The peak temperature in the SZ can be calculated by using the equation mentioned below (Arbegast and Hartley 1999):

$$T_{\max}/T_m = K \{ \omega^2 / (v \times 10^4) \}^\alpha$$

where, T_{\max} is peak temperature in the SZ, T_m is melting point of the material, K is a constant in a range of 0.65–0.75, ω is rotational speed, v is tool transverse speed and the exponent α ranges between 0.04 to 0.06. After substituting the process parameters in the above-mentioned equation, the peak temperature is found to be 0.62 T_m . The melting temperature of A6061-T6 is 660⁰ C (Cao et al. 2013a) and that of A6082-T6 is 555⁰ C (Aalco metals Ltd 2013) . Thus, the value of peak temperature is estimated to be 409⁰ C for A6061-T6 and 344⁰C for A6082-T6.

In the case of artificially aged Al-Mg-Si alloys, fine needle shaped β'' precipitates are the main strengthening phases that provide effective barriers for the dislocation movement which increases hardness significantly (Myhr et al. 2001). These β'' precipitates (Mg_5Si_6) can dissolve at the temperatures of 200⁰ C-250⁰ C and this temperature range can be easily obtained in HAZ (Svensson et al. 2000). The calculated peak temperature in both the SZs is greater than 340⁰C. The atomic radii of Al, Mg and Si are 1.18, 1.45 and 1.11 Angstrom, respectively. As the difference in atomic radii decreases, the solubility of solute in solvent increases. Since, the difference between the solvent (Al) and solutes (Mg, Si) is lower, there is a possibility of solid solution formation of Al with Mg, and Si as

Mg₅Si₆ precipitates dissolved in the Al matrix. The dissolved elements in the SZ appeared to have little influence on retaining the hardness compared to the precipitates and thus the hardness in the SZ dropped. Moreover, the refined grain structure in SZ can have further increased the hardness. It is also observed that the hardness values of the HAZ in both alloys are lower than the base metals. It is further reported that when the temperature reaches 300⁰ C (typical temperature in HAZ) β' precipitates (Mg_{1.7}Si) can be formed in HAZ (Svensson et al. 2000). These β' precipitates do not contribute to hardness in a significant manner. Hence, the lower value of hardness in HAZs than the BMs on both the interfaces can possibly be correlated to the presence of β' precipitates.

4.9.8 Tensile properties of FSWed A6061-T6 and A6082-T6

Fig. 4.119 displays tensile properties of BMs and the welded joint (over-all region and SZ) and Table 4.30 summarizes the results. Tensile specimens were extracted from the SZ in such a way that the centre of the SZ constituted the middle portion of the gage length and the entire gage area remained within the SZ, whereas the over-all region samples composed of BMs, HAZs, TMAZs and SZs of both the samples. As can be seen from Table 4.30, BMs A6061-T6 and A6082-T6 show ultimate tensile strength (UTS) and yield strength (YS) of 321 MPa, 327 MPa and 281 MPa, 284 MPa, respectively. The overall FSWed region and FSWed stir region show UTS and YS of 213 MPa, 213 MPa and 136 MPa, 118 MPa, respectively. Since both the alloys are precipitation hardened alloys, dissolution of all precipitates can occur in SZ because of the higher temperature of this zone (greater than 340⁰C). This tends to reduce the precipitate hardening effect but plays little role in solid

solution strengthening. This apart, the refined grain structure in SZ could have further improved the strength of the SZ.

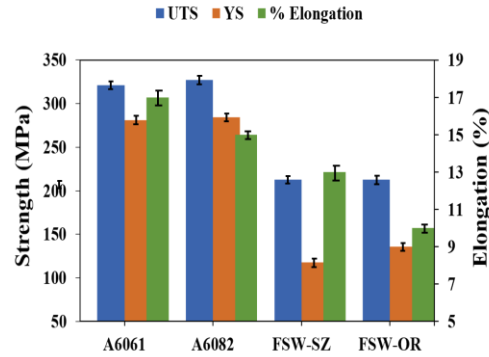


Fig. 4.119 Tensile properties of BMs and FSWed A6061-T6 and A6082-T6 joint (SZ-stir zone and OR-over-all region; Gauge length of BMs & OR is 25 mm and gauge length of SZ is 5 mm)

Table 4.30 Tensile properties of the BMs and FSWed A6061-T6 and A6082-T6 joint

Sample	UTS (MPa)	YS (MPa)	Elongation(%)
A6061-T6	321	281	17
A6082-T6	327	284	15
FSWed (stir region)	213	118	13
FSWed (over-all region)	213	136	10

4.9.9 Fractography of the FSWed A6061-T6 and A6082-T6

Fig. 4.120 shows the SEM images of fractured surfaces of tensile samples of SZ and overall FSWed region. This show dimples indicating a ductile fracture in both the cases.

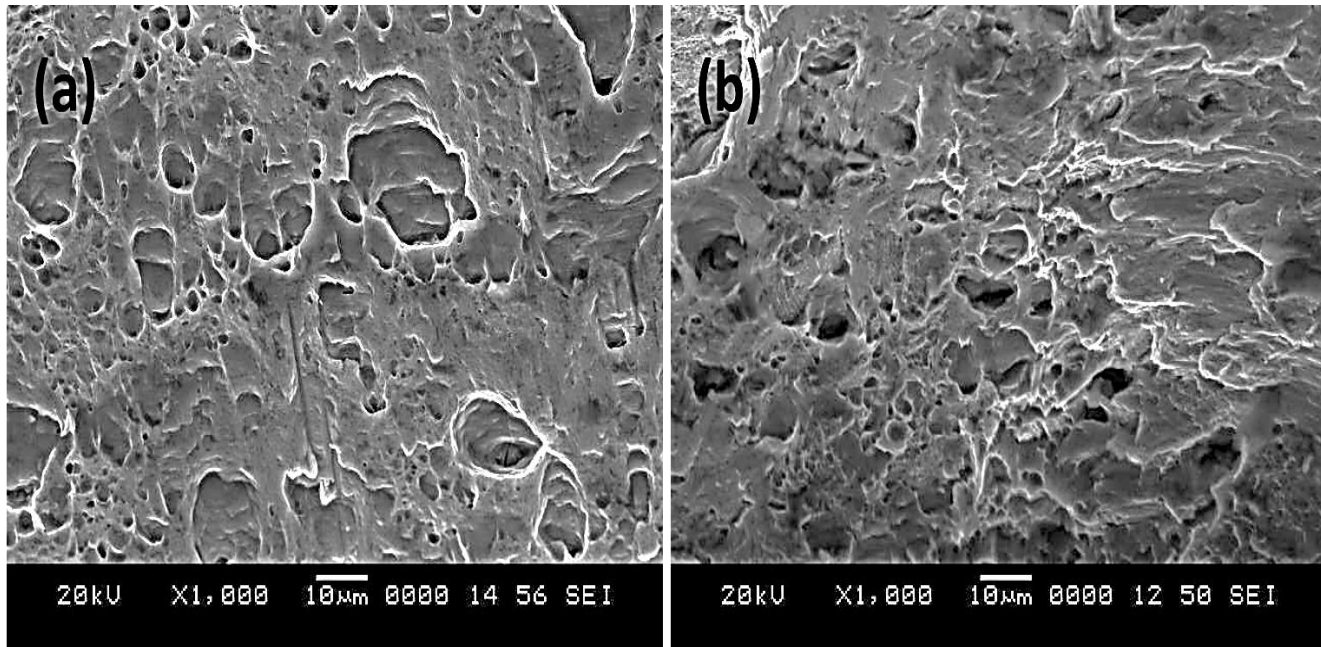


Fig. 4.120 Fractography of fractured specimen in FSWed A6061-T6 and A6082-T6 joint

(a) FSW (SZ) and (b) FSW (over-all region)

4.10 Friction stir welding (FSW) of dissimilar A5754-H111 and A5083-H111

4.10.1 Surface appearance of the FSWed A5754-H111 and A5083-H111

The surface appearance of the FSWed dissimilar aluminium alloys is shown in Fig 4.121. The surface of the weldments was smooth and fine. No defects were detected on the surface of the weldment. Only a small flash was visible on surface of the welded sample. The weldment consisted of a small piece of burr at the beginning and an existing hole at the end.



Fig. 4.121 The surface appearance of the FSWed A5754-H111 and A5083-H111 joint

4.10.2 Macrostructure of transverse section of the FSWed A5754-H111 and A5083-H111

The macroscopic appearance of transverse section of FSW dissimilar aluminium alloys joint is shown in Fig. 4.122. The regions such as the stir zone (SZ) and thermo-mechanically affected zones (TMAZ's) are clearly discernible. It can be noticed that full

penetration is achieved. No defects in the cross section of the welds are visible. A distinct colour difference among different zones is noticeable. The interface between the SZ and TMAZ in AS is very distinct whereas the interface between the SZ and TMAZ in RS is diffused.

A continuous “S” line is noticed at the centre of the SZ. This line zigzagging from top to bottom throughout the thickness of the weld can be considered as the boundary between the two dissimilar aluminium alloys. The “S” line initiated from the weld centre line at the top region and stretched to AS (i.e., A5754) at the middle region. It further prolonged into RS (i.e., A5083) and thereafter extended into AS (i.e., A5754) at the bottom region. In the case of top to middle region and lower middle region to bottom region, it is understandable that during FSW the stirred material in RS (i.e., A5083) crossed the weld centre line and got pushed into AS (i.e., A5754) in the centre region of the SZ. On the other hand, the stirred material from AS (i.e. A5754) crossed the weld centre line and got pushed into RS (i.e., A5083) in the lower middle region of the SZ. Robe et al. (Robe et al. 2015) have reported about this “S” line interface, terming it as ‘tip-border shape interface’ in the welding of dissimilar 2xxx aluminium alloys.

The quality of the joint produced through FSW mainly depends on heat input and material flow during welding. There are three material flow states, namely inadequate material flow state, balance material flow state and excessive material flow state (Zhang et al. 2011). Improper selection of tool rotation speed and tool transverse speed are the possible reasons for inadequate and excessive flow of work-piece materials. Such two-state (inadequate and excessive) material flow can easily induce defects during FSW. As soon as the work-piece

material experiences a larger heat input, the material becomes very hot that results in surface galling, flash and collapse in the SZ due to excessive material flow. In contrast, once the material experiences a lower heat input the flow of materials is insufficient that produces lack of fill on the surface and in worm hole (Arbegast 2008). The balance material flow state is an essential requirement during FSW that ensures a defect free joint. The weld surface appearance and the macro and microstructures have not shown any welding defects indicating thereby that the chosen parameters in the present study have created a balance material flow during FSW and produced defect free welding.

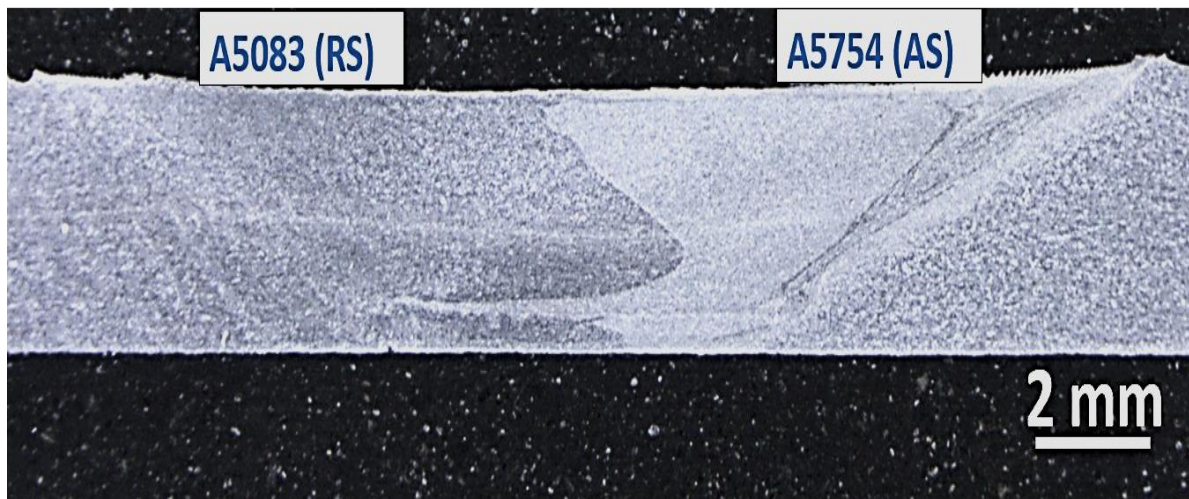


Fig. 4.122 Macrostructures of transverse section of FSWed A5754-H111 and A5083-H111 joint (AS denotes advancing side and RS denotes retreating side of the weldment)

4.10.3 EBSD maps of BMs and FSWed A5754-H111 and A5083-H111

Fig. 4.123(a-d) shows EBSD maps of BM and different zones of the A5754 (AS) region and Fig. 4.124(a-d) shows EBSD maps of BM and different zones of the A5083(RS) region

in the FSWed joint. The colour variation observed in individual grains is due to the difference in crystallographic orientation. The SZs clearly exhibit fine grains. The presence of refined grain structure is marginal in the SZ of A5754 (Fig 4.123(d)) as compared to the SZ of A5083[Figs. 4.124(d)].

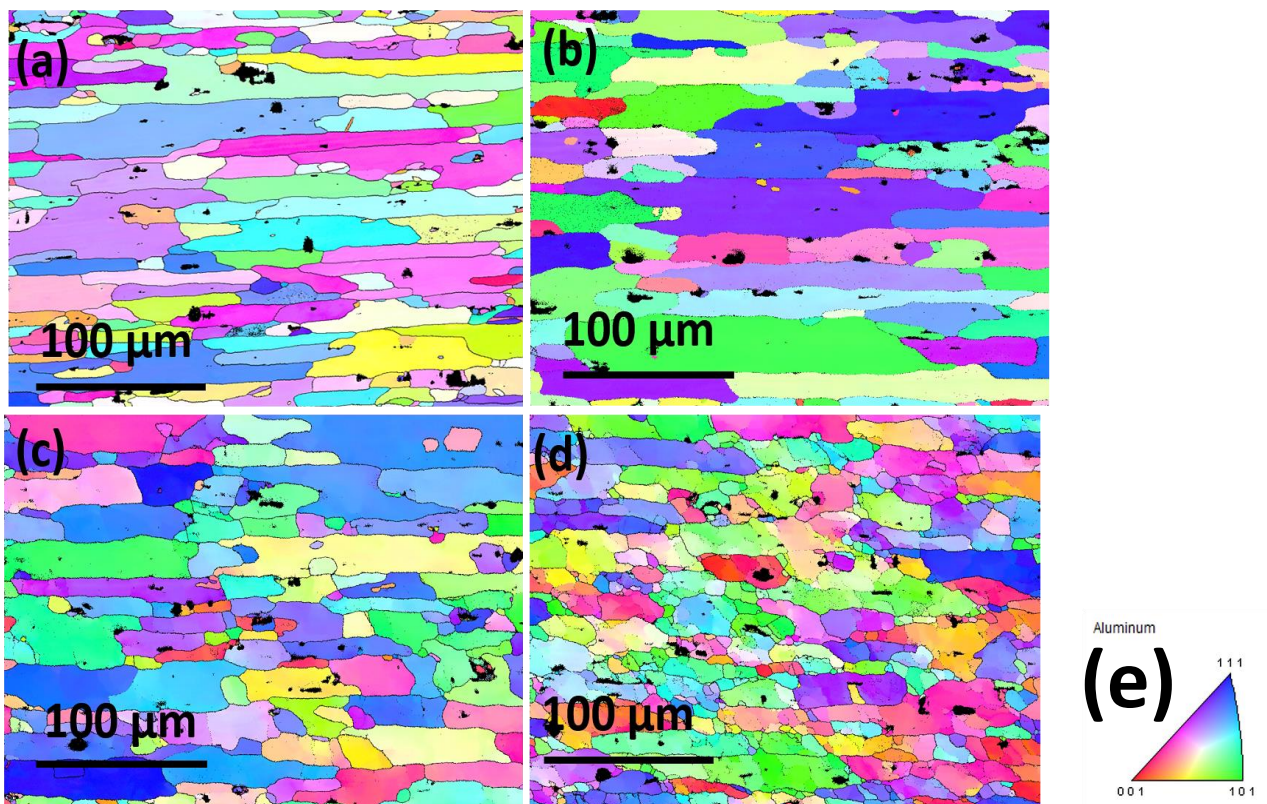


Fig. 4.123 OIM images of advancing side (AS) for A5754-H111 alloy in FSWed A5754-H111 and A5083-H111 joint: (a) BM; (b) HAZ; (c) TMAZ; (d) SZ and (e) Orientation triangle that shows the correspondence between colors and crystallographic orientations

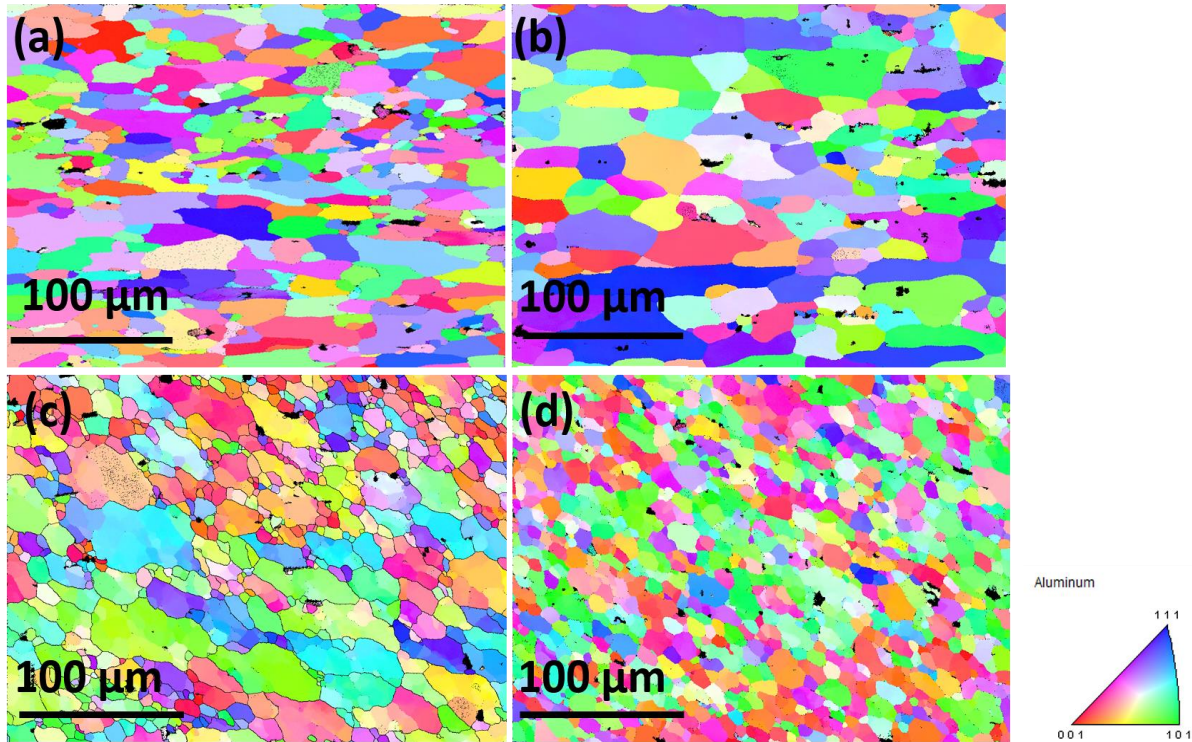


Fig. 4.124 OIM images of retreating side (RS) for A5083-H111 alloy in FSWed A5754-H111 and A5083-H111 joint: (a) BM; (b) HAZ; (c) TMAZ; (d) SZ and (e) Orientation triangle that shows the correspondence between colors and crystallographic orientations

Fig. 4.125 (a-b) shows the grain shape aspect ratio charts of the BMs and weld regions. It can be seen that the aspect ratio is higher in the SZ. As the distance increases from the center of the SZ to BM, the aspect ratio correspondingly decreases. It is observed that compared to BM, the HAZ has not shown any obvious difference in grain shape aspect ratio in both the alloys. The grain shape aspect ratios are almost similar in BM as well as HAZ regions. However, there is an evidence of grain growth in the HAZ of both the alloys, A5754 and A5083, due to the frictional temperature effect of pin rotation. A significant difference in the aspect ratio is noticed in the TMAZ and SZ as compared to BM. This indicates that the fraction of equiaxed grains is increased in the TMAZ and SZ as compared

to BM. The SZ of A5083 alloy exhibits the highest aspect ratio among all the zones due to the presence of a larger amount of fine equiaxed grains in the microstructure.

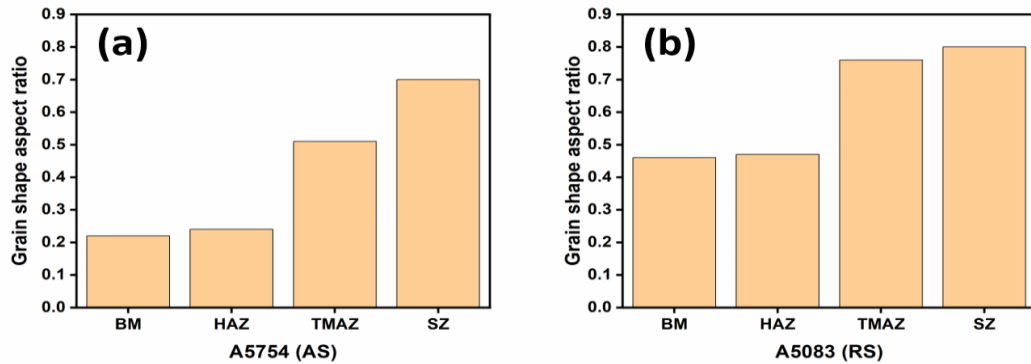


Fig. 4.125 Grain shape aspect ratio of different zones of BMs and weld regions in FSWed A5754-H111 and A5083-H111 joint (a) advancing side (AS) and (b) retreating side (RS)

4.10.4 Grain boundary character maps of BMs and FSWed A5754-H111 and A5083-H111

Fig. 4.126(a-d) shows grain boundary character maps of A5754 base metal and FSWed regions of A5754. Fig. 4.127(a-d) shows grain boundary character maps of A5083 base metal and FSWed regions of A5083. These figures clearly indicate the distribution of low angle grain boundaries (LAGBs, 2° - 15°) and high angle grain boundaries (HAGBs $> 15^\circ$), that are displayed in different colours. The LAGBs with misorientation angle range of 2° - 5° are shown in red and LAGBs with misorientation angle range of 5° - 15° are shown in green. The distribution of HAGBs of 15° - 65° are shown in blue. The fractions of LAGBs and HAGBs at different zones in AS and RS are shown in Fig. 4.128(a-b). The distribution density of LAGBs in FSWed zones is higher than that in the BMs. However, the

distribution of HAGBs in FSWed zones is lower than the BMs. The fraction of LAGBs (2° - 15°) for BMs A5754 and A5083 are 0.10 and 0.12, respectively. The fractions of LAGBs in weld regions HAZ, TMAZ and SZ are 0.18, 0.39 and 0.57, respectively, for A5083 and those for A5754 are 0.37, 0.44 and 0.68, respectively. This indicates that the fraction of LAGBs is quantitatively higher in FSWed zones, particularly the SZ, than that in the BMs.

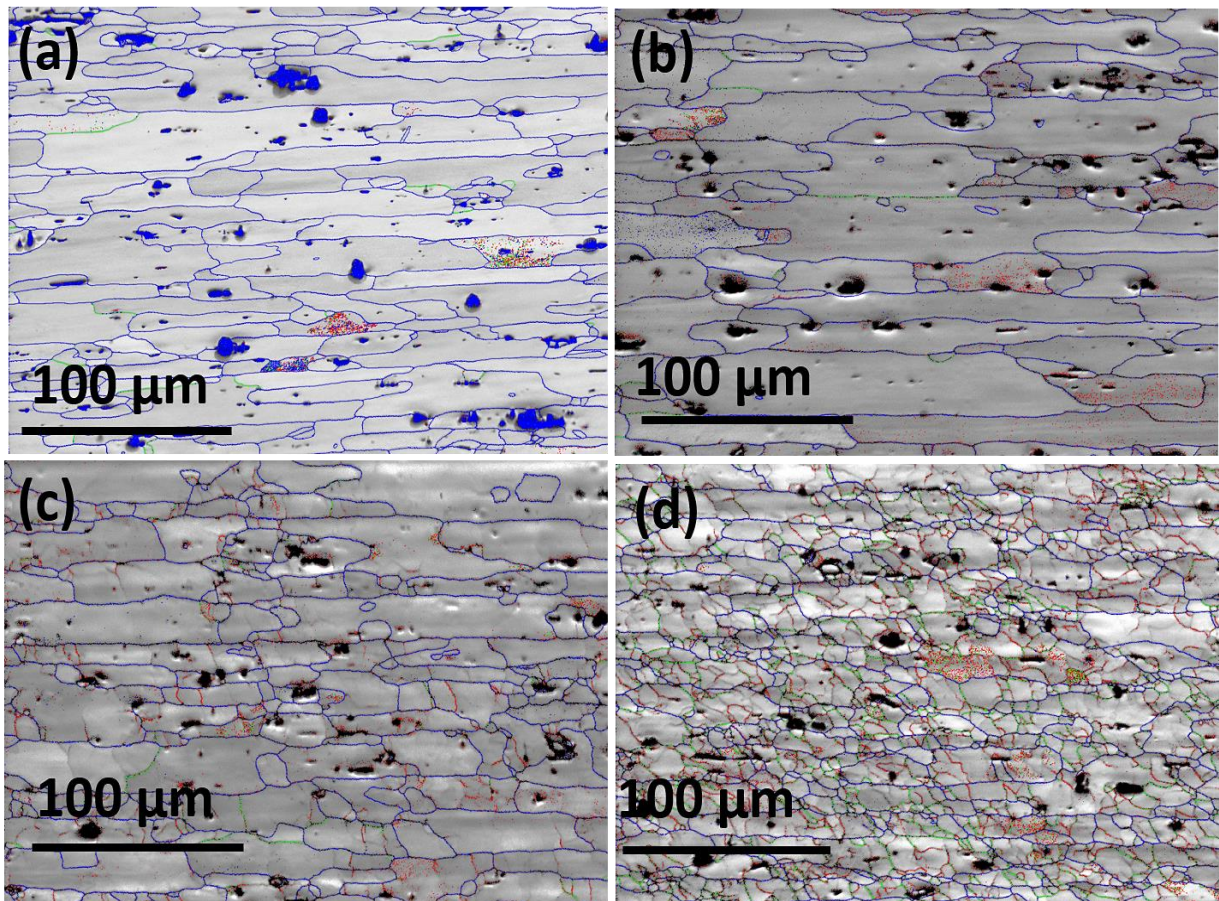


Fig. 4.126 Grain boundary character maps of advancing side (AS) of A5754-H111 alloy in FSWed A5754-H111 and A5083-H111 joint: (a) BM; (b) HAZ; (c) TMAZ and (d) SZ

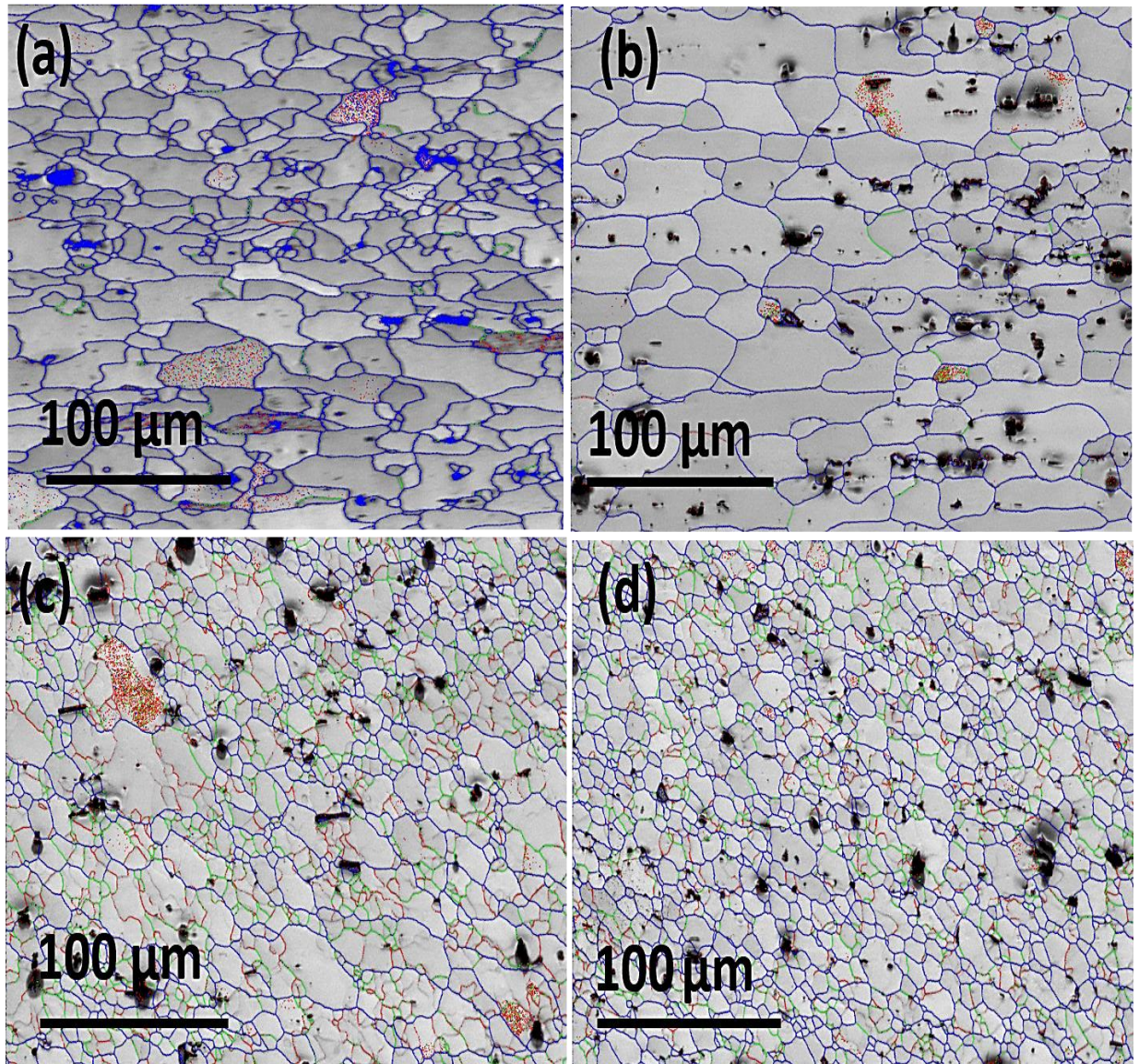


Fig. 4.127 Grain boundary character maps of retreating side (RS) of A5083-H111 alloy in FSWed A5754-H111 and A5083-H111 joint (a) BM; (b) HAZ; (c) TMAZ and (d) SZ

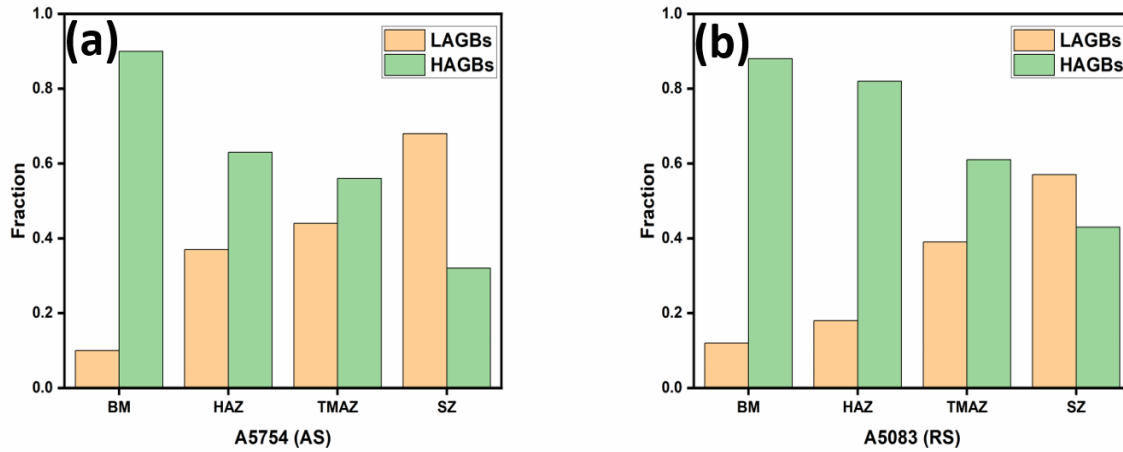


Fig. 4.128 Fraction of LAGBs and HAGBs at different zones in advancing side (AS) and retreating side (RS) of the FSWed A5754-H111 and A5083-H111 joint

4.10.5 KAM maps of BMs and FSWed A5754-H111 and A5083-H111

Fig. 4.129(a-d) shows Kernel Average Misorientation (KAM) maps of BM and different zones of the A5754 (AS) region and Fig. 4.130(a-d) shows KAM maps of BM and different zones of the A5083(RS) region in the FSWed joint. The local dislocation density distribution can be seen from the KAM maps. High dislocation densities (high strain areas) can be identified by green color. The blue color region indicates low dislocation densities (low strain areas). The increase in high strain areas indicates that the amounts of geometrically necessary and statistically stored dislocations have increased (Gurao and Suwas 2013). As can be seen from Fig. 4.129(a-d) and Fig. 4.130(a-d), the fraction of green color regions in SZs is higher than in the respective BMs. This indicates that local dislocation densities and dislocation pile ups have increased after FSW. Most of the refined GBs of SZs display a bright green color revealing that dislocation densities near GBs are

higher. This indicates that most of the grains are deformed sub grains not recrystallized grains. Thus, dynamic recrystallization is not complete in most of the grains and only a few of the grains have undergone this phenomenon.

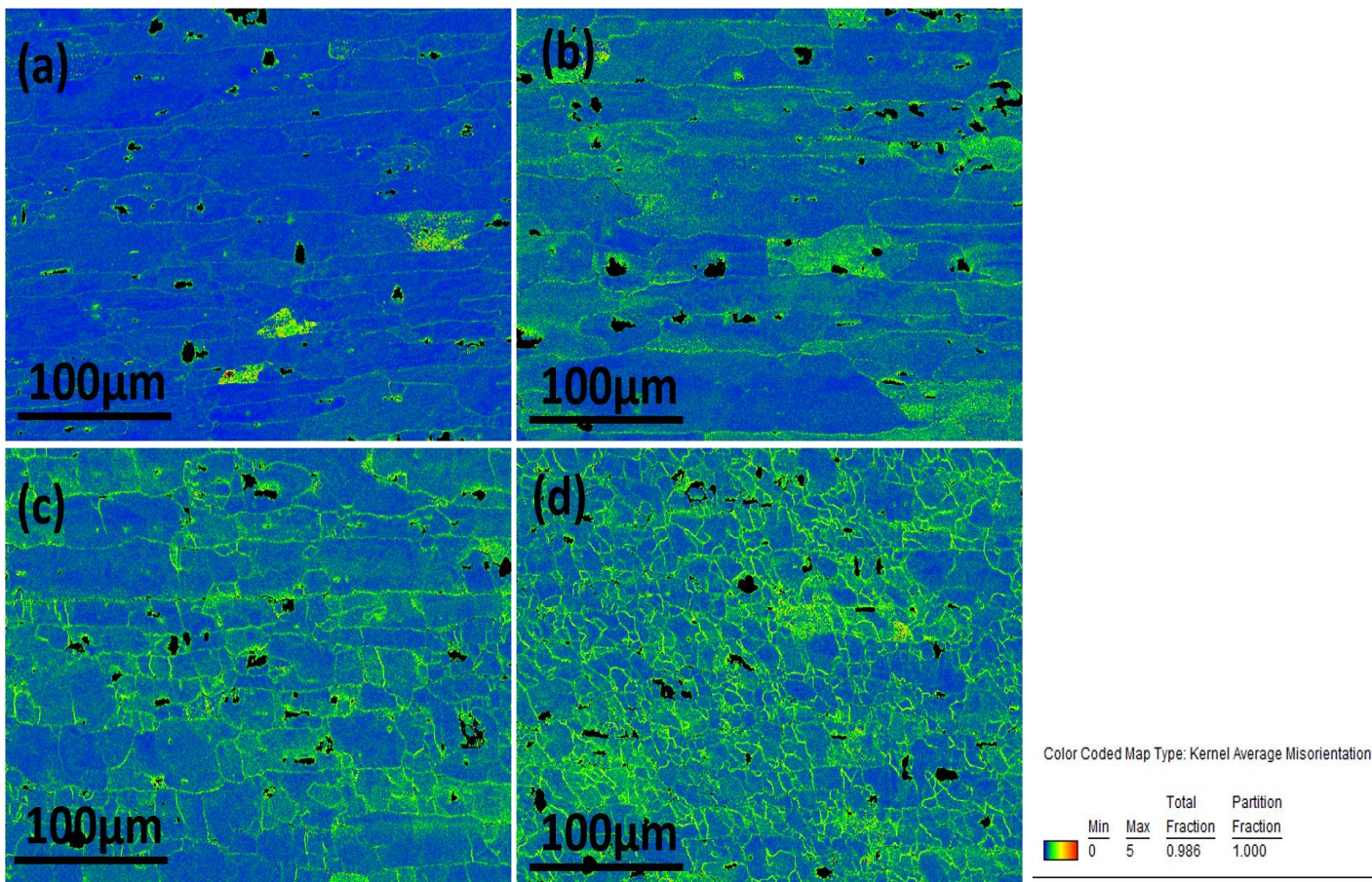


Fig. 4.129 KAM maps of advancing side (AS) of A5754-H111 alloy in FSWed A5754-H111 and A5083-H111 joint (a) BM; (b) HAZ; (c) TMAZ and (d) SZ

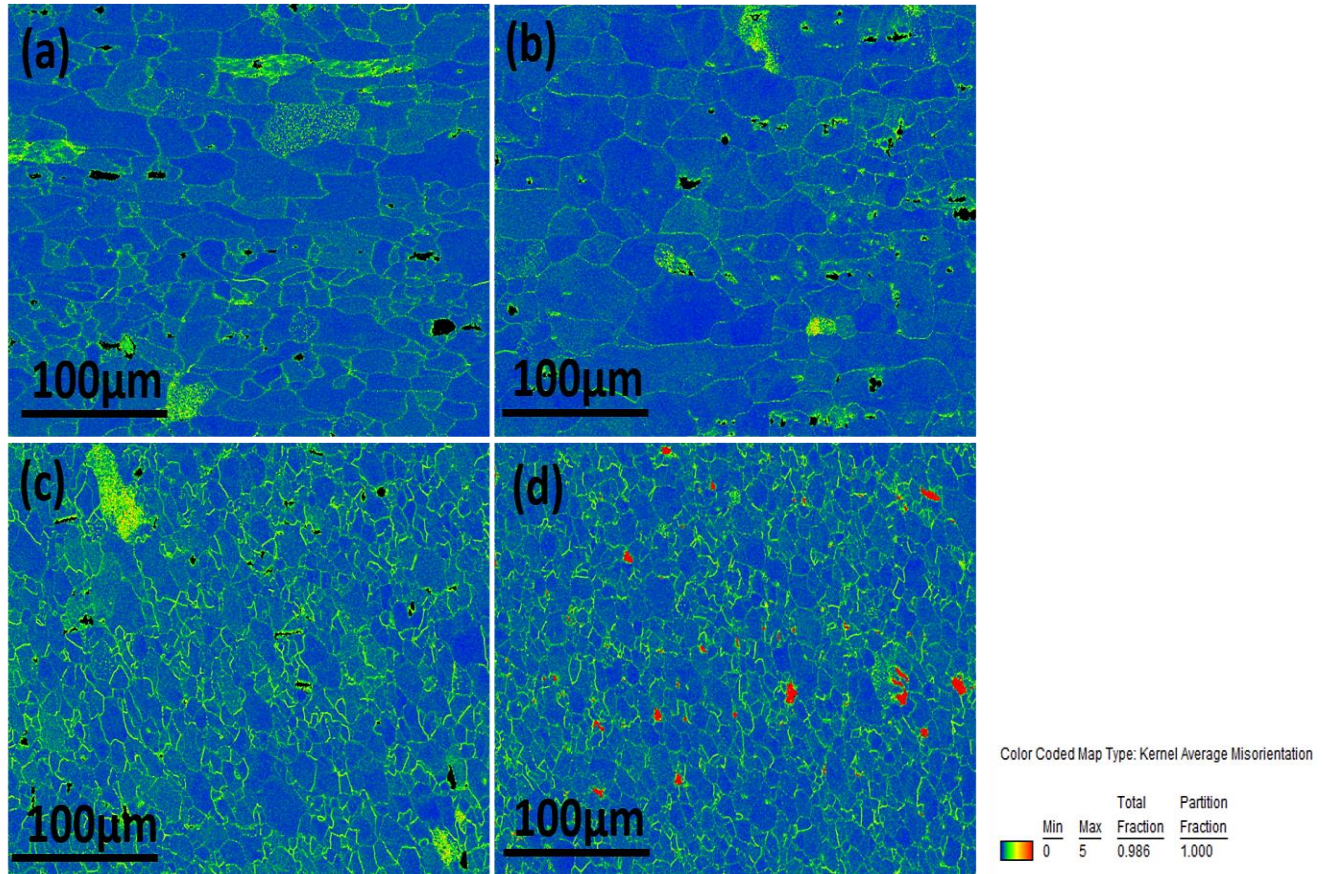


Fig. 4.130 KAM maps of retreating side (RS) of A5083-H111 alloy in FSWed A5754-H111 and A5083-H111 joint (a) BM; (b) HAZ; (c) TMAZ and (d) SZ

4.10.6 GOS maps of BMs and FSWed A5754-H111 and A5083-H111

Fig. 4.131(a-d) shows grain orientation spread (GOS) maps of BM and different zones of the A5754 (AS) region and Fig. 4.132(a-d) shows those of the A5083 (RS) region in the FSWed joint. The colors inside the grains have varied with varied degrees of strain. The values of GOS can be used to identify a recrystallized grain. When the material undergoes deformation, the grains became distorted resulting in higher accumulation of dislocations,

thus deformed grains exhibit high GOS values (Polkowski et al. 2014). On the other hand, recrystallized grains (deformation free) grains exhibit low GOS values close to zero due to lower accumulation of dislocations. The SZs have exhibited the entire range of GOS values. This implies that complete recrystallization is not achieved in both the SZs. Moreover, the fraction of recrystallized grains represented in blue color (low GOS values) is found to be lower in both SZs. At the same time, the presence of recrystallized grains is quantitatively higher in SZ of A5083 than the SZ of A5754.

It is well known that during FSW the material in the SZ undergoes extensive plastic deformation that introduces a large number of dislocations in the SZ. Since aluminium is a high SFE metal, during hot deformation cross slip, glide and climb activities of the dislocations are faster resulting in the formation of low angle GBs in the SZ through dynamic recovery mechanism. Further, hot deformation induced sub grain (LAGBs) rotation activity accommodates a larger number of dislocations into the boundaries giving rise to the formation HAGBs. In the present study, LAGBs dominate in both the SZs confirming that the refined grains are sub grains formed through dynamic recovery mechanism. At the same time, the presence of a few HAGBs in both the SZs suggests that some fraction of sub grains has transformed to recrystallized grains. The domination of LAGBs and reduction of HAGBs can possibly be related to incomplete recrystallization. The phenomenon of incomplete recrystallization occurs due to lower heat input, high cooling rate and insufficient plastic deformation as the time available for dislocation interaction and rearrangement is limited (Nayan et al. 2017). Thus, the fraction of HAGBs decreased from 0.88 to 0.43 in the SZ of A5083 (RS) and 0.90 to 0.32 in the SZ of A5754

(AS) alloy. Moreover, it is also noticed that the formation of HAGBs has decreased more in the SZ of A5754 (AS) than in the SZ of A5083 (RS).

The degree of plastic deformation is also an important factor for the variation in fraction of HAGBs in the SZs. It is reported that because of the characteristic sequence of material flow during FSW, the amount of plastic deformation in the SZ of AS is lower than that of RS (Zhang and Wang 2018). Thus, the SZ of A5083 (RS) experienced more plastic deformation with higher stored energy in association with increased temperature than the SZ of A5754 (AS) leading to a significant decrease in the number of LAGBs in the SZ of A5083 (RS).

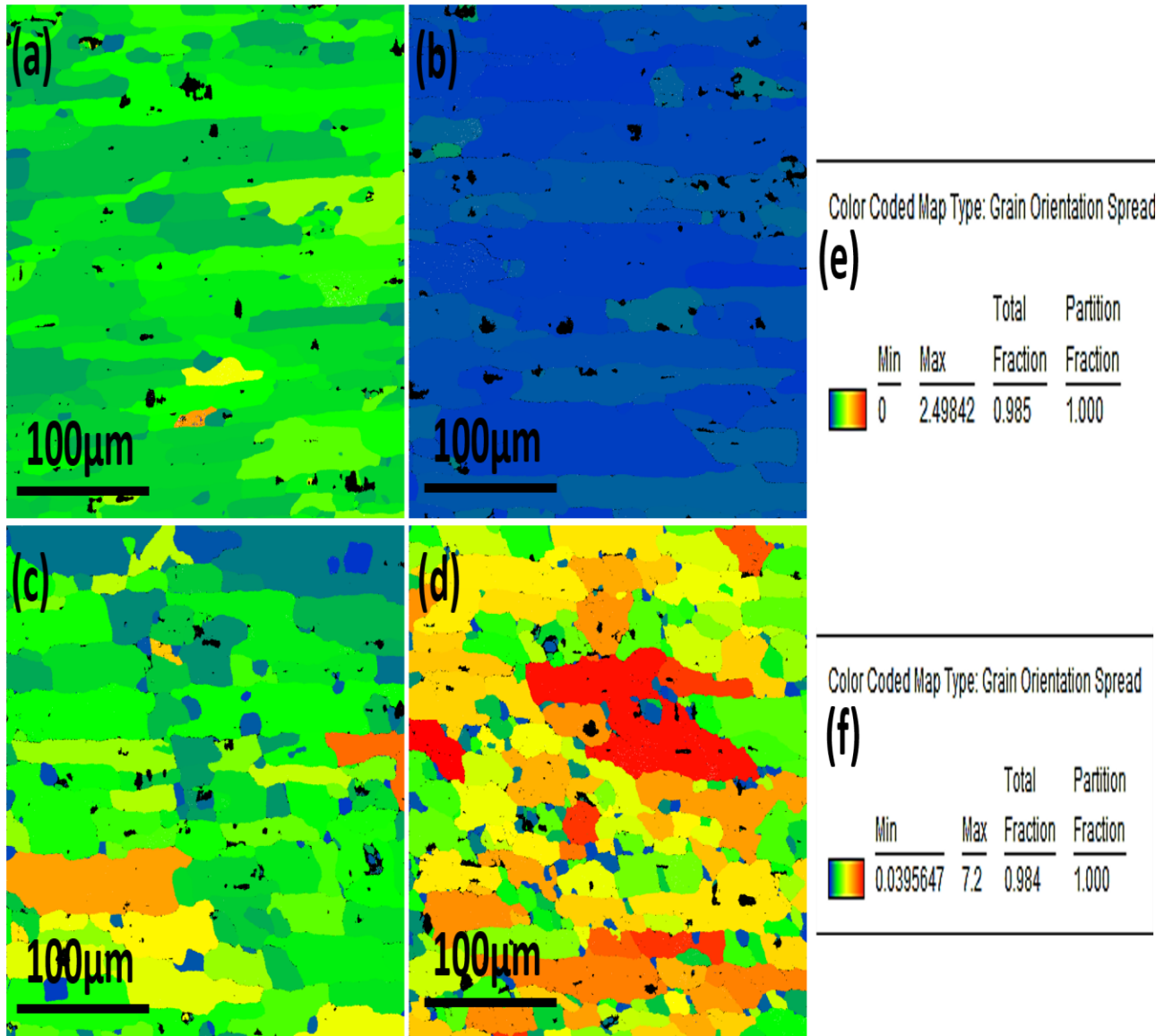


Fig. 4.131 GOS maps of advancing side (AS) of A5754-H111 alloy in FSWed A5754-H111 and A5083-H111 joint (a) BM; (b) HAZ; (c) TMAZ; (d) SZ; (e) Color code map for GOS map of BM and (f) Color code map for GOS maps of HAZ, TMAZ and SZ

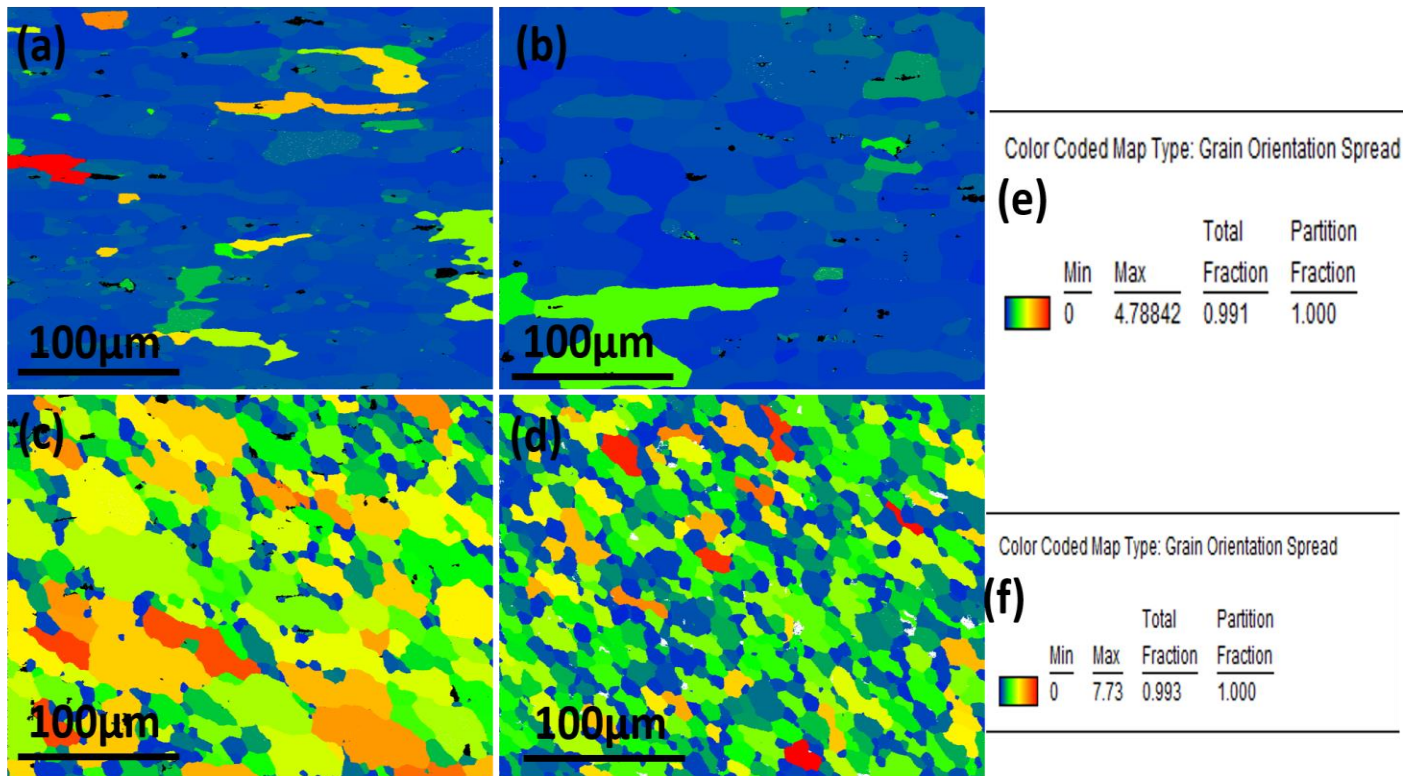


Fig. 4.132 GOS maps of retreating side (RS) of A5083-H111 alloy in FSWed A5754-H111 and A5083-H111 joint (a) BM; (b) HAZ; (c) TMAZ; (d) SZ; (e) Color code map for GOS map of BM and (f) Color code map for GOS maps of HAZ, TMAZ and SZ

4.10.7 Microhardness of the FSWed A5754-H111 and A5083-H111

Microhardness test results of welded joints are shown in Fig. 4.133. The hardness in the SZ of the alloy is only somewhat higher and at the HAZ it is slightly lower than the base 5754-H111 alloy. In contrast, the hardness values in A5083 alloy exhibit a significant difference. The SZ of A5083 shows higher hardness than any other region of the weld. It is also observed that the hardness values of the HAZ in both the alloys are nearly the same

as the hardness values of the base metals. This is in consonance with the observations of previous research work (Mishra and Ma 2005). Generally, in fusion welding process the grains in the HAZ are coarser than in the base metal due to higher heat input that results in lower hardness. However, in FSW process the generated heat is much lower than in fusion welding process. Due to this, there is no significant grain growth in the HAZ, which is reflected in the hardness values. SZ of 5083 alloy shows higher hardness value than the of A5754 alloy. It is reported that the presence of HAGBs in the microstructure increases grain boundary strengthening (Starink and Wang 2003) HAGBs effectively restrict the movement of dislocations and thus the hardness and strength of the material increase. The significant hardness increment in the SZ of 5083 as compared to SZ of A5754 alloy is possibly due to presence of higher fraction of HAGBs and larger amount of fine equiaxed grains.

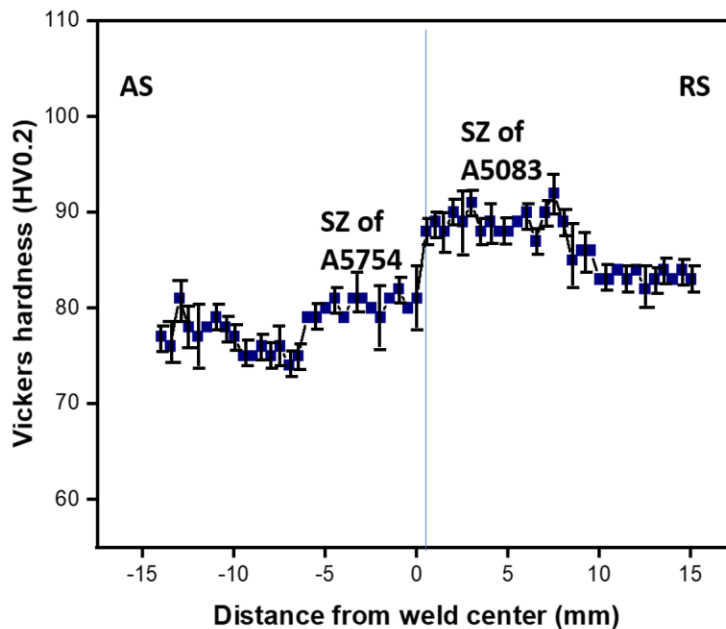


Fig. 4.133 Vickers microhardness of the FSWed A5754-H111 and A5083-H111 joint

4.10.8 Tensile properties of the FSWed A5754-H111 and A5083-H111

Table 4.31 shows tensile properties of the samples. Fig. 4.134 shows tensile properties of BMs and the welded joint (over-all region and SZ). The SZ tensile samples were prepared in such a manner that the centre of the SZ constituted the middle portion of the gage length and the entire gage area remained within the SZ. The entire gage area in the 'over-all' sample consisted of SZ, TMAZ and HAZ of A5754, base A5754 alloy, TMAZ and HAZ of 5083, base A5083 alloy.

SZ has exhibited significant improvement in strength and this can be related to the presence of large amounts of fine equiaxed grains. Also, solid solution hardened aluminium alloys contain secondary phase particles in large quantities (Kannan et al. 1998). It has been reported that the 5xxx series aluminium alloys basically contain Al_6Mn and Mg_2Si second phase particles in the microstructure (McShane et al. 1990; Svensson et al. 2000). During FSW process, these particles are stirred vigorously, and the size of these particles is reduced significantly. Due to stirring, the secondary phase particles are generally dispersed more homogeneously in the SZ. The particles effectively hinder dislocation motion at grain interiors and grain boundaries. Hence, it is understandable that both grain size as well as particle distribution can influence the strength in the SZ of the dissimilar joint.

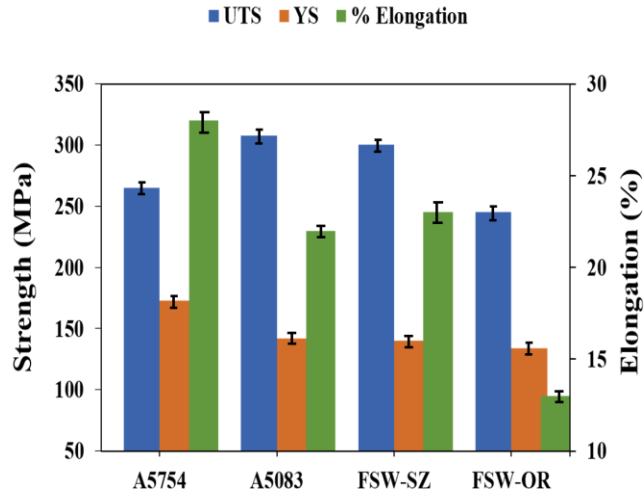


Fig. 4.134 Tensile properties of BMs and FSWed A5754-H111 and A5083-H111 joint (SZ-stir zone and OR-over-all region; Gauge length of BMs & OR is 25 mm and gauge length of SZ is 5 mm)

Table 4.31 Tensile properties of the FSWed A5754-H111 and A5083-H111 joint

Sample	UTS (MPa)	YS (MPa)	Elongation(%)
A5754	265	173	28
A5083	308	142	22
FSWed (stir region)	300	140	23
FSWed (over-all region)	245	134	13

4.10.9 Fractography of the FSWed A5754-H111 and A5083-H111

To identify the mode of failure in FSWed joints the fracture surface was analyzed by SEM.

Fig. 4.135 shows the SEM images of fractured surfaces of tensile samples of SZ and overall FSWed region that display micro voids indicating a ductile fracture.

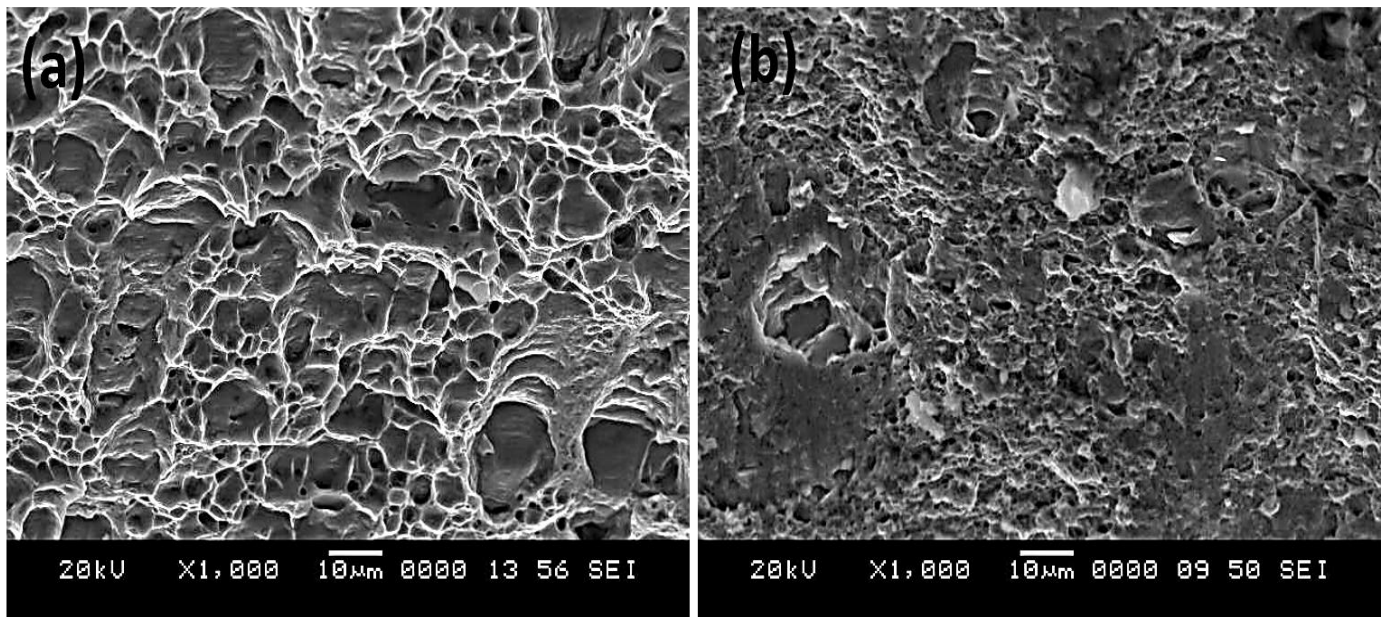


Fig. 4.135 Fractography of fractured specimen in FSWed A5754-H111 and A5083-H111 joint (a) FSW (SZ) and (b) FSW (over-all region)

Chapter 5

COMPARATIVE STUDY OF DISSIMILAR JOINTS

5.1 Comparative study of interface tensile properties of dissimilar A6061-T6 and A6082-T6 joint

5.1.1 Analysis of tensile properties of A6061-T6 interface using ER4043 filler

Fig. 5.1 shows comparison of tensile properties at A6061 interface in dissimilar A6061-T6 and A6082-T6 joint. Table 5.1 lists tensile properties of A6061-T6 interface in dissimilar A6061-T6 and A6082-T6 joint. CMT weld shows ultimate tensile strength (UTS), yield strength (YS) and % elongation of 171 MPa, 52 MPa and 12%, respectively. The UTS, YS and % elongation of TIG weld show 236 MPa, 71 MPa and 15%, respectively. TIG weld exhibits higher mechanical properties (UTS, YS and % elongation) than the CMT weld at A6061 interface in dissimilar A6061-T6 and A6082-T6 joint. In CMT weld, when ER4043 filler is used, a number of porosities are present at the 6061-T6 interface, whereas any such porosities are absent at the same interface in TIG welds. Due to the existence of porosities in the CMT weld joints, there is a decrease in load bearing area and, as a result, tensile properties of the CMT joints are reduced significantly than the TIG joints at A6061-T6 interface. According to a previous research work, both strength and ductility of the weld joint have decreased with the presence of porosities (He et al. 2018). Therefore, the lower % elongation in CMT welds at A6061-T6 interface is possibly due to the presence of porosities. Moreover, GB liquation phenomenon is noticed in the PMZ of A6061-T6

interface in CMT welds, whereas it is completely absent in the PMZ of same interface in TIG welds. Presence of GB liquation leads to increase the PMZ cracking susceptibility (Ghaini et al. 2009). The presence of porosities and GB liquation at A6061-T6 interface in CMT welds have lowered their mechanical properties than TIG welds.

5.1.2 Analysis of tensile properties of A6061-T6 interface using ER5356 filler

When ER5356 filler is used to weld A6061-A6082 dissimilar joint, at A6061 interface, as can be seen from the Table 5.1, CMT weld shows ultimate tensile strength (UTS), yield strength (YS) and % elongation of 250 MPa, 171 MPa and 33%, respectively. The UTS, YS and % elongation of TIG weld show 224 MPa, 191 MPa and 12%, respectively. Thus, UTS and % elongation is higher in CMT welds and YS is higher in TIG welds. A6061-T6 interface of TIG and CMT welds using ER5356 exhibits EQZ in microstructure. According to a published research work, the phenomenon of solute segregation at GBs of EQZ reduces the mechanical properties (Dev et al. 2008). Thus, the presence of EQZ in 6061-T6 interface reduces its strength in TIG and CMT welds. The elongation of the PMZ decreases as the GB eutectics increases (Li et al. 2015). The eutectic Si at GBs are little higher in EQZ of TIG welds than the EQZ of CMT welds at A6061-T6 interface. Therefore, because of the presence of more eutectic Si at GBs of EQZ, TIG weld shows lower elongation values than the CMT welds at A6061-T6 interface. HAZ of A6061 in CMT weld contains rod shape precipitates (β' phase) and spherical shape precipitates. Whereas only rod shaped precipitates are present in HAZ of 6061-T6 interface in TIG weld. A spherical precipitates in Al-Mg-Si alloys can effectively hinder the dislocation movement thereby increases strength (Yuan et al. 2007). Due to the absence of spherical shape precipitates, its

strengthening contribution is completely absent in TIG weld at A6061-T6 interface. Therefore, the UTS and % elongation of CMT weld is higher as compared to TIG weld at A6061-T6 interface.

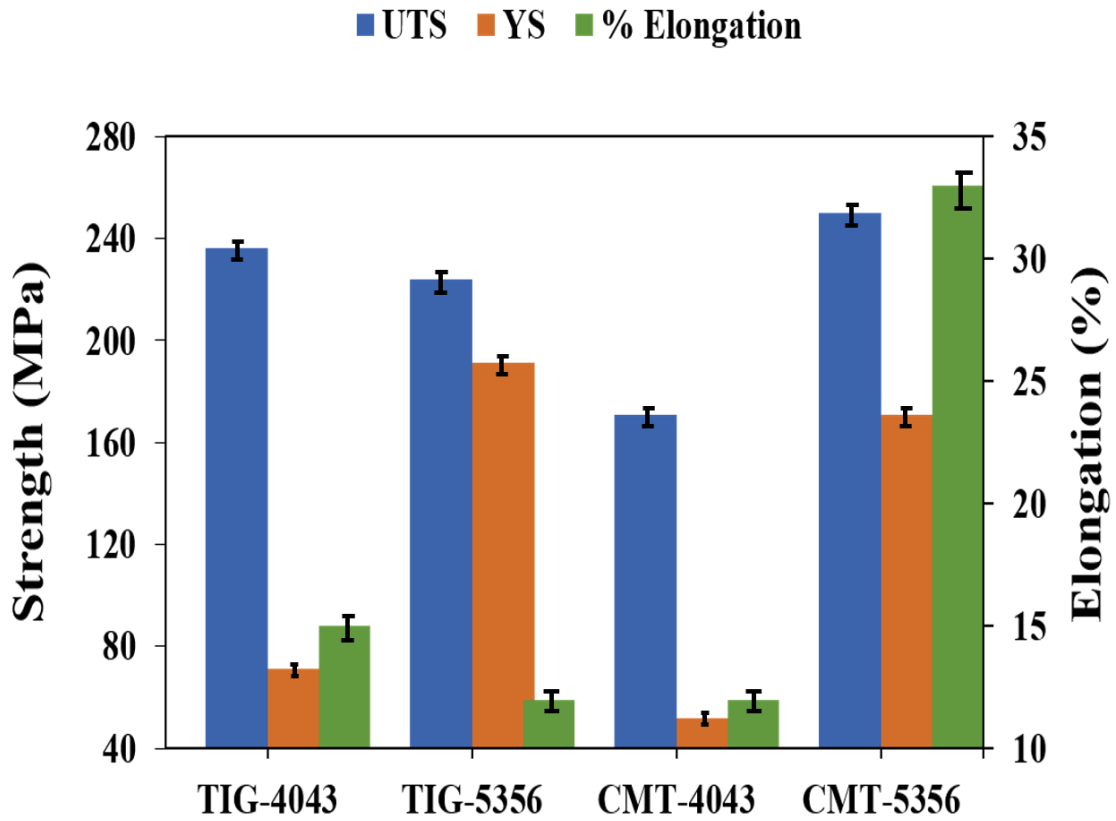


Fig. 5.1 Comparison of tensile properties of A6061 interface in dissimilar A6061-T6 and A6082-T6 joint produced using TIG and CMT welding processes with ER4043 and ER5356 filler wires (Gauge length of the samples is 5mm)

Table 5.1 Tensile properties of A6061-T6 interface in dissimilar A6061-T6 and A6082-T6 joint produced using TIG and CMT welding processes with ER4043 and ER5356 filler wires (Gauge length of the samples is 5mm)

Sample	UTS (MPa)	YS (MPa)	Elongation (%)
TIG weld joint (ER4043)	236	71	15
TIG weld joint (ER5356)	224	191	12
CMT weld joint (ER4043)	171	52	12
CMT weld joint (ER5356)	250	171	33

5.1.3 Analysis of tensile properties of A6082-T6 interface using ER4043 filler

Fig. 5.2 shows comparison of tensile properties at A6082 interface in dissimilar A6061-T6 and A6082-T6 joint. Tensile properties of A6082-T6 interface in dissimilar A6061-T6 and A6082-T6 joint are summarized in table 5.2. CMT weld shows UTS, YS and % elongation of 243 MPa, 119 MPa and 19%, respectively. The UTS, YS and % elongation of TIG weld show 300 MPa, 236 MPa and 9%, respectively. UTS and YS is higher in TIG weld than the CMT weld. Whereas % elongation of TIG weld is lower than the CMT welds. When ER4043 filler is used, both TIG and CMT welding process do not exhibit any porosities at A6082-T6 interface. At the same time, it is worth mentioning that Al-Si eutectic phases are

distributed as fine particles in larger quantity along the GBs of PMZ for TIG welding, whereas PMZ of A6082-T6 interface of CMT welding contains very few Al-Si eutectic particles that are coarser in size. Due to the above-mentioned reasons, the TIG welds have exhibited higher strength (UTS and YS) than the CMT welds at A6082-T6 interface.

5.1.4 Analysis of tensile properties of A6082-T6 interface using ER5356 filler

When the ER5356 filler is used to weld A6061-A6082 dissimilar joint, at A6082 interface, as can be seen from the Table 5.2, CMT weld shows UTS, YS and % elongation of 290 MPa, 195 MPa and 30%, respectively. The UTS, YS and % elongation of TIG weld show 265 MPa, 205 MPa and 21%, respectively. UTS and % elongation of CMT weld is higher than the TIG weld. However, YS of CMT weld is somewhat lower than the TIG weld. The dendrites of CCZ of the A6082 interface in CMT weld is finer than the dendrites of CCZ of the A6082 interface in TIG weld. The number of spherical shape precipitates are higher in the HAZ of A6082 interface in CMT weld than the HAZ of A6082 interface in TIG welds. According to previous research work a spherical precipitates in Al-Mg-Si alloys have a stronger interaction with the dislocations (Yuan et al. 2007). As the number of precipitates increases there is an increase in dislocation pinning points in each slip plane. Due to the high number of spherical shape precipitates in HAZ of A6082 interface in CMT weld, dislocation pinning points are more thereby increases its strength than the A6082 interface in TIG weld. Therefore, finer dendrites in CCZ and high number of spherical shape precipitates in HAZ of increases the strength of A6082 interface in CMT weld than the A6082 interface of TIG weld.

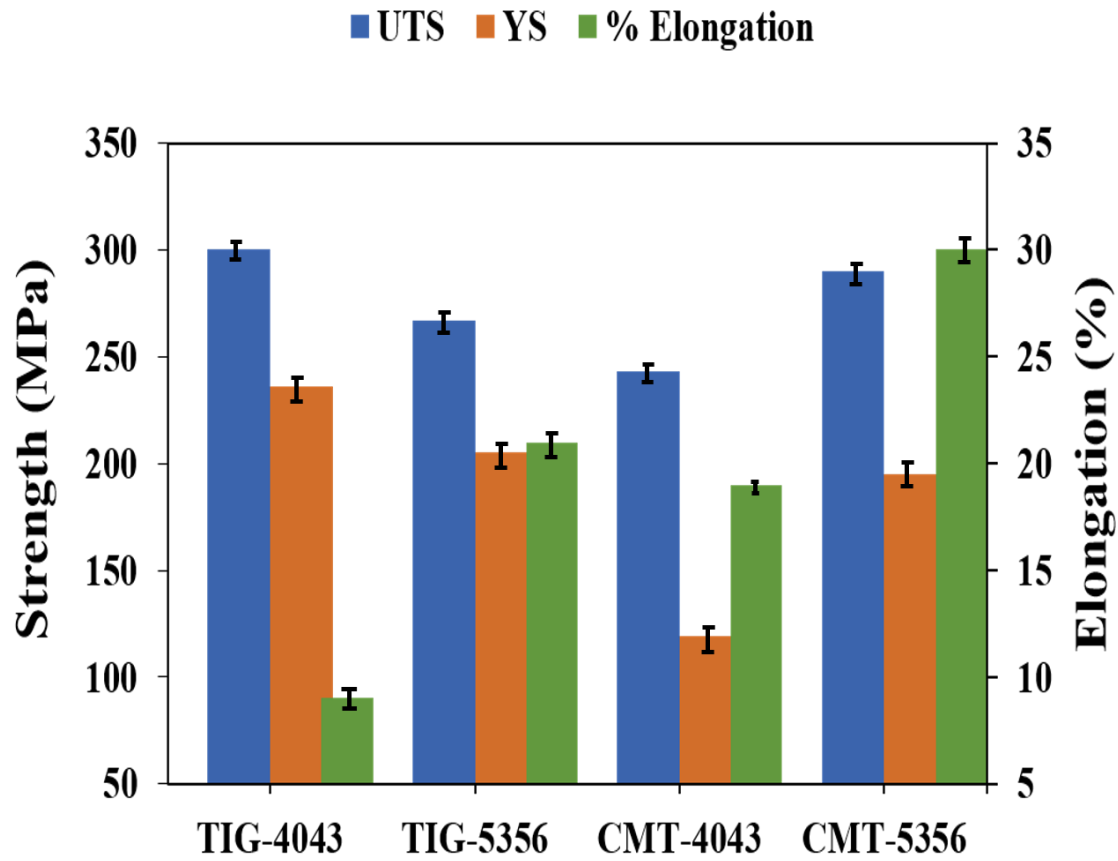


Fig. 5.2 Comparison of tensile properties of A6082 interface in dissimilar A6061-T6 and A6082-T6 weld joint produced using TIG and CMT welding processes with ER4043 and ER5356 filler wires (Gauge length of the samples is 5mm)

Table 5.2 Tensile properties of A6082-T6 interface in dissimilar A6061-T6 and A6082-T6 joint produced using TIG and CMT welding processes with ER4043 and ER5356 filler wires (Gauge length of the samples is 5mm)

Sample	UTS (MPa)	YS (MPa)	Elongation (%)
TIG weld joint (ER4043)	300	236	9
TIG weld joint (ER5356)	267	205	21
CMT weld joint (ER4043)	243	119	19
CMT weld joint (ER5356)	290	195	30

5.2 Comparative study on interface tensile properties of dissimilar A5754-H111 and A5083-H111 joint

5.2.1 Analysis of tensile properties of A5754 interface using ER4043 filler

Fig. 5.3 shows comparison of tensile properties at A5754 interface in dissimilar A5754 and A5083 joint. Table 5.3 lists tensile properties of A5754 interface in dissimilar A5754 and A5083 joint. CMT weld shows UTS, YS and % elongation of 161 MPa, 49 MPa and 12%, respectively. The UTS, YS and % elongation of TIG weld show 209 MPa, 130 MPa and 7%, respectively. UTS and YS of TIG weld is higher than the CMT weld. However, % elongation of TIG weld is lower than the CMT weld. When ER4043 filler is used, the presence of EQZ is noticed in A5754 interface in CMT welds. Si segregation is more at

GBs of EQZ. According to a published research work, the phenomenon of solute segregation at GBs of EQZ reduces the mechanical properties (Dev et al. 2008). No such EQZ is evolved at A5754 interface in TIG welds. Thus, the absence of EQZ has led to higher strength (UTS and YS) of TIG welds than the CMT welds at A5754 interface.

5.2.2 Analysis of tensile properties of A5754 interface using ER5356 filler

When the ER5356 filler is used to weld A5754-A5083 dissimilar joint, at A5754 interface, as can be seen from the Table 5.3, CMT weld shows UTS, YS and % elongation of 210 MPa, 108 MPa and 33%, respectively. The UTS, YS and % elongation of TIG weld show 208 MPa, 63 MPa and 25%, respectively. CMT weld exhibits superior mechanical properties (UTS, YS and % elongation) than the TIG weld. The dendrites in CCZ are finer at CMT welds than the dendrites in CCZ of TIG welds at A5754 interface. The grains at HAZ and PMZ of TIG welds at A5754 interface are significantly coarser than the grains at HAZ and PMZ of CMT welds at A5754 interface. For these reasons, the mechanical properties of CMT welds at A5754 interface is higher than the mechanical properties of TIG welds at A5754 interface.

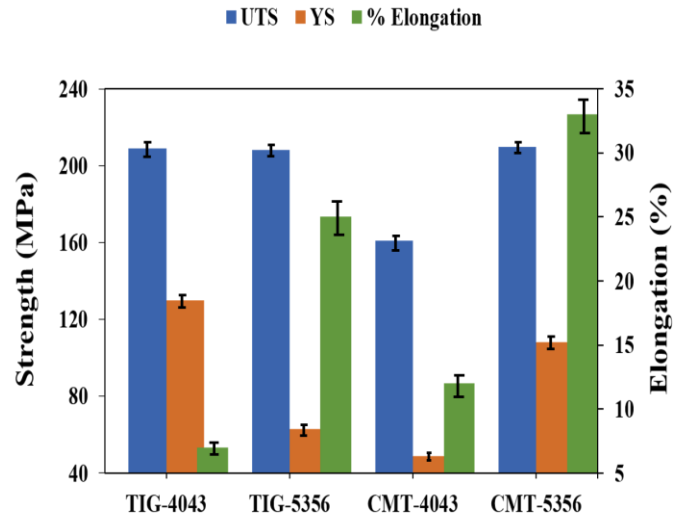


Fig. 5.3 Comparison of tensile properties of A5754 interface in dissimilar A5754 and A5083 weld produced using TIG and CMT welding processes with ER4043 and ER5356 filler wires (Gauge length of the samples is 5mm)

Table 5.3 Tensile properties of A5754 interface in dissimilar A5754 and A5083 weld produced using TIG and CMT welding processes with ER4043 and ER5356 filler wires (Gauge length of the samples is 5mm)

Sample	UTS (MPa)	YS (MPa)	Elongation (%)
TIG weld joint (ER4043)	209	130	7
TIG weld joint (ER5356)	208	63	25
CMT weld joint (ER4043)	161	49	12
CMT weld joint (ER5356)	210	108	33

5.2.3 Analysis of tensile properties of A5083 interface using ER4043 filler

Fig. 5.4 shows comparison of tensile properties at A5083 interface in dissimilar A5754 and A5083 joint. Tensile properties of A5083 interface in dissimilar A5754 and A5083 joint are listed in table 5.4. CMT weld shows UTS, YS and % elongation of 209 MPa, 63 MPa and 9%, respectively. The UTS, YS and % elongation of TIG weld show 227 MPa, 136 MPa and 12%, respectively. TIG weld exhibits superior mechanical properties (UTS, YS and % elongation) than the CMT weld. At A5083 interface both TIG and CMT welds show EQZ when ER4043 filler is used. According to previous research cracks are nucleated and propagated at GBs of EQZ in the Al weld joint (Gutierrez and Lippold 1998). The fracture in Al weld joint mainly occurs at the EQZ during deformation at both ambient as well as cryogenic temperatures (Shah 1993). It is observed that Si films at the GBs of EQZ is thicker at CMT welds and it is comparatively less in TIG welds. As the thickness of Si films in GBs increases, correspondingly GBs becomes weak. This means that under tensile stress cracks nucleation and propagation is much easier as GBs of EQZ contains thicker Si films (Han et al. 2017). According to a published work elongation of the joint decreases when the eutectic phases at GBs of PMZ increases (Li et al. 2015). The eutectic Si at GBs are higher in EQZ of CMT welds than the EQZ of TIG welds at A5083 interface. Thus, CMT weld shows lower elongation values than the TIG welds at A5083 interface. Therefore, due to the thicker Si films at GBs of EQZ, the mechanical properties (UTS, YS and % elongation) of CMT welds is lower than the TIG welds at A5083 interface.

5.2.4 Analysis of tensile properties of A5083 interface using ER5356

When the ER5356 filler is used to weld A5754-A5083 dissimilar joint, at A5083 interface as can be seen from the Table 5.4, CMT weld shows UTS, YS and % elongation of 230 MPa, 135 MPa and 27%, respectively. The UTS, YS and % elongation of TIG weld show 285 MPa, 101 MPa and 21%, respectively. UTS is higher in TIG welds than the CMT welds. Presence of secondary phase particles affect the strength of the interfaces. The pinning of dislocations by secondary phase particles usually strengthen the materials. The presence of Mg_2Si and Al_3Mg_2 phases have a strong interaction with dislocations that increases the strength (Lu et al. 2003; Shahid and Scudino 2018). Moreover, it is reported that Al_6MnFe phases are improving the mechanical properties of the Al alloys (Du et al. 2018). It is obvious that the secondary phase particles such as Al_3Mg_2 , Mg_2Si and Al_6MnFe are present in the HAZ of A5083 interface in TIG welds, whereas Al_6MnFe phases are completely absent in the HAZ of A5083 interface in CMT welds. The absence of strengthening contribution by Al_6MnFe phases may be the possible reason for the reduced UTS in CMT welds at A5083 interface.

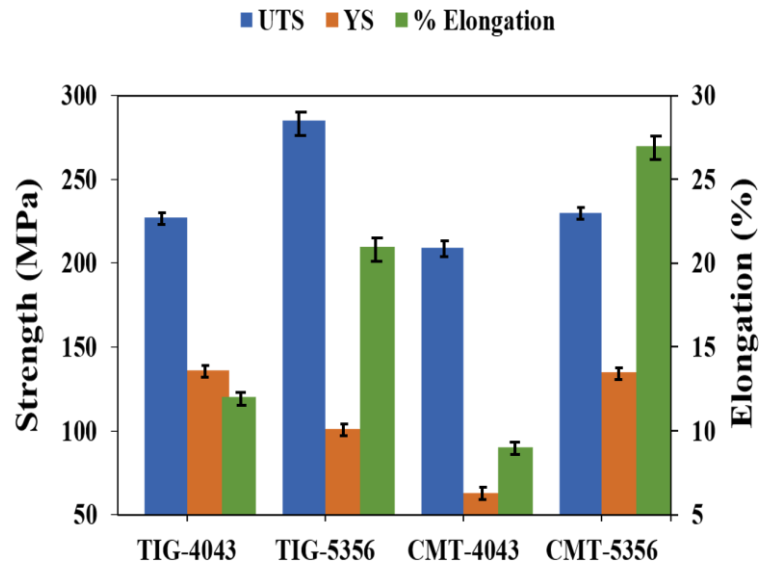


Fig. 5.4 Comparison of tensile properties of A5083 interface in dissimilar A5754 and A5083 weld produced using TIG and CMT welding processes with ER4043 and ER5356 filler wires (Gauge length of the samples is 5mm)

Table 5.4 Tensile properties of A5083 interface in dissimilar A5754 and A5083 weld produced using TIG and CMT welding processes with ER4043 and ER5356 filler wires (Gauge length of the samples is 5mm)

Sample	UTS (MPa)	YS (MPa)	Elongation (%)
TIG weld joint (ER4043)	227	136	12
TIG weld joint (ER5356)	285	101	21
CMT weld joint (ER4043)	209	63	9
CMT weld joint (ER5356)	230	135	27

5.3 Comparative study of overall joint tensile properties of dissimilar joints

The comparative study of overall joint tensile properties of dissimilar joints is important for identifying a suitable welding process to join A6061-A6082 and A5754-A5083 dissimilar joints. Fig. 5.5 and Fig. 5.6 show comparison of tensile properties of over-all region with respect to welding process in A6061-A6082 and A5754-A5083 dissimilar joints, respectively. Table 5.5 and Table 5.6 list tensile properties of over-all region with respect to welding process in A6061-A6082 and A5754-A5083 dissimilar joints, respectively. Since FSW is a solid-state process, no filler is used. Among the A6061-A6082 dissimilar joints, the CMT joint produced by ER5356 filler and FSW joint exhibit higher mechanical properties (UTS,YS and % elongation) than the other joints. The mechanical properties of A6061-A6082 dissimilar CMT joint produced by ER5356 filler and FSW joint are nearly same. Even though the above-mentioned joints exhibit nearly the same mechanical properties, the FSW process is chosen as preferable joining method among these processes, because the FSW process does not use any shielding gas, filler materials, and surface preparation is not critical. The aforementioned reasons can play a vital role to reduce the cost in an effective manner. Moreover, CMT welding processes, fumes are evolved and to protect molten pool shielding gases also used. Both these produce adverse effect on the environment. Due to the absence of fumes and shielding gases FSW process is environment friendly. In the case of A5754-A5083 dissimilar joints, FSW joint shows higher mechanical properties than the other joints. The A5754-A5083 dissimilar joint produced by TIG welding process using ER5356 shows little higher % elongation than the FSW joint whereas UTS and YS is lower than the FSW joint. Therefore, it is concluded

that FSW process is a preferable joining method for A6061-A6082 and A5754-A5083 dissimilar joints.

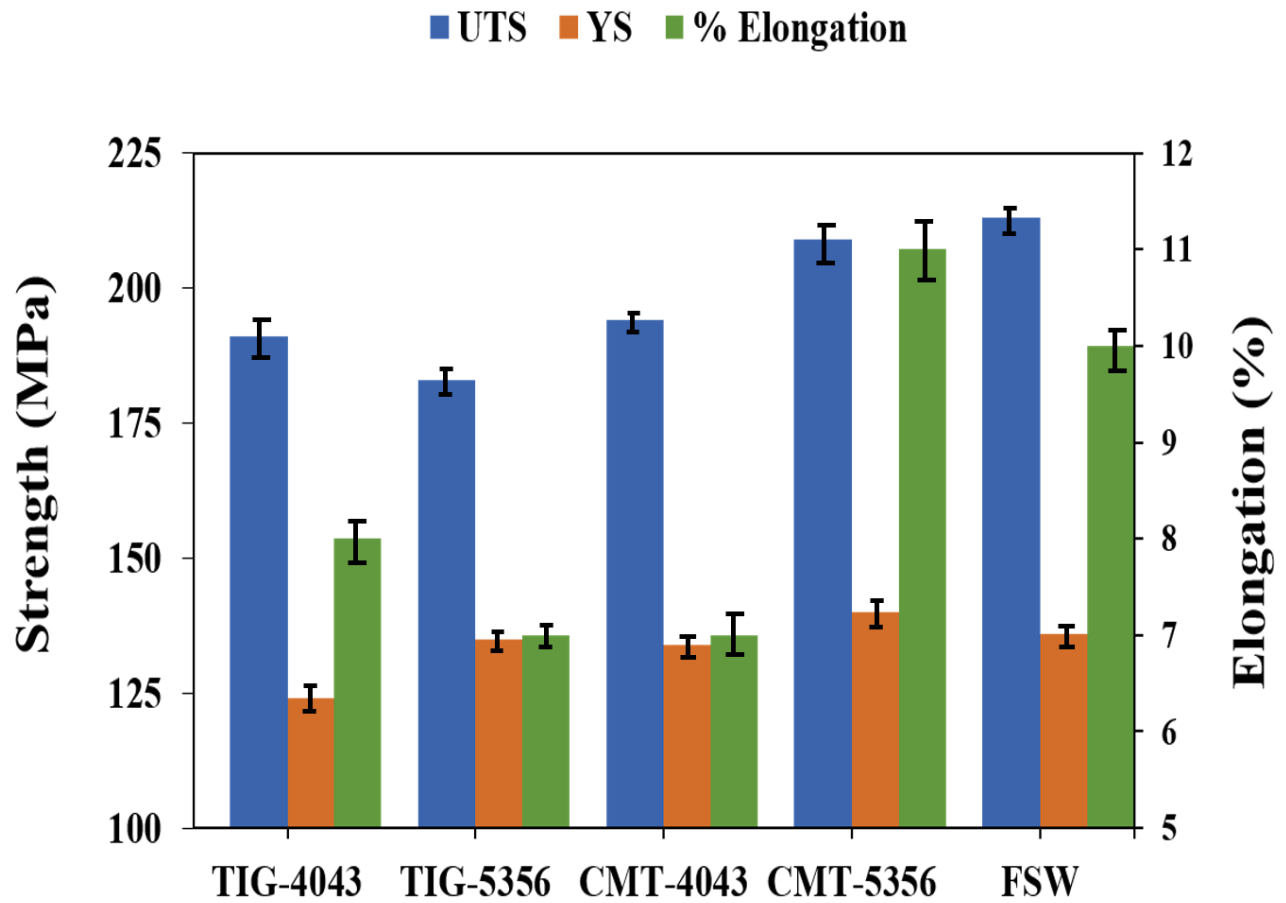


Fig. 5.5 Comparison of tensile properties of over-all region in A6061-A6082 dissimilar joint with respect to welding process (Gauge length of the samples is 25mm)

Table 5.5 Tensile properties of over-all region in A6061-A6082 dissimilar joint with respect to welding process (Gauge length of the samples is 25mm)

Welding process	UTS (MPa)	YS (MPa)	Elongation (%)
TIG weld joint (ER4043)	191	124	8
TIG weld joint (ER5356)	183	135	7
CMT weld joint (ER4043)	194	134	7
CMT weld joint (ER5356)	209	140	11
FSW joint	213	136	10

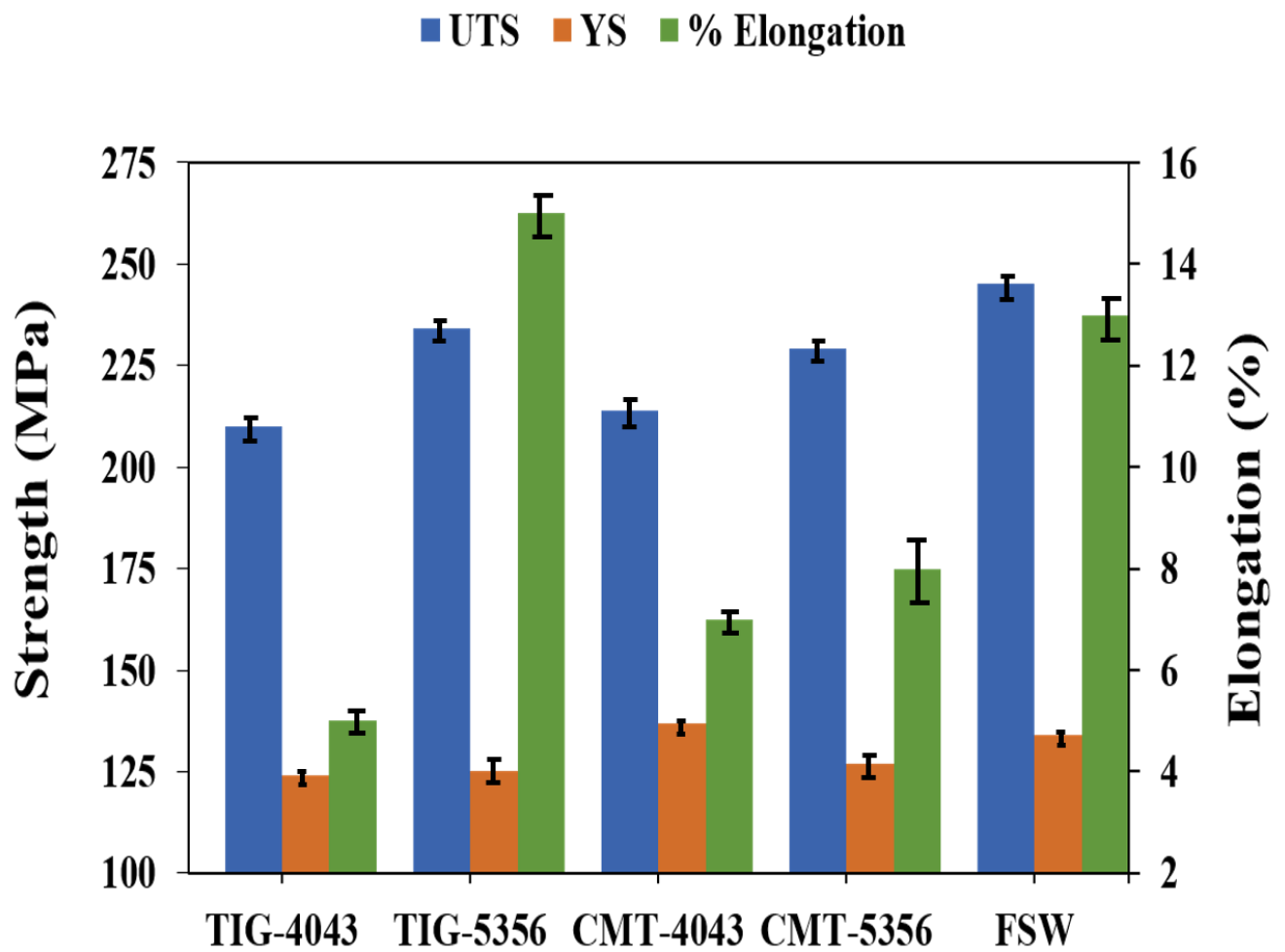


Fig. 5.6 Comparison of tensile properties of over-all region in A5754-A5083 dissimilar joint with respect to welding process (Gauge length of the samples is 25mm)

Table 5.6 Tensile properties of over-all region in A5754-A5083 dissimilar joint with respect to welding process (Gauge length of the samples is 25mm)

Welding process	UTS (MPa)	YS (MPa)	Elongation (%)
TIG weld joint (ER4043)	210	124	5
TIG weld joint (ER5356)	234	125	15
CMT weld joint (ER4043)	214	137	7
CMT weld joint (ER5356)	229	127	8
FSW joint	245	134	13

5.4 Summary of joint strength results

- When ER4043 filler is used, at A6061-T6 interface, porosities and GB liquation are present in CMT weld. This lowers its mechanical properties than TIG welds at the A6061-T6 interface.
- The CMT welds at A6061-T6 interface using ER5356 contains spherical shape precipitates along with rod shape precipitates (β' phase) at HAZ that increase its UTS than the TIG welds.

- The TIG welds at A6082-T6 interface using ER4043 shows distribution of fine Al-Si eutectic phases in larger quantity along the GBs of PMZ. This increases its strength than CMT welds at the A6082-T6 interface.
- When ER5356 filler is used, at A6082-T6 interface, CMT weld shows finer dendrites in CCZ and high number of spherical shape precipitates in HAZ. This increases its strength than TIG welds at the A6082-T6 interface.
- When ER4043 filler is used, the presence of EQZ is noticed in A5754 interface in CMT welds. The absence of EQZ leads to improve the strength of TIG welds than the CMT welds at A5754 interface.
- When ER5356 filler is used, dendrites in CCZ and grains in HAZ and PMZ at A5754 interface of CMT welds are finer than those in the TIG welds. This increases the strength of CMT welds at A5754 interface than the TIG welds at A5754 interface.
- When ER4043 filler is used, at A5083 interface, Si segregation is more severe at EQZ of CMT welds and it is comparatively less in TIG welds. Due to this, the strength of TIG welds is higher than the CMT welds at A5083 interface.
- When ER5356 filler is used, at A5083 interface higher strength is exhibited in TIG welds than the CMT welds. This is mainly attributed to the presence of a Al_6MnFe phases along with the Al_3Mg_2 , and Mg_2Si phases in the HAZ of TIG welds.
- The overall joint tensile properties of dissimilar joints are important for identifying a suitable welding process to join A6061-A6082 and A5754-A5083 dissimilar joints. Among the A6061-A6082 dissimilar joints, the CMT joint produced by

ER5356 filler and FSW joint exhibits higher mechanical properties (UTS, YS and % elongation) than the other joints. FSW process does not use any shielding gas, filler materials, the surface preparation is not critical and it is environment friendly. These factors can play a vital role to reduce the cost of welding in an effective manner. In the case of A5754-A5083 dissimilar joints, FSW joint shows higher mechanical properties than the other joints. Therefore, FSW process is a preferable joining method for A6061-A6082 and A5754-A5083 dissimilar joints.

Chapter 6

SUMMARY AND CONCLUSIONS

In the present study dissimilar aluminium alloy combinations A6061 T6 - A6082 T6 and A5754 H111 and A5083 H111 are welded using CMT (Cold metal transfer) process, tungsten inert gas (TIG) welding and friction stir welding (FSW) processes. The following conclusions are drawn from the experimental findings and analysis.

- In the case of dissimilar A6061-T6 and A6082-T6 joint, among the interfaces, 6082-T6 side displays higher mechanical properties (YS, UTS) in comparison with 6061-T6 side when the joint is welded by CMT process using ER4043 filler. The presence of finer dendrites at fusion zone near the interface, the absence of liquation phenomenon at grain boundaries and grain interiors and the complete absence of porosities are the possible reasons for improvement in mechanical properties of the 6082-T6 interface.
- The dissimilar A6061-T6 and A6082-T6 joint welded by CMT process using ER5356 filler exhibits higher strength in A6082 interface in comparison to the A6061 interface. A combined result of the absence of EQZ (thereby fewer liquation cracks) and the presence of the rod-shaped precipitates in HAZ increases the strength of A6082 interface.
- The dissimilar A5754 and A5083 joint welded by CMT process using ER4043 filler exhibits higher strength at A5083 interface than the A5754 interface. The higher strength of A5083 interface can be ascribed to lesser EQZ width, finer grains at

EQZ, finer dendrites at WMZ interface and the distribution of secondary phase particles in larger quantity at PMZ and HAZ.

- In the case of dissimilar A5754 and A5083 joint, the interface region of the A5083 side exhibits higher strength than the interface region of A5754 when the joint is welded by CMT process using ER5356 filler. This is attributed to the higher volume of finer secondary phase particles distribution at the HAZ and PMZ of the A5083 side than the other side.
- When dissimilar A6061-T6 and A6082-T6 joint welded by TIG process using ER4043 filler, A6082-T6 interface exhibits superior mechanical properties than the A6061-T6 interface. Absence of EQZ, presence of finer Al-Si eutectic phase particles at PMZ and the presence of finer dendrites at CCZ have improved the strength of A6082-T6 interface than the A6061-T6 interface.
- In the case of dissimilar A6061-T6 and A6082-T6 joint, the strength of 6082-T6 interface is higher as compared to 6061-T6 interface when joint is welded by TIG process using ER5356 filler. The rod shaped precipitates are present in HAZs of 6061-T6 interface. Other than the few rod shaped β' precipitates, a considerable amount of spherical shaped Si rich precipitates appearing dark grey is also found in the HAZ of A6082 interface. Moreover, the absence of EQZ is noticed in A6082-T6 interface. Due to all these the strength of the 6082-T6 interface has increased compared to 6061-T6 interface.
- A5083 interface shows slightly higher strength values than the A5754 interface when A5754 and A5083 joint is welded by TIG process with ER4043 filler. No

significant improvement in strength is observed in A5083 interface than the A5754 interface. The presence of EQZ in A5083 could have significantly reduced the strength.

- In dissimilar A6061-T6 and A6082-T6 FSWed joint, the SZ of the weld joint exhibits maximum hardness among the TMAZ and HAZ regions. The refined grain structure in SZ increases hardness and strength. Fractured surfaces of tensile samples indicate a ductile fracture.
- Among the SZs, SZ of A5083 exhibit higher hardness as compared to SZ of A5754 alloy in dissimilar A5754 and A5083 FSWed joint. The presence of higher fraction of HAGBs and larger amount of fine equiaxed grains are the reasons for the increase in hardness of A5083 SZ than the A5754 SZ.
- The overall joint tensile properties of dissimilar joints are important for identifying a suitable welding process to join A6061-A6082 and A5754-A5083 dissimilar joints. Among the A6061-A6082 dissimilar joints, the CMT joint produced by ER5356 filler and FSW joint exhibit superior mechanical properties (UTS, YS and % elongation) than the other joints. Moreover, FSW process does not use any shielding gas, filler materials, and the surface preparation is not critical. These factors can play a vital role to reduce the cost of welding in an effective manner. Also, FSW process is environment friendly, due to the absence of fumes and shielding gases. In the case of A5754-A5083 dissimilar joints, FSW joint shows superior mechanical properties than the other joints. Therefore, the FSW process

can be recommended as the preferable joining method for joining A6061-T6 and A6082-T6 and A5754 and A5083 dissimilar joints.

REFERENCES

- A. Kostrivas, J. C. L. (2006). "FUSION BOUNDARY MICROSTRUCTURE EVOLUTION IN ALUMINIUM ALLOYS." *Weld world*, 50, 24–34.
- Aalco metals Ltd. (2013). "Aluminium Alloy 6082 - T6~T651 Plate." 24–25.
- Adderley, C. S. (1988). "Adhesive bonding." *Mater. Des.*, 9(5), 287–293.
- Alshaer, A. W., Li, L., and Mistry, A. (2014). "The effects of short pulse laser surface cleaning on porosity formation and reduction in laser welding of aluminium alloy for automotive component manufacture." *Opt. Laser Technol.*, 64, 162–171.
- Arbegast, W. J. (2008). "A flow-partitioned deformation zone model for defect formation during friction stir welding." *Scr. Mater.*, 58(5), 372–376.
- Arbegast, W. J., and Hartley, P. J. (1999). "Friction stir weld technology development at Lockheed Martin Michoud Space System--an overview." *ASM Int. Trends Weld. Res.*, 541–546.
- Arora, A., De, A., and DebRoy, T. (2011). "Toward optimum friction stir welding tool shoulder diameter." *Scr. Mater.*, 64(1), 9–12.
- Atabaki, M. M., Nikodinovski, M., Chenier, P., Ma, J., Liu, W., and Kovacevic, R. (2014). "Experimental and numerical investigations of hybrid laser arc welding of aluminum alloys in the thick T-joint configuration." *Opt. Laser Technol.*, 59, 68–92.

- Babu, S., Panigrahi, S. K., Ram, G. D. J., Venkitakrishnan, P. V, and Kumar, R. S. (2019). “Cold metal transfer welding of aluminium alloy AA 2219 to austenitic stainless steel AISI 321.” *J. Mater. Process. Tech.*, 266(October 2018), 155–164.
- Balasubramanian, V. (2008). “Relationship between base metal properties and friction stir welding process parameters.” *Mater. Sci. Eng. A*, 480(1–2), 397–403.
- Benedyk, J. C. (2010). *Aluminum alloys for lightweight automotive structures*. Mater. Des. Manuf. Light. Veh., Woodhead Publishing Limited.
- Block-Bolten, A., and Eagar, T. W. (1984). “Metal vaporization from weld pools.” *Metall. Trans. B*, 15(3), 461–469.
- Bloeck, M. (2012). *Aluminium sheet for automotive applications*. Adv. Mater. Automot. Eng., Woodhead Publishing Limited.
- Cao, R., Wang, T., Wang, C., Feng, Z., Lin, Q., and Chen, J. H. (2014). “Cold metal transfer welding – brazing of pure titanium TA2 to magnesium alloy AZ31B.” *J. Alloys Compd.*, 605, 12–20.
- Cao, R., Wen, B. F., Chen, J. H., and Wang, P. (2013a). “Cold Metal Transfer joining of magnesium AZ31B-to-aluminum A6061-T6.” *Mater. Sci. Eng. A*, 560, 256–266.
- Cao, R., Yu, G., Chen, J. H., and Wang, P. (2013b). “Cold metal transfer joining aluminum alloys-to-galvanized mild steel.” *J. Mater. Process. Tech.*, 213(10), 1753–1763.
- Chhangani, S., Masa, S. K., Mathew, R. T., Prasad, M. J. N. V., and Sujata, M. (2020).

- “Microstructural evolution in Al–Mg–Sc alloy (AA5024): Effect of thermal treatment, compression deformation and friction stir welding.” *Mater. Sci. Eng. A*, 772, 138790.
- Chuaiphan, W., and Srijaroenpramong, L. (2020). “Optimization of TIG welding parameter in dissimilar joints of low nickel stainless steel AISI 205 and AISI 216.” *J. Manuf. Process.*, 58(August), 163–178.
- Cieslak, M. J., and Fuerschbach, P. W. (1988). “On the weldability, composition, and hardness of pulsed and continuous Nd: YAG laser welds in aluminum alloys 6061, 5456, and 5086.” *Metall. Trans. B*, 19(2), 319–329.
- Çömez, N., and Durmuş, H. (2019). “Mechanical Properties and Corrosion Behavior of AA5754-AA6061 Dissimilar Aluminum Alloys Welded by Cold Metal Transfer.” *J. Mater. Eng. Perform.*, 28(6), 3777–3784.
- Commin, L., Dumont, M., Masse, J.-E., and Barrallier, L. (2009). “Friction stir welding of AZ31 magnesium alloy rolled sheets: Influence of processing parameters.” *Acta Mater.*, 57(2), 326–334.
- Connor, L. P., and O’Brien, R. L. (1991). *Welding handbook: welding processes*. Amer Welding Society.
- Costa, M. I., Verdera, D., Costa, J. D., Leitao, C., and Rodrigues, D. M. (2015). “Influence of pin geometry and process parameters on friction stir lap welding of AA5754-H22 thin sheets.” *J. Mater. Process. Technol.*, 225, 385–392.
- Cui, L., Li, X., He, D., Chen, L., and Gong, S. (2012). “Effect of Nd : YAG laser welding

on microstructure and hardness of an Al – Li based alloy.” *Mater. Charact.*, 71, 95–102.

Davis, J. R., and others. (1993). *Aluminum and aluminum alloys*. ASM international.

Dawes, C. J., and Thomas, W. M. (1996). “Friction stir process welds aluminium alloys: The process produces low-distortion, high-quality, low-cost welds on aluminium.” *Weld. J.*, 75(3), 41–45.

Dawood, H. I., Mohammed, K. S., Rahmat, A., and Uday, M. B. (2015a). “The influence of the surface roughness on the microstructures and mechanical properties of 6061 aluminium alloy using friction stir welding.” *Surf. Coatings Technol.*, 270, 272–283.

Dawood, H. I., Mohammed, K. S., Rahmat, A., and Uday, M. B. (2015b). “Effect of small tool pin profiles on microstructures and mechanical properties of 6061 aluminum alloy by friction stir welding.” *Trans. Nonferrous Met. Soc. China (English Ed.)*, 25(9), 2856–2865.

Dehghani, M., Amadeh, A., and Akbari Mousavi, S. A. A. (2013). “Investigations on the effects of friction stir welding parameters on intermetallic and defect formation in joining aluminum alloy to mild steel.” *Mater. Des.*, 49, 433–441.

Derazkola, H. A., and Simchi, A. (2019). “An investigation on the dissimilar friction stir welding of T-joints between AA5754 aluminum alloy and poly(methyl methacrylate).” *Thin-Walled Struct.*, 135(November 2018), 376–384.

Dev, S., Murty, B. S., and Rao, K. P. (2008). “Effects of base and filler chemistry and weld techniques on equiaxed zone formation in Al – Zn – Mg alloy welds Effects of base

and filler chemistry and weld techniques on equiaxed zone formation in Al – Zn – Mg alloy welds.” *Sci. Technol. Weld. Join.*, 13(7), 598–606.

Ding, S., Khan, S. A., and Yanagimoto, J. (2018). “Constitutive descriptions and microstructure evolution of extruded A5083 aluminum alloy during hot compression.” *Mater. Sci. Eng. A*, 728, 133–143.

Du, J., Ding, D., Zhang, W., Xu, Z., Gao, Y., Chen, G., You, X., Chen, R., Huang, Y., and Tang, J. (2018). “Effect of CeLa addition on the mechanical properties of Al--Cu--Mn--Mg--Fe alloy.” *Mater. Sci. Technol.*, 34(8), 917–925.

Dutra, J. C., e Silva, R. H. G., Savi, B. M., Marques, C., and Alarcon, O. E. (2015). “Metallurgical characterization of the 5083H116 aluminum alloy welded with the cold metal transfer process and two different wire-electrodes (5183 and 5087).” *Weld. World*, 59(6), 797–807.

Elangovan, K., Balasubramanian, V., and Valliappan, M. (2008). “Influences of tool pin profile and axial force on the formation of friction stir processing zone in AA6061 aluminium alloy.” *Int. J. Adv. Manuf. Technol.*, 38(3–4), 285–295.

Elrefaey, A. (2015). “Effectiveness of cold metal transfer process for welding 7075 aluminium alloys.” *Sci. Technol. Weld. Join.*, 20(4), 280–285.

Engler, O., Kuhnke, K., and Hasenclever, J. (2017). “Development of intermetallic particles during solidification and homogenization of two AA 5xxx series Al-Mg alloys with different Mg contents.” *J. Alloys Compd.*, 728, 669–681.

Fahimpour, V., Sadrnezhad, S. K., and Karimzadeh, F. (2012). "Corrosion behavior of aluminum 6061 alloy joined by friction stir welding and gas tungsten arc welding methods." *Mater. Des.*, 39, 329–333.

Fang, X., Song, M., Li, K., and Du, Y. (2010). "Precipitation sequence of an aged Al-Mg-Si alloy." *J. Min. Metall. B Metall.*, 46(2), 171–180.

Fu, B., Qin, G., Li, F., Meng, X., Zhang, J., and Wu, C. (2015). "Friction stir welding process of dissimilar metals of 6061-T6 aluminum alloy to AZ31B magnesium alloy." *J. Mater. Process. Technol.*, 218, 38–47.

Ghaffarpour, M., Kazemi, M., Mohammadi Sefat, M. J., Aziz, A., and Dehghani, K. (2017). "Evaluation of dissimilar joints properties of 5083-H12 and 6061-T6 aluminum alloys produced by tungsten inert gas and friction stir welding." *Proc. Inst. Mech. Eng. Part L J. Mater. Des. Appl.*, 231(3), 297–308.

Ghaini, F. M., Sheikhi, M., Torkamany, M. J., and Sabbaghzadeh, J. (2009). "The relation between liquation and solidification cracks in pulsed laser welding of 2024 aluminium alloy." *Mater. Sci. Eng. A*, 519(1–2), 167–171.

Gungor, B., Kaluc, E., Taban, E., and Aydin, S. I. K. (2014a). "Mechanical and microstructural properties of robotic Cold Metal Transfer (CMT) welded 5083-H111 and 6082-T651 aluminum alloys." *Mater. Des.*, 54, 207–211.

Gungor, B., Kaluc, E., Taban, E., and S, A. S. I. K. (2014b). "Mechanical and microstructural properties of robotic Cold Metal Transfer (CMT) welded 5083-H111

and 6082-T651 aluminum alloys.” *Mater. Des.*, 54, 207–211.

Guo, S.-Q., and Li, X.-H. (2011). “Numerical simulation of solidification and liquation behavior during welding of low-expansion superalloys.” *Front. Mater. Sci.*, 5(2), 146–159.

Guojin, L., Peilei, Z., Xi, W., Yunpeng, N., Zhishui, Y., Hua, Y., and Qinghua, L. (2018). “Gap bridging of 6061 aluminum alloy joints welded by variable-polarity cold metal transfer.” 255(January), 927–935.

Gurao, N. P., and Suwas, S. (2013). “Deformation behaviour at macro- and nano-length scales: The development of orientation gradients.” *Mater. Lett.*, 99, 81–85.

Gutierrez, A., and Lippold, J. C. (1998). “A proposed mechanism for equiaxed grain formation along the fusion boundary in aluminum-copper-lithium alloys.” *Weld. J.*, 77(3).

Haboudou, A., Peyre, P., Vannes, A. B., and Peix, G. (2003). “Reduction of porosity content generated during Nd: YAG laser welding of A356 and AA5083 aluminium alloys.” *Mater. Sci. Eng. A*, 363(1–2), 40–52.

Hamada, A. S., Järvenpää, A., Ahmed, M. M. Z., Jaskari, M., Wynne, B. P., Porter, D. A., and Karjalainen, L. P. (2015). “The microstructural evolution of friction stir welded AA6082-T6 aluminum alloy during cyclic deformation.” *Mater. Sci. Eng. A*, 642, 366–376.

Hamilton, C., Dymek, S., and Sommers, A. (2008). “A thermal model of friction stir

welding in aluminum alloys.” 48, 1120–1130.

Han, B., Tao, W., Chen, Y., and Li, H. (2017). “Double-sided laser beam welded T-joints for aluminum-lithium alloy aircraft fuselage panels : Effects of filler elements on microstructure and mechanical properties.” *Opt. Laser Technol.*, 93, 99–108.

Han, H. N., and Clark, J. P. (1995). “Lifetime costing of the body-in-white: steel vs. aluminum.” *JOM*, 47(5), 22–28.

Han, M. S., Lee, S. J., Park, J. C., Ko, S. C., Woo, Y. Bin, and Kim, S. J. (2009). “Optimum condition by mechanical characteristic evaluation in friction stir welding for 5083-O Al alloy.” *Trans. Nonferrous Met. Soc. China (English Ed.*, 19(SUPPL. 1), s17–s22.

He, E., Liu, J., Lee, J., Wang, K., Politis, D. J., Chen, L., and Wang, L. (2018). “Effect of porosities on tensile properties of laser-welded Al-Li alloy: an experimental and modelling study.” *Int. J. Adv. Manuf. Technol.*, 95(1), 659–671.

Hirsch, J. (2011). “Aluminium in Innovative Light-Weight Car Design.” *Mater. Trans.*, 52(5), 818–824.

Jamshidi Aval, H. (2015). “Microstructure and residual stress distributions in friction stir welding of dissimilar aluminium alloys.” *Mater. Des.*, 87, 405–413.

Jannet, S., Mathews, P. K., and Raja, R. (2014). “Comparative investigation of friction stir welding and fusion welding of 6061 T6--5083 O aluminum alloy based on mechanical properties and microstructure.” *Bull. Polish Acad. Sci. Tech. Sci.*, 791–795.

Kannan, K., Hamilton, C. H., and Johnson, C. H. (1998). "A study of superplasticity in a modified 5083 Al-Mg-Mn alloy." *Metall. Mater. Trans. A*, 29(4), 1211–1220.

Kavitha, K. R., Kumar, G., Lakshmi, G., Mercy, J. L., Sivashankari, P., and Joy, N. (2021). "Evaluation study of mechanical properties of dissimilar materials through TIG welding process." *Mater. Today Proc.*, 44, 3894–3897.

Kim, N. K., Kim, B. C., An, Y. G., Jung, B. H., Song, S. W., and Kang, C. Y. (2009). "The effect of material arrangement on mechanical properties in friction stir welded dissimilar A5052/A5J32 aluminum alloys." *Met. Mater. Int.*, 15(4), 671–675.

Kostrivas, A., and Lippold, J. C. (2006). "Fusion boundary microstructure evolution in aluminium alloys." *Weld. World*, 50(11), 24–34.

Kotari, S., Punna, E., Reddy, S. M. G., and Venukumar, S. (2020). "Experimental Investigation and Micro Structural Characteristics of GTAW and FSW Welded Dissimilar Aluminum Alloys." *IOP Conf. Ser. Mater. Sci. Eng.*, 12036.

Kou, S. (2003). "Welding metallurgy." *New Jersey, USA*, 431–446.

Kutsuna, M., and Yan, Q. (1999). "Study on porosity formation in laser welds of aluminium alloys (Report 2). Mechanism of porosity formation by hydrogen and magnetism." *Weld. Int.*, 13(8), 597–611.

Lakshminarayanan, A. K., Balasubramanian, V., and Elangovan, K. (2009). "Effect of welding processes on tensile properties of AA6061 aluminium alloy joints." *Int. J. Adv. Manuf. Technol.*, 40(3–4), 286–296.

Li, Q., Wu, A., Li, Y., Wang, G., Yan, D., and Liu, J. (2015). “In fl uence of temperature cycles on the microstructures and mechanical properties of the partially melted zone in the fusion welded joints of 2219 aluminum alloy.” *Mater. Sci. Eng. A*, 623, 38–48.

Li, X., Li, X., Xiong, H., Li, Y., Guo, S., and Zhang, X. (2007). “Microstructure and Crack Susceptibility of Aluminium-Lithium Alloy Weldment.” *J. Aeronaut. Mater.*, 27(3), 55.

Liang, Y., Shen, J., Hu, S., Wang, H., and Pang, J. (2018). “E ff ect of TIG current on microstructural and mechanical properties of 6061- T6 aluminium alloy joints by TIG – CMT hybrid welding.” *J. Mater. Process. Tech.*, 255(August 2017), 161–174.

Lin, D. C., Wang, G. X., and Srivatsan, T. S. (2003). “A mechanism for the formation of equiaxed grains in welds of aluminum-lithium alloy 2090.” *Mater. Sci. Eng. A*, 351(1–2), 304–309.

Lin, J., Ma, N., Lei, Y., and Murakawa, H. (2013). “Shear strength of CMT brazed lap joints between aluminum and zinc-coated steel Steel.” *J. Mater. Process. Tech.*, 213(8), 1303–1310.

Liu, Y. B., Sun, Q. J., Sang, H. B., and Feng, J. C. (2015). “Microstructure and mechanical properties of cold metal transfer welded aluminium/nickel lap joints.” *Sci. Technol. Weld. Join.*, 20(4), 307–312.

Liu, Y., Wang, W., Xie, J., Sun, S., Wang, L., Qian, Y., Meng, Y., and Wei, Y. (2012). “Microstructure and mechanical properties of aluminum 5083 weldments by gas tungsten

arc and gas metal arc welding.” *Mater. Sci. Eng. A*, 549, 7–13.

Lu, L., Thong, K. K., and Gupta, M. (2003). “Mg-based composite reinforced by Mg₂Si.” *Compos. Sci. Technol.*, 63(5), 627–632.

Massalski, T. B., Okamoto, H., Subramanian, P. R., and Kacprzak, L. (1990). “Binary alloy phase diagrams.” *ASM Int. Materials Park, Ohio*, 2nd editio, 212.

Mathers, G. (2002). *The welding of aluminium and its alloys*. Woodhead publishing.

McShane, H. B., Lee, C. P., and Sheppard, T. (1990). “Structure, anisotropy, and properties of hot rolled AA 5083 alloy.” *Mater. Sci. Technol.*, 6(5), 428–440.

Messler Jr, R. W. (1999). “Principles of Welding; Processes, Physics, Chemistry, and Metallurgy, John Willey & Sons.” *Inc., New York*.

Messler, R. W. (2004). *Joining of materials and structures: from pragmatic process to enabling technology*. Butterworth-Heinemann.

Milani, A. M., and Paidar, M. (2016). “Investigation on effect of pulse correction on structure property in dissimilar welds of galvanized steel and aluminum alloy obtained by gas metal arc welding cold metal transfer.” *Russ. J. Non-Ferrous Met.*, 57(5), 467–476.

Mishra, A. (2018). “Friction Stir Welding of Dissimilar Metal: A Review.” *Int. J. Res. Appl. Sci. Eng. Technol.*, 6(1), 1551–1559.

Mishra, R. S., and Ma, Z. Y. (2005). “Friction stir welding and processing.” *Mater. Sci. Eng. R Reports*, 50(1–2), 1–78.

- Murray, J. L. (1982). "The Al- Mg (aluminum- magnesium) system." *J. Phase Equilibria*, 3(1), 60.
- Murray, J. L., Bennett, L. H., and Baker, H. (1986). *Binary alloy phase diagrams*. ASM International (OH).
- Murray, J. L., and McAlister, A. J. (1984). "The Al-Si (Aluminum-Silicon) system." *Bull. Alloy Phase Diagrams*, 5(1), 74–84.
- Myhr, O. ., Grong, Ø., and Andersen, S. . (2001). "Modelling of the age hardening behaviour of Al–Mg–Si alloys." *Acta Mater.*, 49(1), 65–75.
- Myhr, O. R., Grong, Fjær, H. G., and Marioara, C. D. (2004). "Modelling of the microstructure and strength evolution in al-mg-si alloys during multistage thermal processing." *Acta Mater.*, 52(17), 4997–5008.
- Nami, H., Adgi, H., Sharifitabar, M., and Shamabadi, H. (2011). "Microstructure and mechanical properties of friction stir welded Al/Mg₂Si metal matrix cast composite." *Mater. Des.*, 32(2), 976–983.
- Nayan, N., Murty, S. V. S. N., Chhangani, S., Prakash, A., Prasad, M. J. N. V., and Samajdar, I. (2017). "Effect of temperature and strain rate on hot deformation behavior and microstructure of Al-Cu-Li alloy." *J. Alloys Compd.*, 723, 548–558.
- Ning, J., Zhang, L., Bai, Q., Yin, X., Niu, J., and Zhang, J. (2017). "Comparison of the microstructure and mechanical performance of 2A97 Al-Li alloy joints between autogenous and non-autogenous laser welding." *Mater. Des.*, 120, 144–156.

- Oates, W. R., and Saitta, A. M. (1998). "Welding Handbook. Vol. 4. Materials and Applications--Part 2." *Am. Weld. Soc. 550 NW LeJeune Rd, P. O. Box 351040, Miami, FL 33135, USA, 1998. 621.*
- Palanivel, R., Koshy Mathews, P., Murugan, N., and Dinaharan, I. (2012). "Effect of tool rotational speed and pin profile on microstructure and tensile strength of dissimilar friction stir welded AA5083-H111 and AA6351-T6 aluminum alloys." *Mater. Des.*, 40, 7–16.
- Patel, V., Li, W., Vairis, A., and Badheka, V. (2019). "Recent Development in Friction Stir Processing as a Solid-State Grain Refinement Technique: Microstructural Evolution and Property Enhancement." *Crit. Rev. Solid State Mater. Sci.*, 44(5), 378–426.
- Pavan, N., Vendan, S. A., and Shanmugam, N. S. (2016). "Investigations on the parametric effects of cold metal transfer process on the microstructural aspects in AA6061." *J. Alloys Compd.*, 658, 255–264.
- Peasura, P., and Watanapa, A. (2012). "Influence of shielding gas on aluminum alloy 5083 in gas tungsten arc welding." *Procedia Eng.*, 29, 2465–2469.
- Pickin, C. G., Williams, S. W., and Lunt, M. (2011). "Journal of Materials Processing Technology Characterisation of the cold metal transfer (CMT) process and its application for low dilution cladding." *J. Mater. Process. Tech.*, 211(3), 496–502.
- Pickin, C. G., and Young, K. (2006). "Evaluation of cold metal transfer (CMT) process for welding aluminium alloy." *Sci. Technol. Weld. Join.*, 11(5), 583–585.

Polkowski, W., Józwik, P., and Bojar, Z. (2014). “EBSD and X-ray diffraction study on the recrystallization of cold rolled Ni₃Al based intermetallic alloy.” *J. Alloys Compd.*, 614, 226–233.

Ramasamy, S., and Albright, C. E. (2001). “CO₂ and Nd–YAG laser beam welding of 5754–O aluminium alloy for automotive applications.” *Sci. Technol. Weld. Join.*, 6(3), 182–190.

Rao, D., Huber, K., Heerens, J., Santos, J. F. Dos, and Huber, N. (2013). “Asymmetric mechanical properties and tensile behaviour prediction of aluminium alloy 5083 friction stir welding joints.” *Mater. Sci. Eng. A*, 565, 44–50.

Reddy, G. M., Gokhale, A. A., and Prasad, K. S. (1998). “Chill zone formation in Al – Li alloy welds Chill zone formation in Al-Li alloy welds.” *Sci. Technol. Weld. Join.*, 3(4), 208–212.

Robe, H., Zedan, Y., Chen, J., Monajati, H., Feulvarch, E., and Bocher, P. (2015). “Microstructural and mechanical characterization of a dissimilar friction stir welded butt joint made of AA2024-T3 and AA2198-T3.” *Mater. Charact.*, 110, 242–251.

Rodriguez, R. I., Jordon, J. B., Allison, P. G., Rushing, T., and Garcia, L. (2015). “Microstructure and mechanical properties of dissimilar friction stir welding of 6061-to-7050 aluminum alloys.” *Mater. Des.*, 83, 60–65.

S. Kou, Y. L. (1986). “Nucleation Mechanisms and Grain Refining of Weld Metal.” *Weld. Research Suppl.*, 65(December), 305–313.

Shah, S. R. (1993). “Microstructural analysis of the failure mode in Al-Cu and Al-Cu-Li alloy VPPA welds.” Vanderbilt University.

Shahid, R. N., and Scudino, S. (2018). “Microstructure and Mechanical Behavior of Al-Mg Composites Synthesized by Reactive Sintering.” *Metals (Basel)*, 8(10), 762.

Shang, J., Wang, K., Zhou, Q., Zhang, D., Huang, J., and Li, G. (2012). “Microstructure characteristics and mechanical properties of cold metal transfer welding Mg / Al dissimilar metals.” *Mater. Des.*, 34, 559–565.

Shang, X., Zhang, H., Cui, Z., Fu, M. W., and Shao, J. (2020). “A multiscale investigation into the effect of grain size on void evolution and ductile fracture: Experiments and crystal plasticity modeling.” *Int. J. Plast.*, 125(May 2019), 133–149.

Simoncini, M., and Forcellese, A. (2012). “Effect of the welding parameters and tool configuration on micro-and macro-mechanical properties of similar and dissimilar FSWed joints in AA5754 and AZ31 thin sheets.” *Mater. Des.*, 41, 50–60.

Singh, G., Singh, K., and Singh, J. (2014). “Modelling of the effect of process parameters on tensile strength of friction stir welded aluminium alloy joints.” *Exp. Tech.*, 38(3), 63–71.

Singh, R. K. R., Sharma, C., Dwivedi, D. K., Mehta, N. K., and Kumar, P. (2011). “The microstructure and mechanical properties of friction stir welded Al-Zn-Mg alloy in as welded and heat treated conditions.” *Mater. Des.*, 32(2), 682–687.

Sivashanmugam, M., Kumar, K. A., Kajabanthanas, R., and Ahaned, M. A. E. (2014).

“Effect of process parameters on tensile strength in gas metal arc welding joints AA7075-T6 aluminium alloy by using regression and response surface model.” *Int. J. Res. Eng. Technol.*, 3, 162–166.

Sivashanmugam, M., Kumar, T., Shanmugam, C. J., and Sathishkumar, M. (2010). “Investigation of microstructure and mechanical properties of GTAW and GMAW joints on AA7075 aluminum alloy.” *Front. Automob. Mech. Eng.*, 241–246.

Starink, M. J., and Wang, S. C. (2003). “A model for the yield strength of overaged Al-Zn-Mg-Cu alloys.” *Acta Mater.*, 51(17), 5131–5150.

Straumal, B. B., Baretzky, B., Kogtenkova, O. A., Straumal, A. B., and Sidorenko, A. S. (2010). “Wetting of grain boundaries in Al by the solid Al₃Mg₂ phase.” *J. Mater. Sci.*, 45(8), 2057–2061.

Straumal, B. B., Gust, W., and Molodov, D. A. (1995). “Wetting transition on grain boundaries in Al contacting with a Sn-rich melt.” *Interface Sci.*, 3(2), 127–132.

Straumal, B., Muschik, T., Gust, W., and Predel, B. (1992). “The wetting transition in high and low energy grain boundaries in the Cu (In) system.” *Acta Metall. Mater.*, 40(5), 939–945.

Suresha, C. N., Rajaprakash, B. M., and Upadhya, S. (2011). “A study of the effect of tool pin profiles on tensile strength of welded joints produced using friction stir welding process.” *Mater. Manuf. Process.*, 26(9), 1111–1116.

Svensson, L., Karlsson, L., Larsson, H., Karlsson, B., Fazzini, M., and Karlsson, J.

(2000). “Microstructure and mechanical properties of friction stir welded aluminium alloys with special reference to AA 5083 and AA 6082.” *Sci. Technol. Weld. Join.*, 5(5), 285-296.

Tehyo, M., Palasai, P., Mekharat, A., Muangjunburee, P., Suthummanon, S., Binraheem, A., Bin-ahmad, H., Meengam, C., and Chainarong, S. (2018). “Experimental Comparison of TIG and Friction Stir Welded for Dissimilar Aluminum Alloy Plates.” *2018 Third Int. Conf. Eng. Sci. Innov. Technol.*, 1–5.

Tisza, M., and Czinege, I. (2018). “Comparative study of the application of steels and aluminium in lightweight production of automotive parts.” *Int. J. Light. Mater. Manuf.*, 1(4), 229–238.

Trueba Jr, L., Heredia, G., Rybicki, D., and Johannes, L. B. (2015). “Effect of tool shoulder features on defects and tensile properties of friction stir welded aluminum 6061-T6.” *J. Mater. Process. Technol.*, 219, 271–277.

Tsao, C.-S., Chen, C.-Y., Jeng, U.-S., and Kuo, T.-Y. (2006). “Precipitation kinetics and transformation of metastable phases in Al–Mg–Si alloys.” *Acta Mater.*, 54(17), 4621–4631.

Ünel, E., and Taban, E. (2017). “Properties and optimization of dissimilar aluminum steel CMT welds.” *Weld. World*, 61(1), 1–9.

Wang, J., Feng, J. C., and Wang, Y. X. (2008). “Microstructure of Al–Mg dissimilar weld made by cold metal transfer MIG welding.” *Mater. Sci. Technol.*, 24(7), 827–831.

Wang, Q., Chen, H., Zhu, Z., Qiu, P., and Cui, Y. (2016a). "A characterization of microstructure and mechanical properties of A6N01S-T5 aluminum alloy hybrid fiber laser-MIG welded joint." *Int. J. Adv. Manuf. Technol.*, 1375–1384.

Wang, T., Zou, Y., and Matsuda, K. (2016b). "Micro-structure and micro-textural studies of friction stir welded AA6061-T6 subjected to different rotation speeds." *Mater. Des.*, 90, 13–21.

Yan, F., Liu, S., Hu, C., Wang, C., and Hu, X. (2017). "Liquation cracking behavior and control in the heat affected zone of GH909 alloy during Nd: YAG laser welding." *J. Mater. Process. Technol.*, 244, 44–50.

Yan, Z., Liu, X., and Fang, H. (2016). "Effect of Sheet Configuration on Microstructure and Mechanical Behaviors of Dissimilar Al–Mg–Si/Al–Zn–Mg Aluminum Alloys Friction Stir Welding Joints." *J. Mater. Sci. Technol.*, 32(12), 1378–1385.

Yang, S., Zhang, J., Lian, J., and Lei, Y. (2013). "Materials and Design Welding of aluminum alloy to zinc coated steel by cold metal transfer." *Mater. Des.*, 49, 602–612.

Yuan, S. P., Liu, G., Wang, R. H., Pu, X., Zhang, G. J., Sun, J., and Chen, K. H. (2007). "Coupling effect of multiple precipitates on the ductile fracture of aged Al-Mg-Si alloys." *Scr. Mater.*, 57(9), 865–868.

Yunjia, H., Frost, R. H., Olson, D. L., and Edwards, G. R. (1989). "Grain refinement of aluminum weld metal." *Weld. J.*, 68(7), 280s--289s.

Zhang, H. T., Feng, J. C., He, P., Zhang, B. B., Chen, J. M., and Wang, L. (2009). "The

arc characteristics and metal transfer behaviour of cold metal transfer and its use in joining aluminium to zinc-coated steel.” 499, 111–113.

Zhang, L., and Wang, X. (2018). “Microstructure evolution and properties of friction stir welding joint for 6082-T6 aluminum alloy.” *Mater. Res.*, 21(6), 1–10.

Zhang, Z., Xiao, B. L., Wang, D., and Ma, Z. Y. (2011). “Effect of alclad layer on material flow and defect formation in friction-stir-welded 2024 aluminum alloy.” *Metall. Mater. Trans. A*, 42(6), 1717–1726.

Zhao, H., and Debroy, T. (2001). “Weld metal composition change during conduction mode laser welding of aluminum alloy 5182.” *Metall. Mater. Trans. B*, 32(1), 163–172.

Zhou, M., Lin, Y. C., Deng, J., and Jiang, Y.-Q. (2014). “Hot tensile deformation behaviors and constitutive model of an Al–Zn–Mg–Cu alloy.” *Mater. Des.*, 59, 141–150.

LIST OF PUBLICATIONS

PUBLICATIONS IN PEER-REVIEWED JOURNALS

1. **R. Rajeshkumar**, K. Devakumaran and Kumkum Banerjee, “Role of interfacial microstructure on mechanical properties of cold metal transfer welded dissimilar A6061-T6 and A6082-T6 joints”, Materials Letters 279 (2020) 128521.
2. **R. Rajeshkumar**, V. L. Niranjani, K. Devakumaran and Kumkum Banerjee, “Fusion boundary microstructure evolution and mechanical properties of cold metal transfer welded dissimilar A5754 and A5083 joint”, Materials Letters 284 (2021) 128877.
3. **R. Rajeshkumar**, V. L. Niranjani, K. Devakumaran and Kumkum Banerjee. “Evolution of non-dendritic equiaxed zone and its influence on mechanical properties of tungsten inert gas welded dissimilar A6061-T6 and A6082-T6 joint”. Materials Letters 303 (2021) 130569.
4. **R. Rajeshkumar**, V. L. Niranjani, K. Devakumaran and Kumkum Banerjee, “Structure-property correlation of weld metal zone and interface regions of cold metal transfer welded dissimilar Al-Mg-Mn alloys joint”, Materials Today: Proceedings (2021).
5. **R. Rajeshkumar**, K. Devakumaran and Kumkum Banerjee, “Microstructure and mechanical properties of friction stir welded dissimilar Al-2.6Mg-0.5Mn (A5754) and Al-4.5Mg-1.0Mn (A5083) joint”, (Under Review).

6. **R. Rajeshkumar**, V. L. Niranjani, K. Devakumaran and Kumkum Banerjee, “Evolution of hot cracks and its effect on mechanical properties of cold metal transfer welded (CMT) dissimilar Al-Mg-Si alloys joint”, (Under Review).
7. **R. Rajeshkumar**, V. L. Niranjani, K. Devakumaran and Kumkum Banerjee, “Effect of filler materials on microstructural evolution and mechanical properties of tungsten inert gas welded dissimilar A5754 and A5083 joint”, (Under preparation).
8. **R. Rajeshkumar**, V. L. Niranjani, K. Devakumaran and Kumkum Banerjee, “Microstructure and mechanical properties of friction stir welded dissimilar A6061-T6 and A6082-T6 joint”, (Under preparation).

CONFERENCE PRESENTATIONS

1. **R. Rajeshkumar**, V. L. Niranjani, K. Devakumaran and Kumkum Banerjee, “Structure-property correlation of weld metal zone and interface regions of cold metal transfer welded dissimilar Al- Mg-Mn alloys joint”, International Conference on Smart and Sustainable developments in Materials, Manufacturing and Energy Engineering (SME-2020) at NMAM Institute of Technology, Nitte, Karnataka, India, December, 2020 (Oral presentation).
2. **R. Rajeshkumar**, V. L. Niranjani, K. Devakumaran and Kumkum Banerjee, “Microstructure and mechanical properties of friction stir welded dissimilar A6061 and A6082 aluminium joint” 57th National Metallurgist’s Day (NMD) and the 73rd Annual Technical Meeting (ATM) at Thiruvananthapuram, Kerala, November, 2019 (Poster presentation).

3. **R. Rajeshkumar**, K. Devakumaran and Kumkum Banerjee, “A study on microstructure and mechanical properties in friction stir welding of dissimilar A5754 and A5083 aluminium” International conference on advanced materials and manufacturing process for strategic sectors (ICAMPS) at Thiruvananthapuram, Kerala, November, 2018 (Poster presentation).
4. **R. Rajeshkumar**, K. Devakumaran and Kumkum Banerjee, “Welding of dissimilar A6061-T6 and A6082-T6 alloys using GTAW process” International Symposium on Joining of Materials (SOJOM), at BHEL, Trichy, Tamil Nadu, April, 2018 (Oral presentation).

CURRICULUM VITAE

Name : R.RAJESHKUMAR

Permanent Address: A232, NGO-A colony, Tirunelveli, Tamilnadu- 627007

Contact No. : +91-7204312447

Email ID : rrajeshkumarmech@gmail.com

EDUCATION

Master of Engineering (M.E) in Industrial Metallurgy (2013) from PSG College of Technology, Coimbatore, (Anna University, Chennai); (CGPA: 8.7/10, Distinction)

Bachelor of Engineering (B.E) in Mechanical Engineering (2009) from Arulmigu Kalasalingam college of engineering, Srivilliputhur, (Anna University, Chennai); (77%, Distinction)

WORK EXPERIENCE

Worked as a Project Fellow in National Institute for Interdisciplinary Science and Technology, (NIIST-CSIR Lab) Thiruvananthapuram, India (August 2013 to January 2016).